



**Swansea University**  
**Prifysgol Abertawe**

# Novel Galvanic Coatings for Airport Ground Support Equipment

**Daniel Michael Murphy**

Swansea University

Submitted to Swansea University in fulfilment of the  
requirements for the Degree of Engineering Doctorate.

June 2024

## **Declarations**

This work has not previously been accepted in substance for any degree and is not being concurrently submitted in candidature for any degree.

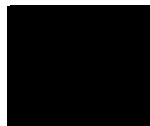
Signed



Date: 22/05/2025

This thesis is the result of my own investigations, except where otherwise stated. Other sources are acknowledged by footnotes giving explicit references. A bibliography is appended.

Signed



Date: 22/05/2025

I hereby give consent for my thesis, if accepted, to be available for electronic sharing

Signed



Date: 22/05/2025

The University's ethical procedures have been followed and, where appropriate, that ethical approval has been granted.

Signed



Date: 22/05/2025

# Acknowledgements

I would firstly like to thank my EngD supervisor Prof. Dave Penney for his guidance and leadership in completing this project. Dave's patience and support during the rollercoaster ride of this project has been essential and I will be forever grateful for his willingness to help and offer advice. Also, his readiness to reply to an email or Whatsapp message at any time of day or night, sometimes across several time zones is greatly appreciated and a testament to his commitment in driving the research forward! Cheers Dave!

Thanks also to my secondary supervisor Prof. Jim Sullivan. Jim's suggestions and ability to look outside of the box has been pivotal to many aspects of this project.

Special thanks to Dr. Amar Malla. Amar's help in training me on several pieces of equipment and assistance in completing many experiments has been essential to the completion of this project and thesis. I am incredibly grateful for all his help.

To everyone at Swansea University, past or present, that helped in any way with this project or keeping me sane during it. To name but a few: Everyone at the Materials, Manufacturing and Modelling Academy (M2A) – I am forever grateful for the opportunity, Dr Chris Griffiths, Dr Tom Lewis, Gareth Davies, the B216 office crew (!), all the staff at the SPECIFIC PMRC, Dr Lee Bridgeman, Francis Moseray and Tumaini Odero.

Special thanks to Dr Daniel Rees (*Innovation ILA, School of Management, Swansea University*) for his steadfast friendship and support throughout this project and my whole life for the past ~29 years! For the many pints, coffees, meals and times we've shared, I'm so very thankful and look forward to many more.

Thanks to all the staff at the Innovation ILA at Swansea University's School of Management. My time as an intern there was an absolute blast, and I am so very thankful to the amazing team for all their coffee, ongoing support and encouragement.

To my wife, Nicole, I owe perhaps the biggest thank you of all. Your support and belief in me have been astounding. You've put up with so much while I complete this project and I'm so thankful to you for allowing me to chase this dream. From supporting me financially during write-up to comforting me when times got tough, it is certain that I would not be where I am today without your love and compassion.

Also, to the best good boy in the world, Smithwick, our much-loved dog! The best writing partner I could ask for, laying in his favourite spot under my desk.

To my sister Siân, brother-in-law Stuart (and his family), my grandmother Betty and all my family, I am so thankful for all the support you have offered me over the last 5 years. Your belief in me seems to know no bounds and I will be forever indebted to you all in so many ways. I am so glad to have you all in my life.

Thank you to the Jackson family for all your support and assistance with everything the past few years. The help you have given to Nicole and I in building our life together has been incredible and I am forever grateful for everything you've all done for us.

All my friends, far and wide, you have made this past five years bearable just by being there. Too many to list here and more appreciated than I can express, I would be lost without you all. Cheers!

Lastly, I would like to dedicate this work to my late parents, Gaynor and Michael Murphy. If it was not for all their support from a young age, I simply would not be writing this. My parents instilled in me the drive and determination that has made this work possible. Always loving, always loved.

# Abstract

The motivation for the work presented in this thesis is the need for a low-temperature solution for the corrosion protection of steel Ground Support Equipment and the repair of failed hot-dipped galvanised (HDG) components. With this development, it is hoped that lead time on projects and some overhead costs will be cut. This would be potentially possible as the need to outsource galvanising would be no longer necessary.

Hot-dip galvanising can be an expensive process with the need to transport large products to dedicated galvanising baths making it logistically inefficient and costly. Another issue is the repair of galvanised products, often leading to the expulsion of toxic Zn fumes and leaving the repaired area unprotected against corrosive attack. Zinc-rich paints (ZRPs) are a commonly used coating in the repair of HDG. Several issues are reported with conventional zinc-rich paints and the need for a more durable and protective solution for steel components is evident.

To achieve this, a novel coating is developed using zinc-rich paints as a model, instead replacing the organic/inorganic binder with a metallic matrix. The inclusion of a metallic component with the zinc, seeks to overcome the adhesion and deterioration failures often found in ZRPs.

Bismuth-tin (Bi-Sn) fusible alloy was chosen as the metallic matrix component for a new coating, owing to its well-known low-temperature properties that see it utilised across industry and society. To develop the coating, various Zn loadings in Bi-Sn were trialled and analysed via scanning electron microscopy of the resulting microstructure. Time and temperature of heat treatment were also analysed in the same way. It was found that a composition of 20 wt% Zn and 80 wt% Bi-Sn heated at 245 °C for 45 minutes produced a microstructure that showed Zn “islands” surrounded by a Bi-Sn matrix. Time dependent heating trials showed that Bi-Sn coalesced and coarsened with time, peaking at 50 minutes.

Several coating compositions were tested for corrosion protection. Scanning Vibrating Electrode Technique (SVET) experiments showed that the addition of Zn to Bi-Sn made for a sustained galvanic protection throughout a 24 hour test. 20 wt% Zn and 30 wt% Zn exhibited the galvanic protection necessary, 10 wt% Zn showed instances of internal coupling.

Open Circuit Potential (OCP) measurements showed that the novel Bi-Sn + Zn coating exhibited a lower OCP than that of steel, explaining the SVET results. Linear Polarisation Resistance showed low readings for polarisation resistance values, but comparable to other coatings in literature. Zero Resistance Ammetry confirmed SVET and OCP results, showing current flow from Bi-Sn + Zn coating to the steel substrate. However, the relationship between Bi-Sn and steel required further investigation and cathodic sweeps found that steel acts as a better cathode than Bi-Sn and explained the coating system’s protection of steel.

Lifetime estimations are presented through calculations involving Zn volume and mass along with SVET – derived mass loss values. An estimated lifetime range of around 12-30 years is given.

Mechanical properties such as adhesion and hardness were also investigated. It was shown that Zn addition had no effect on hardness. Adhesion testing showed that 20 wt% Zn / 80 wt% Bi-Sn offered good adhesion to the substrate under harsh bend test conditions with no cracking, flaking or delamination present.

Near infrared (NIR) heating was explored as an alternative heating method to offer rapid curing of the novel coating. It was shown that 30% of the NIR power (up to  $250 \text{ kWm}^{-2}$ ) with a belt speed of 0.5 m/min offered the best microstructural results. Powers below 30% did not heat up to high enough temperatures and powers above 30% took the temperature of the sample too high.

Fluxing was also investigated. Two fluxes, Zinc chloride and phosphoric acid flux, were compared for their wetting of Bi-Sn to a steel substrate. Zinc chloride showed superior wetting, owing to a thin layer of tin wetting to the steel surface.

# Table of Contents

## Contents

List of Figures .....	6
List of Tables .....	12
Definitions.....	13
Chapter 1: Introduction and Literature Review .....	14
1.1 Research Objectives and Aims .....	15
1.2 Literature Review.....	17
1.2.1 Introduction.....	17
1.2.2 Corrosion.....	24
1.2.3 Hot-Dip Galvanising.....	29
1.2.4 Cold Galvanising Coatings .....	35
1.2.5 Fusible Alloys .....	39
1.2.6 Wetting and Fluxes .....	46
1.2.7 Conclusion .....	49
Chapter 2: Experimental Procedure .....	50
2.1 Materials .....	51
2.1.1 Metals.....	52
2.1.2 Novel Coating .....	52
2.2 Coating Production .....	53
2.2.1 Substrate Surface Preparation and Coating Application.....	53
2.2.2 Alternative Heating/ Curing.....	55
2.3 Metallographic Preparation.....	55
2.4 Microscopy .....	56
2.5 Hardness Testing.....	56

2.5.1 Vickers Hardness Testing .....	57
2.5.2 Testing Parameters .....	58
2.6 Adhesion Testing .....	58
2.7 Electrochemical Measurements .....	59
2.7.1 Open Circuit Potential (OCP) .....	59
2.7.2 Zero Resistance Ammetry (ZRA) .....	61
2.7.3 Potentiodynamic Sweeps .....	62
2.8 Scanning Vibrating Electrode Technique (SVET).....	63
2.8.1 Calibration of the SVET .....	66
2.8.2 SVET Sample Preparation .....	68
2.8.3 Manipulation and Analysis of SVET Data.....	69
2.8.4 Limitations of SVET.....	71
2.9 Long Term Exposure Testing .....	71
Chapter 3: Development and Optimisation of Microstructure and Process for a Novel	
Galvanic Coating .....	73
3.1 Introduction.....	74
3.2 Experimental Details.....	77
3.2.1 Materials .....	77
3.2.2 Sample Preparation .....	78
3.3 Methods.....	79
3.4 Results.....	80
3.4.1 Zn Loading for Microstructure Optimisation.....	80
3.4.2 Curing Time and Temperature Optimisation for Microstructure.....	89
3.5 The Effect of Heating Time on Bi-Sn Matrix Development.....	96

3.6 The Effect of Alloying Zn with Bi-Sn on Microstructure.....	98
3.7 Discussion.....	100
3.6 Conclusions.....	105
Chapter 4: An Electrochemical Investigation into the Galvanic Protection of Bi-Sn + Zn	
Coating.....	107
4.1 Introduction.....	108
4.2 Experimental Methods .....	110
4.2.1 Sample Preparation .....	110
4.2.2 Scanning Vibrating Electrode Technique (SVET) Procedure.....	111
4.2.3 Open Circuit Potential (OCP) .....	112
4.2.4 Potentiodynamic Sweeps .....	113
4.2.5 Zero Resistance Ammetry (ZRA) / Galvanic Corrosion Tests (GalvCorr).....	113
4.2.6 Long Term Exposure Tests .....	114
4.3 Results.....	115
4.3.1 SVET Testing of Candidate Coatings.....	115
4.3.2 SVET Derived Mass Loss.....	120
4.3.3 Open Circuit Potential (OCP) Measurements .....	121
4.3.4 Polarisation Resistance .....	124
4.3.5 Zero Resistance Ammetry (ZRA) .....	125
4.3.6 Potentiodynamic Sweeps .....	129
4.3.7 Long-Term Exposure Testing .....	131
4.3.8 Lifetime Estimation Calculations.....	134
4.4 Discussion.....	139
4.5 Conclusions.....	144



Chapter 5: Physical Properties of a Novel Bi-Sn + Zn Coating.....	147
5.1 Introduction.....	148
5.2 Experimental Details and Methods .....	149
5.2.1 Sample Preparation .....	149
5.2.2 Vickers Hardness Testing .....	150
5.2.3 Adhesion Testing .....	150
5.2.4 Wetting.....	151
5.3 Results.....	153
5.3.1 Vickers Hardness Testing as a Function of Zn Content.....	153
5.3.2 Adhesion Testing .....	154
5.3.3 Wettability of Coating Constituents.....	155
5.4 Discussion.....	157
5.5 Conclusions.....	160
Chapter 6: Alternative Production Methods for a Novel Galvanic Coating .....	162
6.1 Introduction.....	163
6.2 Experimental Details and Methods .....	164
6.2.1 NIR Curing.....	164
6.2.2 Alternative Fluxing .....	166
6.2.3 Microscopy .....	167
6.3 Results.....	167
6.3.1 NIR Heat Treatment.....	167
6.3.2 Alternative Fluxes.....	177
6.4 Discussion.....	180
6.5 Conclusions.....	186

Chapter 7 : Conclusions and Further Work .....	189
7.1 Conclusions.....	189
7.2 Future Work.....	191
Chapter 8 References .....	193

# List of Figures

Figure 1. 1 - Pourbaix diagram for iron in water at 25°C [41].....	25
Figure 1. 2 - Schematic of Evans diagram, from [50].....	27
Figure 1. 4 - Pourbaix Diagram for Zinc in water at 25°C [45].....	29
Figure 1. 7 - Binary alloy phase diagram for Bi-Sn.....	41
Figure 1. 8 - a) Optical image of Bi-Sn microstructure and b) post-corrosion SEM image of Bi-Sn showing selective attack on the Sn-rich phase, taken from [67].....	42
Figure 1. 9 - Ternary Phase Diagram of Bi-Sn-Zn isothermal section at 160C from [70].....	45
Figure 1. 10 - A schematic showing various wetting qualities: a) absolute wetting, b) good wetting, c) bad wetting and d) absolute nonwetting [77].....	46
Figure 2. 1 - Camera image showing a 50 x 50 mm steel coupon bar-coated in novel Bi-Sn + Zn coating. ....	54
Figure 2. 2 - Schematic of a standard Vickers diamond-shaped indenter.....	57
Figure 2. 3 - Schematic showing the process of adhesion testing.....	58
Figure 2. 4 - Schematic of OCP experimental set up. ....	60
Figure 2. 5 - Schematic of ZRA experimental set up.....	61
Figure 2. 6 - Schematic of experimental setup for potentiodynamic sweeps and Linear Polarisation Resistance (LPR). ....	62
Figure 2. 7 - Schematic of SVET set up .....	63
Figure 2. 8 - A schematic representing current flux and iso-potential lines above an anode. ....	65
Figure 2. 9 - Current emerging from a point current source. ....	66
Figure 2. 10 - Schematic of two-compartment cell used in SVET calibration. ....	67
Figure 2. 11 - Schematic of Top and Side View of prepared SVET sample. ....	68
Figure 2. 12 - Representative SVET colour map of resolved current density, created with SVET data using Golden's Surfer 10. ....	69

Figure 2. 13 - Map showing location of long-term exposure testing at SPECIFIC PMRC. Taken from Google maps.....	72
Figure 3.1 - Digital Camera picture of the Bi-Sn paste, as received. Shown here on a wooden splint.	
Figure 3.2 - An SEM micrograph of Bi-Sn microstructure and the corresponding EDS map with Bi represented in red and Sn in green. ....	77
Figure 3.3 - schematic of intended coating design showing Zn islands enveloped by a Bi-Sn matrix. ....	81
Figure 3. 4 - SEM image of 100BiSn heat treated at 180C for 10 minutes. ....	81
Figure 3. 5 - EDS map of 100BS, Bi is represented in blue and Sn in red.....	88
Figure 3. 6 - EDS map of 20Z, Bi is blue, Sn is red, and Zn is neon green. A region of interest is circled in yellow. ....	81
Figure 3. 7 - SEM image of 20Z showing poor melting of the Sn Bi phase, with the area of interest circled in red.....	90
Figure 3. 8 - SEM image of 50Z at 1000x magnification. ....	91
Figure 3. 9 - EDS map of 50Z at 5000x magnification.....	91
Figure 3. 10 - SEM image of 90Z at 1000x magnification. ....	93
Figure 3. 11 - EDS map of 90Z. Bi is red, Sn is green, and Zn is dark blue.....	93
Figure 3. 12- EDS maps showing 20Z heated at 200°C for a) 20mins and b) 40mins. ....	95
Figure 3. 13 - Digital Microscope image of 20Z, cured for 40mins at 245°C at 1000x magnification. ....	96
Figure 3. 14 - EDS maps showing 50Z heated at 200°C for a) 20mins and b) 40mins. ....	97
Figure 3. 15 - Digital Microscope images of a) 10Z, b) 30Z and c) 40Z, at 2500x magnification. ....	99

Figure 3. 16 - SEM images showing 20wt% Zn / 80wt% Bi-Sn samples heat treat at 245°C for a) 10 minutes, b) 20 minutes, c) 30 minutes, d) 40 minutes and e) 50 minutes. ....	100
Figure 3. 17 - SEM image of 20wt% Zn / 80wt% Bi-Sn coating heat treated at 245°C for 24 hours (1440 minutes). ....	101
Figure 3. 18 - SEM image of 80wt% Bi-Sn 20wt% Zn alloy heated at 480 °C for 2 hours and furnace cooled. ....	102
Figure 3. 19 - Images of a 20wt% Zn / 80wt% Bi-Sn sample heated to 480C for 2 hours and furnace cooled: a) EDS scanned image, b) EDS colour map for Bi, Sn and Zn, c) EDS colour map for Zn, d) EDS colour map for Bi and e) EDS colour map for Sn .....	103
Figure 3. 20 - SEM image of the as-received Zn dust/powder. ....	104
Figure 3. 21 - Manipulated image showing wetting angle of Bi-Sn on Zn. ....	106
Figure 3. 22 - "Microscopic configuration at solid/liquid interfaces: For $\theta_Y \gg 90^\circ$ , at microscopic scale, the liquid contacts the rough surface of the solid only at a few points. During cooling the solidified liquid detaches spontaneously from the solid." [37]. ....	107
Figure 4. 1 - Schematic of a prepared SVET sample, showing the size of the sample and its placement. ....	110
Figure 4. 2 - SVET resolved colour map representing normal current above a cut-edge sample of 100BS. Coating was applied on the right-hand side. ....	115
Figure 4. 3 - SVET resolved colour map representing normal current above a cut-edge sample of 10Z. Coating was applied on the right-hand side. ....	117
Figure 4. 4 - SVET resolved colour map representing normal current above a cut-edge sample of 20Z. Coating was applied on the left-hand side. Focal anodes of interest are circled in green. ....	118
Figure 4. 5 - SVET resolved colour map representing normal current above a cut-edge sample of 30Z. Coating was applied on the right-hand side. ....	120

Figure 4. 6 - Time dependent metal/mass loss for 20wt% Zn / 80wt% Bi-Sn in 1% NaCl electrolyte.....	121
Figure 4. 7 - Graph showing obtained open circuit potentials for samples listed in Table 4.2. ....	123
Figure 4. 8 - Polarisation resistance ( $R_p$ ) for 20Z over 24 hours in 1% NaCl electrolyte. ...	125
Figure 4. 9 - ZRA/Galvanic corrosion plot for each sample, as outlined the legend at the left of the chart. ....	<b>Error! Bookmark not defined.</b>
Figure 4. 10 - Cathodic Potentiodynamic Sweep for IFS .....	130
Figure 4. 11 - Cathodic Potentiodynamic Sweep for 100BiSn .....	131
Figure 4. 12 - Digital Camera images of samples laid out for long-term exposure testing. Each one is comprised of interstitial-free steel, coated in a) 20Z, b) HDG and c) ZRP. ....	132
Figure 4. 13 - Digital Camera images of after 6 months of long-term exposure testing. Each one is comprised of interstitial-free steel, coated in a) 20Z, b) HDG and c) ZRP. ....	133
Figure 4. 14 - Representative of use of GIMP software, showing distance of 10m in pixels. ....	135
Figure 4. 15 - SEM image showing numbered Zn regions on a 20wt% Zn/80wt% Bi-Sn sample. Numbers were assigned to perform volume measurements. ....	136
Figure 5. 1 - Schematics for 0t bend test showing a sample bent in a tensile/compression tester then fully bent using a vice until the "legs" are parallel. ....	151
Figure 5. 2 - Plot showing average Vickers hardness ( $H_v$ ) of coating samples heat treated for 20 mins and 40 mins as a function of Zn content. Error bars show standard deviation.....	153
Figure 5. 3 - Image of a 100% Bi-Sn coating on a 50 x 50 mm coupon of IF Steel, during a 0t bend test. ....	154
Figure 5. 4 - Image of a 20wt% Zn / 80wt% Bi-Sn coating on IF Steel, during a 0t bend test. ....	154

Figure 5. 5 - Image of a 50wt% Zn / 50wt% Bi-Sn coating on IF Steel, during a 0t bend test. .....	155
Figure 5. 6 - As-taken image of a molten Bi-Sn droplet on a 50mm x 30 mm Zn sheet section. ....	156
Figure 5. 7 - Close up image of the wetting angle between the Bi-Sn droplet and the Zn Sheet, displaying the angle measure tool in the red box. ....	157
Figure 6. 1 - Diagram of electromagnetic spectrum with the NIR region pointed out. Source: <a href="https://www.kpmanalytics.com/articles-insights/near-infrared-measurements-how-do-they-work">https://www.kpmanalytics.com/articles-insights/near-infrared-measurements-how-do-they- work</a> .....	163
Figure 6. 2 - Schematic of NIR AdPhos NIR Furnace.....	165
Figure 6. 3 - Time vs Temperature graph for 20% Power NIR at 1m/min .....	167
Figure 6. 4 - Keyence Optical Image of 20wt% Zn / 80wt% Bi-Sn cured at 1m/min with 20% NIR Power. ....	168
Figure 6. 5 - a digital microscope image of a 20wt% Zn / 80wt% Bi-Sn sample heated at 20% NIR power at a belt speed of 0.5m/min. ....	169
Figure 6. 6 - Temperature profile for 20wt% Zn / 80wt% Bi-Sn at 30% NIR Power and 1m/min belt speed. ....	170
Figure 6. 7 - Digital Microscope Image of 20wt% Zn / 80wt% Bi-Sn coating, heated at 30% NIR power at a belt speed of 1 m/min. ....	171
Figure 6. 8 - Digital microscope image of 20wt% Zn / 80wt% Bi-Sn sample heated at 30% NIR power at belt speed of 0.5m/min. ....	172
Figure 6. 9 - Temperature profile for 20wt% Zn / 80wt% Bi-Sn heated at 40% NIR power and belt speed of 1m/min. ....	173
Figure 6. 10 - Digital microscope image of 20wt% Zn / 80wt% Bi-Sn heated at 40% NIR power with belt speed of 1m/min.....	173

Figure 6. 11 - Digital microscope image of 20wt% Zn / 80wt% Bi-Sn coating heat treated at 40% NIR power at 1m/min. ....	174
Figure 6. 12 - Temperature profile for 20wt% Zn / 80wt% Bi-Sn at 50% NIR Power at 1m/min .....	175
Figure 6. 13 - Digital microscope image of 20wt% Zn / 80wt% Bi-Sn heat treated at 50% NIR power and belt speed of 1m/min .....	176
Figure 6. 14 - Digital microscope image of 20wt% Zn / 80wt% Bi-Sn heated at 50% power at belt speed of 0.5m/min.....	177
Figure 6. 15 - Digital microscope image at 1500x magnification. of a cross-section of Bi-Sn coated onto IFS with a production process using Zinc Chloride flux. The area highlighted by the blue box is a layer of Sn at the substrate surface. ....	178
Figure 6. 16 - Digital microscope image at 1500x magnification. of a cross-section of Bi-Sn coated onto IFS with a production process using Phosphoric Acid flux. ....	179
Figure 6. 17 - Digital microscope image at 500x magnification. of a cross-section of Bi-Sn coated onto IFS with a production process using Phosphoric Acid flux. The area circled in red shows signs of good adhesion.....	180
Figure 6. 18 - Schematic diagram of the polished Cu substrate from [161]. ....	186



# List of Tables

Table 2. 1 - Details of Materials used in this body of work.....	51
Table 2. 2 - Sample references and their compositional makeup. ....	53
Table 2. 3 - Sample compositions and test conditions for SVET experiments.....	110
Table 3. 1 - Heat treatment details for all samples – a tick is indicative of a sample being prepared, a cross shows a decision not to move forward with that sample.	79
Table 3. 2 - Sample Names and their Compositions.....	80
Table 3. 3 - Sample names and corresponding compositions for Ancillary Samples .....	93
Table 3. 4 - Heat treatment times for 20wt% Zn samples and their sample names. ....	96
Table 4. 1 - Couples tested for Galvanic relationships using ZRA.....	114
Table 4. 2 - Sample names and corresponding materials used in OCP experiments within this chapter.....	122
Table 4. 3- Measurements and calculations for Zn regions shown in Figure 4.20 .....	137
Table 4. 4 - Zn mass in grams for different unit areas of Bi-Sn + Zn coating. ....	138
Table 5. 1 - Table of samples used in Vickers Hardness testing. ....	150
Table 6. 1 - Parameters used to heat treat samples of 20wt% Zn / 80wt% Bi-Sn coated steel in this chapter. ....	165
Table 6. 2 - Table showing details of fluxes investigated in this chapter. ....	166

# Definitions

Wt%	Weight percentage
$\mu\text{m}$	Microns
E	Electrode potential
$E_{\text{corr}}$	Free corrosion potential
$i_{\text{corr}}$	Corrosion current
i	Current
$i_a$	Anodic current density
$i_c$	Cathodic current density
F	Faradays constant ( $96487 \text{ C.mol}^{-1}$ )
R	universal gas constant ( $8.31 \text{ J mol}^{-1} \text{ K}^{-1}$ )
$\text{A.m}^2$	Amps per metre <sup>2</sup>
Q	Charge (C)
n	No. of electrons
jz	Normal current density
$R_p$	Polarisation Resistance
HDG	Hot-dip galvanisation
SVET	Scanning vibrating electrode technique
SEM	Scanning electron microscopy
EDS	Energy-dispersive X-ray spectroscopy
OCP	Open circuit potential
SCE	Saturated calomel electrode
ZRP	Zinc-rich Paint
CGC	Cold Galvanising Coating
IFS	Interstitial Free Steel
ZAC	Zinc Ammonium Chloride
NIR	Near Infrared

# **Chapter 1:**

## **Introduction and Literature**

### **Review**

## **1.1 Research Objectives and Aims**

This Engineering Doctorate project has been sponsored by the aerospace ground support company, JBT. This primary aim of this project is to investigate an alternative zinc rich paint for the repair of galvanised structures and to identify an alternative galvanic coating for steel that can be applied locally, rather than at a dedicated batch galvanising plant. The research laid out in this thesis analyses and optimises the performance of a novel corrosion coating, consisting of Bi-Sn and Zn. The issues listed in section 1.2.3 and 1.2.4 with HDG and CGCs/ZRPs leave a gap in the market for a resilient coating system. Such a coating would bridge the gap between short-lived ZRPs and time-consuming HDG, by being applied locally but offering sustained adhesion and galvanic protection. Techniques employed include Scanning Electron Microscopy (SEM), Electron Dispersive X-Ray Spectroscopy (EDS), Scanning Vibrating Electrode Technique (SVET), OT Bend Testing and many associated and complementing techniques.

The following chapters address the aims and objectives in a systematic and comprehensive way as listed in the chapter summary below:

**Chapter 1:** A comprehensive review of the current literature surrounding the subject matter of this thesis and associated topics including corrosion, fusible alloys, and coating technology.

**Chapter 2:** Information detailing the materials, experimental methods, equipment, and techniques used in this body of research.

**Chapter 3:** This chapter regards development and optimisation of a novel Bi-Sn + Zn alloy coating. The mixing technique, curing time, temperature and method of heat

treatment are all explored. Results in the form of SEM and EDS images allow for analysis of the effects of the production process on the resultant microstructure.

**Chapter 4:** Analysis and exploration of the corrosion performance of the novel Bi-Sn + Zn coating developed in previously. SVET testing is used to show galvanic protection in terms of anodic and cathodic activity. To understand the kinetics and thermodynamics of the corrosion mechanisms within the new coating system, Open Circuit Potential (OCP), Zero Resistance Ammetry (ZRA) and Potentiodynamic Polarisation Sweeps are conducted. A comprehensive testing regime is undertaken to comprehend whether and how the coating offers a sustained galvanic protection to a steel substrate.

**Chapter 5:** An assessment of the mechanical aspect of the coating behaviour. The adhesion of the coating to a steel substrate is assessed using OT bend tests and crack or flake formation assessed. Vickers Hardness values as a function of Zn content is provided, to assess the effect of Zn addition on the hardness of the novel alloy. The wetting of the novel coating components will also be analysed and suggestions for improvement of this function will be given.

**Chapter 6:** Alternative heating methods, compositions, fluxes and additions are explored. Near Infrared (NIR) heating is tested as a rapid curing prospect for industrial applications. Compositions including a zinc phosphate addition are tested for their corrosion performance. Alternative fluxes will be used in the production process and their effect on the adhesion of fusible alloys to a steel substrate will be investigated. Comparisons will be made against the methods and coatings designed earlier in the thesis.

## **1.2 Literature Review**

### **1.2.1 Introduction**

Ground support equipment (GSE) plays a vital role in the safety and efficiency of aircrafts and airports around the world. GSE encompasses all support equipment at airports, necessary for the function and logistical operation of airports, air bases and other aviation facilities. GSE can be divided into two categories: powered equipment and non-powered equipment [1]. Non-powered equipment includes manually operated apparatus such as aircraft service stairs, dollies, and tripod jacks [1,2]. Powered equipment, on the other hand, encompasses those machines which are powered by electricity or fuel, such as buses, passenger boarding steps, belt loaders and de-icing vehicles [1,2]. It is evident that GSE is essential to the aviation industry as a whole but also to adjacent industries such as tourism, freight, cargo, and business.

In 2019, the global GSE market was worth \$13.02 billion, and is projected to reach a value of \$22.0 billion by 2027 [1]. For such a lucrative market, the need for robust, durable, and climate-appropriate equipment is evident. With a recent article claiming that 25% of the world's busiest airports are in coastal regions, environmental conditions are of serious concern for GSE producers [3]. In addition to this, a large amount of GSE is produced for military clients and is thus done to a rigid specification [4]. The deployable nature of military equipment means that it must be resistant to an extensive range of environmental damage, from desert heat and rainforest humidity to arctic cold and sub-zero conditions [4].

Many different factors can have an effect on the serviceability of GSE. As mentioned above, much of the product range is deployable or is leased by different airlines or airport operators. As a result of their agility and necessity, GSE sees a very high use

volume over its lifetime. This could be the number of passengers on aircraft stairways, or the amount of mass lifted by a pallet loader, to give just two of many scenarios. These actions and loads are repeated numerous times a day, introducing fatigue and creep as material factors that must be considered during construction. It should be noted that all mechanical properties are of utmost important when designing load bearing components like GSE, in particular when it comes to human safety, whether that be passenger, staff or crew member. Properties like yield stress, ultimate tensile stress, ductile to brittle transition temperature and others should be considered [5,6].

A major influence on performance and lifetime is corrosion. Corrosion is the degradation of a material's properties by chemical and/or electrochemical reaction with the environment [7,8] . This process converts the metal into a more stable form such as an oxide or hydroxide and is the result of attack on the metal by the electrolyte [9]. As shown by Francois et al, corrosion leads to an undesirable decrease in mechanical properties of steel, such as ultimate elongation, which can affect the compliance of the metal with industry standards [10]. Other studies have also indicated a loss in mechanical integrity of steel and other metals due to the effects of corrosion [11–13].

The problem of corrosion is a global issue affecting all sectors of industry.

According to the IMPACT study undertaken by the National Association of Corrosion Engineers (NACE) in 2013, the global cost of corrosion was estimated to be US\$2.5 trillion, equivalent to 3.4% of the global GDP at the time. NACE estimates that using current corrosion protection measure, savings of between 15 and 35% of the cost of corrosion could be realized (between US\$375 and \$875 billion

annually on a global basis) [14]. This indicates demand for development of corrosion control methods in order to save money currently spent on maintenance, replacement, forced shutdowns and accidents [14]. The same report indicates that the cost of corrosion was equivalent to 3.8% of GDP in the European Region in 1970 [14]. These figures make corrosion prevention and protection highly sought after and thus, a widely researched field.

The corrosion of GSE can be attributed to a number of factors present at airports and air bases. These factors include, but are not limited to, moisture in air, salt particles in coastal winds, industrial pollutants from fuel, tropical climates accelerating corrosion, marine atmospheres, acid rain, contact with chemicals, and soils and dust in the atmosphere [4,13]. Corrosion is an issue for GSE and other aircraft ancillary components as it can lead to failure resulting in significant downtime for structural repair or, even worse, a catastrophic accident. Repair and the time-out-of-service comes at a vast financial cost for GSE companies, whereas an accident could come at a cost of reputation or in a worst-case scenario, human life. For these reasons, corrosion prevention through means of protective coatings is of utmost importance; as well as a strict programme of corrosion inspection and repair.

Traditional means of protection against corrosion mainly centre around Hot-Dipped Galvanising (HDG) [15]. This is the process of applying a protective zinc layer to steel in order to prevent corrosion of a component or structure. Some of the issues associated with HDG can include dross, mottling, flaking, peeling or delamination and a premium cost. Cost is primarily due to the need to outsource galvanising to external contractors, especially for GSE producers that do not have the capacity or capability to undertake the process in-house. This also means that getting a



component galvanised can take a great amount of time to complete and affects lead time on GSE. This could, in turn, lead to customer dissatisfaction and a financial loss for the manufacturer. HDG is also expensive in itself, and a cheaper alternative would be of great benefit to producers and users of GSE alike. HDG can also lead to aesthetic flaws in products when coupled with other treatments such as cleaning, priming, painting, and curing.

HDG also happens at high temperatures of  $\sim 450\text{ }^{\circ}\text{C}$  [15,16]. This requires a great amount of energy and would be impossible to implement in-house for GSE producers. Meaning that companies are stuck paying the high cost in time and money of outsourcing, as explained above. A lower-temperature alternative would be much more feasible for manufacturers of GSE to bring into their factories etc. and would allow for enormous cost-cutting.

Another method of protection is cold galvanising coatings (CGCs). CGCs have been researched widely in the past; including, but not limited to, their sacrificial protection via SVET, electrochemical properties using electrochemical impedance spectroscopy (EIS) and adhesion tested using the pull-off method [17–21]. Many issues can occur with CGCs, such as flaking, poor adhesion, lack of metallic bond and galvanic protection [22]. CGCs do offer a more flexible and cost-effective solution to corrosion issues but their problems are many. The elimination of expensive outsourcing of HDG work is one major benefit of CGCs as it could be applied on-site and in-situ. However, the level and timespan of protection offered could suffer due to several factors, as mentioned before.

Another use for CGCs is in the repair of galvanised parts. This process involves the removal of the galvanising zinc layer for welding, thus avoiding toxic zinc fumes being inhaled [23]. The newly repaired section is then without protection against

electrolytic attack. To overcome this susceptibility, CGCs such as Zinc Rich Paint (ZRP) are often used to coat the repaired area [24]. ZRP and CGC are used somewhat interchangeably in most contexts, in that most cold galvanising systems use a zinc-rich element, but it could also be said that ZRP is a type of CGC and that more complex CGC systems do exist that are not just a paint of >98% Zn, like that used in [17]. ZRPs use an organic or inorganic matrix with a very high zinc addition to create a coating offering a dual protection – barrier protection as a paint layer and galvanic protection through the aforementioned high concentration of zinc (>98wt%) [25–27]. However, much like HDG, ZRPs are laden with issues [28]. It is known that their adhesion is less than satisfactory, causing peeling and flaking from steel substrates – again leaving areas exposed to possible corrosive aggress. The matrixes used in ZRPs are also an issue, many of them degrade over time in UV light – a particular weakness when these coatings are used outside, often in direct sunlight. These properties lead to the question of lifetime, ZRPs are known to have a relatively short lifetime to failure and require frequent reapplication. An additional concern in regard to ZRPs is that of the level of galvanic protection genuinely offered [25,29,30]. This question arises from the inorganic or organic nature of matrixes used. The distribution of zinc particles must be perfect and plentiful in order to fully offer galvanic protection. It is necessary for the zinc particles to be in contact with the substrate surface and each other through the whole thickness of the coating. This is in order to maintain electrical contact; thus, electrons can flow freely from the coating surface to the substrate, offering galvanic protection and making the ZRP the anode [31]. Here, matrixes used are non-metallic and offer no electrical conduction. This must instead be facilitated by the Zn alone.

These issues would portend that ZRPs are not a good option for long-term corrosion protection of steel substrates or repaired areas of GSE.

This work explores the avenue of improving upon the weaknesses exhibited by ZRPs by creating a novel coating in a bid to eliminate the issues mentioned above in regard to ZRPs. The issues associated with CGCs and ZRPs are focussed mainly within the matrixes used as vehicles for the zinc particles. One approach to this problem is the introduction of a metallic matrix to a zinc-containing coating. Fusible alloys offer an excellent solution to this as they can be cured at intermediate temperatures having been applied like a paint or paste [32–35]. Bismuth-tin (Bi-Sn) has a very low melting temperature, making it an excellent candidate for the matrix material in such a coating [36]. The low temperature at which Bi-Sn melts, has seen it used heavily as a replacement for lead-based solders in plumbing and heating engineering applications [34,37,38]. This application exploits the fact that the fusible alloy not only melts at a desirably low temperature but is also workable at room temperature, this also means it is easily mixed into a paste or paint-type coating.

The addition of zinc to this coating is in line with its inclusion in ZRPs and, in fact, HDG as an incredibly robust galvanic protector of steel [15,25,39–41]. Including a metallic matrix around the zinc ensures that the electric contact through the whole coating to the substrate. This will allow electron transfer from the coating to the steel, providing the much-sought-after corrosion protection [31,42].

In creating a coating using a fusible alloy matrix combined with zinc, a novel coating will be developed containing bismuth (Bi), tin (Sn) and zinc (Zn). The establishment and advancement of this coating will require careful attention to several factors.

Metallurgy and microstructure are both important facets of this research. To make the coating a powerful protector against corrosion, it is important that the optimum

microstructure be found. Also important is exploration of the temperature necessary to cure the novel coating to provide such a microstructure. The production and application process must be analysed and refined for optimal performance of the coating.

It could be argued that the main function of such a coating is to protect the structural properties of a steel substrate from attack by corrosive electrolyte. In order to do this, it must provide either a physical environmental barrier to shield the steel from moisture, or act sacrificially and corrode preferentially to the steel – known as galvanic protection – or both. Both accelerated and in-situ, long-term ambient exposure testing will be undertaken to evaluate the corrosion behaviour of the system.

Another factor to consider is the mechanical properties of the coating, including hardness and adhesion to substrate. As described above, one of the major weaknesses of ZRPs is their adhesion. This would need to be improved upon to deliver an improvement on the existing industrial standard.

The objective of this literature review is to analyse contemporary studies and current thinking around the subject matter of corrosion and surrounding themes. Some related subjects include corrosion performance, protection and prevention. Work done on corrosion protection forms a great deal of the literature. The topics of galvanising and corrosion performance of steel in particular are extremely relevant to this project. This is due to the common use of steel in ground support equipment and the excellent galvanic protection offered by galvanising. Due to the high costs and damaging effect associated, the protection of metals against corrosion is essential for service longevity and economic stability [9–14].

### 1.2.2 Corrosion

The corrosion of metal in the presence of water or an electrolyte requires four fundamental factors: an anode, a cathode, a pathway for electrical contact and an electrolyte. In nature, an electrolyte typically presents itself as rain or salt solution arising from seawater in coastal regions.

At the anodic site, an oxidation process will take place. This is referred to as metal dissolution and is represented in Equation 1.1:



During the anodic reaction, electrons are released, as shown in Equation 1.1. These electrons are transferred through the bulk metal to the cathodic site. There are several different possible cathodic reactions, dependent on the electrolytic conditions, such as pH and oxygen concentration.

Hydrogen evolution will occur when the pH is lower than neutral, through Equation 1.2:



Per Equation 1.3, at neutral pH oxygen reduction will take place:



To understand the thermodynamics of corrosion, a Pourbaix diagram is commonly used. This type of diagram was first proposed by Marcel Pourbaix in the 1930s and 40s [43] and is seen in Figure 1.1 [44].

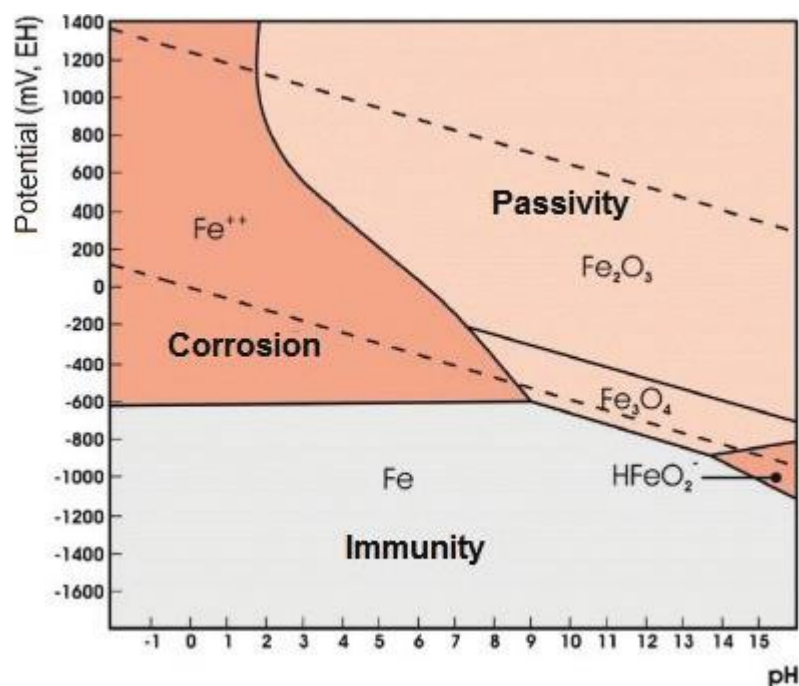


Figure 1. 1 - Pourbaix diagram for iron in water at 25°C [41].

Figure 1.1 shows the most stable conditions for a metal depending on the potential and pH in a system. The three conditions noted by the Pourbaix diagram are immune, corroding and passive [43]. The regions represent the metal (immunity), a metal ion (corrosion) or a metal oxide (passivation), each of which occur under the specific potential and pH conditions denoted by the axes. The lines of a Pourbaix diagram represent the equilibrium points between these different regions, where transition from one region to another is possible [43,45]

Corrosion will occur at a concentration of  $>10^{-6}$  M of ions in the solution while immunity occurs below this benchmark. Passivity presents a more complex idea as it occurs due to insoluble corrosion products formed on the metal surface preventing electrolyte contact with the surface, vastly slowing the corrosion rate [43]. The most thermodynamically states for iron in water are shown in Figure 1.1. The two sloping, dashed lines on the Pourbaix diagram (Figure 1.1) represent other reactions that can possibly take place in aqueous solution, the top one is oxidation of water to produce

oxygen gas and the lower dashed line represents production of hydrogen gas through reduction of hydrogen.

The current densities of cathodic and anodic reaction are what govern the rate of corrosion in a system. This is defined as the current strength per unit area with the anodic value represented by  $i_a$  and the cathodic by  $i_c$ , which are equal when the system is at equilibrium. The equilibrium value is known as the exchange current density and is denoted by  $i_0$ .

A corroding metal with both anodic and cathodic activity is termed a polyelectrode. This is defined as a system containing two or more couples which are not in thermodynamic equilibrium, acting simultaneously on an electrode surface [46]. The additivity principle in [46] is shown in Equation 1.4. The principle states that the sum of currents produced by individual currents on a corroding metal surface is equal to the total overall current flowing into an external circuit when a metal is freely corroding:

$$\sum i_{anode} = -\sum i_{cathode} = i_{corr} \quad \text{Equation 1.4}$$

Where;

$\sum i_{anode}$  is the anodic current density,

$-\sum i_{cathode}$  is the cathodic current density,

$i_{corr}$  is the rate of corrosion at the metal surface, expressed as a current.

These currents are dependent upon potential and as such the corroding metal system will also have a unique potential, known as  $E_{corr}$ , the free corrosion potential.

It was discovered by Tafel [47,48] that a relationship exists between the current and potential and is given by:

$$I_{Cathodic} \propto \exp(-E) \quad \text{Equation 1.5}$$

$$I_{Anodic} \propto \exp(E)$$

Equation 1.6

Plotting  $E$  against  $\log(i)$  produces a Tafel plot, giving a straight line. Tafel plots of individual electrodes can be combined into an Evans diagram, shown in Figure 1.2.

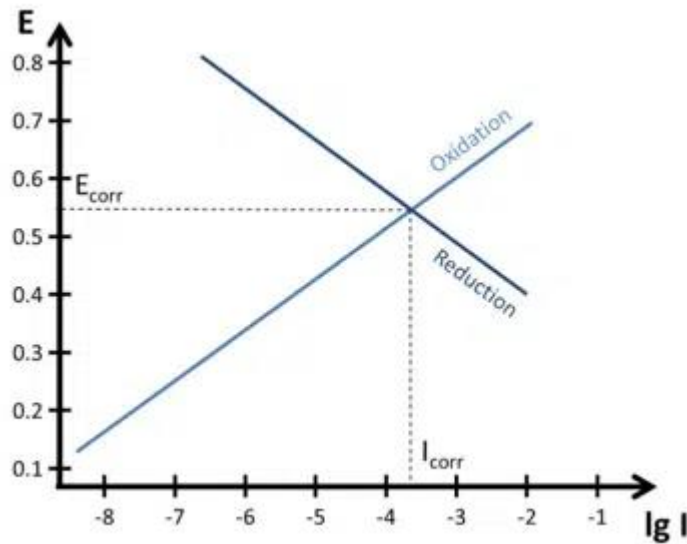


Figure 1. 2 - Schematic of Evans diagram, from [50]

The Evans schematic in Figure 1.2 from [49] is representative of corrosion of a metal in contact with an electrolyte. Knowing  $i_{corr}$  from the above Equation 1.4 and shown here as the intersection of the tafel slopes for oxidation and reduction, it is possible to find  $E_{corr}$  using an Evans diagram.  $E_{corr}$ , the free corrosion potential, is the driving force for a corrosion reaction.

### 1.2.2.1 Galvanic Corrosion

Also known as dissimilar metals corrosion, this corrosion mechanism requires a cell where the anode and cathode are two (or more) metals that are found in different positions in the galvanic series. Despite being a potentially rapid and common form of corrosion, the use of galvanic couples is also utilised as a form of corrosion protection. Some elements of the galvanic series are presented in Table 1.1:



Table 1.1 - Selected elements in Galvanic Series

No.	Material	Approx. Voltage (V vs SCE)
1.	Magnesium	-1.6
2.	Zinc	-1
3.	Beryllium	-0.95 to -1
4.	Aluminium Alloys	-0.7 to -1
5.	Cadmium	-0.65 to -0.73
6.	Mild Steel & Cast Iron	-0.58 to -0.8
7.	Low Alloy Steel	-0.55 to -0.65
8.	Austenitic Iron	-0.42 to -0.53
9.	Bismuth	-0.38 to -0.45
10.	Aluminium Bronze	-0.32 to -0.42
11.	Brass (Naval, Yellow, Red)	-0.32 to -0.4
12.	Tin	-0.32 to -0.35
13.	Copper	-0.32 to -0.4
14.	Stainless Steel, grades 410, 416	-0.25 to -0.38
15.	Nickel Silver	-0.25 to -0.3
16.	Lead	-0.16 to -0.26
17.	Silver	-0.1 to -0.15
18.	Titanium	+0.05 to -0.15
19.	Gold, Platinum	+0.2 to +0.08
20.	Graphite	+0.35 to +0.2

A lower value of free corrosion potential increases the reactivity of the metal. This means a less noble (lower voltage  $E_{\text{corr}}$ ) metal would corrode preferentially when in electrical contact with a more noble metal (higher voltage  $E_{\text{corr}}$ ), thus protecting the more noble metal. In this instance, the metal which is corroding is said to be acting sacrificially. Although this can be a common problem in industry, careful design and planning can help avoid it completely or employ this mechanism for protection of substrates.

An example would be the coating of steel in a layer of zinc, utilised across industry and known as galvanising. From Figure 1.3, we can see that Zn has a lower potential than mild steel and thus protects it galvanically.

### 1.2.2.2 Zinc Corrosion

As mentioned in Section 1.2.1, Zn is of particular importance to this work. The corrosion of Zn is represented in a Pourbaix diagram in Figure 1.4, taken from [45].

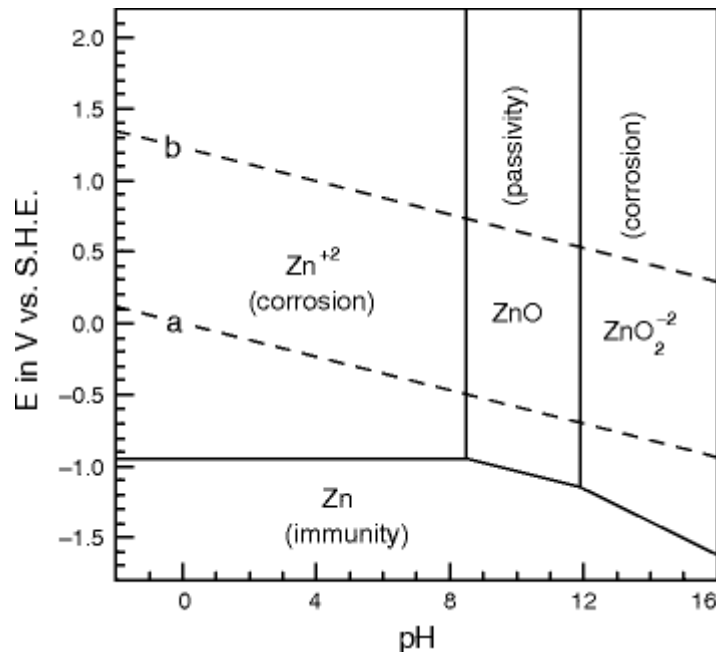


Figure 1. 3 - Pourbaix Diagram for Zinc in water at 25°C [45]

Figure 1.4 shows that Zn is immune below potentials of  $\sim 0.98$  V. At pH 0-9, above 0.98 V, Zn actively corrodes and produces  $\text{Zn}^{2+}$  ions due to zinc dissolution. From pH 9-12 ZnO is formed as corrosion product and the zinc becomes passive, the oxide layer forming a barrier to electrolyte. Taking the pH above 12, corrosion would again occur as  $\text{ZnO}_2^{2-}$  ions are produced [45].

### 1.2.3 Hot-Dip Galvanising

By far the most common method of galvanic protection in industry is hot dip galvanising (HDG) [15]. Zinc coating on steel has been prominent for over 200 years but in the last 20 or so years, more and more research has been devoted to the field. This is a result of many new applications for HDG across a variety of industrial sectors such as automotive and construction [15]. A review by Marder gives a good technical overview of the processes involved and the state of the field in 2000 [15].

HDG can be split into two types of coating processes, batch galvanising and continuous galvanising [15]. For batch processing, the substrate is degreased, rinsed and then pickled. Pickling is done in hydrochloric acid to rid the substrate of any oxides or corrosion product that has built up [15]. After pickling, it is rinsed and then subject to either a wet or dry process from this point. The wet process includes passing the substrate through a blanket of molten flux salts on the surface of the galvanising bath [15]. This is to remove oxides from the substrate and keep the bath surface free of oxides also [15]. The process consists of a preflux in an aqueous solution at up to 80 °C [15]. The steel must then be dried immediately to avoid spatter and splash marks on the piece and also to reduce the risk of explosion [15]. The steel is then immersed in the bath of molten zinc which sits at between 445 °C to 455 °C for between 3 and 6 minutes [15]. The immersion time can be altered in order to change coating thickness on the substrate and also the amount of coating that contains interfacial iron-zinc alloys beneath the zinc top layer [15]. Controlling the cooling is essential as further reaction can take place and galvanising can continue during the cooling process [15]. Problems such as mottling, a common surface defect, can arise from failure to control these parameters [15].

Continuous processes see large coils of welded sheet steel coated at up to 200 m/s in a line-type process [15]. The sheet is first cleaned in the cleaning section of the line, this a  $N_2/H_2$  reducing atmosphere at around 500-760 °C in order to further reduce surface oxides and remove any residual organic contamination [15]. Annealing of the sheet then takes place in the heating and holding section, above the recrystallisation temperature at about 700 °C. Before immersion, the strip passes through gas jets that cool it to 460 °C, close to the bath temperature mentioned above [15]. After immersion, gas knives are used to control the thickness of the galvanised coating by

eliminating excess zinc from the surface to attain the correct thickness [15]. The strip, now galvanised, is then force-cooled and re-coiled or cut as desired by the customer [15].

Some recent research in the HDG field has centred around the galvanising of prior-nickel-coated interstitial-free (IF) steel [16,50,51]. It has been shown that adding a nickel coating prior to galvanising can control the Fe-Zn reaction in steels [50].

Other steels show an increase in corrosion protection and a thinner Fe-Zn layer when coated with nickel prior to undergoing HDG [50]. Electrodepositing of nickel onto the steel substrate to be galvanised can provide a uniform and cavity-free coating [50]. It is established that pre-Ni coated steels offer a superior performance to conventionally galvanised steels [16,50–52]. The addition of Al to the bath is a new development in the specific research field of pre-Ni coated steels, although the use of Al in HDG has been the norm for many years longer than Ni-additions [52]. Further work in this field is necessary to compare the performance properties of the intermediate layer with those of the delta and gamma phases. Key properties to consider, especially in the scope of this project, are adhesion, hardness and corrosion protection. This is necessary to evaluate the optimal amount of Al addition to the galvanising bath in order to provide a coating which would exhibit the best possible performance in the above-mentioned areas and properties.

More recent research in the field has increasingly focused on Zinc- Magnesium - Aluminium (ZMA) coatings an alternative to traditional HDG. ZMA is comprised of a dendritic primary zinc phase which is encompassed by a coarse binary eutectic phase and a fine ternary phase. The binary eutectic is made up of Zn and  $MgZn_2$ , whilst the ternary contains  $MgZn_2$ , Zn and Al nodules [53–55]. Studies have found that ZMA coatings show an improved corrosion performance over HDG in terms of

mass loss, passive barrier effect, corrosion resistance and long-term exposure [56–59]. This superior performance has been attributed to the complex microstructure of ZMA coatings and the formation of stable corrosion products on ZMA, which is not characteristic of HDG [60,61]. In 2023, Malla et al. found that mass loss and anodic growth was much less prominent in ZMA coatings of a larger thickness [53]. This study varied ZMA coating weights and analysed microstructure, corrosion performance using SVET and Time-Lapse Microscopy as well as electrochemical testing with OCP and Linear Polarisation Resistance (LPR). It noted that the microstructure for the lightest coating weight appeared much finer than the heavier coating weights, which exhibited a coarser microstructure of larger and more developed dendritic Zn regions [53]. A coating weight of  $200 \text{ gm}^{-2}$  showed the highest volume-fraction of magnesium-rich eutectic. Both the  $200 \text{ gm}^{-2}$  and  $310 \text{ gm}^{-2}$  showed better corrosion performance than the  $80 \text{ gm}^{-2}$  coating, this was due to both samples having a higher volume-fraction of the Mg-rich eutectic [53]. Anodic activity initiates at the most electronegative phase, the  $\text{Zn}_2\text{Mg}$  phase [54,55] and spreads through the Mg-Rich eutectic due to galvanic dissolution of the  $\text{Zn}_2\text{Mg}$  and discharge of  $\text{Mg}^{2+}$  ions which hydrolyse in water and increase alkalinity of the solution to levels where Zn regions are passive and Zn corrosion products are stable, thus slowing the corrosion rate for the thicker coatings [53,62]. This also translates to SVET-derived metal loss values where the thickest coating outperformed the other coatings, losing significantly less metal.

It was discovered that coatings containing 3.7 wt% Al and 3 wt% Mg performed better, in terms of corrosion resistance, than traditional galvanised steel [63]. The corrosion products formed by the ZMA alloys in [63] varied with electrolyte composition but were different than those formed by traditional galvanised steel of

Zn-Al alloy coatings, once again highlighting the importance of Mg in ZMA coatings – admittedly the author highlights the need for further investigation here, but it is evident from other publications [53,55,62] that they were correct [63].

The performance of ZMA alloys in marine environments was tested in [64]. It was shown, by weight loss data, that the rate of corrosion significantly reduced over time during the experiment. This was attributed to the presence and corrosion reaction of Mg, which produced insoluble corrosion products which protected the substrate from further attack, this was supported by a decrease in corrosion current density [64] and is in agreement with [53]. The corrosion resistance of ZMA is also attributed to the formation of a “closed framework structure” preventing penetration of any corrosive attack; as well as  $\text{Al}_2\text{O}_3$  preventing the detachment of the corrosion product, allowing further delay of the corrosion process. This means ZMA performs well in marine environments [64].

Phosphates have long been known to work effectively as corrosion inhibitors on galvanised steels [65–68]. A study was conducted in [55] to assess the viability of phosphate as a corrosion inhibitor on ZMA-coated steel. It was shown via time-lapse microscopy (TLM) that the Mg-rich eutectic phase was preferentially attacked, leading to de-alloying of the  $\text{MgZn}_2$  phase and dissolution of Zn-rich phases. The ongoing corrosion was always associated with eutectic attack with the TLM showing decrease in corroded area with increase of Mg and Al addition [55]. This is in agreement with the corrosion mechanism observed elsewhere [53,69]. It is shown via TLM that the deposition of  $\text{Na}_3\text{PO}_4$  (trisodium phosphate) passivated numerous anodic events, with filament-like precipitates of phosphate growing rapidly [55]. This suggested that the anodic loss of metal ions in the electrolyte above the corroding surface produced a super saturated solution which facilitated the

nucleation and growth of the deposition surface of the phosphate [55]. Mass loss data derived from SVET experiments showed a 98% decrease in mass loss for ZMA-coated steel when compared to a sample with no inhibitor addition [55].

Most ZMA-coated steels are overcoated with an organic coating in order to supply further barrier-protection and to allow for manipulation of aesthetics [69]. These overcoats have been known to be susceptible to failure, via aggressive ions that penetrate the coating at defects [70]. One particular failure method is filiform corrosion – a type of corrosion initiated at high humidity due to breach of an organic coating by an electrolyte, which then comes into contact with the metal beneath and results in “anodic undercutting” and detachment of the coating at the electrolyte-containing “filament head” [70,71]. The use of an anion-exchange pigment, hydrotalcite, has been shown to improve protection against filiform corrosion in several parameters when added in-coating [69]. It was shown that the hydrotalcite addition reduced the total filiform corroded area, the average filament length and number of observed filiform “heads” on ZMA-coated steel [69]. Hydrotalcite works by scavenging acetate via anion exchange and diluting the electrolyte within the filament head which accompanied by evaporation decreases the amount of electrolyte in the filament head, which, in turn, decreases the head width and reduces corrosion rate [69]. The study shows hydrotalcite to be a viable option for protection of ZMA coatings against filiform corrosion, making their performance even more robust.

Overall, hot-dipped ZMA coatings present a viable focus for the future of the industry. The coatings succeed in corrosion protection and when coupled with inhibitors, they offer a robust solution to issues surrounding the coating of steel and its protection from corrosive degradation [53–55,57,63,64,69].

#### 1.2.4 Cold Galvanising Coatings

A cold galvanising coating (CGC) is a zinc rich paint (ZRP) containing at least 92 wt% pure Zn metal when cured [17,72]. A similar cathodic protection to HDG is expected and an active coupling is produced with a steel substrate [73]. To enhance protection, it also exhibits a passive layer due to corrosion products precipitating on the surface, producing a barrier to aggressive corrosion ions [74]. CGCs have a medium-term lifespan, around 30 years for a mild environment and only 15 years in a heavily industrial environment; this is an area with much room for improvement [75]. Another shortfall of CGCs is adhesion, due to the cold nature of the coatings they do not form a metallic bond with the substrate like HDG and a weak bond between substrate and coating has been known to compromise the structural and aesthetic integrity of CGCs, especially true when high percentages of Zn are added, as the epoxy or matrix facilitates adhesion [76]. In order to create an effective CGC that is able to compete with HDG, adhesion characteristics must be vastly improved [17].

The adhesion of ZRPs has been shown to be poor. This is due to the very high percentage of Zn powder, > 92%, and also the non-metallic nature of the binder in the coating [76,77]. The adhesion and application of ZRPs are also hindered by several other issues such as high viscosity, difficulties in spraying, poor surface levelling and segmentation of zinc dust during storage [77]. Some ZRPs showed deterioration of cathodic protection due to binder type used, represented by a rise in  $E_{\text{corr}}$  value to almost that of steel [78]. Atmosphere-driven degradation has also been a major downfall of CGCs and ZRPs. It has been shown that ZRPs and zinc-rich primers can suffer degradation and failure in environments such as marine, marine-industrial and industrial, owing to the permeation of water in the coating leading to



delamination, blistering and corrosion of the substrate [79]. This is perpetuated by aggressive alkali cations found in the corrosion products associated with the system [79]. An alternating hot and cold atmosphere (45 °C for 12h, 25 °C for 12h) also proved to promote degradation of the ZRPs due to high temperatures accelerating permeation of water into the coating and the corrosion of the substrate [79].

Alternation of temperature can also cause expansion and contraction stresses within the coating, leading to a loss of cohesive force between coating and substrate.

The cathodic protection of ZRPs, in particular zinc-rich epoxy (ZRE) coatings – ZRPs that utilise epoxy as a binder – can be surmised in 4 stages, judging by research available [72]. The first stage is the activation stage, where a continuous rapid drop in potential occurs. A constant increase in zinc-steel active area ratio leads to continuous activation of zinc particles. A decrease in the electrolyte diffusion rate and coating porosity are said to be active factors in this process [80].

Secondly is the cathodic protection stage where large areas of zinc particles activate, and the zinc-steel active area reaches a critical size where corrosion potential falls below -860 mV (critical corrosion potential for galvanic effect of Zn). The behaviour of the potential shift then governs which sub-stage takes place. A growth substage occurs when the activation of the zinc particles takes place more quickly than its sacrificial dissolution rate and potential continues to drop while zinc-steel active area continues to increase. A stabilisation/transition substage occurs when the activation rate of Zn particles and the sacrificial dissolution rate are approximately equal, and corrosion potential is maintained at a constant level. A decline substage takes effect when activation of zinc particles happens at a rate slower than its corrosive consumption rate, this causes corrosion potential rises with a correlating decrease in zinc/steel active area ratio [81].

Thirdly is the shielding stage. This refers to the formation of Zn corrosion products creating a long-term barrier protection against corrosive media. The corrosive activation of Zn continues but cannot generate a significant galvanic effect and so the potential rises above -860 mV meaning cathodic protection is no longer occurring and the coating is utilising barrier protection only [82].

Lastly is the failure stage. At this stage, blistering and peeling of the coating start to occur due to the accumulation of corrosive agents like water, chloride ions and oxygen. This leads to rust appearing on the surface of the coating and the coating ultimately loses shielding protection and the potential fluctuates to around -650 mV, the corrosion potential of steel [83].

A sharp focus of the research area is the enhancement of ZRPs and ZREs to further bolster their performance. This has been researched in several different methods aiming to improve barrier protection performance or the cathodic protection aspect of the coatings. One such area is the surface modification of Zn particles within the ZRPs. It has been shown that a surface modification can lead to suppression of dissolution rate meaning electrical percolation is maintained but electrochemical reactivity is curbed [84]. Many of the modifications made to Zn include pre-treatment with a corrosion inhibitor. It has been shown that pre-treatment with phosphates directly reduced the electrochemical activity of the Zn particles and the water-uptake in the coating, bringing about improved corrosion resistance due to enhanced barrier effects and lower reactivity of the coating [85]. Other corrosion inhibitors were tested as pre-treatments in [86]. It was shown via EIS and SVET that pre-treating the Zn with 2-mercaptobenzothiazole, 3-glycidoxypropyltrimethoxysilane and cerium nitrate respectively offered no observed improvements over standard Zn powder, but that the replacement of Zn

with 55AlZn exhibited a better corrosion protection than a commercial automotive-industry standard system [86].

Organosilanes have been used to modify the Zn dust particles with good effect [87]. Organosilanes are widely-used as coupling agents to promote adhesion between the inorganic metal substrate and the organic coating [88]. Due to their superior ability to disperse pigments and hydrophobic properties of silanes, organosilanes can be used to maximize the stability of zinc particles to prolong the galvanic lifetime of the coatings in question [87]. Testing from [87] using polarisation testing, salt spray testing and EIS showed that coatings containing organosilane-modified Zn exhibited a better corrosion -performance than those containing unmodified Zn; directly due to an organosilane layer that developed on the surface of Zn particles.

Another enhancement method is the partial substitution of Zn particles to promote corrosion performance. This approach aims to formulate low-percentage Zn coatings without compromising cathodic protection. Pigments including carbon black, graphite, zinc oxide, aluminium and micaceous iron oxide have been shown to increase percolation within ZRP coatings, enhancing effectiveness [89]. ZnO pigments, when combined with Zn particles, illicit a dual-protection system of cathodic and barrier-protection while creating a p-n junction at their interface which provides an electron flow resulting in a positive charge in ZnO particles, lessening the electrochemical reactivity of Zn and providing far greater levels of protection. ZnO also acts as a barrier protection mechanism and seals pores within the coating [90].

Carbon Nano Tubes (CNT) are another candidate for partial substitution of Zn particles. These are one-dimensional allotropes of carbon and are one of the best candidates for reinforcing metal-polymer anticorrosion coatings due to their inherent

electrical conductivity, high aspect ratio and high stiffness [72]. In a hybrid coating of ZRP and CNT, the CNT assemble as a thread-like network throughout the coating, providing mechanical integrity to the coating. This network also transports electrons to the Zn particles to create other Zn compounds [91,92]. The highly conductive nature of CNTs means that a much smaller amount of Zn is needed to provide sufficiently large electrical conduction between isolated Zn particles and the metal substrate. This increases adhesion properties by lowering the amount of Zn needed and thus allowing for more binder, which provides adhesion to the substrate. The balance between pigment and binder is optimised for mechanical properties and thus improves barrier protection against corrosion, as well as coating flexibility and surface adhesion, impact and abrasion resistance, and fatigue and tensile strength [77].

Further work would need to focus on sacrificial and galvanic protection while also paying attention to adhesion properties. Future studies would make use of direct comparison between HDG and CGCs in an effort to gain comprehensive understanding of the differences and challenges that lay ahead for CGCs / ZRPs.

### **1.2.5 Fusible Alloys**

Fusible alloys have long been postulated as candidates for low temperature solders as well as other low-temperature applications due to their relatively low melting point [93]. This property has seen fusible alloys used widely across industry, from dentistry [94], to photocatalytic applications [95] and most notably plumbing and soldering [93]. There are many fusible alloys in existence including Sn-Ag alloys, other Sn-based alloys, as well as alloys containing indium, bismuth, lead, cadmium, zinc and sometimes thallium. Sn-Ag-Zn alloys are used in microelectronics and some packaging applications to great effect and success but do have a melting

temperature of  $\sim 215\text{ }^{\circ}\text{C}$ , which is slightly high for the current application [96].

A study on indium alloys found that they exhibited improved mechanical properties such as ultimate tensile strength (UTS) and hardness when doped with a small amount of Ni [97]. Their melting temperature of  $72\text{ }^{\circ}\text{C}$  could be deemed too low in some applications and they also have a very large comparative cost, making their use on an industrial scale somewhat infeasible [97]. These alloys are mainly used in high-value items such as expensive electronics and semiconductors.

Some other fusible alloys include Wood's Metal, Field's Metal, Rose Metal and Galinstan. All of these are historically used in brazing and soldering, although all exhibit very low melting points, as low as  $-19\text{ }^{\circ}\text{C}$  for Galinstan (commercial product, near eutectic) and  $11\text{ }^{\circ}\text{C}$  for GalInStan (eutectic of Gallium, Indium and Tin) [98–100].

Bismuth-tin (Bi-Sn) is another such alloy. It has the inherent low-temperature properties expected and is also cheap [37]. The phase diagram for Bi-Sn is shown in Figure 1.7 and shows that the eutectic composition is 57% Sn/43% Bi with a eutectic temperature of  $139\text{ }^{\circ}\text{C}$  [101].

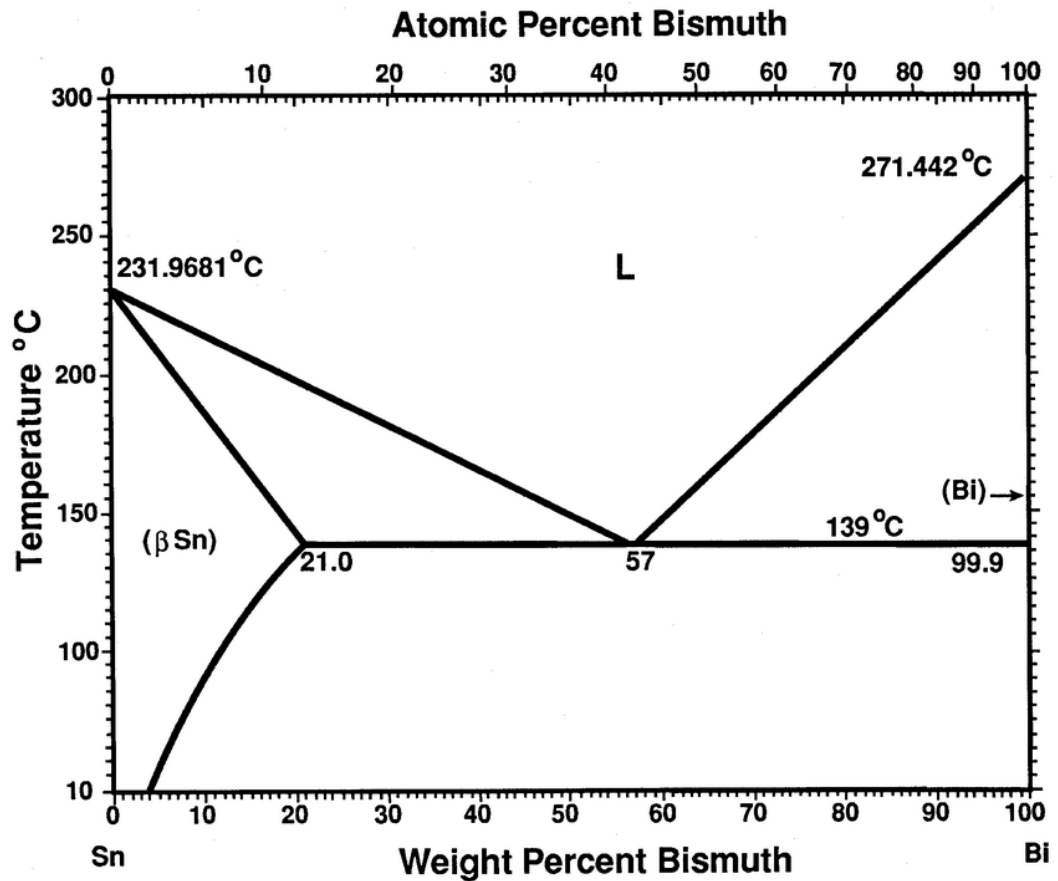


Figure 1. 4 - Binary alloy phase diagram for Bi-Sn

Literature in this area is difficult to come by, with one 2019 review of the field stating that there is a severe lack of fundamental work in the area and, as such, a lack of data and understanding to base sizeable decisions upon [102].

The corrosion of Bi-Sn and other fusible alloys is an area of particular interest and a key factor in the performance of any novel coating developed. Most work on Bi-Sn or similar fusible alloys centres around their use as alternatives to lead (Pb) based solders. One such study found that Bi-Sn performed acceptably in corrosion testing, showing a low corrosion rate and passivation and notably shows much better performance than a Sn-Zn alloy [103]. It has also been shown that a Sn-Zn-Bi alloy exhibits corrosion behaviour similar to that of pure Zn in NaCl 3wt% during open circuit potential (OCP) experiments [104].

It has been shown in [105] that Bi additions to Sn-Zn can be beneficial, when working above a certain wt% Bi. Addition of only a small amount of Bi was shown to have detrimental effects on corrosion performance, analysed using potentiodynamic polarisation and EIS [105]. However, at addition of 7wt% and above, the Bi phase exhibited a barrier effect which counteracted the detrimental effect caused by Zn-rich precipitates as Zn corrodes and is depleted [105]. This leads to a much-improved corrosion performance [105].

Corrosion of Bi-Sn is known to happen through a selective attack mechanism. This occurs on the continuous Sn-rich phase. The Sn phase is attacked preferentially to the more noble lamella Bi phase. Sn corrodes more readily than Bi-Sn and so protects it galvanically but suffers oxidation of the Sn itself. This means that the formation of Sn corrosion products is likely, namely SnO [103].

The selective attack of Sn is shown in Figure from [103].

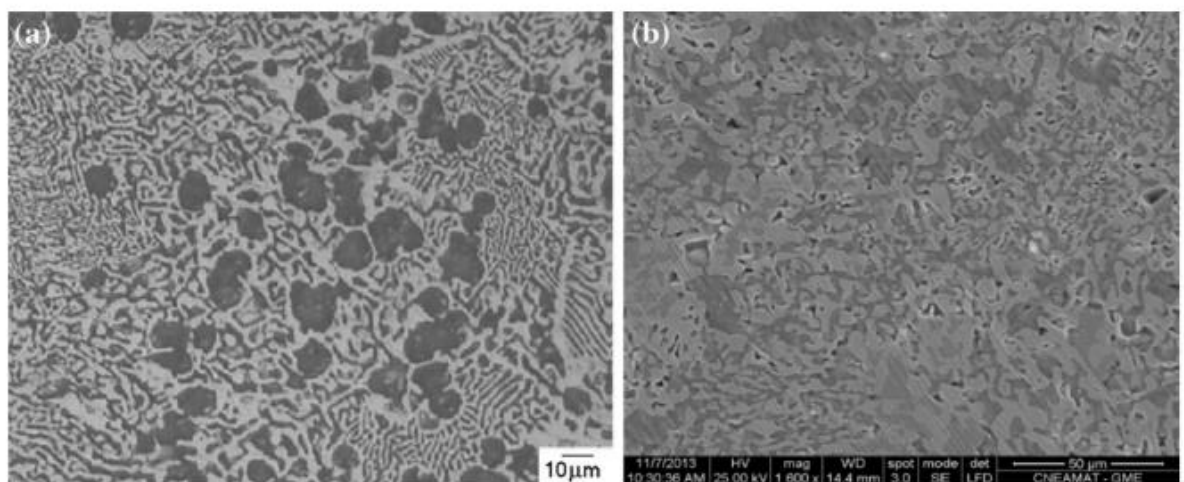


Figure 1.5 - a) Optical image of Bi-Sn microstructure and b) post-corrosion SEM image of Bi-Sn showing selective attack on the Sn-rich phase, taken from [67].

The performance of Sn57-Bi solder in 1% NaCl was investigated alongside a group of other Pb-free solders and pure Sn by Farina in [103]. OCP tests showed that The Sn-Bi alloy was more noble than all other samples tested: Sn-Ag-Cu, Sn-Ag, Sn-Cu, Sn-Pb, pure Sn and Sn-Zn which showed a similar  $E_{oc}$  value to that of pure Zn and the least noble of the samples [103,106].

LPR testing of the solders showed that Sn-Bi had the least negative  $E_{corr}$ , least negative passivity current, which indicates the slowdown of corrosion due to corrosion products and also least negative breakdown potential, above which corrosion resumes in the form of localised corrosion such as pitting [103]. Of all the solders tested, Sn-Zn had the lowest  $E_{Corr}$  but also exhibited a behaviour known as “pseudopassivation” where it seemed to be passive but the alloy underwent aggressive corrosive attack in that particular potential area [103].

To understand corrosion resistance, the passivation domain must be analysed, this is the difference between  $E_{OC}$  and  $E_B$  (breakdown potential). In the study conducted in [103], a large passivation domain was desirable for good corrosion protection. While the  $E_{Corr}$  and  $E_B$  of Sn-Bi showed good results, its passivation domain was the smallest of the candidate group of solders. This meant that the alloy showed worse performance than all the other alloys, apart from Sn-Zn which exhibited a different behaviour than others due to no passivation range [103].

$R_P$  values were also gleaned from LPR testing to assess the resistance of each alloy to a uniform corrosive attack [103]. The Bi-Sn value showed the second lowest  $R_P$  value, better than only Sn-Zn out of all samples.  $R_P$  values are useful as they give an indication of corrosion rate. The relationship between  $R_P$  and corrosion rate is given by finding  $i_{Corr}$  and then using obtained B values, which are calculated using anodic and cathodic values from the polarisation curve  $\beta_A$  and  $\beta_C$  [103]. This can then be



utilised to give a minimum and maximum  $i_{\text{Corr}}$ , considering that B may vary from 10 mV to 100 mV.

Sn-Bi was found to have the second highest corrosion rate of the group, meaning a poor corrosion performance. The highest corrosion rate was Sn-Zn and the lowest corrosion rate was exhibited by Sn-Ag-Cu [103].

The corrosion performance of bismuth-tin alongside the alloy constituents and other solders was also investigated in sulphuric and nitric acids [107]. It was found that Bi did not dissolve from Bi-Sn in sulphuric acid, but that pure Bi did, and the dissolution of tin was accelerated in the acid.

In nitric acid, pure Bi dissolved rapidly. When Bi-Sn was tested it was found that the presence of the Bi greatly accelerated the dissolution of Sn in the nitric acid [107].

This is similar to the behaviour of Bi-Sn in a NaCl electrolyte, with selective attack on Sn and subsequent Sn dissolution taking place [103,107].

It has also recently been demonstrated that Sn can have a positive effect on corrosion performance when added to steels [108]. Sn-containing Cr-Mo steels are shown to have better corrosion-resistance than those without [108]. Sn addition provides uniformity to the plate or lath-like microstructure of bainite, and also shows grain refinement [108]. Small carbon-rich phases, of only nanometres in size, are present between the bainite-ferrite plates - greatly reducing the cathodic area available for galvanic corrosion and improving the corrosion resistance of the steel [108]. The corrosion products of Sn are also found to show excellent stability and great substrate protection [108]. Although this may not seem directly relevant to a Bi-Sn +

Zn galvanic coating, it goes someway to prove the viability of Bi-Sn in a corrosion resistant system.

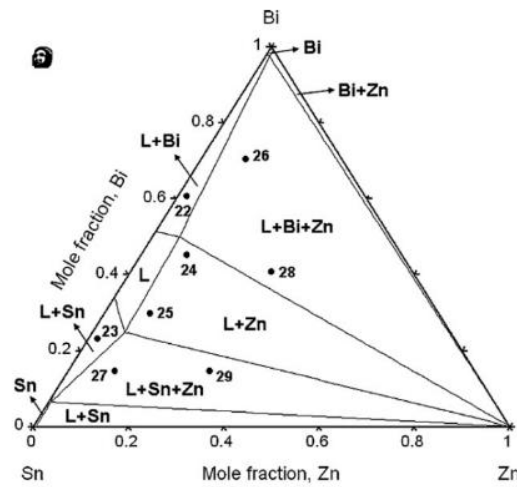


Figure 1. 6 - Ternary Phase Diagram of Bi-Sn-Zn isothermal section at 160°C from [70]

Literature on a Bi-Sn-Zn alloy is fairly scarce but a 2008 did investigate the potential development of a ternary alloy [109]. The system was produced by homogenising appropriate amounts of Bi, Sn and Zn at 800 °C under vacuum in quartz capsules for 3 days and then quenching [109]. After quenching, the samples were annealed at 160 °C for 10-15 weeks and then analysed in terms of microstructure and metallography [109]. An isothermal section at 160 °C is used to produce and propose a ternary phase diagram as seen in Figure 1.7 [109]. Figure 1.9 is proposed based on ternary phase equilibria data and phase diagrams of constituent binary systems [109]. This is in agreement with experimental data from the study, gathered by calculating enthalpies of mixing in the system using the electromotive force (EMF) method [109]. It is shown that no ternary compounds are found in the isothermal system at 160°C [109].

More recently, Zhou et al proposed a Sn-45Bi-2.62Zn alloy as an alternative to eutectic Bi-Sn [110]. This alloy showed an increase in tensile elongation, owing perhaps to the lower amount of brittle Bi [110].

## 1.2.6 Wetting and Fluxes

### 1.2.6.1 Wetting

For a coating to fully adhere to a substrate, it is preferable for the coating to have good wetting to the substrate. Wetting is defined as the ability of a liquid to spread on and maintain contact with a solid surface, as a result of intermolecular interactions between the two [111,112]. The quality of wetting is measured using the contact angle of a droplet on a solid surface, a contact angle below  $90^\circ$  constitutes good wetting and above  $90^\circ$  is poor wetting. A schematic example is shown in Figure 1.10 taken from [113].

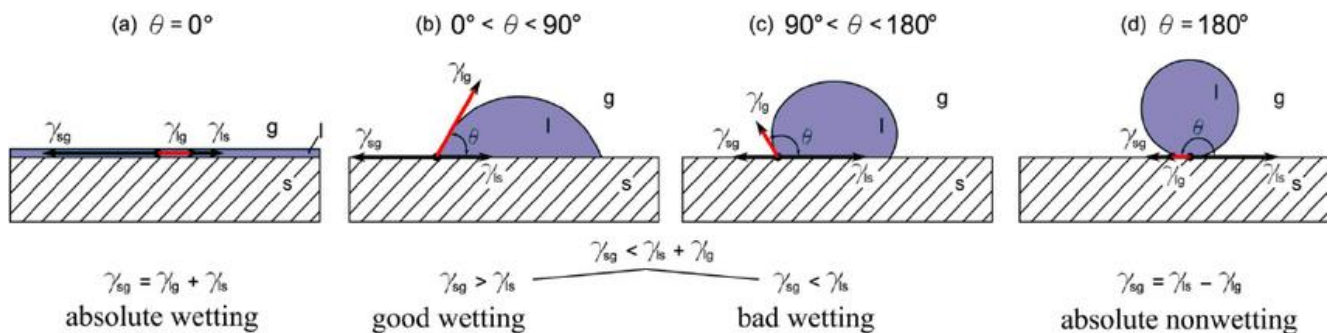


Figure 1. 7 - A schematic showing various wetting qualities: a) absolute wetting, b) good wetting, c) bad wetting and d) absolute nonwetting [77].

The wetting of fusible alloys to copper substrates has been researched previously. It was shown that Sn-58Bi wet the copper substrate with an angle of  $35^\circ$  [34]. This shows that the Bi-Sn has good wetting to a Cu substrate. This is known to be due to the formation of an intermetallic compound at the Bi-Sn / Cu substrate interface [114]. The most commonly found intermetallic is  $\text{Cu}_6\text{Sn}_5$  [114]. Upon aging of the

coated substrate, another intermetallic compound,  $\text{Cu}_3\text{Sn}$  had formed between the  $\text{Cu}_6\text{Sn}_5$  and the Cu substrate itself [114]. It is this good affinity between Cu and Bi-Sn that has seen Bi-Sn become a commonly used plumbing solder [34,37,38,93]. Bi-rich phases were left near the Cu-Sn / Bi-Sn interface due to the consumption of Sn in creating the intermetallic layers [114]. Aging was shown to bring about Bi segregation, which resulted in embrittlement of the interface. Embrittlement was shown by a change in fracture mechanism from ductile interfacial fracture along the solder-intermetallic interface to brittle interfacial fracture along the intermetallic-copper interface [114].

Element additions to Bi-Sn and their affect were also reviewed in [34]. It was shown that Al addition reduced the wettability of Bi-Sn [115]. The addition of silver, antimony and some rare earth elements were shown to improve the wettability of Bi-Sn to Cu substrates [116–118].

Another fusible alloy, indium-tin (InSn), was tested in terms of wetting to Cu-Zn substrates. A wetting angle of  $35^\circ$  between the InSn and the Cu substrate was measured [119]. Other alloys were also tested for wettability and showed good contact angle, including Sn-In-Ag ( $31^\circ$  and  $28^\circ$ ) and Sn-Ag ( $50^\circ$ ).

Fusible alloys offer good wetting and additions are shown to have varied effects. Bi-Sn in particular has desirable wetting properties. Care must be taken during heating or aging to avoid embrittlement.

#### **1.2.6.2 Fluxing**

Flux is defined as a chemical cleaning agent which act as a reducing agent to stop the evolution oxides on a metal surface [120]. A common use of fluxes is in HDG and a commonly used flux is zinc ammonium chloride ( $\text{ZnCl}_2 \cdot 2\text{NH}_4\text{Cl}$ ) (ZAC) [120]. A

ZAC flux is applied to the steel and dried. As the steel is dipped into the galvanising bath, zinc oxide on the bath surface clings to the steel surface. If left unaltered, this can cause disruption in the formation of vital iron-zinc intermetallic compounds which promote adhesion of the Zn to the steel substrate [120]. The addition of a dried preflux allows for the easy conversion of zinc oxides to zinc salts that readily melt thanks to the production of hydroxy acids [120]. Hydroxy acid formation happens as the prefluxed steel is dipped into the molten Zn bath causing the flux to melt and the  $\text{NH}_4\text{Cl}$  is split into  $\text{HCl}$  and  $\text{NH}_3$  [120]. From the split, reactions occur which result in the formation of two hydroxy acids, which melt the zinc oxides and are then dragged into the Zn and later boiled off meaning the essential intermetallic compounds can form freely [120].

Recent work on fluxing was done by Sui et al in 2023 [121]. The effect of a rosin-ethanol flux and an orthophosphoric acid aqueous solution flux on the wettability of a gallium-indium (GaIn) eutectic to Al, Cu and 430 stainless steel substrates was investigated [121]. Both fluxes showed good contact angles across all three substrates. Contact angles between the GaIn and Al substrate were around  $5^\circ$  for rosin-ethanol and around  $12.5^\circ$  for orthophosphoric acid [121]. For the Cu substrate, the rosin-ethanol contact angle measured around  $7^\circ$  and orthophosphoric acid had an angle of approximately  $20^\circ$ . When applied to 430 stainless steel, the wetting angles of GaIn were approximately  $10^\circ$  for rosin-ethanol flux and  $13^\circ$  for orthophosphoric acid [121].

It was determined that interfacial tension was decreased by the GaIn adsorbing  $\text{R}\cdot\text{COO}^-$  ions in the rosin-ethanol solution which decreases contact angle with time [121]. The orthophosphoric acid appears to exhibit a typical reactive wetting reaction, which is in line with the classical reaction product control (RPC) model

[121]. Both fluxes showed satisfactory performance and wetting angles far below the 90 ° threshold for a contact angle representative of good wetting.

### **1.2.7 Conclusion**

There is evidently much more to learn about this area and the present work will seek to address this in a systematic and comprehensive manner. The goal herein is to develop a novel low-temperature Bi-Sn + Zn coating which will be employed as a corrosion resistant coating for steel which is more logistically favourable and offers on-site and in-situ application with no need for outsourcing.

# **Chapter 2: Experimental Procedure**

## 2.1 Materials

This chapter lays out the materials used in all experimental work undertaken to achieve the aims and objectives outlined in Section 1.1. *Table 2.1* provides details of the materials used.

*Table 2. 1 - Details of Materials used in this body of work.*

Material	Provider	Purity/ Composition
Hot dipped galvanised (HDG) steel	TATA Steel UK	GI grade (0.2wt% Al remainder Zn)-
Zinc powder	Sigma	>98%
Zinc sheet	Metal Offcuts	99.999%
Bismuth-tin solder paste	Somerset Solders	43% Sn/57% Bi
Bismuth-tin pellets	Somerset Solders	43% Sn/57% Bi
Interstitial-Free (IF) Steel	TATA Steel UK	-
Zinc ammonium chloride flux	Plater Group	-
Tin	Goodfellow	99.995%
Bismuth		
HCl	Sigma	99.995%
NaCl	Sigma	99.995%
Ethanol	Sigma	99.995%
PTFE Tape	RS	-
Phosphoric acid flux	Somerset Solders	75%
Zinc chloride flux	Somerset Solders	30-40%



ZINGA zinc rich paint	Rawlins Paints	-
Ethanol	In-situ	-
Deionised water, H <sub>2</sub> O	In-situ	180MΩ-cm

### 2.1.1 Metals

HDG was used as an industrial benchmark during outdoor prolonged exposure corrosion tests. Supplied by TATA Steel UK, it was coated on 0.7 mm gauge mild steel with 20 µm of zinc per side and was provided without any pre-treatments or oils.

IF steel was also supplied by TATA Steel UK and was 0.7 mm gauge. This was used as a substrate in all tests where the Bi-Sn + Zn coating was coated onto steel. IF is a formable grade of mild steel.

### 2.1.2 Novel Coating

Both the Bi-Sn paste, and pellets were employed as the fusible alloy matrix in the novel coating. The paste was 88% metallic powder (43% Sn/57% Bi) and remainder liquid flux. Weight percentages were calculated using the actual solid metallic content of the paste: The pellets had the same composition as the paste (43% Sn/57% Bi) but contained no flux or other additions. Pellets were mainly utilised in study of the matrix itself. The composition included here was chosen as it had optimal thermal properties, outlined in section 1.2.5.

Zinc powder was also utilised in the creation of the coating, making up the zinc content of each sample. Zinc sheet was used to replicate HDG in electrochemical testing, due to it being an accurate representation of the surface of a Zn-dipped steel HDG sample.

Ethanol was used as a solvent in the coating. This was in order to reduce the viscosity of the mixture so that it could be more easily applied to the substrate.

## 2.2 Coating Production

To create the novel Bi-Sn + Zn coating, varying quantities of Zn powder and Bi-Sn paste were combined to a total weight of 100 g. This was then combined with solvent ethanol and shear mixed at 250 RPM for 15 minutes using the IKA Eurostar 20 until mixing is complete.

4 different initial coating compositions were used and are detailed in Table 2.2.

*Table 2. 2 - Sample references and their compositional makeup.*

Coating Reference	Wt% Zn	Wt% Bi-Sn
10Z	10	90
20Z	20	80
50Z	50	50
90Z	90	10

Commercial benchmarks used were Hot-Dip Galvanised steel and steel coated in Zinc Rich Paint (ZRP) (Rawlins Paints ZZIN-P1KG-AA-1PK-1KG-V1) also known as Cold Galvanising Coating (CGC).

### 2.2.1 Substrate Surface Preparation and Coating Application

The substrate was first abraded using a 1500 grit Silicon Carbide (SiC) grinding paper. Coupons were then pickled in 33% Hydrochloric Acid (HCl) in water for 20 seconds before being rinsed in cold water and then placed in a bath of flux consisting

of 2:1 water to Zinc Ammonium Chloride powder heated to 60°C.

Alternative fluxes were used in later experimental programmes. These were Zinc Chloride flux and phosphoric acid “stainless steel” flux. These fluxes were chosen due to their prominence in industry and ease of purchase and use. The substrate was submerged in the flux in a fume hood for health and safety reasons.

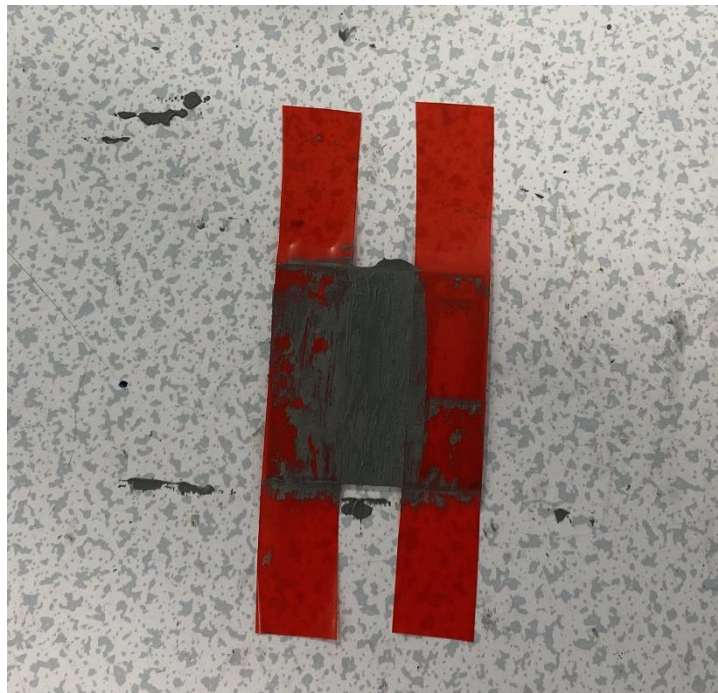


*Figure 2. 1 - Camera image showing a 50 x 50 mm steel coupon bar-coated in novel Bi-Sn + Zn coating.*

Samples were removed after 120 seconds and then dried, before the coating was applied using bar-coating, shown by photograph in figure 2.1. Bar-coating was used due to it being a flexible and easy method to use in a laboratory setting, it ensures an even coating of an area, and the thickness can be controlled by the tape height.

After 5 minutes of air curing for physical stability, the coated coupons were placed into an electrically heated atmospheric furnace at the chosen time and temperature variation.

### **2.2.2 Alternative Heating/ Curing**

As an alternative the furnace heating mentioned above, alternative methods of curing the coating were explored. This was done in order to provide options for application and curing within an industrial setting. These methods are as follows:

Near Infrared (NIR) Furnace: A bar coated sample was placed on the stage of an AdPhos CoilLab NIR Furnace, with a thermocouple attached. Several different parameters were tested on the NIR to analyse and determine the best settings for coating curing. NIR settings are not based on temperature but on speed of travel through the furnace and percentage power of the NIR source activated. A belt speed of 1m/min was utilised to give the sample sufficient time under the NIR lamps.

Different power percentages used were 20%, 30%, 40%, 50%. These are of the total power of the NIR,  $250 \text{ kWm}^{-2}$ . The results for 50% power proved that the sample was heating to a much higher temperature than desired and thus, any higher power percentages would be unnecessary.

### **2.3 Metallographic Preparation**

The samples were sectioned using an ATM Brilliant 250 Abrasive Cutter and mounted in a cold mount resin (Kleer-Set, Met Prep). Once mounted, samples were ground in sequential stages of finer grit and polished to a  $1\mu\text{m}$  mirror-finish, free of scratches. Samples that were to be imaged were polished further using Colloidal Silica. If etching was necessary, 2% nital acid was used for matter of seconds, samples were then rinsed with deionised water and dried to reveal the microstructure.

## **2.4 Microscopy**

Microscopic images were captured using a Keyence VHX Digital microscope. Fully metallurgically prepared samples, polished to a 1  $\mu\text{m}$  finish, were imaged for microstructural analysis. Particular use was made of the 3D imaging and depth composition tools, where the lowest part of the microstructure was focussed, and the microscope then built an image upwards creating a 2D image of the dynamic microstructure. Scanning electron microscope (SEM) images and Energy Dispersive X-Ray Spectroscopy (EDX/EDS) were both obtained using a Zeiss EVO SEM and Hitachi TM4000 microscope fitted with a Bruker Energy EDS unit. SEM and EDS were used for phase and elemental analysis. The accelerating voltage employed for the SEM beam was 15 kV. To identify the phases, a Bruker D8 Discover X-ray Diffractometer (XRD) equipped with a Copper source operating at 40 kV and 40 mA was utilised. Since the samples were mounted in a non-conductive resin, electron flow between the sample and the SEM stage was facilitated by applying a strip of conductive tape.

## **2.5 Hardness Testing**

Hardness is defined as the resistance of a material to permanent deformation under load. An indenter is introduced to the surface of a sample under a 1 kg force load for 10 seconds. The area of the indent is measured, and a value is given - the larger the indent, the softer the material as the indenter has displaced more material than a smaller indentation.

### 2.5.1 Vickers Hardness Testing

The indenter used in Vickers hardness testing is a pointed pyramid shape with a square base. The triangular faces of the pyramid have an included angle of  $136^\circ$  and have base angles of  $22^\circ$ . A schematic of the indenter is shown in figure 2.2.

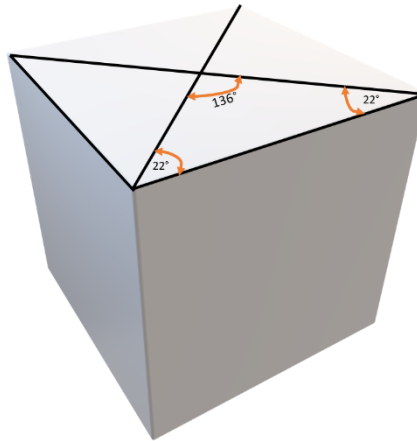


Figure 2. 2 - Schematic of a standard Vickers diamond-shaped indenter.

The indenter is applied to the surface of the material at a known pressure (P) and area of resulting diamond indent is measured, and the Vickers Hardness (Hv) is given by Equation 2.1 below:

$$Hv = \frac{P}{A} \quad \text{Equation 2.1}$$

Where P is applied pressure and A is the area of the diamond indentation.

The surface area of the diamond indentation is given by:

$$A = \frac{d^2}{2 \sin(\frac{136^\circ}{2})} = \frac{d^2}{1.8554} \quad \text{Equation 2.2}$$

Where d is the average diagonal length of the indent.

To simplify, Hv can be given by:

$$Hv = \frac{1.8554 P}{d^2} \quad \text{Equation 2.3}$$

### 2.5.2 Testing Parameters

Samples were prepared as in section 2.3. Hardness testing was undertaken on an Innovatest Vickers Hardness testing machine. Each coating, and the steel substrate, was tested 5 times and an average Vickers Hardness (Hv) value determined. Hv is a nominal, arbitrary unit but is useful to compare values of the various tested samples, whereby a higher Hv value represents a harder material.

### 2.6 Adhesion Testing

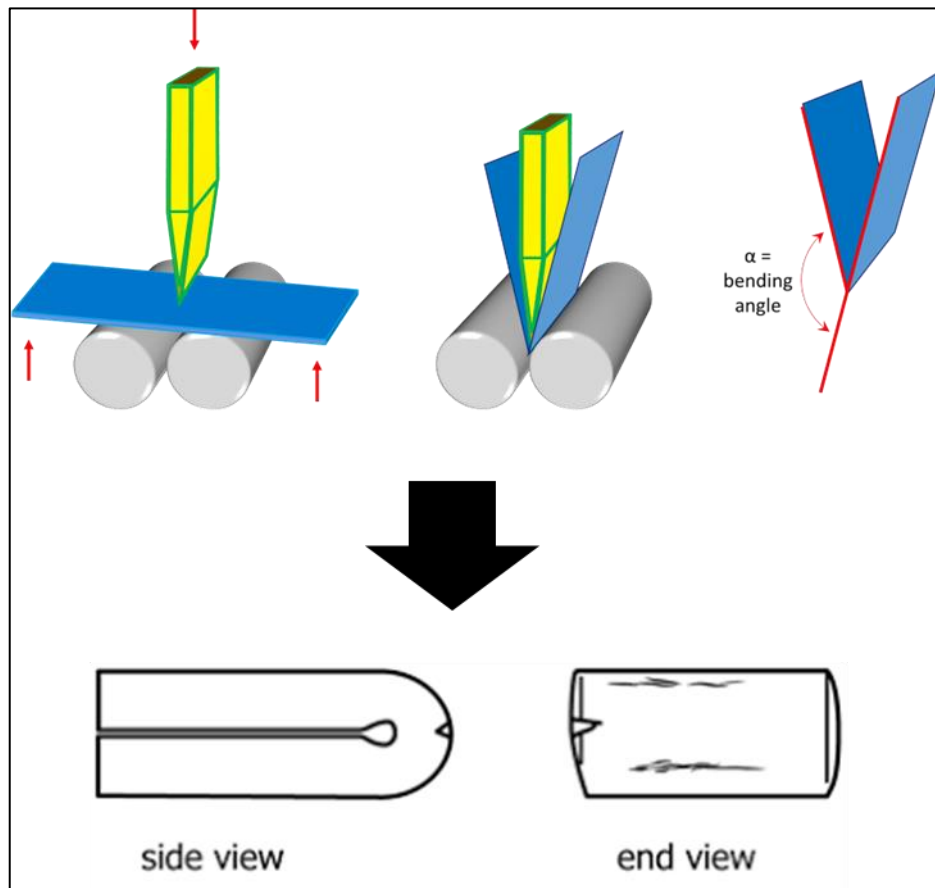


Figure 2. 3 - Schematic showing the process of adhesion testing

Coating adhesion was analysed using OT bend testing. A coated sample was cured at 245 °C for 40 mins and cooled overnight and then placed into a 3pt bend testing rig,

coating side down and bent, as shown in Figure 2.3, until no further bending was possible using that method. The two ends of the sample were placed in a vice, which was tightened until the legs were parallel (also shown in Figure 2.3). Digital images were then taken of the sample which were assessed in a qualitative nature for cracking, flaking and coating removal.

## **2.7 Electrochemical Measurements**

### **2.7.1 Open Circuit Potential (OCP)**

Open Circuit Potential occurs when the net measurable current of a working metal is zero and therefore the metal is neutral. This happens because any electrons produced during the anodic reaction are consumed during the cathodic reaction. The more positive the OCP value, the more noble the metal is. OCP is the voltage measured in a circuit when no current is flowing, giving rise to  $E_{\text{CORR}}$  (corrosion potential) – the potential a material assumes when it is immersed in a corrosive media with no external circuit connected and it is corroding freely. This is measured in reference to a known Reference electrode. The reason for utilising this method was to understand galvanic properties of samples.

A  $0.78 \text{ cm}^2$  sample of the material of interest was inserted into a commercial sample holder that was manufactured to isolate this predetermined area of material. It was then connected to a Gamry potentiostat, using a sample holder, along with a saturated calomel electrode (SCE) acting as a counter/reference electrode. The



working electrode was the sample of interest.

The two electrodes were immersed in a beaker of 1% NaCl while connected to the potentiostat (shown in Figure 2.4). Upon starting the experiment, no current is applied, and the sample remains undriven. The potential of the working electrode is measured with respect to the SCE. This gives an indication of resting potential and can be compared to the OCP of other coatings/substrates/materials to assess comparative likelihood of corrosion. Most tests were carried out at 20 °C for 24hrs, while others were 1-week long experiments. Experimental setup is shown in figure 2.4.

Samples tested were: Zn/HDG, ZRP, Steel, Novel Coating and Bi-Sn

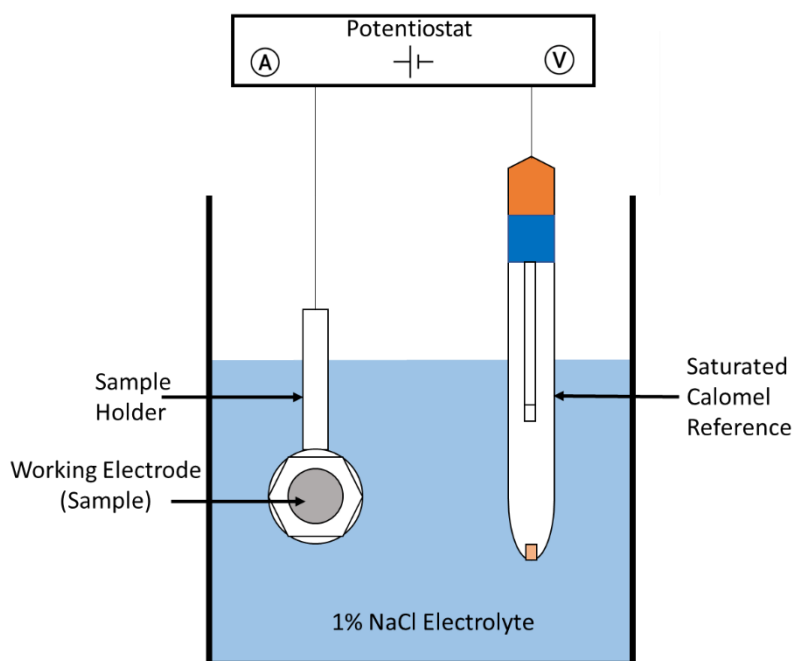


Figure 2. 4 - Schematic of OCP experimental set up.

### 2.7.2 Zero Resistance Ammetry (ZRA)

ZRA is a technique used to measure the current flowing between two electrodes connected in a galvanic couple subjected to no impressed potential (0V). This is utilised to assess galvanic corrosion and the direction of current flow. As current is measured against time, a positive current indicates current flow from the working electrode to the reference/counter electrode. This would show that the working electrode is galvanically protecting the reference/counter electrode.

The experimental apparatus was set up in a similar way to that detailed in (OCP) and is shown in Figure 2.5. Each metal to be tested was placed into a sample holder that exposed 0.78 cm<sup>2</sup> of material surface. These samples were then connected accordingly to a Gamry potentiostat as the working and counter/reference respectively.

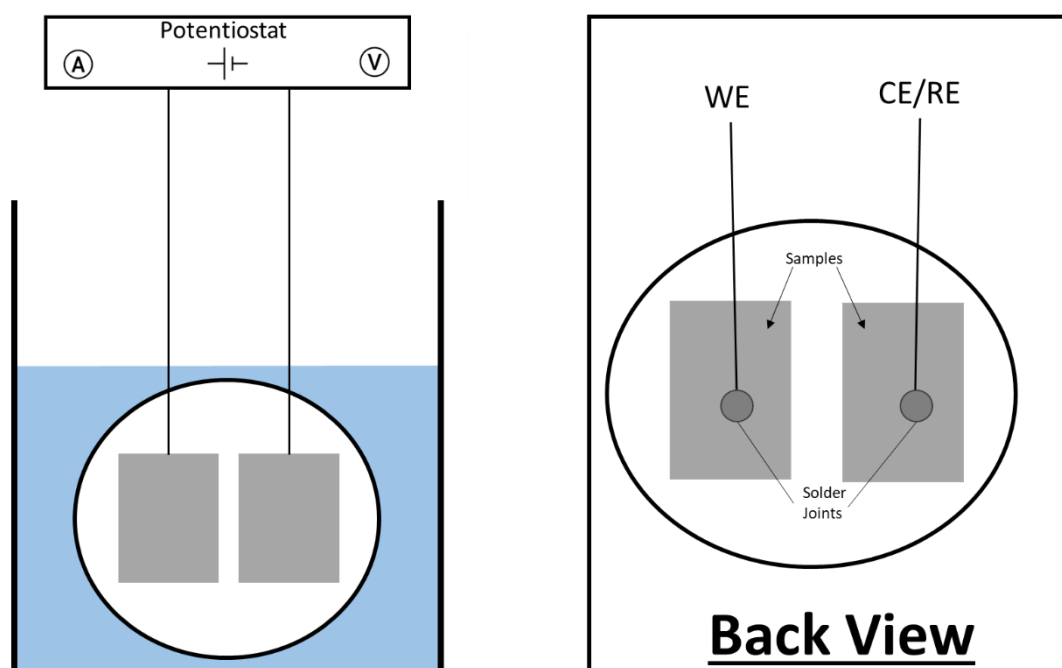


Figure 2. 5 - Schematic of ZRA experimental set up.

As in (OCP), the samples were placed into a beaker which was filled with 1% NaCl until both samples were fully submerged. Measurements were taken for 2 min, every hour, for 24 hrs. The end point of data capture for each hour was collated into a graph representing a 24 hrs experiment.

### 2.7.3 Potentiodynamic Sweeps

Potentiodynamic polarisation experiments were used in this research to assess the governing reactions for the corrosion of samples. In particular, cathodic sweeps were utilised to assess the dominant cathodic action during the corrosion of the samples. Setup involves very similar apparatus to the OCP experiment and is shown in Figure 2.6, but a counter electrode is employed alongside the working and reference. This experiment took place in 1% NaCl at room temperature. The equilibrium potential of the sample was determined, and an external potential of  $\pm 1.5$  V was applied to the working electrode at a rate of  $1 \text{ mVs}^{-1}$  from equilibrium and the

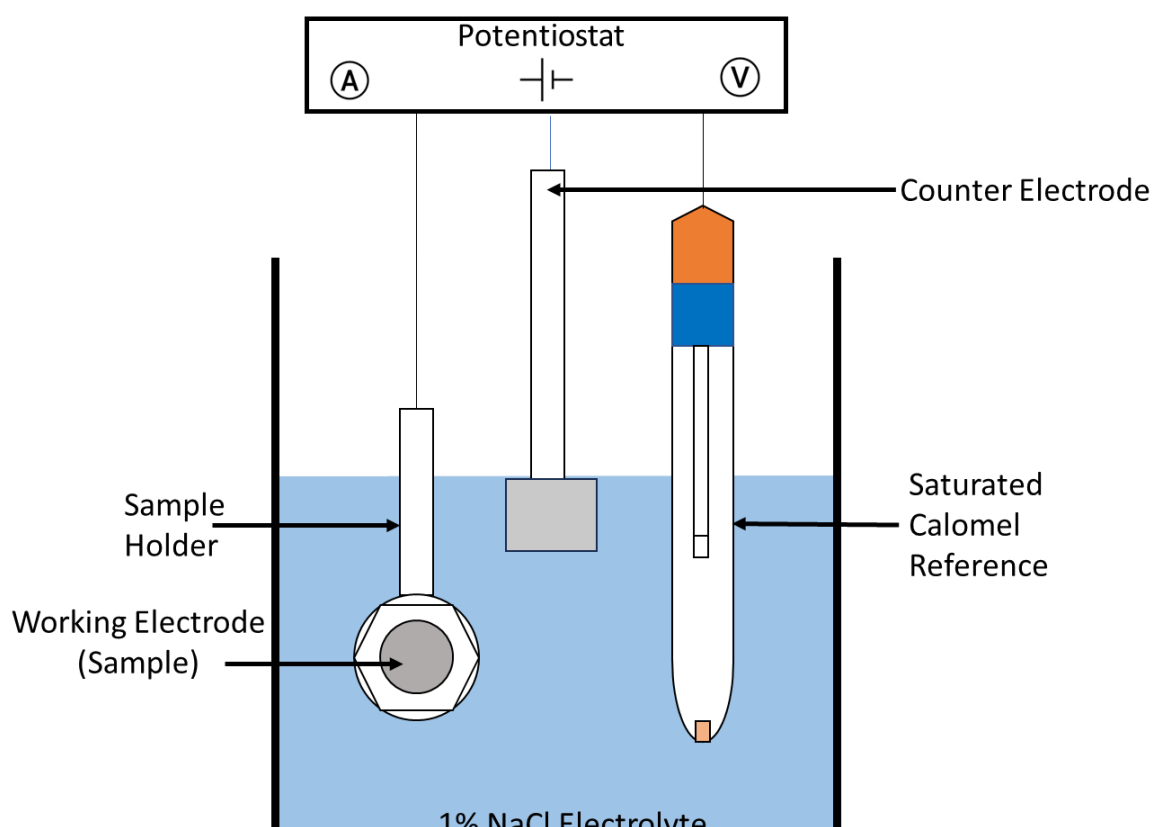


Figure 2. 6 - Schematic of experimental setup for potentiodynamic sweeps and Linear Polarisation Resistance (LPR).

resulting current was measured. This moved the sample away from its equilibrium potential until the curve became linear. The flowing net current depended on whether the displacement from the equilibrium is positive or negative.

An anodic current would mean oxidation reactions were occurring at positive overpotentials, and cathodic currents indicated reduction reactions at negative overpotentials.

## 2.8 Scanning Vibrating Electrode Technique (SVET)

The scanning vibrating electrode technique (SVET) is widely considered as an evolution of the scanning reference electrode technique (SRET) and is utilised to analyse corrosion behaviour of metals and allows for comprehension of corrosion mechanics in an aqueous, electrolytic environment [122]. This technique has been used extensively to research both cut-edge and surface corrosion of metallic coatings and is widely considered a standard-practise technique for analysis of corrosion performance [122–128].

In this thesis, SVET is used to compliment, corroborate, and substantiate the other

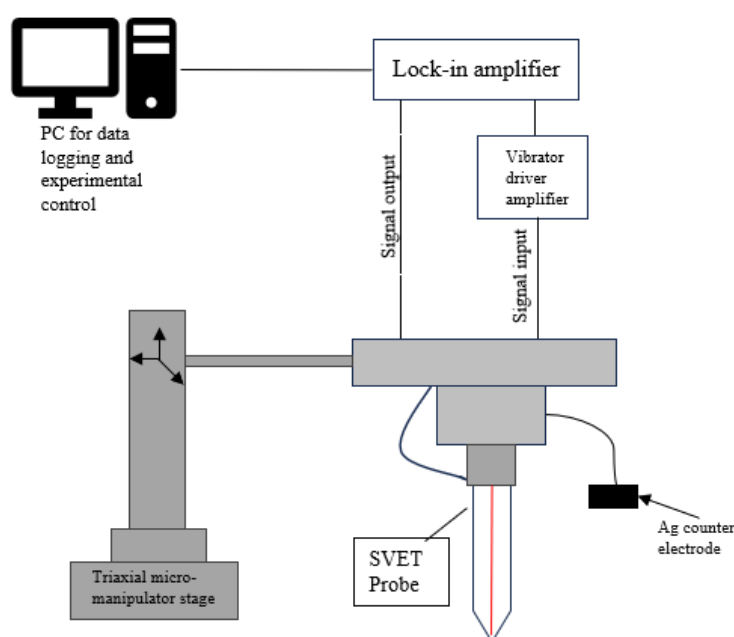


Figure 2. 7 - Schematic of SVET set up

electrochemical experiments explained above which also, in turn, explain the results provided by the SVET experiments. SVET provides anodic current density which can be used to determine mass loss value, making it a partly quantitative technique. Figure 2.7 shows a schematic of the SVET setup. The probe of the SVET consists of a 125  $\mu\text{m}$  diameter platinum wire micro-tip which is encased in an insulating glass tube and vibrates at a constant amplitude, frequency and height above the sample surface when submerged in an electrolyte for experimental purposes. The lock-in amplifier (EG&G Instruments 7265) provides vibration of 140 Hz and an amplitude of 25  $\mu\text{m}$  to the probe in the z direction, via an external amplifier. The probe scans in a set-wise manner in the x and y-direction, 100  $\mu\text{m}$  above the sample surface. The triaxial micro-manipulator stage and PC work in conjunction to provide the movement of the probe. The set-up, instrumental design and operating procedure for SVET has been described at length elsewhere [55,62,67,84,85,122–126].

As a metallic sample corrodes, an ionic current flux is produced and an iso-potential field is established in the electrolyte around the anode, as shown in Figure 2.8. The SVET probe is able to cross the lines of current flux and register the alternating potential, which is directly proportional to the potential gradient in the z-direction produced by the ionic current flux. This data can be represented graphically on colour contour maps and can also be used in calculating current density by using a calibration factor, obtained during the calibration process described below.

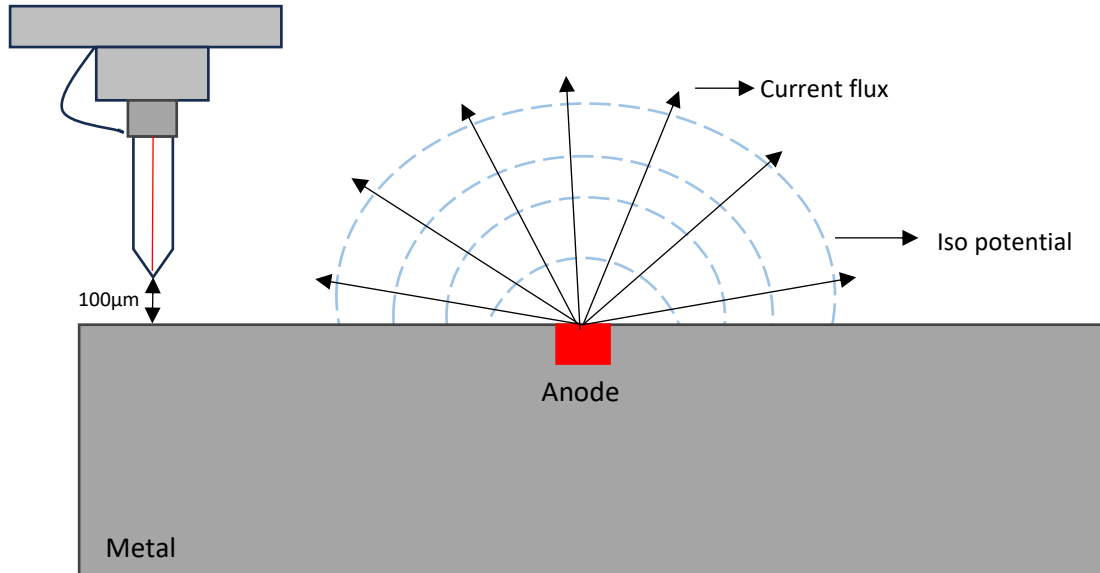


Figure 2. 8 - A schematic representing current flux and iso-potential lines above an anode.

The electric field strength (F) or potential gradient due to point source measured by SVET probe in direction of vibration (normal to the sample surface or z-direction) is given by:

$$F = \frac{dE}{dz} = \frac{-iz}{2\pi k(x^2 + y^2 + z^2)^{1.5}} \quad \text{Equation 2.4}$$

k = electrolyte conductivity

x,y,z = coordinate plane value

i = current source

The maximum possible field strength ( $F_{\max}$ ) is found at the exact height z above the origin (x=0, y=0) and is given by:

$$F_{max} = \frac{-1}{2\pi k z^2} \quad \text{Equation 2.5}$$

This inverse-square relationship between probe height and  $F_{max}$  means scanning height is critically important when undertaking SVET.

### 2.8.1 Calibration of the SVET

SVET measures potential gradients in nanovolts (nV), which can be converted into current density values, measured in  $\text{Am}^{-2}$  by means of calibration. This is achieved using a point current source.

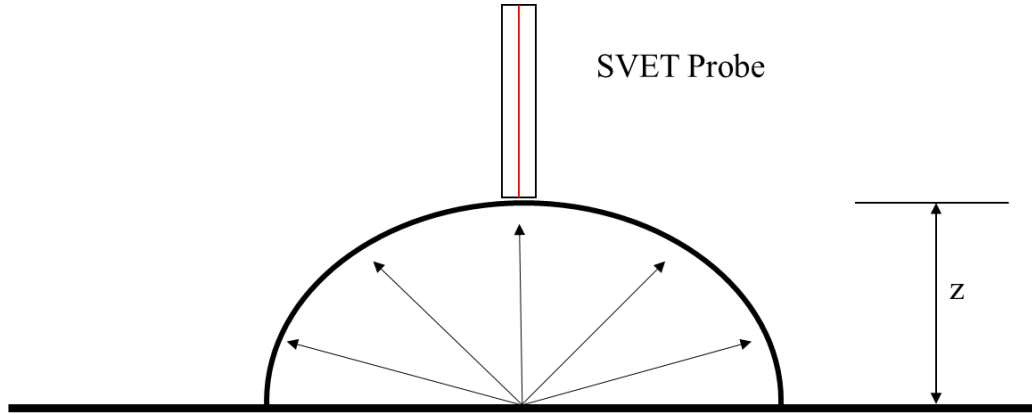


Figure 2. 9 - Current emerging from a point current source.

At a point of current source, current fluxes transpire from the centre and are distributed evenly in a hemispherical manner as shown in Figure 2.9. The current density ( $j_z$ ) in the direction of probe vibration (z-direction) is thus given by dividing the applied current by the surface area of the hemisphere ( $2\pi z^2$ ), as shown below:

$$j_z = \frac{i}{2\pi z^2} \quad \text{Equation 2.6}$$

$i$  = applied current

$z$  = height of hemisphere, i.e., height of SVET probe from sample surface

By plotting peak-to-peak SVET voltage signal ( $V_{pp}$ ) vs  $j_z$ , it is possible to convert SVET voltage signal to current density in the direction of probe vibration.

SVET calibration was completed using a two-compartment cell, shown in schematic from in Figure 2.10.

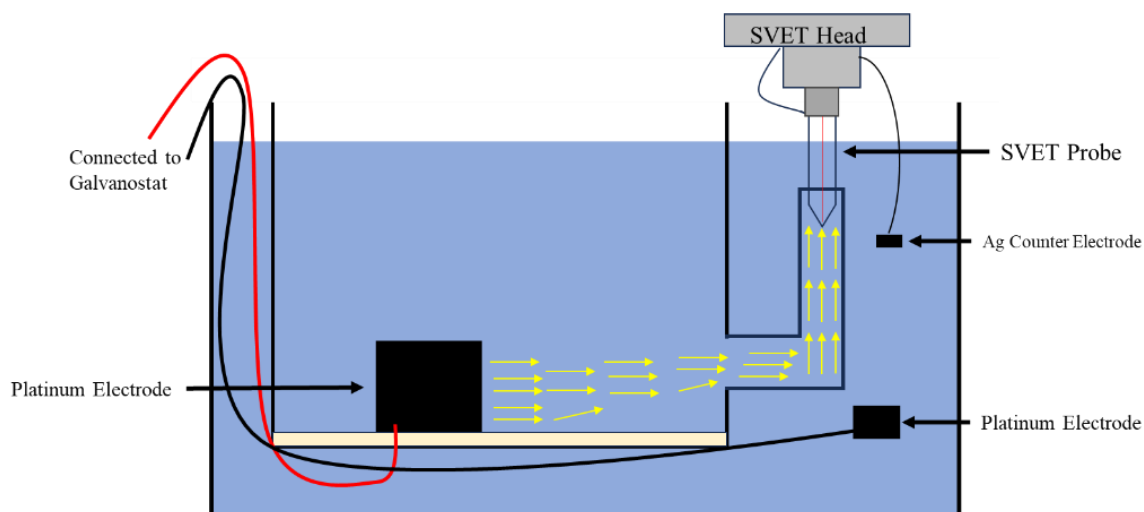


Figure 2. 10 - Schematic of two-compartment cell used in SVET calibration.

Each compartment of the setup in figure 2.10 contained a platinum electrode of  $1\text{cm}^2$  and were connected via a vertical tube with an internal diameter of 4.8mm. The apparatus was then filled with the electrolyte considered for the study; in this case it was 1%NaCl. To calibrate the SVET, the probe tip was lowered into the vertical tube and applied with a range of various currents using a battery-powered galvanostat. The tube enables the flow of current to align vertically, running parallel to the tube axis, resulting in a consistent current density along the direction of SVET



probe vibration. For each applied current, a current density was calculated for the area of the glass tube, where radius was equal to  $0.5 \times 4.8$  mm, giving 2.4 mm. The current density for each respective applied current is plotted against the measured SVET voltage – the gradient of which provides a calibration factor for the combination of SVET instrument and electrolyte under analysis. All in all, this method provides a swift calibration which is independent of the probe height and facilitates an effective means of converting measured SVET potential (voltage) into current density.

### 2.8.2 SVET Sample Preparation

For cut-edge SVET analysis, samples were trimmed to a length of 2.5 cm along the cut edge, providing a non-exposed surface area of 5 cm<sup>2</sup>, as illustrated in Figure 2.11. This sizing facilitated ample scanning coverage for the cut edge, maintaining a straightforward mounting procedure. The coated samples were subsequently affixed in clear epoxy resin (Met Prep LTD) and allowed to cure overnight. Post-curing, the samples underwent grinding and polishing to achieve a 1 µm finish. No etching was performed on the samples.

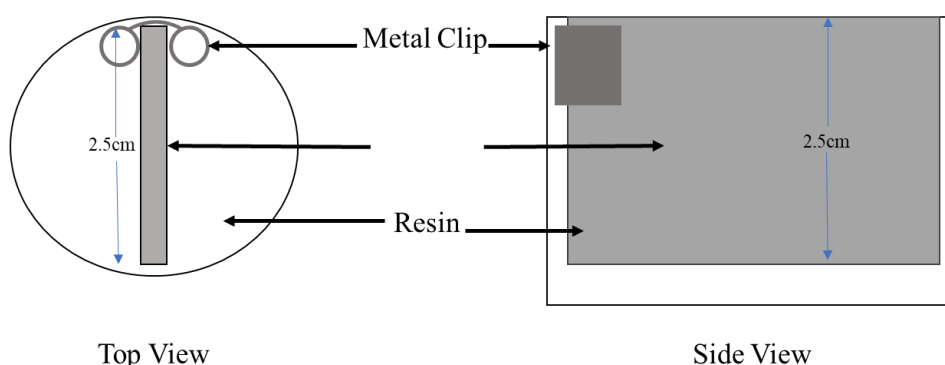


Figure 2. 11 - Schematic of Top and Side View of prepared SVET sample.

Experiments were undertaken at room temperature (25 °C) and the dissolved oxygen concentration in bulk solution was assumed to be constant at  $2.8 \times 10^{-4}$  mol dm<sup>-3</sup>, the

equilibrium concentration for air saturated water.

An area was exposed using PTFE tape for scanning purposes. This area scanned by the SVET probe was 10 mm along the length of the cut edge and 3 mm along its width. 40 measurements were made along the cut edge length of the sample, and 30 measurements were taken along the width of the sample, totalling 1200 measurements for every scan. One scan was taken every hour for a period of 24 hours in a 1%NaCl solution. Three repeat tests were carried out for each test undertaken.

### 2.8.3 Manipulation and Analysis of SVET Data

By applying a conversion factor, the recorded data (outlined in section 2.8.1) is converted to a normal current density ( $j_z$ ). Spatially resolved maps of normal current density are produced by implementing a surface modelling software package;

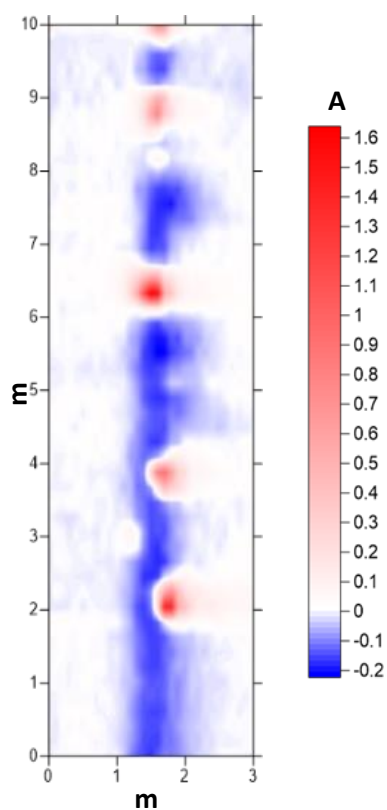


*Figure 2. 12 - Representative SVET colour map of resolved current density, created with SVET data using Golden's Surfer 10.*

Golden's Surfer 10. As shown in Figure 2.12, the anodic and cathodic sites are denoted by differentiating colours, anodic in red and cathodic in blue.

Current density can also be used to calculate total mass lost as a result of anodic activity. Total anodic current for the scan is given by integrating all positive anodic current densities ( $j_z$ ), as shown in Equation 2.6.

$$I_{at} = \int_0^x \int_0^y [j_z(x,y)] dx dy \quad \text{Equation 2.6}$$

Where;

$I_{at}$  = anodic current,

$j_z$  = normal current density,

x,y = length and width of SVET scan

To get an average anodic current ( $j_{at}$ ), the total anodic current ( $I_{at}$ ) is divided by the scan area (A), as show in equation... below.

$$j_{at} = \frac{I_{at}}{A} \quad \text{Equation 2.7}$$

Hourly charge (Q) can be calculated by assuming that corrosion activity remains consistent for a scan period, 3600 seconds – denoted by time (t), as presented in equation...

$$Q = j_{at} \times t \quad \text{Equation 2.8}$$

Mass loss can then be calculated using the Faraday equation along with other information concerning the corrosion of the metal under investigation, as shown in equation ....

$$\text{Mass Loss} = \frac{Q}{nF} A_r \quad \text{Equation 2.9}$$

Where;

Q = charge (C)

F = Faraday's constant (96487 C mol<sup>-1</sup>)

n = number of electrons involved

A<sub>r</sub> = atomic weight of corroding material

To calculate total mass loss, each hourly mass loss calculated using equation 2.9 should be added together.

#### **2.8.4 Limitations of SVET**

The SVET is only able to resolve localised current events that are separated by a distance greater than 1.5 times that of the scan height of 100 µm, so 150 µm. It is also only able to detect normal current density and will not detect current loops that terminate under the scan plane of 100 µm. This thesis assumes a constant corrosion rate during SVET scans whereas realistically, the rate of corrosion could vary in a real-life application. Despite the above limitations, SVET has proved an indispensable tool in analysis of corrosion performance for the novel coatings considered herein and in wider literature considering countless metals and alloys.

### **2.9 Long Term Exposure Testing**

Samples coated in HDG, ZRP and a novel Bi-Sn + Zn coating were tested to long exposure in an outdoor environment, in order to test the long-term viability of the coating and how its performance compares to market and industry leaders. The samples were coated as described in *section 2.2.1*, ensuring that all cut-edges were sealed.



# **Chapter 3: Development and Optimisation of Microstructure and Process for a Novel Galvanic Coating**

### 3.1 Introduction

In light of the issues surrounding Zinc Rich Paints (ZRP), mentioned in Chapter 1, a need has been identified for a more reliable and robust coating solution for protection of repaired Hot Dip Galvanised steel (HDG) [77–79,129]. A metallic-matrix coating would provide good electrical contact between the galvanic particles in the coating and the steel substrate. Fusible alloys are identified as the best starting point in introducing a metallic matrix into a coating system, based on their properties and mechanical attributes [34,93,102,103,130].

Fusible alloys, termed low-melting alloys, are a diverse range of alloys that can contain silver, copper, tin, gallium, mercury, bismuth, lead. They are grouped in various ways depending on source, but some well-known examples include Wood's Metal, Field's Metal, Rose Metal and Galinstan, as mentioned in Chapter 1. In selecting a low-melting alloy that could be used in a commercial situation cost and availability is important. In terms of melting point, for this application anything below 250 °C is considered low melting. Many fusible alloys are alluded to in section 1.2.5, demonstrating the wide application of this group of materials.

However, it seems that bismuth-tin (Bi-Sn) is an excellent potential candidate for a metallic matrix due to its low melting temperature, good availability, popularity in certain industries and easy application as a paste, [94,95]. Bi-Sn was introduced as an alternative to lead (Pb) based alloys in areas such as plumbing meaning its properties are well understood, is already in industrial use and is readily available. In order to provide galvanic protection to steel, it will be necessary to include an addition to the coating that will provide galvanic protection to the substrate while being kept in electrical contact with the steel via the Bi-Sn matrix. Zinc is the obvious choice as a galvanic element to the coating, given it is widely known to offer

protection properties especially when coated onto steel substrates and is has a free corrosion potential below that of iron [15,39,131–133].

This chapter will firstly focus on the initial creation and development of the coating system. It will investigate the effect of Zn loading. The different loading percentages will be assessed using SEM and EDX analysis. The desired microstructure will be comparable to that of a ZRP – only with Bi-Sn surrounding the “islands” of Zn as opposed to the organic or inorganic matrix often seen in ZRPs, in order to provide maintained electrical contact between Zn and steel substrate.

The heat treatment cycle for the coating was metallographically assessed. The melting point of Bi-Sn is known to be 139 °C, while that of Zn is 420 °C [15,93].

One of the major logistical drawbacks of HDG is the requirement to heat the substrate to around 450°C where the zinc is molten [120,134]. The need to hold a substrate at this temperature can, in the case of high strength steels with non-equilibrium phases, a deterioration in mechanical properties. The aim of this work is for this new coating to cure at a much lower temperature. This would make the application process of the coating onto substrates much more dynamic and flexible, expelling the need for large baths of molten metal at extremely high temperatures and potentially offering a galvanic system to steels which currently cannot be galvanised using the traditional method. The intention is for the coating to be applied in almost any scenario; as part of production at a factory, on-site by maintenance or even in-situ by the customer team; and cured easily with a mobile heat source. This would mean a much lower temperature process than HDG. This would be especially beneficial for high-strength steels that suffer liquid-metal embrittlement during galvanising. This is caused by cracking due to Zn infiltration of grain boundary areas



and segregation of additions such as Mn and Si causing unstable phases to form. As a result, cracks form and propagate, this weakening the steel [135–138].

Surface treatment is an essential part of the coating process. In this chapter, a standard treatment is used. Abrasion of steel removes surface oxide and scale and creates a surface that promotes keying between the substrate and the coating thereby, theoretically improving adhesion. Cleaning, acid pickling and fluxing of steel surfaces is a common practice in industry. The use of dilute hydrochloric acid (HCl) in this chapter as a pickling agent, to remove oxidation, rust, and other undesired corrosion products, is in line with industry standard at present. Fluxing is the act of chemically reacting an agent with the steel to protect it from oxidation. Zinc Ammonium Chloride ( $(\text{NH}_4)_2\text{ZnCl}_4$ ) is a commonly used flux in industry, applied as an aqueous solution to the steel substrate during galvanising to reduce any oxides present and prevent oxide formation. This allows for optimal adherence and wetting of Zn to the steel in HDG, and its use is adopted in this work [139]. In Chapter 6 of this thesis, fluxing is once again discussed as alternative fluxes are offered and analysed.

Here, the initial Zn loading of the coating will be determined in terms of microstructure, against our desired plan for percolation. This will provide the composition of our coating as we move forward. The heating temperature and time will be also tested in order to determine the best curing cycle to study further.

## 3.2 Experimental Details

### 3.2.1 Materials

Bi-Sn was supplied by Somerset Solders, containing a eutectic 42 % Sn, 58 % Bi alloy composition. The paste was grey and slightly granular as received as shown in the macroscopic image in figure 3.1 The paste was produced by Qualitek using a flux, with metal content being 88%. Figure 3.2 shows an SEM image alongside an EDS map of the Bi-Sn alloy, after heat treatment.



Figure 3. 2 - Digital Camera picture of the Bi-Sn paste, as received. Shown here on a wooden splint.

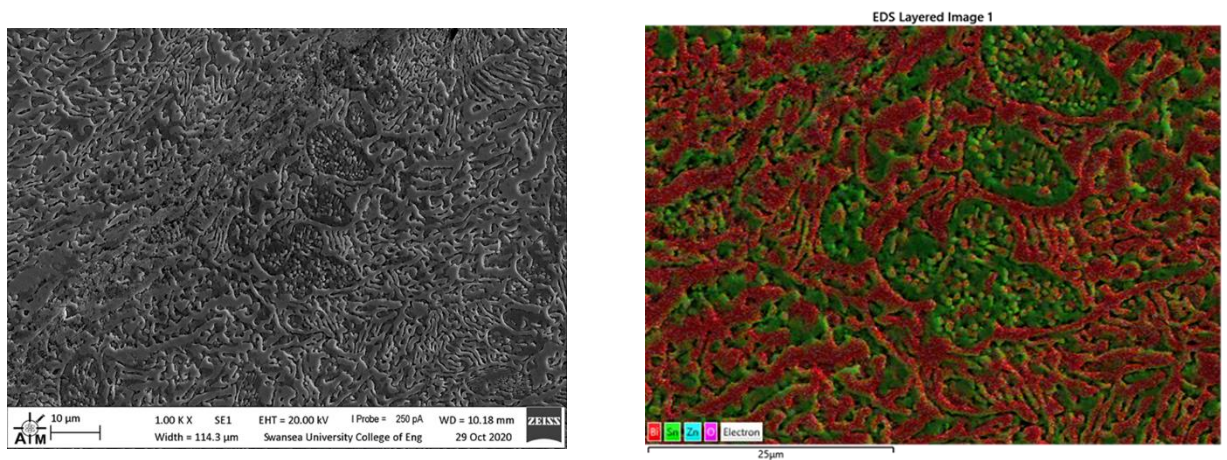


Figure 3. 1 - An SEM micrograph of Bi-Sn microstructure after heat treatment at 180 °C for 10 mins, and the corresponding EDS map with Bi represented in red and Sn in green.

On the EDS map in figure 3.2, the red sections represent bismuth (Bi) and green sections are tin (Sn), representing a typical eutectic composition for the alloy.

Zinc (Zn) powder was acquired from Sigma Aldrich and has a purity of >98 %.

The substrate used was interstitial-free (IF) steel with a gauge of 0.7 mm, provided by Tata Steel UK. This material was chosen for its widespread use as a substrate for HDG and its similar properties to other widely used steels.

Zinc Ammonium Chloride (ZAC) flux salt was obtained from Plater Chemicals Group and was mixed with water at a ratio of 2:1 water to ZAC and heated to 60°C.

### 3.2.2 Sample Preparation

Coating production is detailed in Chapter 2. As shown there, varying quantities of Zn were added to Bi-Sn paste in order to make up the coating. To find the correct weight of Zn and Bi-Sn to add, in order to get the accurate Bi-Sn metal content, the below set of equations was created and utilised:

$$Wt_{Zn} = \%_{Zn} \cdot Wt_{TOT} \quad \text{Equation 3.1}$$

$$Wt_{Bi-Sn_M} = \%_{Bi-Sn} \cdot Wt_{TOT} \quad \text{Equation 3.2}$$

$$Wt_{Bi-Sn_{ACT}} = Wt_{Bi-Sn_M} \cdot 1.136364 \quad \text{Equation 3.3}$$

Where,

$Wt_{Zn}$  is the weight of Zn added for mixing,

$\%_{Zn}$  is the desired percentage weight of Zn for the particular trial,

$Wt_{TOT}$  is the total weight of the metallic coating for the trial,

$Wt_{Bi-Sn_M}$  is the weight of Bi-Sn metal, not paste as the paste contains flux also,

$\%_{Bi-Sn}$  is the desired percentage weight of Bi-Sn for this particular trial,

$Wt_{Bi-Sn_{ACT}}$  is the physical amount of Bi-Sn paste needed to ascertain the correct weight of metallic Bi-Sn, as required.

It should be noted that the 1.136364 figure denotes the multiplication factor between the metal content of the Bi-Sn paste (88 %) and the actual weight of the paste, inclusive of flux (100 %). This is necessary to add the correct amount of paste for the accurate desired weight of Bi-Sn metal.

The steel substrate was cleaned and fluxed as outlined in Chapter 2.

### 3.3 Methods

The prepared coating containing desired Zn weight percentage was bar coated onto the clean substrate and allowed to cure in air for 5 minutes, as detailed previously in *section 2.2.1*. The coated samples were then inserted into a furnace, preheated to 180 °C. The time and temperature were varied as part of the study within this chapter, in an effort to find the optimal curing cycle for the coating, as dictated by the introduction for this chapter.

The heating/curing cycles are shown in *table 3.1*. Once cool they were sectioned and prepared metallographically for analysis. Analysis took place according to the methods mentioned in Chapter 2 for SEM, Digital Microscopy and EDS.

*Table 3. 1 - Heat treatment details for all samples – a tick is indicative of a sample being prepared, a cross shows a decision not to move forward with that sample.*

Heat Treatment	100 % Bi-Sn	80 % Bi-Sn 20 % Zn	50 % Bi-Sn 50 % Zn	90 % Zn 10 % Bi-Sn
<b>180 °C 10 min</b>	✓	✓	✓	✓
<b>200 °C 20 min</b>	N/A	✓	✓	☒
<b>200 °C 40 min</b>	N/A	✓	✓	☒

245 °C 40 min	N/A	✓	☒	☒
------------------	-----	---	---	---

### 3.4 Results

#### 3.4.1 Zn Loading for Microstructure Optimisation

The aim is to consistently produce a microstructure similar to that shown *figure 3.3* where the Bi-Sn matrix melts and flows around the zinc particles, as outlined in section 3.1. This produces Zn “islands” ranging in size from around 0.5 - 21µm surrounded by a continuous Bi-Sn matrix. Zn loading was varied to identify any limits to the amount of zinc included in the coating, which will ultimately influence the longevity of the final coated system. Initial Zn weight percentages trialled were as shown in *table 3.2*, along with their sample name.

*Table 3. 2 - Sample Names and their Compositions.*

Sample Name	Zn wt%	Bi-Sn wt%
100BiSn	0	100
20Z	20	80
50Z	50	50
90Z	90	10

For initial trials, 100% Bi-Sn solder was heated for 10 mins at 180 °C. This is higher than the melting point for Bi-Sn alloy and provides adequate time for the relevant flow to occur.

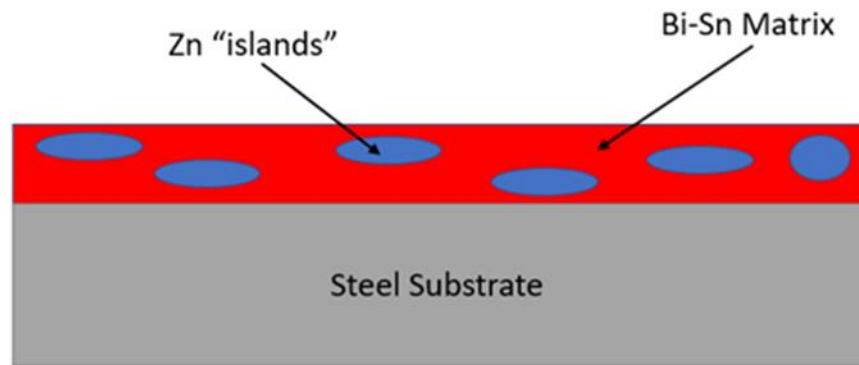


Figure 3. 3 - schematic of intended coating design showing Zn islands enveloped by a Bi-Sn matrix.

#### 3.4.1.1 100% Bi-Sn (100BiSn)

The sample 100BiSn was only included in order to assess the microstructure of the Bi-Sn, to give context and understand what to expect from a typical eutectic microstructure. *Figure 3.4* below shows 100BiSn after the initial trial.

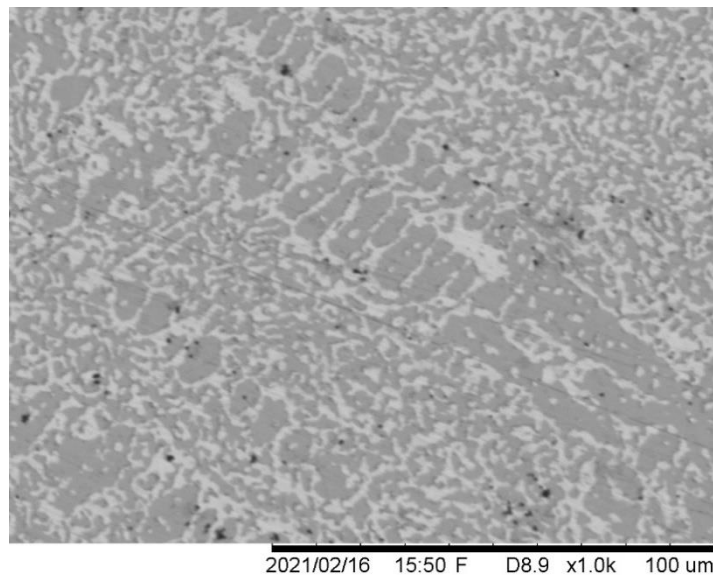


Figure 3. 4 - SEM image of 100BiSn heat treated at 180C for 10 minutes.

It is crucial that the microstructure in figure 3.3 is understood. The micrograph shows a heterogeneous microstructure characterised by a typical lamella eutectic

structure. The shape and size of the grains, offer an insight into the recrystallisation of the alloy upon cooling [140].

A closer inspection reveals the presence of lamella structures. This lamella-type microstructure is characteristic of eutectic Bi-Sn and is indicative of the alloy's solidification history. Formed during the transition from liquid to solid, the directional growth of the dendrites could also provide an insight into cooling rates and thermal properties of the alloy. This information is all relevant context for the mechanical properties of the material [35,140–145].

When considering *figure 3.5*, which shows the corresponding EDS map of the image in *figure 3.4*, the compositional microstructure of the alloy is evident. There is clear distinction between the blue bismuth-rich and red tin-rich areas . Again, the structure is even more pronounced as we see the clear-cut differences between the regions. Of interest, however, are the regions where blue and red seem to blend to make a darker red or purple-like colour show up on the map, interspersed throughout the micrograph. The purple areas are the characteristic intermetallic phases present in the Bi-Sn microstructure. These phases are characterised by unique morphologies and significantly influence the mechanical performance of the alloy, giving it an inherent brittleness that can be detrimental when considering the applications of Bi-Sn and the desired outcome of this body of work.

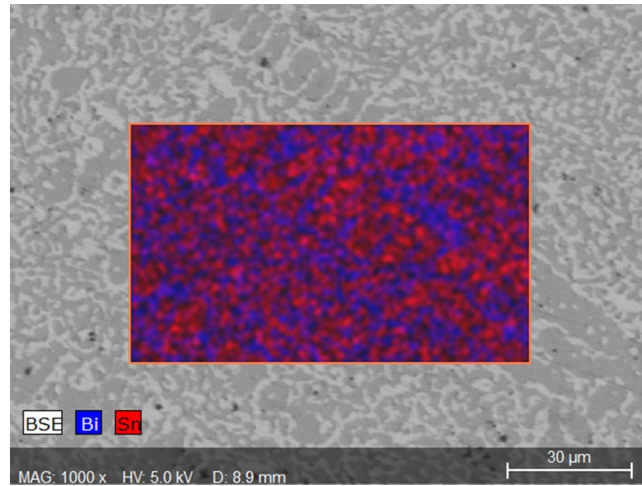


Figure 3.5 - EDS map of 100BS, Bi is represented in blue and Sn in red.

Figures 3.4 and 3.5 show a typical eutectic, 100 % Bi-Sn microstructure and EDS map.

#### 3.4.1.2 20wt% Zn, 80wt% Bi-Sn (20Z)

When 20 wt% Zn was added to the Bi-Sn, figure 3.6 of sample 20Z, there is a dramatic change in the microstructure. Whilst the blue and red are still present in the EDS map presented here, representing Bi and Sn respectively; Zn (coloured green) can be clearly seen in between the larger Bi-Sn particles.

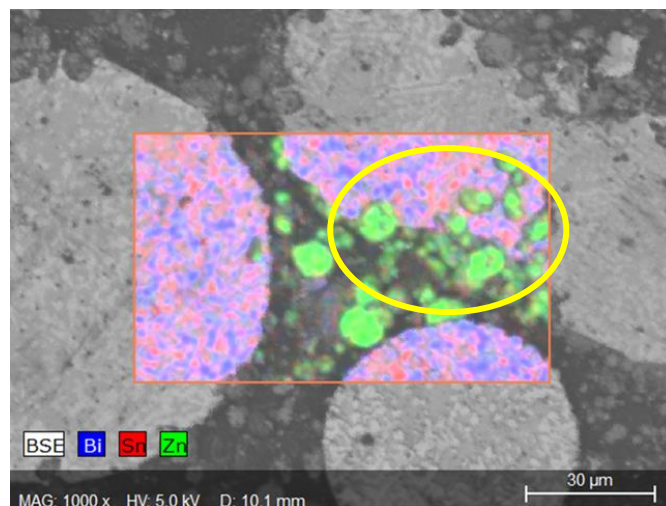


Figure 3.6 - EDS map of 20Z, Bi is blue, Sn is red, and Zn is neon green. A region of interest is circled in yellow.



It can be seen that the Bi-Sn has formed large, round, or oblong spheres/areas, whilst maintaining its eutectic microstructure. The Zn particles are heterogeneously distributed around the Bi-Sn regions. The darker regions are deeper-laying Zn particles, although no analysis was done for iron (Fe) here so it cannot be ruled out that it is steel substrate. Again, the darker particles are thought to be Zn laying deeper in the coating, but the possibility of exposed Fe cannot be ruled out.

The Bi-Sn does not appear to have flown around the zinc particles, instead, they have retained their spherical structure. This is not the desired microstructure since the open voids between the Bi-Sn and Zn particles could allow water ingress.

However, if attention is turned to just the right of the centre of the micrograph, there is a region of particular interest, circled in yellow. Here, Zn clusters can be seen distinctly within a eutectic Bi-Sn area. There is also a small zinc particle to the left, showing it has occurred in more than one area. This image of Zn “islands” in a, albeit localised and very small, Bi-Sn matrix shows that the target microstructure is achievable. The 20 wt% sample shows promise in a microstructural regard as a candidate for a coating solution to the corrosion issues faced by steel GSE. The mixing of the two constituents is believed to be a dual-action result of both the shear mixing of the coating before application and the melting of the Bi-Sn under the heat.

However, areas of the coating are still segregated Bi-Sn and Zn, existing separately. A strategy to improve the flow of molten solder around the zinc particles is to increase the peak temperature. A higher temperature cycle will promote better flow of the Bi-Sn and allow it to envelope the Zn “islands”, as required by the initial microstructural aims. This need will be addressed at a later point within this chapter when time and temperature variations are considered.

Figure 3.7, a corresponding SEM image for the alloy under consideration in figure 3.6, confirms the initial thoughts about the sample. There are eutectic Bi-Sn globules/spheres surrounded by the powdered Zn. A similar area of interest as in figure 3.7 is circled in red. Here, there is clear mixing of the Zn into a Bi-Sn region at the bottom middle of the micrograph and in the Bi-Sn region to the left.

Overall, the 20Z sample showed potential as a candidate for the coating composition, where microstructure was considered. The corrosion and adhesion properties are discussed in Chapter 4.

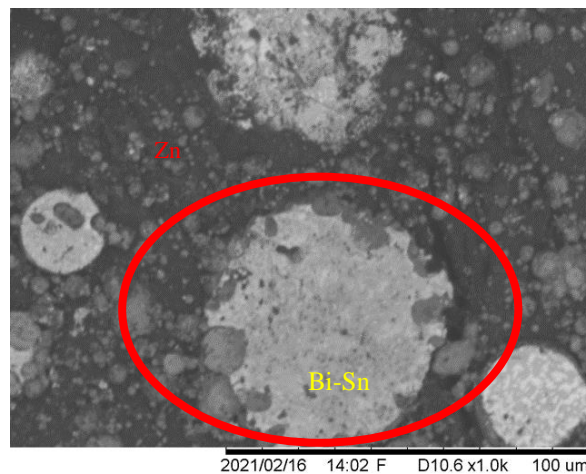


Figure 3. 7 - SEM image of 20Z showing poor melting of the Sn Bi phase, with the area of interest circled in red.

#### 3.4.1.3 50wt% Zn, 50wt% Bi-Sn (50Z)

A composition of 50 wt% Zn - 50 wt% Bi-Sn was investigated to understand the effects of higher Zn loading on the microstructure of the coating. A micrograph of this composition heated for 10 minutes at 180 °C is shown in figure 3.8.

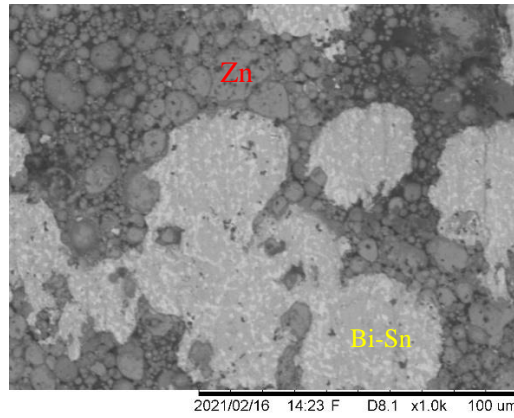


Figure 3.8 - SEM image of 50Z at 1000x magnification

Figure 3.8 shows a clear segregation between the Zn and Bi-Sn particles after heat treatment. The lighter regions show the same eutectic Bi-Sn microstructure as previously seen in sections 3.4.1.1 and 3.4.1.2. These light regions are surrounded by a darker, more grey regions of Zn powder. There is some evidence of mixing in this sample, with Zn particles among the large Bi-Sn region in the middle of the image. However, this mixing is not as optimal as in figures 3.6 and 3.7.

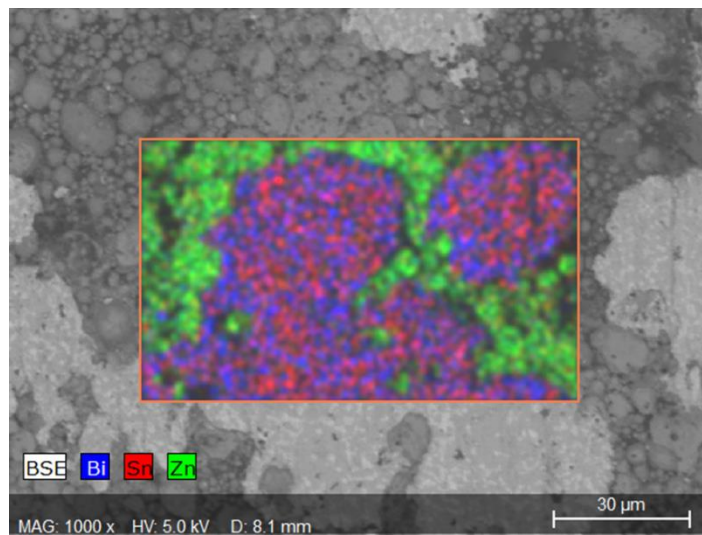


Figure 3.9 - EDS map of 50Z at 5000x magnification.

The EDS map in *figure 3.9* confirms the analysis of *figure 3.9*. There are clearly segregated, meaning poorly mixed, sections of Bi-Sn and Zn. Bi is represented in blue, Sn in red and Zn in green. The evidence of Zn particles being mixed into the Bi-Sn regions seen in *figure 3.8* is much less pronounced here, although *figure 3.7* is at 5 times the magnification of 3.8. Despite this, there is more clearly distinct separation between the regions or phases of Bi-Sn and Zn than that witnessed in *figure 3.6*. The position and location of the Bi-Sn and Zn confirms that 50Z does not exhibit a resemblance to the desired coating, as there has been no flow of Bi-Sn around the Zn.

Whilst 50Z shows small allusions to some of the features outlined in the aims of this thesis, the microstructure presented within this section is not ideal when compared to the aforementioned aims. With 20Z showing so much promise, it is proposed that 50Z would be inferior to that coating due to its powdery nature and lack of Bi-Sn coalescence around the high volume of Zn powder. This could have very detrimental consequences for the mechanical properties and structural integrity of the coating. It seems that 50 wt% Zn is too high when considering the composition of the coating. The result is a granular coating with a segregated microstructure exhibiting a lack of incorporation of Zn into Bi-Sn regions - seemingly insufficient for the goals of this study.

#### **3.4.1.4 90wt% Zn, 10wt% Bi-Sn (90Z)**

Despite the previous section reaching the initial conclusion that 50 wt% Zn is not feasible within the novel Bi-Sn + Zn coating, in order to get a more complete view of the effects of Zn loading, results for 90Z are presented below.

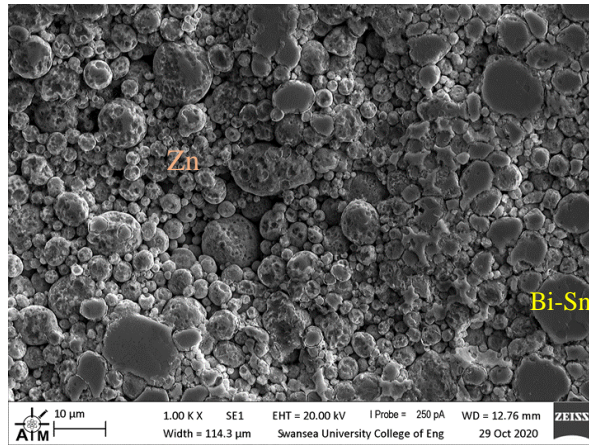


Figure 3.10 – SEM image of 90Z at 1000x magnification.

Figure 3.10 displays the microstructure of 90 wt% Zn 10 wt% Bi-Sn. It exhibits a granular microstructure. Whilst it is difficult to identify each constituent, it is possible to denote the larger spheres, over 20 µm, likely being Bi-Sn and the smaller, very fine, powder-like spheres being Zn powder. There are a few regions that appear to exhibit no microstructure whatsoever, however these areas look like Zn powder on a substrate.

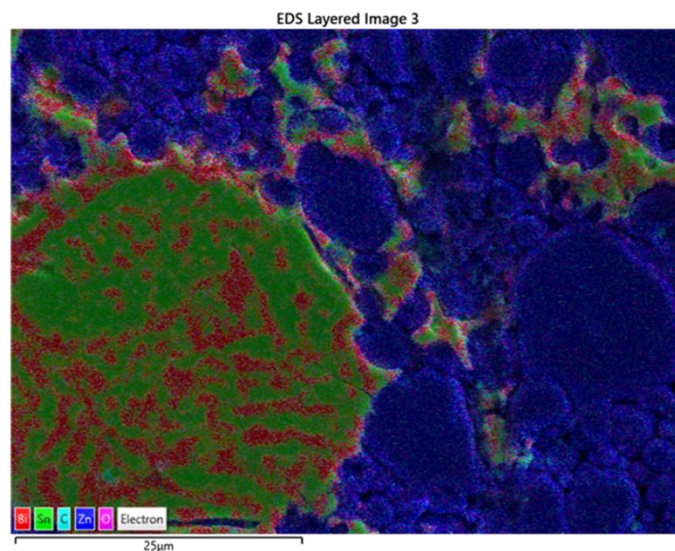


Figure 3.11 - EDS map of 90Z. Bi is red, Sn is green, and Zn is dark blue.

The EDS map in *figure 3.11* confirms the larger sphere is clearly Bi-Sn (red and green), and the smaller ones are Zn (dark blue). It also confirms that the remaining phase is Zn. There also appears to be smatterings of Bi-Sn with the much larger Zn-dominant regions.

Much like with 50Z, the microstructure of 90Z does not compare to the microstructural aims laid out in *section 3.4.1*. The aim of a Bi-Sn matrix interspersed with islands of Zn has not been achieved here. It is obvious that the volume of powdered Zn is far too high for this to occur. In the observed microstructure, a deviation from the intended structural composition is evident, failing to align with the targeted microstructural specifications. The heightened volume of Zn clearly surpasses an acceptable level, impeding the desired action of Bi-Sn to form the requisite microstructure. This imbalance in Zn content disrupts the targeted envelopment of Zn by Bi-Sn.

### **3.4.2 Curing Time and Temperature Optimisation for Microstructure**

After finding the Zn loading with the most potential for success, it was necessary to optimise that microstructure. This would be achieved through developing a suitable heat treatment cycle to foster the desired microstructure. Such a heating cycle would allow for microstructural development to a point where the obtained microstructure bears overall resemblance to that outlined in the research aims of this work.

#### **3.4.2.1 20Z Time and Temperature Variation**

Time and temperature variations are shown in *table 3.1*. With 20Z showing the best microstructure from the initial testing, it will be included first in the temperature variation results. 20Z was cured at 200 °C for 20 minutes and 40 minutes respectively. The results are shown below in *Figure 3.12*.

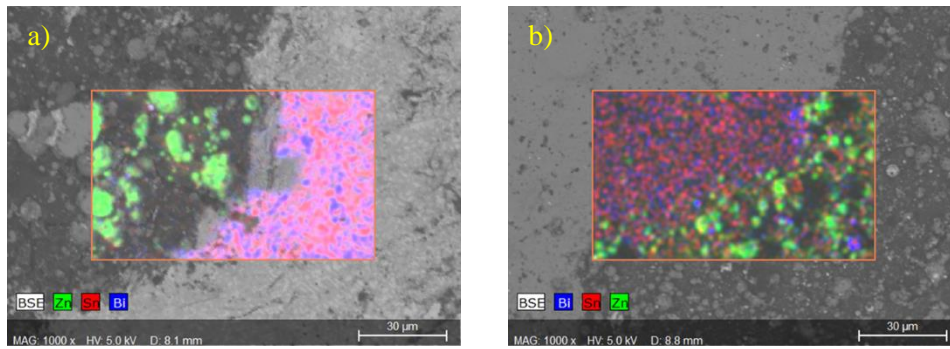


Figure 3.12 - EDS maps showing 20Z heated at 200°C for a) 20mins and b) 40mins.

The EDS maps in *figure 3.12* show some progress over those seen in 3.6 and 3.7.

Considering image 3.12a) initially, there is very little melting of Bi-Sn and envelopment of discrete Zn regions at all at 200 °C. This was a persistent result across 3 repeats, represented by the image. It appears that the Bi-Sn has not been able to melt sufficiently, if at all, and encase the Zn powder. This could be a result of the Zn content affecting the flow at the new elevated temperature or a need for longer/more intense shear mixing. There is also a possibility of the Zn absorbing much of the heat and not allowing the Bi-Sn to fully melt [38,146,147].

However, looking at image b), it is notable that there appears to be much more mixing present. The EDS map shows several green Zn instances in amongst the blue and red Bi-Sn regions. It could be postulated that this is due to the longer heating time allowing more melting of the Bi-Sn. Despite this, neither a) nor b) show melting of the Bi-Sn phase.

It is known that the typical reflow temperature for a lead-free solder is around 240 °C [148], with this in mind, it was decided to heat the coating to 245 °C. This would allow for much better melting, and it was hoped that heating to above reflow temperatures would see the Bi-Sn melt much more completely and fully envelope the



Zn particles or “islands”. 245 °C is still well below the industry standard temperature for HDG, which takes place at around 450 °C.

Samples were heated to 245 °C for 40 mins to allow enough time for reflow to occur and for the necessary diffusion-type action to take place. It is crucial to allow time for the coating microstructure to develop and the Bi-Sn to fully melt and surround the Zn.

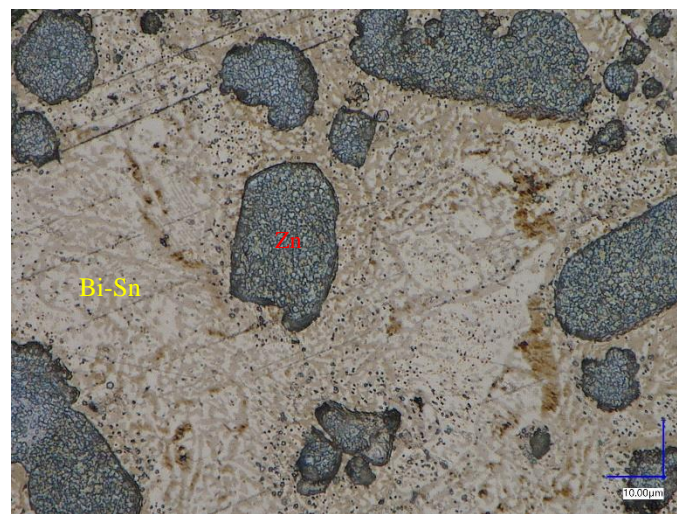


*Figure 3.13 - Digital Microscope image of 20Z, cured for 40mins at 245°C at 1000x magnification.*

The resultant micrograph is presented in *figure 3.13*, showing the microstructure of a 20Z sample after curing in a 245 °C furnace for 40 mins. Eutectic Bi-Sn is very



evident when comparing to previous micrographs. Zn areas are the grey regions in *figure 3.13*.

The micrograph shows a number of Zn particles, ranging in size from  $\sim 10\mu\text{m}$  to  $\sim 30\mu\text{m}$ , surrounded by the Bi-Sn microstructure. The Bi-Sn appears to have formed a matrix around the Zn, creating so-called “islands” of Zn.

As mentioned in Chapter 1, this microstructure does resemble that of a ZRP only with a metallic matrix of Bi-Sn rather than an organic or inorganic binder. Another difference would be that ZRPs often include a much higher Zn content, typically 95 % at a minimum. The image presented in *figure 3.12* proves that the hypothesis of this research is possible and can be achieved. It is thought that the higher temperature and longer time has facilitated and driven better flow of the Bi-Sn, allowing it to fully engulf the Zn. This has led to the formation of Zn dispersions throughout the Bi-Sn region. The Zn being in contact at such a high rate with the Bi-Sn will should allow for excellent galvanic protection. With a metallic matrix, the Zn will be in constant electrical contact with the steel substrate beneath the coating, protecting it from corrosion and potential mechanical compromise. 20Z, when cured at  $245^\circ\text{C}$  for 40 mins exhibits a microstructure that accurately fits the design targets.

#### 3.4.2.2 50Z Time and Temperature Variation

50Z, containing 50 wt% Bi-Sn and 50 wt% Zn, was cured at  $200^\circ\text{C}$  for 20 mins and 40 mins respectively. The resultant microstructures are shown in EDS maps in *figure 3.14*.

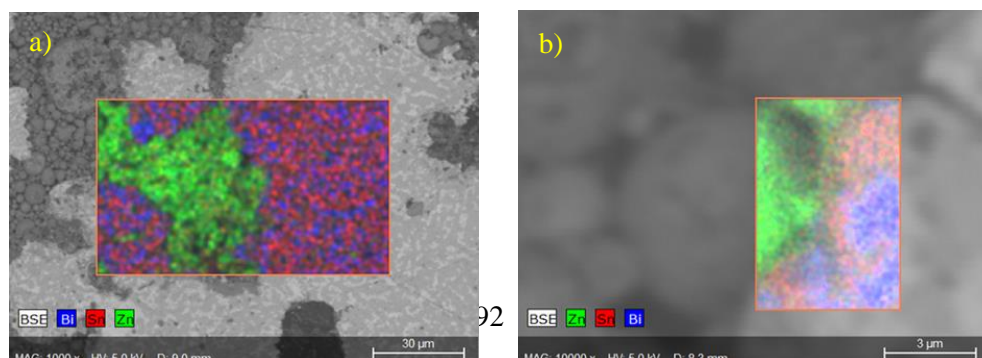


Figure 3.14 - EDS maps showing 50Z heated at 200°C for a) 20mins and b) 40mins.

Figure 3.14 a) shows a large area of Bi-Sn next to a completely separate area of Zn. This was fully expected from the initial Zn loading trials. In a similar result, figure 3.14 b) also shows incredibly segregated areas of Bi-Sn and Zn. The resulting coating is too granular to be successful and does not offer the microstructure desired. For this reason, it was decided not to test curing 50Z at 245 °C.

#### 3.4.2.3 90Z Curing Time and Temperature Variation

It should be noted that 90Z failed the initial trial in a far worse manner than 50Z and so it was deemed illogical to proceed with the sample. Therefore, 90Z was subjected to no further testing with regard to optimisation of microstructure. At this point, 90Z could be considered an unsuccessful candidate.

#### 3.4.2.4 Ancillary Composition Testing

As well as the original sample set, it was decided that some intermediate compositions be tested at 245 °C. This temperature was selected as it had the best outcome for 20Z. The compositions selected are presented in Table 3.3.

Table 3. 3 - Sample names and corresponding compositions for Ancillary Samples

Sample Name	Zn wt%	Bi-Sn wt%
10Z	10	90
30Z	30	70
40Z	40	60

The compositions shown in Table 3.3 were selected for different reasons. 10Z was chosen for its lower Zn content than 20Z – to determine if the same effect was

possible with less Zn and more Bi-Sn to envelop it. The 30Z option was taken for much the same reason, but opposite – slightly more Zn and slightly less Bi-Sn than 20Z. 40Z was selected as it contained 10 wt% less Zn than the highest unsuccessful candidate, 50Z. The selection of 40Z could be used to determine an “upper limit” for Zn content in the coating while still maintaining a cohesive coating and avoiding the granular nature of 50Z and 90Z. The samples were cured for 40 mins at 245 °C.

Three repeats for each sample were undertaken and resultant representative digital microscope images for 10Z, 30Z and 40Z can be seen in *Figure 3.15*, labelled a, b and c respectively.



*Figure 3. 15 - Digital Microscope images of a) 10Z, b) 30Z and c) 40Z, at 2500x magnification.*

From *figure 3.15 a*, it is evident that 10Z does not offer the same promise as 20Z.

The microstructure is incredibly segregated, round areas of Bi-Sn approximately 20μm in diameter dominate the micrograph. These globules are discrete shapes and have not coalesced, the Zn can be seen as much smaller grey spheres. Although the Bi-Sn regions are discrete from one another and have not coalesced, they are <1 μm apart and so could with a longer cure, potentially develop into a matrix. However, for the purpose of this study, it's evident the desired microstructure was not achieved. The disparity could also be due to process variability, although shear mixing was the same for all samples.

30Z is represented in *figure 3.15 b*. There is clearly a higher Zn content when compared to *figure 3.15 a*. Although, it is visible that the Bi-Sn has yet again failed

to fuse in the necessary way. Again, there are large regions of Bi-Sn, but they are disconnected from each other, ranging from approximately 10 – 20  $\mu\text{m}$  in diameter. The Zn is again grey but here, takes up a larger and more pronounced area of the image. There is no formation of a matrix around any Zn islands. This could be attributed to the higher Zn content not allowing the melting and diffusion of the Bi-Sn around the Zn. The rounds of Bi-Sn are varyingly spaced, so the argument that a longer cure could lead to better amalgamation, isn't as sound in this case. Within this research, 30Z does not present the microstructure outlined as a target.

The microstructure presented in *figure 3.15 c* is that of 40Z. Here again there are those distinctive round regions of eutectic Bi-Sn – this time ranging in approximate diameter from 10  $\mu\text{m}$  to 30  $\mu\text{m}$ . These white and brown spheres, or hemispheres, are surrounded, once again, by a large amount of Zn powder – more prominent here than in either of *3.14, a, or b*. This is evidently a result of the higher Zn content, again too much for the Bi-Sn to melt sufficiently and envelop it fully. It could be argued that a higher temperature or longer cure could lead to a microstructure resembling the target, however with so much Zn it is uncertain how high the temperature would have to be. The microstructure presented here does not resemble or achieve the target microstructure.

The reason for not attempting a higher temperature cure was that the main purpose of the study was to offer a lower temperature, more efficient alternative to batch HDG. Any higher than 245 °C and there is a risk of the efficiency and flexibility of the whole application process being compromised. To keep within capabilities of on-site and production line type application, it is important not to stray too far from the brief and research objectives.

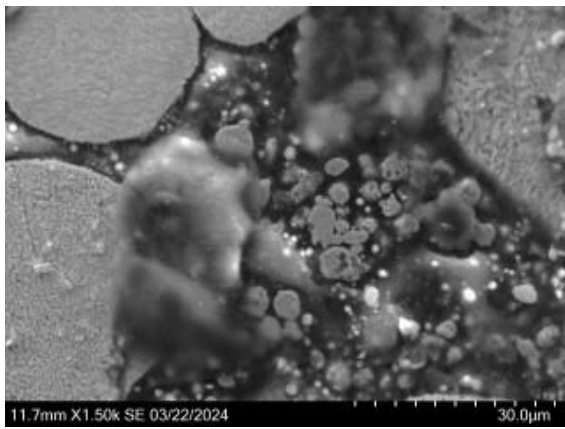
### 3.5 The Effect of Heating Time on Bi-Sn Matrix Development

To analyse Bi-Sn flow and coalescence improvement with time, samples of 20Z were produced in line with Section 2.2 and heated treated at 245 °C for increasing amounts of time. These times are detailed in Table 3.4.

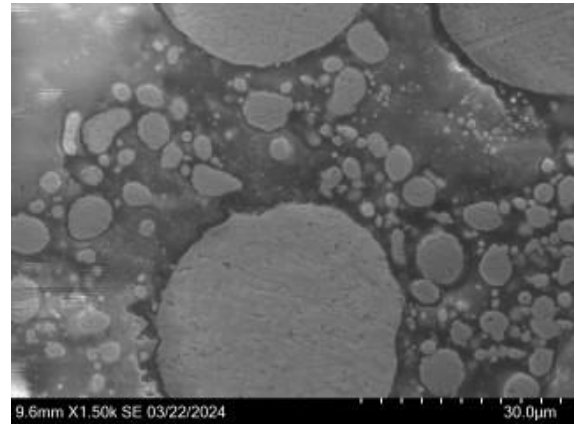
*Table 3. 4 - Heat treatment times for 20wt% Zn samples and their sample names.*

Sample Name	Heat Treatment Time (minutes)
10HT	10
20HT	20
30HT	30
40HT	40
50HT	50
24HT	1440 (24 hours)

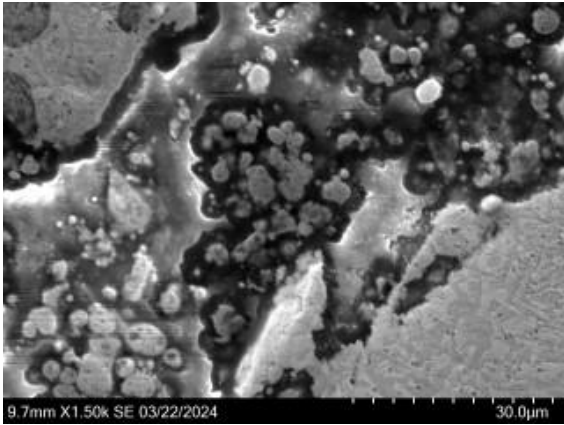
The resultant SEM images are shown in Figure 3.16 and 3.17.



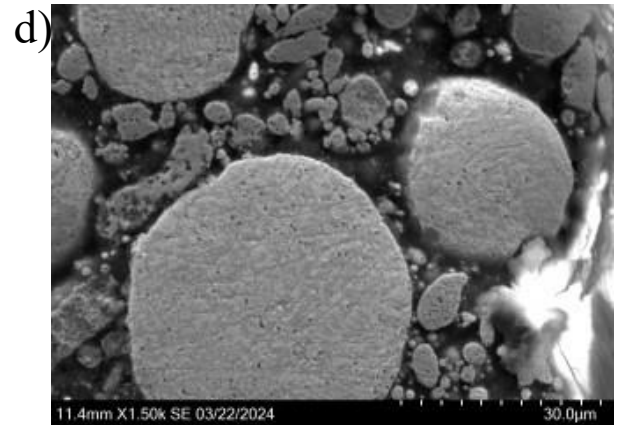
a)



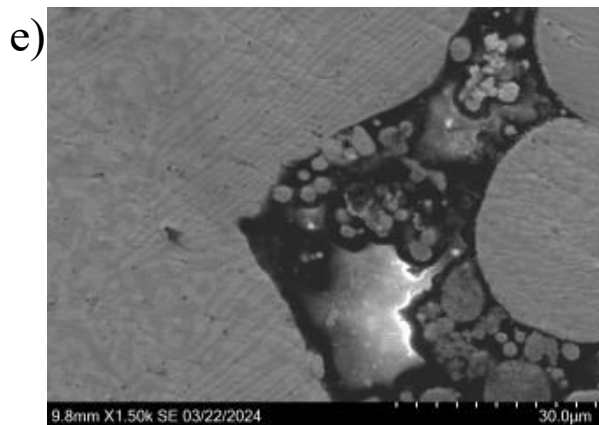
b)



c)



d)



e)

Figure 3.16 - SEM images showing 20wt% Zn / 80wt%Bi-Sn samples heat treat at 245°C for a) 10 minutes, b) 20 minutes, c) 30 minutes, d) 40 minutes and e) 50 minutes.



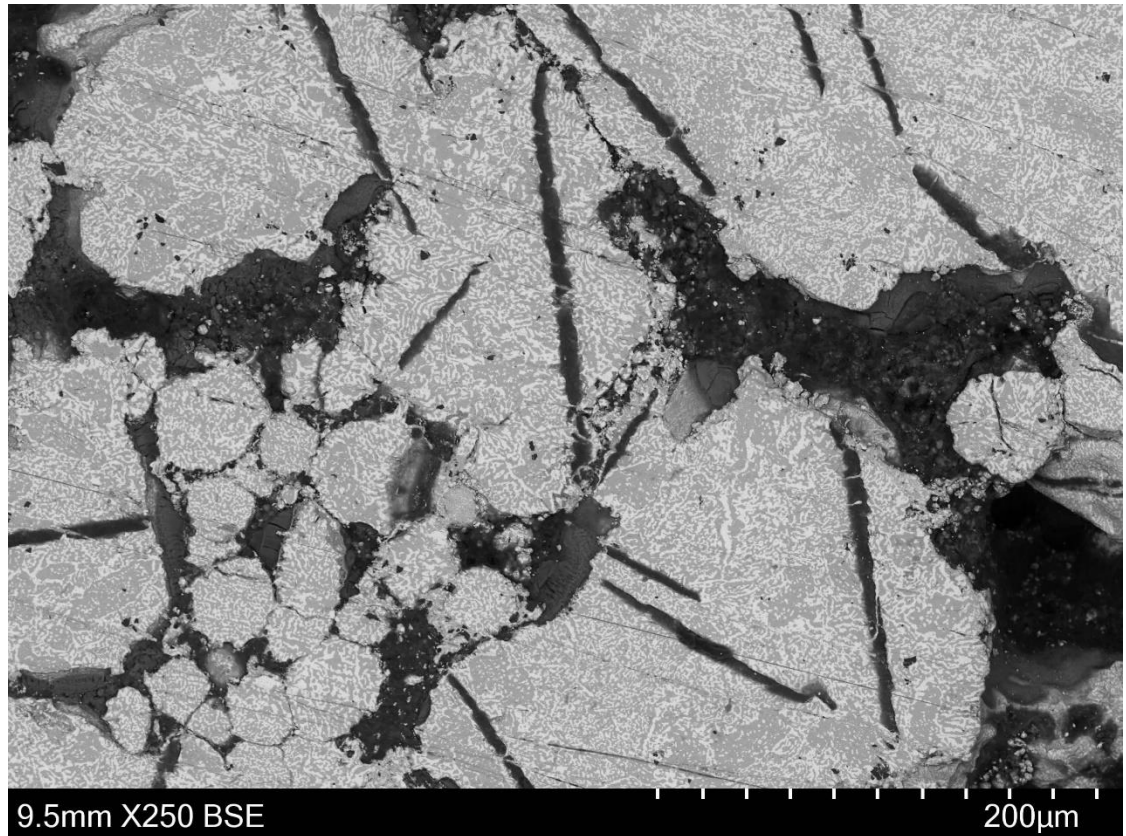


*Figure 3.17 - SEM image of 20wt% Zn / 80wt% Bi-Sn coating heat treated at 245°C for 24 hours (1440 minutes).*

Figures 3.16 a) - e) show an increase in the melted/coalesced regions of Bi-Sn with time. The Bi-Sn regions in a) are the smallest and most discrete, and these regions gradually grow in size until in e), the Bi-Sn has coalesced into a comparatively very large region and is surrounding the Zn.

In Figure 3.17, the microstructure of a 20Z sample heat treated for 24 hours is presented. The Bi-Sn appears to have formed large regions, over 400 µm in length and all regions are in contact with each other and are surrounding Zn clusters.

### **3.6 The Effect of Alloying Zn with Bi-Sn on Microstructure**

For academic completeness, it was decided that an alloy of Bi-Sn-Zn would be created. 100 g of alloy, containing 80 g Bi-Sn and 20 g Zn was heated to 480 °C and held for 2 hours. The furnace was then switched off and the alloy was allowed to

cool completely. The cast was then sectioned down the centreline and imaged using the SEM as detailed in Section 2.4.

80 g of eutectic Bi-Sn contains 45.6 g Bi and 34.4 g Sn. Therefore, the alloy created was 45.6Bi-34.4Sn-20Zn. The resulting Microstructure is shown in Figure 3.18.

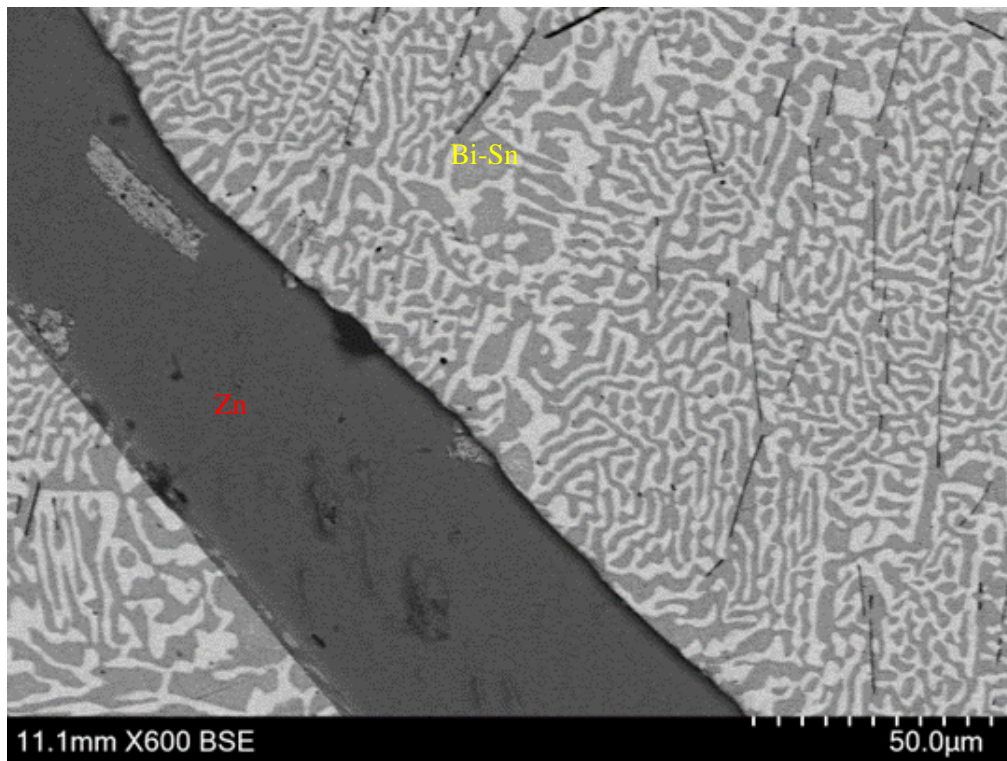


Figure 3.18 - SEM image of 80wt% Bi-Sn 20wt% Zn alloy heated at 480 °C for 2 hours and furnace cooled.



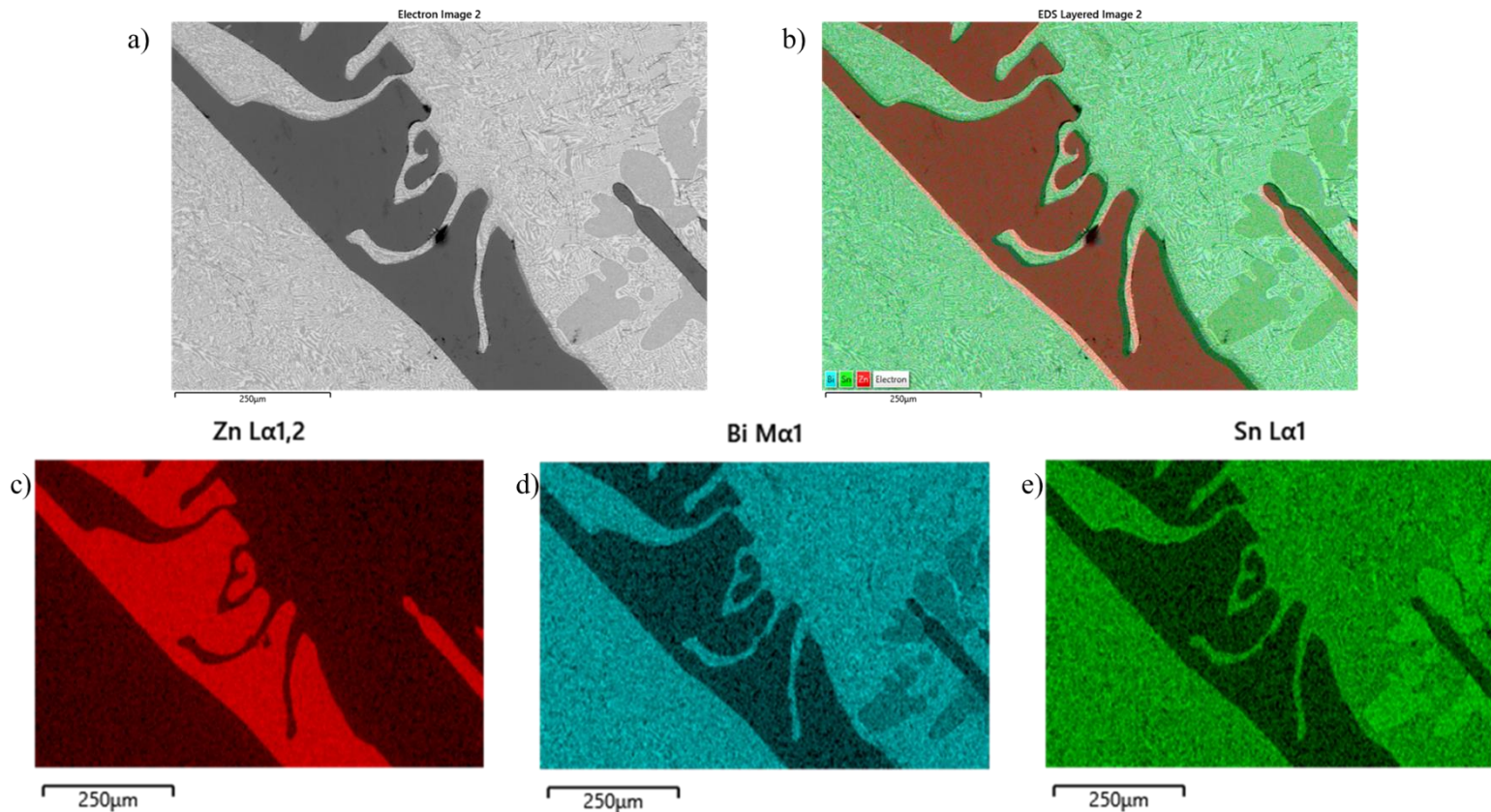


Figure 3.19 - The following images of a 20wt% Zn / 80wt%Bi-Sn sample heated to 480C for 2 hours and furnace cooled: a) EDS scanned image, b) EDS colour map for Bi, Sn and Zn, c) EDS colour map for Zn, d) EDS colour map for Bi and e) EDS colour map for Sn

Figure 3.18 shows a large Bi-Sn area encompassed a large Zn flake, showing melting of Bi-Sn has been good and the Zn has cooled in flakes, dispersed in a Bi-Sn matrix. The EDS data in Figure 3.19 confirms this. Showing the same site from further away (Figure 3.19a)), the encapsulation of the Zn flake by the Bi-Sn matrix is evident. This is supported by the colour maps in Figure 3.19 b) – e), confirming the location of each element, the Zn flake surrounded by a Bi-Sn matrix.

### 3.7 Discussion

The investigation of the effect of Zn loading on microstructure of the novel Bi-Sn + Zn coated suggested that increasing Zn additions above 20 wt% will potentially hamper the development of the microstructure. Above 20 % Zn addition shows several un-melted regions of Bi-Sn, meaning the Zn islands are not fully enclosed

within a matrix. It is thought that this is a result of too much Zn volume. Upon heating, it is more difficult for the Bi-Sn to melt and flow sufficiently due to the high percentage of Zn present. The as-received Zn powder is presented in figure 3.20.

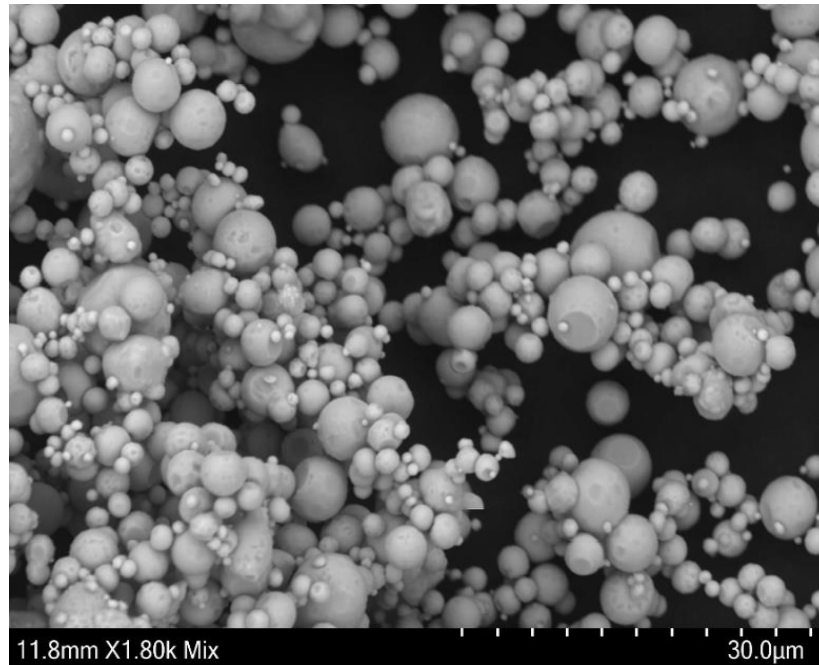


Figure 3. 20 - SEM image of the as-received Zn dust/powder.

One explanation is that that irregular powder particle morphology can affect the melting of molten powder mixes, like the Bi-Sn paste, when particulate powder additions are introduced [149]. The literature, regarding plasma-sprayed coatings, suggests that this is because powder particles with irregular morphology are less likely to be retained within a melt due to non-uniform movement of the powder during melting [149]. Varying size of powder was evident in the as-received Zn, shown in *figure 3.20*, with a range of approximately  $0.5\ \mu\text{m}$  –  $21\ \mu\text{m}$  particle size, determined using GIMP Image Manipulation Software. The movement and collisions of powder particles with irregular morphology as heat or molten metal is introduced can produce random rebound-like movements and can result in non-melted regions in the system [149]. This leads to a higher chance of non-melted

regions of the powder/paste [149]. Despite plasma spraying and the process for this work being different, the literature shows the need for particle size and morphology consistency as well as alluding to the effect of pre-mixing on coalescence. The resulting coating is an incredibly viscous and powdery paste, as evidenced by the amount of powder-like substance in *figure 3.8*.

Another explanation could be the agglomeration and clumping of Zn powder particles, shown in *figure 3.20*. The Zn powder particles seem almost bound to each other, a possible result of storage or of particle size, smaller powder particles ( $<1\mu\text{m}$ ) are shown to bond together through Van Der Waals forces but also forces due to pendular moisture, electrostatic forces from undissipated charge, solid bridging forces from precipitated impurities and mechanical forces from the interlocking of powder particles [150]. Metal powder agglomeration has been shown to disrupt the melting and fluidizing of metal powders when melting, and result in partial coating and/ or covering of a substrate [151].

A lack of cohesive melting could also be a result of oxide formation, which has shown to be detrimental to wetting of liquid metals onto solid metal [152]. One possibility is zinc oxide (ZnO) forming on the Zn powder, due to humidity during storage, it is known that ZnO forms after as little as 6 hours exposure of Zn to any kind of electrolytic atmosphere [153]. While there is no evidence of ZnO formation on the as-received Zn Powder, visible in *figure 3.20*, Zn has been known to oxidise in air with electrolyte present, as shown in Zinc-Air Batteries [154], although no bulk electrolyte is used in the coating process, ethanol is present as is water from surface cleaning.

Another possibility is the formation of tin oxide (SnO) affecting the melting in same way, this is possible as Sn is less noble than Bi and would corrode preferentially

within the alloy system [155]. It has been shown that during corrosion, Bi-Sn alloys undergo a selective attack on the continuous Sn-rich, which is attacked preferentially to the lamella Bi phase, meaning SnO formation is a possibility [103]. Unfortunately the traditional method for reduction of both SnO and ZnO involve heating up to very high temperatures with solid Carbon [156,157], although ongoing progress has been made on chemical and electrochemical reduction of oxides within the nuclear materials field and could be a possible way forward for this application in the future [158,159]

While the wetting of fusible alloys and lead-free solders on copper substrates has been extensively researched [160,161], little is known about the wettability of the coating constituents. The wetting of Bi-Sn and Zn was investigated also to analyse whether that could be affecting the melting of the Bi-Sn around the Zn. Here in figure 3.21, it is evident from the angle that wetting between the two constituents is high at 129.17 °.

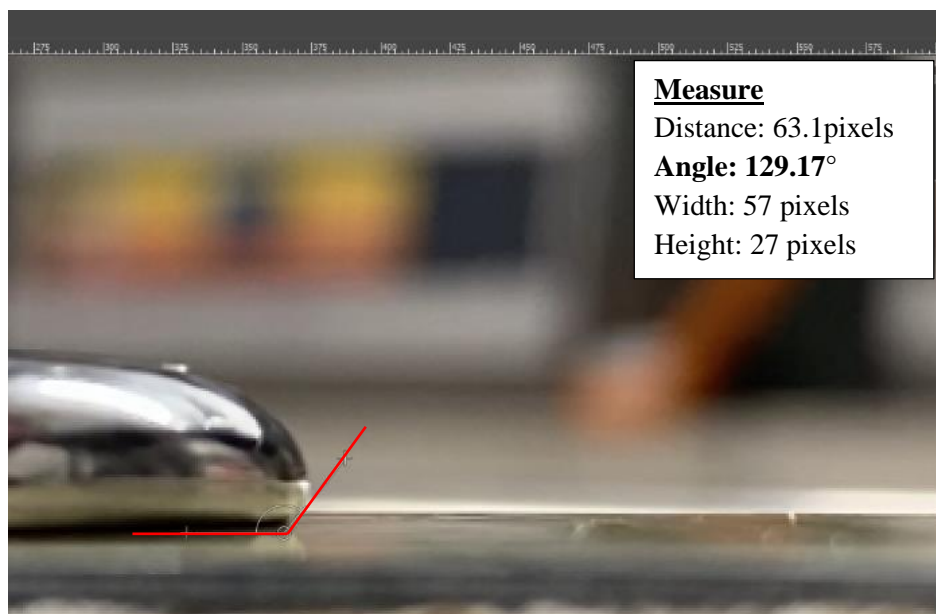


Figure 3. 21 - Manipulated image showing wetting angle of Bi-Sn on Zn

With a wetting angle of  $129.17^\circ$ , it can be surmised that wetting between the two constituents is not good and the two constituents have not wetted to each other [162].

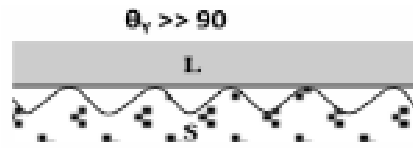


Figure 3. 22 - "Microscopic configuration at solid/liquid interfaces: For  $\theta_Y \gg 90^\circ$ , at microscopic scale, the liquid contacts the rough surface of the solid only at a few points. During cooling the solidified liquid detaches spontaneously from the solid." [37].

Literature also indicates that bad wetting can impede the physical flow or spread of a metal when in contact with a solid surface [160,161], and this could be a reason for the behaviour of the Bi-Sn. Bad wetting can be the result of many occurrences, including insufficient surface energy, surface roughness, the degree of heterogeneity such as surface oxides and other surface contaminations, leading to formation of "composite interfaces" which are partly solid-liquid and partly-solid vapour, shown in figure 3.22 [162,163]. In such instances as shown in figure 3.22, stress produced during the cooling of the metal can cause detachment of the liquid metal from the solid, entirely due to adhesive rupture [163].

Although additions above 20 wt% exhibited poor results, it should be noted that 20 wt% itself showed great promise in terms of microstructure. This was particularly apparent after the fusing temperature was increased to  $245^\circ\text{C}$ , as shown in figure 3.13. The temperature of  $245^\circ\text{C}$  was chosen as it presents a peak reflow temperature for many lead-free solders [148] and well above that of Bi-Sn, noted as somewhere between  $180^\circ\text{C}$  –  $220^\circ\text{C}$  [164,165]. This temperature is also well above the known melting temperature for eutectic Bi-Sn and still below that of Zn [15,36] – leaving a melted Bi-Sn matrix enveloping solid Zn powder regions.

The Bi-Sn paste also contained an organic flux which, in theory, should help with wetting [15], possibly helping to explain the results seen in figure 3.13. However the

same effect was not achieved with higher Zn additions, this could possibly be explained by the flux burning off during the heat cycle due to their typically low boiling points [166].

Time spent in heat cycle is also shown to be of importance. *Figure 3.12* shows samples heated for 10 and 40 minutes respectively. The sample heated for 40 mins shows much more potential with more melted and coalesced Bi-Sn regions. It is widely known that a longer time of heat treatment in a metal allows for the sufficient reactions and diffusion-type processes to take place, such as in steel – although the mechanisms seen here are different [167]. With more time to melt, it is postulated that the Bi-Sn is able to flow more around the Zn. When the temperature is increased again to 245 °C, the Bi-Sn has been fully able to melt around the Zn powder regions, showing that the double action of increased time and temperature allowed for better melting of the Bi-Sn and can be seen in *figure 3.13*.

### **3.6 Conclusions**

This chapter has presented the procedure by which the composition and curing cycle for a novel Bi-Sn + Zn coating has been optimised. The goal was to create a microstructure consisting of a matrix of Bi-Sn, surrounding Zn particles or “islands” – to provide constant electrical contact to a steel substrate and thus offer galvanic protection.

To achieve the results presented within this chapter, numerous compositions were prepared and tested, as laid out in *tables 3.1 and 3.2*. These samples, containing varying amounts of Zn addition, were subjected to an initial test to allow for microstructural understanding and optimisation. Having determined the composition with most potential, the samples then underwent heating for various times at various

temperatures, in order to establish the feasibility of achieving the target microstructure desired.

Key findings from this chapter are as follows:

- Initial testing showed that 20Z, comprises a 20 wt% Zn addition had the most potential to achieve the desired microstructure.
- During initial testing 90Z was deemed to be too granular, with too high of a Zn content and was not tested further.
- Heating the samples at 200 °C showed little improvement over the initial run at 180 °C. This is true for both 20Z and 50Z when heated for both 20 and 40 mins.
- When heated to 245 °C for 40mins, 20Z exhibited a microstructure akin to that desired. It was deemed to have achieved the research aims of this work, in terms of microstructure. This coating is the prime candidate for the composition of a novel Bi-Sn + Zn coating.
- 10Z, 30Z and 40Z offer no improvement on 20Z and are, in fact, worse candidates. This is thought to be due to Zn levels not being optimal.

With these findings in mind, 20Z will become a major part of the research as the following chapters progress. Other compositions will still be analysed to determine which composition offers the best performance overall, regarding all facets of this study. As corrosion protection, mechanical properties and alternative curing methods are investigated, 20Z will be a driving force behind the research.

# **Chapter 4: An Electrochemical Investigation into the Galvanic Protection of Bi-Sn + Zn Coating**



## 4.1 Introduction

This chapter investigates the corrosion properties of the Bi-Sn – Zn coatings.

Corrosion is an issue for manufacturers of steel-based structures, including GSE. The most traditional and widely used method of protection is Hot Dip Galvanising (HDG), the issues and concerns surrounding which for producers of larger structures, have been laid out in Chapter 1 [15].

While this work seeks to provide a more flexible and dynamic solution to the problem, this chapter will specifically evaluate the performance of the coating with regard to corrosion protection of a steel substrate. The corrosion performance of Bi-Sn is fairly unknown, but some studies have considered alloys of Bi-Sn and found that Bi-containing alloys of Sn performed less favourably than other alloys, and that adding Bi-Sn to other metals, such as Al, can cause deterioration in corrosion performance [103,105,168–171]. However, the corrosion performance of Zn is a known quantity and has been for many years. Zn is widely used within the corrosion field as a sacrificial anode or coating for corrosion protection of steel structures and substrates [15,19,27,39,120,131,132,147]. HDG is the primary example, utilising a thin layer of Zn to completely cover the steel surface and galvanically protect the substrate. Other uses of Zn in coatings include Zinc Rich Paints (ZRP), Cold Galvanising Coating (CGCs), continuous galvanising and thermal spraying. It is hoped that adding Zn with Bi-Sn can outweigh the negative performance mentioned above.

The proposed mechanism of protection is that the Bi-Sn keeps the Zn in constant electrical contact with the steel substrate. This will allow for electron transfer to occur continuously from the anode (Zn) to the cathodic steel substrate. Stemming

from issues surrounding ZRPs and CGCs, the need has been identified to improve upon the functionality and lifetime of these protection methods.

This chapter will mainly focus on accelerated corrosion experiments. This is in order to assess, on a lab scale, the effectiveness of a given coating. These tests will include the Scanning Vibrating Electrode Technique (SVET), used to analyse the anodic and cathodic activity of a corroding sample. Open Circuit Potential tests will also be undertaken in order to evaluate the free corrosion potential of different samples. Galvanic Corrosion tests or Zero Resistance Ammetry will also be employed, this sees two examples linked in a galvanic couple to determine which one is acting sacrificially.

Industrial benchmarks will be tested also or, where available and known, previous other works will be referenced. The goal of creating a new corrosion-protection coating is to develop something that stands up to current industrial techniques and products, and the most important application of such a product is the protection of steel from corrosion.

Considering this background, this chapter will be a comprehensive analysis of the ability of several coatings to protect steel against corrosion. Chapter 3 gives a unanimous favouring to 20Z, meaning this coating was the focus here although, it is other compositions were also tested in some experiments to get a broader view of the problem and its solution.

## 4.2 Experimental Methods

### 4.2.1 Sample Preparation

Samples were produced and metallographically prepared as described in *Chapter 2, Sections 2.2 and 2.4* with some additional steps dependent on the test being undertaken using each specific sample.

*Table 2. 3 - Sample compositions and test conditions for SVET experiments.*

Sample	Zn Content (wt%)	Bi-Sn Content (wt%)	Conditions
100BiSn	0	100	1% NaCl for 24 hours
10Z	10	90	1% NaCl for 24 hours
20Z	20	80	1% NaCl for 24 hours
30Z	30	70	1% NaCl for 24 hours

Cut edge samples were tested using SVET to determine whether the coating can provide galvanic protection to the steel substrate. The SVET produces maps of corrosion activity over time and can provide mechanistic information on the location of anodes and cathodes over the 24-hour experiment. Samples for cut-edge SVET were cut to a cut-edge length of 25 mm, with a non-exposed surface area of 50 mm<sup>2</sup>, as shown in *figure 4.1*. This allowed a sufficient scanning area for a cut edge while

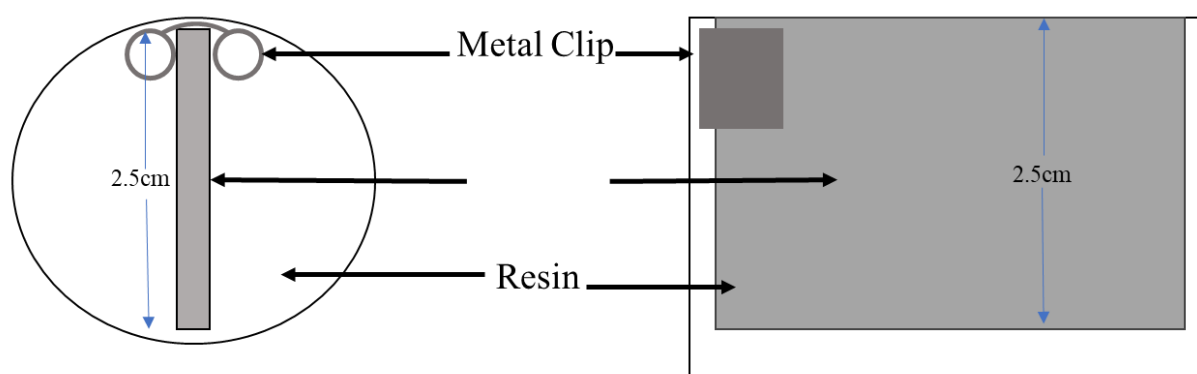


*Figure 4. 1 - Schematic of a prepared SVET sample, showing the size of the sample and its placement.*

keeping the mounting process straightforward. The coated samples were then mounted in clear epoxy resin (Met Prep LTD) and left to cure overnight.

Following curing the samples were ground and polished to a 1 $\mu$ m finish. Samples were not etched.

For OCP, LPR and ZRA, samples were cut to a surface area of 2 cm x 2 cm.

Samples were not polished or etched. These samples were either mounted into a sample holder, as shown in *Chapter 2, Section 2.7.1*, or wires were soldered directly to the samples, as in *Chapter 2, Section 2.7.2* and shielded well using PTFE tape.

All accelerated corrosion tests took place in a 1% Sodium Chloride (NaCl) electrolyte.

#### **4.2.2 Scanning Vibrating Electrode Technique (SVET) Procedure**

The SVET is described in detail in Chapter 2 and elsewhere [122–128]. For surface corrosion, 3x10 mm area was exposed for scanning by punching a hole of 10x10 mm size into PTFE tape and placing it onto the sample. Only the scanning area was exposed to the electrolyte. Double-sided adhesive tape and PTFE tape were used to secure the sample in a dish for testing.

The SVET probe was cleaned using HCl and fine grit paper before every calibration. To calibrate the SVET, the process described in *Chapter 2, Section 2.8.1* was undertaken.

The sample was then put in place the scan origin was determined. This was done by carefully by finding the surface of the sample at the point where the sample would lie at the centre of a 3 mm x-direction scan and the full 10 mm y-direction length was feasibly able to be scanned. A height scan was then undertaken to ensure the sample surface was laid flat and level. Scan height of 100  $\mu$ m was then measured

from this spot. 40 measurements were made along the cut edge length of the sample and 30 measurements were taken along the width of the sample, totalling 1200 measurements for every scan. One scan was taken every hour for a period of 24 hours in a 1%NaCl solution. Three repeat tests were carried out for each test undertaken.

Once the sample was ready to be scanned and the SVET probe tip was in the accurate location, the dish was filled with electrolyte covering the sample and the test was commenced.

### **4.2.3 Open Circuit Potential (OCP)**

A sample was first mounted into the sample holder, as shown in *Section 2.7.1*. The sample was then connected to a potentiostat, using wires from the sample holder connected via crocodile clips to the potentiostat cables, and the sample holder placed in a clamp stand. The reference was then also attached to the same potentiostat and placed in a clamp on the same clamp stand. Both the sample and reference electrodes were then placed inside a beaker with the clamps holding them in place, not touching the bottom of the beaker. The bottom of the reference was placed in line with the middle of the exposed sample and approximately 10 mm apart. Shown in *figure 2.4*.

On the PC connected to the potentiostat, the Gamry Sequence Wizard was used to control these experiments. The time, sample rate, and density settings, as described in Chapter 2 were input to the system. 1% NaCl solution electrolyte was added to the beaker containing the experimental apparatus, making sure the exposed sample was fully submerged. The test was then started and continued automatically for the duration of the 24-hour experiment.

#### **4.2.4 Potentiodynamic Sweeps**

Apparatus for potentiodynamic sweep experiments was set up as outlined in Chapter 2. This set up is very similar to that used in OCP testing. The only difference was the introduction of a platinum counter electrode. 1% NaCl solution was used as an electrolyte. Potentiodynamic Sweeps apply a constant rate of external potential, beginning at the OCP and increase or decrease at a constant rate of  $1\text{mVs}^{-1}$  until a potential of  $\pm 1.5\text{V}$  was achieved. In this study, tests were only carried out for the cathodic branch of the sweep in order to check the feasibility of the Bi-Sn as a cathode to explain to results seen in the ZRA experiments. Each test was repeated three times.

#### **4.2.5 Zero Resistance Ammetry (ZRA) / Galvanic Corrosion Tests (GalvCorr)**

The ZRA test was utilised to determine the current flow direction between samples and thus indicate any galvanic coupling between different sets of coating system constituents. This would be shown as a net positive or negative current flow, and this was measured from the working electrode to the reference/counter. This meant a positive current flow showed that the working electrode was corroding preferentially to the reference/counter electrode. A negative current, of course, would represent the inverse and opposite taking place. Widely known that an anode-to-cathode electron, or current, flow takes place during corrosion.

While the experimental set up for ZRA was quite similar to that of OCP and Potentiodynamic Sweeps, there were a few differences. ZRA did not comprise any specialised counter or reference electrodes, instead two samples were linked to the potentiostat in a galvanic couple using wires welded to the reverse of each sample.

These were connected to the working and reference inputs respectively, with the counter input being connected to the reference.

Both samples were secured tightly into sample holders and placed in to clamp stands. These samples were then lowered into a sufficiently sized beaker while Gamry Sequence Wizard was loaded, and the correct settings inputted. 1% NaCl electrolyte was poured into the beaker and the test was initiated. Measurements were taken for 5 minutes every hour for 24 hours, with the last point of each hourly data set being extracted for plotting of the whole test. The data for each hour was compiled and presented as one graph showing the whole 24-hour test. Couples tested are outlined in *Table 4.1*. Three repeat experiments were done for each couple, the results given here are representative of all repeats.

*Table 4. 1 - Couples tested for Galvanic relationships using ZRA*

<b>Couple Number</b>	<b>Counter/Reference Electrode</b>	<b>Working Electrode</b>	<b>Representative of:</b>
<b>1</b>	100Bi-Sn	IFS	Galvanic relationship between Steel and Bi-Sn with no added Zn
<b>2</b>	IFS	Zn	Zn's galvanic protection of Steel, proof of literature
<b>3</b>	100Bi-Sn	Zn	Galvanic behaviour of novel coating
<b>4</b>	IFS	20 wt% Zn 80 wt% Bi-Sn	Galvanic action of novel Bi-Sn – Zn coating on Steel

#### **4.2.6 Long Term Exposure Tests**

In order to test the long-term viability of a coating, it was necessary to perform environmental exposure tests. These tests involved a coated piece of steel being scribed with a scalpel in a cross-like X shape. This sample was then placed outdoors, in an adequate environment representative of conditions experienced by GSE and analysed at intervals. It was crucial to add context to the test so industrial

benchmarks were also scribed and placed in the same outdoor environment.

Samples exposed were Galvanised Steel (GI), Zinc Rich Paint (ZRP) coated steel and steel coated in the novel 20 wt% Zn/ 80 wt% Bi-Sn (20Z), all coatings were applied using bar coating and edges were sealed to avoid the initiation of cut-edge corrosion.

The X-shaped scribe was kept a consistent size for all samples at 1.5 cm in length.

This meant that even though the samples were not all consistently sized, the same corrosion initiation area. Due to this experiment being primarily qualitative in nature, the size of the sample is unimportant, as the results are viewed as percentage area of each sample, not in a specific unit. The Pilot Manufacturing Research Centre (PMRC) at Swansea University's SPECIFIC site was chosen for the tests. The reason for choosing this location was its coastal location and good exposure to seasonal weather, as highlighted in *Section 2.9*. It is important to test in a variety of conditions, so this location was perfect to emulate some of the conditions undergone by various GSE products. The test was carried out for 6 months with images being captured at the end of the trial.

## **4.3 Results**

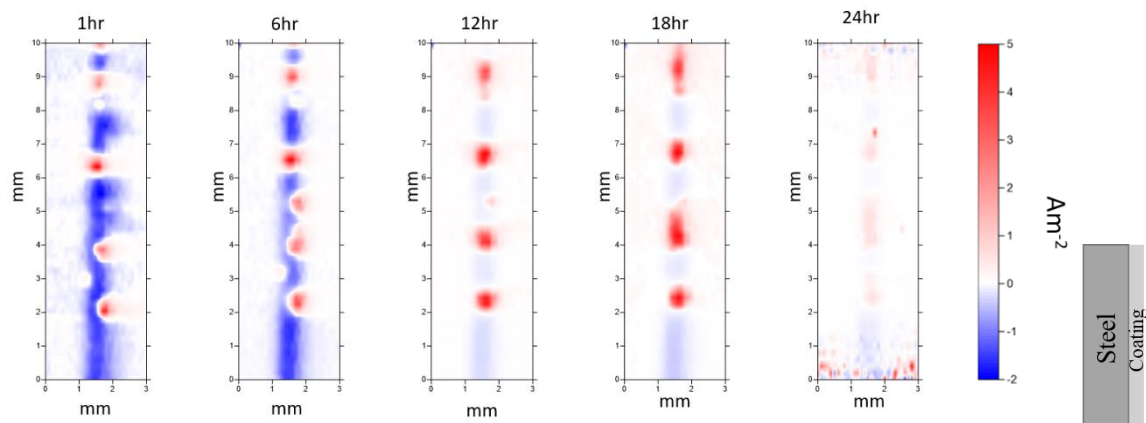
### **4.3.1 SVET Testing of Candidate Coatings**

#### **4.3.1.1 100BS**

For this experiment, 100BiSn was used as a control in order to determine the effect of a non-modified Bi-Sn coating on the corrosion of a steel substrate. This will act as

*Figure 4. 2 - SVET resolved colour map representing normal current above a cut-edge sample of 100BS. Coating was applied on the right-hand side.*





a comparison with coatings containing Zn additions. No galvanic protection is expected.

Figure 4.3 shows cross section SVET colour maps over a 24-hour period in 1%NaCl for 100BiSn coated on steel where anodic areas are shown in red and cathodic regions in blue. It is evident from the very first hour that the coating offered no galvanic protection. Anodes (shown in red) were detected on the substrate within the first hour of the test. The anodes continue to spread extensively until at 18 hours, there are large areas of anodic activity along the length of the substrate. These areas neared current densities of  $5\text{A m}^{-2}$ , showing a rapid corrosion with an extremely high current density at the anodic sites. By 24 hours of submersion, the current densities have reduced due to the build-up of iron corrosion products. From this it can be surmised that 100BS offers no galvanic protection to steel under these conditions. The sample was also noticeably rusty after the experiment with large areas of red/orange iron oxide

#### 4.3.1.2 10Z

The next experiment was 10Z, a coating comprising of 10 wt% Zn and 90 wt% Bi-

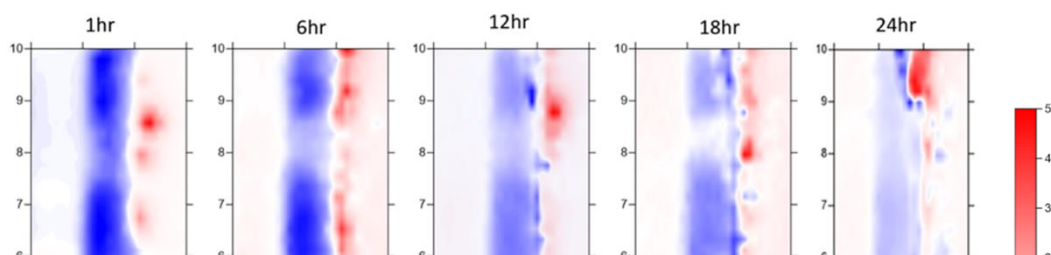


*Figure 4. 3 - SVET resolved colour map representing normal current above a cut-edge sample of 10Z. Coating was applied on the right-hand side.*

The SVET map for 10Z is shown in *figure 4.4*. The coating, which is on the right-hand side of the steel substrate, appears to provide galvanic protection after one hour, with a visible red anodic strip down most of the right-hand side of the sample. However, by hour 18, anodes are detected on the substrate, indicating galvanic protection has been lost. There also appears to be blue cathodic areas within the coating. This could be due to internal coupling of the coating between the Zn and Bi-Sn.

Self-corrosion of the coating appears to develop throughout the scan, culminating in a poor outcome at hour 24. Although some of the aggressive anodic areas on the substrate, visible at hour 18 the whole length of the map at 2mm across, appear to have passivated, there is still evidence of anodic attack on the substrate and internal coupling of the coating.

#### 4.3.1.3 20Z

20Z was the next composition tested using the SVET technique. The resulting colour maps are presented below in *figure 4.5*.

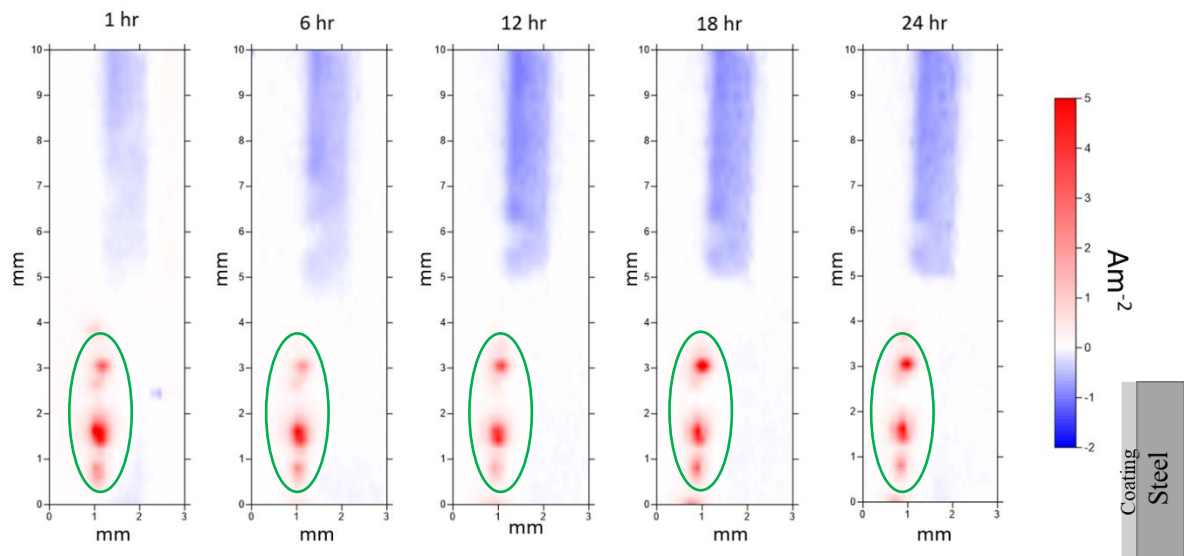


Figure 4. 4 - SVET resolved colour map representing normal current above a cut-edge sample of 20Z. Coating was applied on the left-hand side. Focal anodes of interest are circled in green.

From hour 1, there is clear separation between the red anodic area and blue cathodic area, located on the coating and steel respectively. The anodic area is located on the 20Z coating, at the left-hand side of the cathodic steel substrate, confirming that the coating is offering galvanic protection to the steel.

Protection continues throughout the 24-hour experiment. The maps show focal anodes at 1 mm across and 1 mm, 1.5 mm and 3 mm, circled in green on each map. These areas display a higher anodic current density than anywhere else on the maps, this is possibly due to a concentration of Zn in these areas within the Bi-Sn matrix of the coating, meaning more electrons would be travelling from those areas, this is also seen on HDG. This could be down to variability in the zinc dispersion within the coating.

The cathodic current density of the steel appears to increase over the lifetime of the experiment.

The maps in *figure 4.5* show promise for the viability of 20Z as a coating candidate. The coating offered galvanic protection to the steel substrate throughout the 24 hours of the SVET corrosion test. There appears to be no internal coupling within the coating, although this may not be detectable as the theoretical resolution of the SVET is only 250 $\mu$ m. The anodic action of 20Z becomes more prominent as the test continues and it is evident that this composition offers galvanic corrosion protection to steel substrates.

#### **4.3.1.4 30Z**

To analyse the effect of a higher Zn content, 30Z was also tested using the SVET. The SVET colour map below in *figure 4.6* shows its performance in a 24 hour long accelerated corrosion test with the coating on the right-hand side of the steel.

As with 20Z, there is localised anodic and cathodic regions from the outset. The cathodic region in this map shows the steel substrate immediately becoming cathodic as the coating, shown by the red region to the right, becomes anodic. This observation continued as the test progressed through hours 6, 12, and 18. The steel remained cathodic, becoming increasingly so, indicated by brighter, more solid blue regions. By hour 24, there was no change in the observed trend.

The results presented in *figure 4.5* show that 30Z demonstrated good galvanic protection of a steel substrate. By remaining anodic throughout the 24-hour accelerated corrosion test, it was proved that the coating could protect steel against corrosive attack for a sustained period. It was expected that 30Z would perform well, owing to its high Zn content. This would make it a great coating candidate from a corrosion point of view.

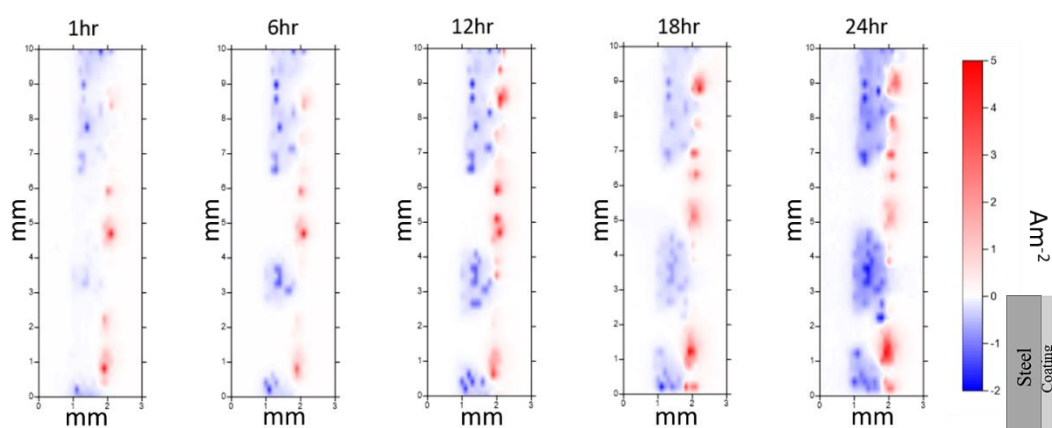


*Figure 4. 5 - SVET resolved colour map representing normal current above a cut-edge sample of 30Z. Coating was applied on the right-hand side.*

#### 4.3.2 SVET Derived Mass Loss

To further assess coating performance, the SVET data was used to calculate mass loss. This was then used to calculate a corrosion rate per year. Given that 20Z has shown the best promise, this coating was used for these calculations.

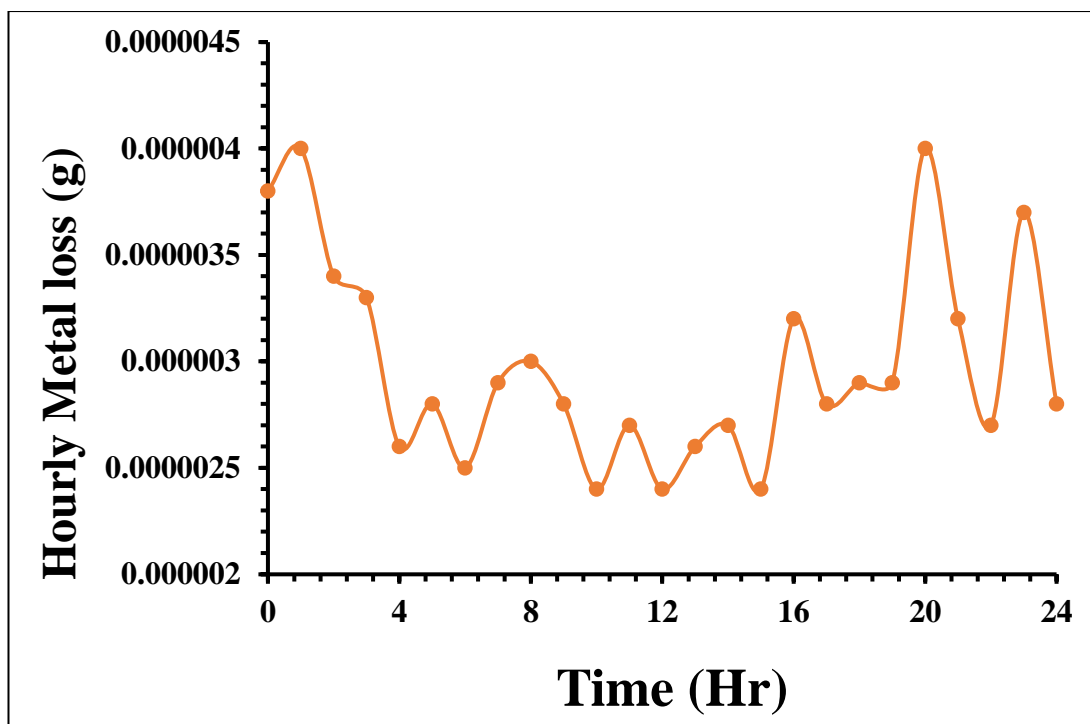


Figure 4. 6 - Time dependent metal/mass loss for 20wt%Zn / 80wt%Bi-Sn in 1%NaCl electrolyte

The hourly mass loss in grams (g) for the 20Z is given in *figure 4.13*. The total mass loss in milligrams (mg) of 20Z over a 24hr period in 1% NaCl is shown in *table 4.4*, found utilising equation 2.9. The metal loss in Figure 4.7 is for a sample of 10 mm<sup>2</sup>. To get the mass loss for 1 m<sup>2</sup>, this figure was multiplied by 1x10<sup>5</sup> (the multiplication factor for converting 10 mm<sup>2</sup> to 1 m<sup>2</sup>) for a result of 7.45 gm<sup>-2</sup> mass loss over a 24-hour period.

#### 4.3.3 Open Circuit Potential (OCP) Measurements

Due to its superior performance in corrosion as well as achieving the desired microstructure, 20Z was chosen for comparison to industrial benchmarks in terms of OCP testing. 20Z represented the group of successful candidates for the above SVET trials, bearing in mind that neither 10Z nor 30Z exhibited a microstructure where the Bi-Sn fully melted around the Zn particles. Samples tested for OCP are listed below in *Table 4.2*.

Table 4. 2 - Sample names and corresponding materials used in OCP experiments within this chapter.

Sample Name	Material	Notes	
100BS		100% Bi-Sn	Paste melted and cured
HDG		100% Zn	Zn used to replicate HDG
20Z		20 wt% Zn, 80 wt% Bi-Sn	Novel Coating representative
IFS		Interstitial-free steel	Substrate
ZRP		Zinc Rich Paint	ZINGA <sup>®</sup> brand

These samples were all chosen as they were materials of interest that are widely used in industry. Such is the case for choosing Zn to represent HDG, due to HDG comprising a thin layer of Zn it was a like-for-like representation.

The graph shown in *figure 4.7* shows the OCP data for selected samples after a test of 24 hours.

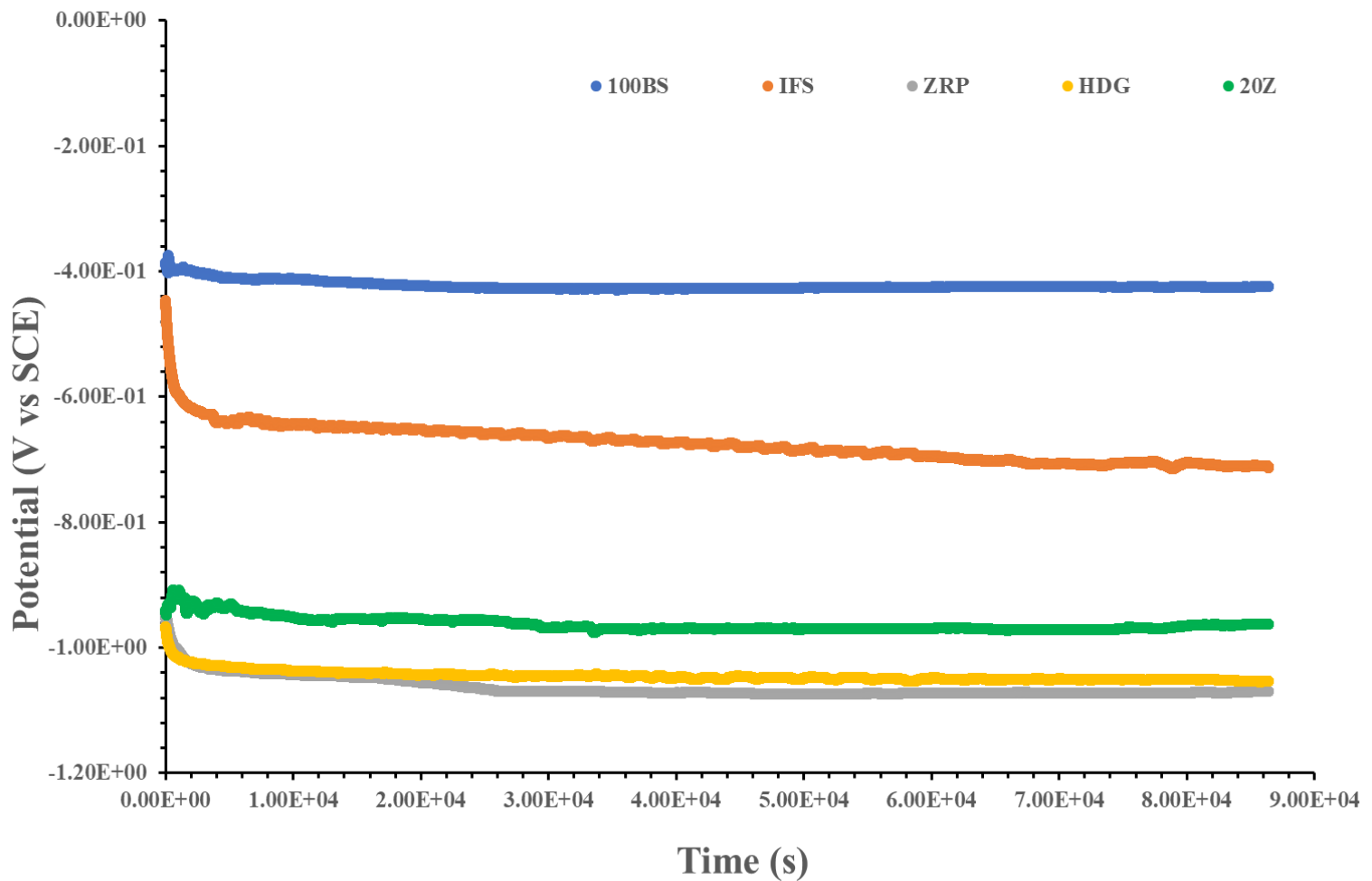


Figure 4. 7 - Graph showing obtained open circuit potentials for samples listed in Table 4.2.

The HDG and ZRP both samples have an OCP of around -1V. With both comprising of entirely, or mostly, zinc, these values were expected [106]. Values of these two samples relative to IFS, registering an OCP value of between -600mV and -700mV, explain the galvanic protection of Zn to steel substrates.

A key consideration is the relationship between 100BS and IFS. 100BS has a measured OCP almost 200mV higher than IFS. This confirms the results in section 4.3.1.1, the reason for the failure of 100BS to protect a steel substrate is explained by



the results given here. IFS, an uncoated IF steel sample representing the substrate, has a lower potential than 100BS. This indicates that the steel is corroding in order to protect the Bi-Sn coating.

However, looking at the OCP for 20Z, which is around -950mV, the effect of Zn in the coating can be seen. The 20Z shows a lower potential than 100BiSn by around 300mV. A crucial point here is that it has been lowered to a below the value of IFS, meaning it will galvanically protect the steel (assuming kinetics are fast enough). This corroborates the SVET results in section 4.3.1.3, where 20Z provided galvanic protection to the steel. By facilitating the protection of the steel substrate, 20Z would allow for such substrates to remain intact and retain their structural integrity.

#### **4.3.4 Polarisation Resistance**

LPR was carried out on 20Z to determine its polarisation resistance and corrosion rate. The time-dependent polarisation resistance is shown below in figure 4.9.

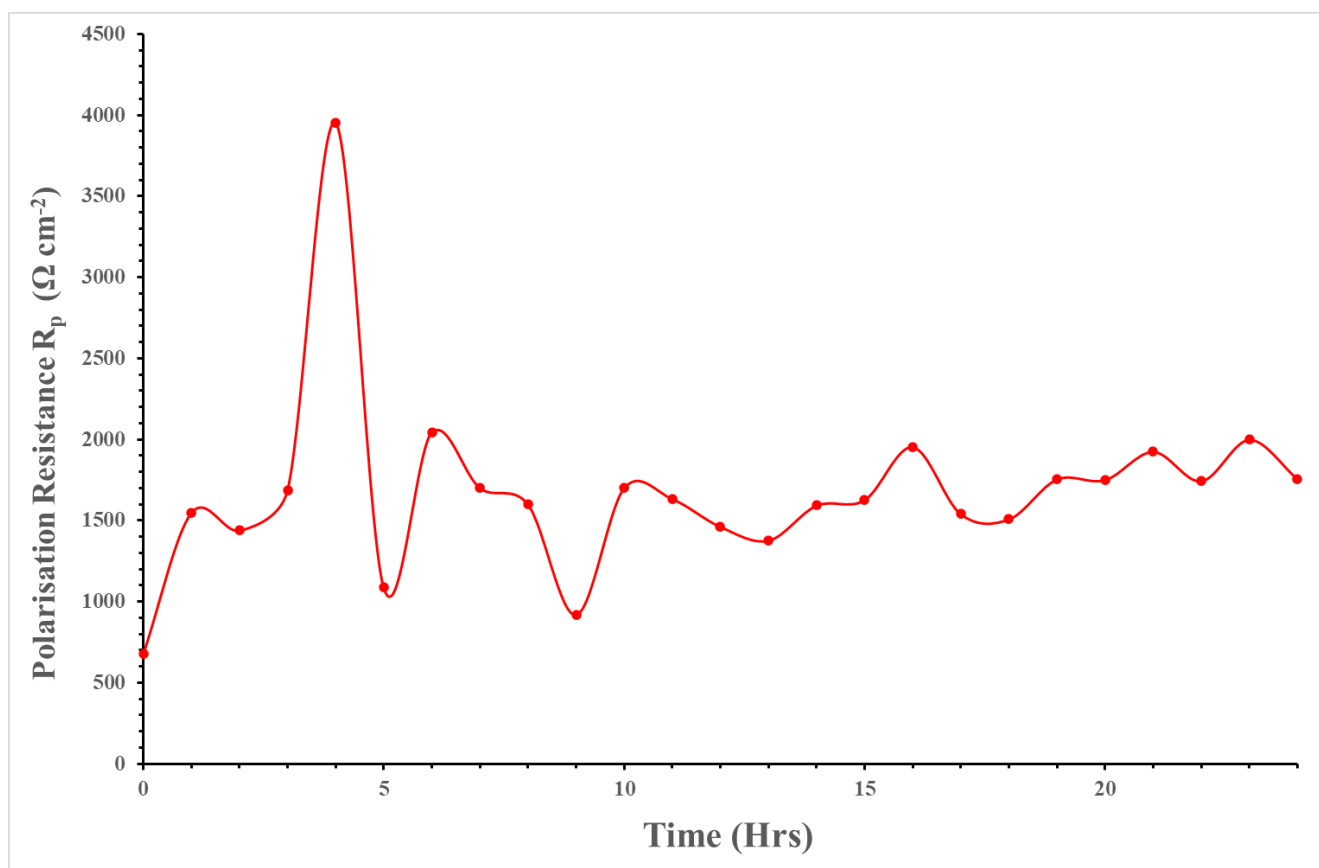


Figure 4. 8 - Polarisation resistance ( $R_p$ ) for 20Z over 24 hours in 1%NaCl electrolyte.

The  $R_p$  values shown in Figure 4.9 are varied. However, overall, they are fairly low when compared to literature, discussed in section 4.4, meaning the possibility of a high corrosion rate.

The corrosion rate given by the software was stable at around 7mpy.

#### 4.3.5 Zero Resistance Ammetry (ZRA)

OCP gives information on the thermodynamic likelihood of corrosion but does not provide information on the kinetics, for that reason Zero Resistance Ammetry (ZRA) is used. ZRA is described earlier in section 4.2.5. and is used to establish the galvanic relationships between the elements in the coating and the steel in a 1% NaCl electrolyte. The magnitude of the flowing current and its polarity, or direction,

allow for a quantification of sacrificial protection. Facilitating an explanation of how and why the coating behaves the way it does, is the goal of completing the ZRA for the particular sets of samples. Three repeats were undertaken, the data below is representative of the results seen in all repeats.

The graph below in figure 4.9 shows the current flow at every hour for each sample.

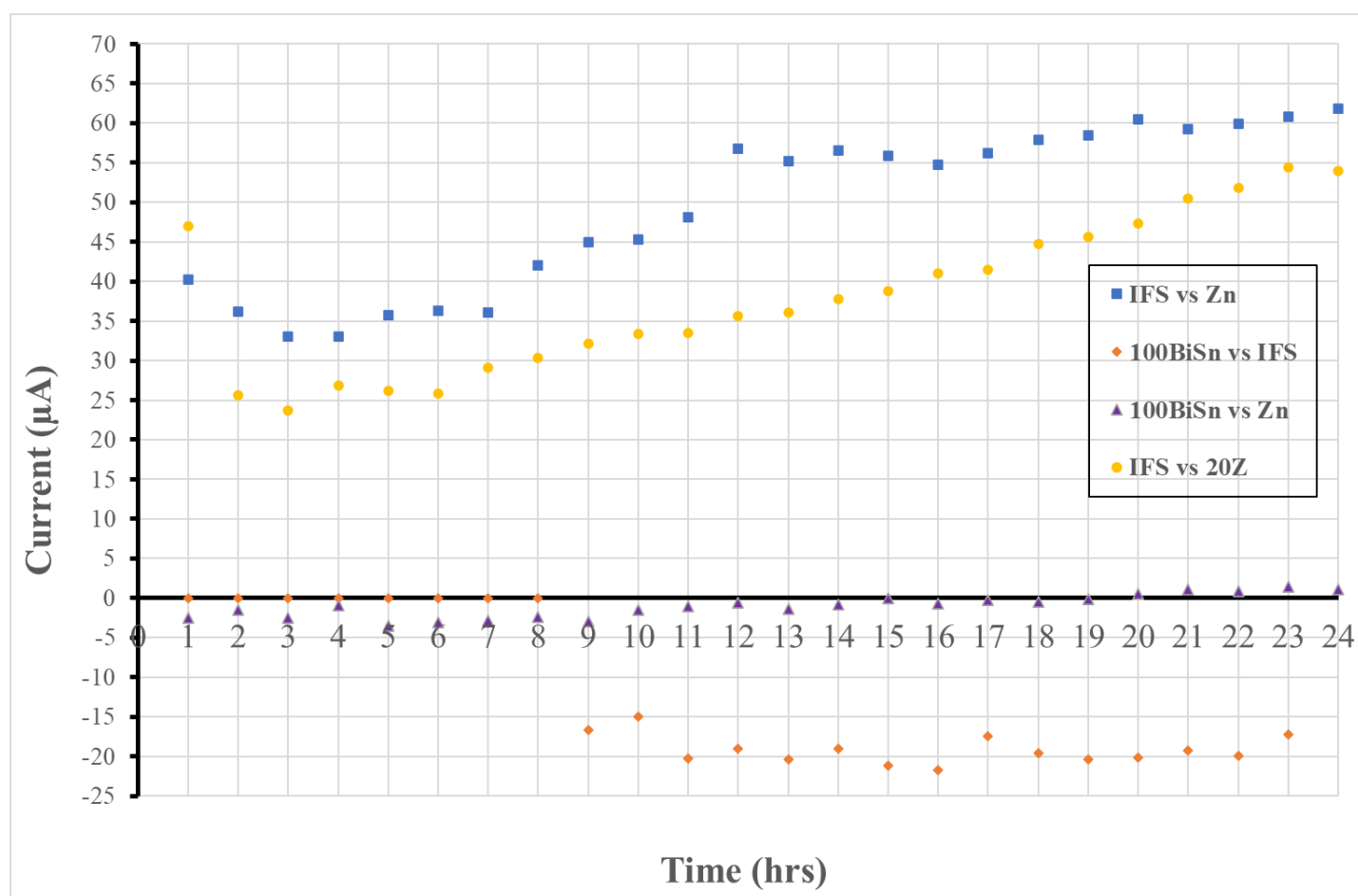


Figure 4. 9 - ZRA/Galvanic corrosion plot for each sample, as outlined the legend at the left of the chart.

As was the case in section 4.3.1.1, 100BiSn was tested on steel to give this set of results academic context, as well as to understand the results of the aforementioned section. In the test, IFS was set up as the counter/reference electrode (CE/RE) while 100BS was utilised as the working electrode (WE).

To begin for 100BiSn vs IFS, the current was very miniscule with a value of 0.012 nA. Although it is positive, this is a negligible current flow, and it would not seem that the WE was offering vast protection to the CE/RE. The current continued to rise slowly until, at hour 7, it reached 13.9 nA, still a negligible amount of current. After this the current dropped to -9.752 nA at hour 8. These changes are difficult to see in *figure 4.9* due to the scale of what happened at hour 9. Current flow became negative, dropping to -16700 nA. A negative current persisted through the remainder of the experiment, dropping even further. At hour 16 a drop to -21730 nA took place and the experiment ends with a current of 21030 nA at hour 24.

To fully understand the results shown in all sections within this chapter, it was necessary to perform a ZRA where IFS was the CE/RE and Zn was the WE. In doing this, it confirmed the OCP results but also determined that the experiment is functionally sound. The expected outcome would be a positive current, indicating current flow from working electrode to counter/reference electrode.

As expected for Zn and IFS, the current flow here in *figure 4.9* is positive. Beginning at around 40 $\mu$ A at hour 1, the current does drop slightly to 33.06 $\mu$ A and 33.08 $\mu$ A for hours three and four respectively. This could be down to stabilising of the couple. For the rest of the test, however, there is a consistent rise in current, indicating a current flow from the working electrode to the counter/reference electrode. At hour 24, the current is 61.83 $\mu$ A. The Zn is sacrificially corroding to protect the steel, as expected, and widely known.

To address the possible galvanic coupling within the coating itself, it was decided that a ZRA test should be undertaken of 100BiSn and Zn. This test will serve to analyse the behaviour of the coating, separated into its constituents, with the absence

of a substrate, when left to corrode in an electrolyte. In the experiment set-up, Bi-Sn was designated as the counter/reference electrode and Zn was allocated as the working electrode.

In this series, there was an evident trend in current flow. A negative current of -2.537 nA was observed to begin the test at hour 1. This then increased through hour 4 to -0.971 nA. A sudden drop then occurred to -3.56 nA at hour 5. From hour 5 all the way through the remainder of the test, an overall rise was seen in the current measured. At hour 20 there is a noticeable increase, as the current changes direction from negative (CE/RE to WE) to positive (WE to CE/RE). Despite this, the overall trend of current flow is positive from hour 5 to the end of the test at hour 24. It should also be remarked that the unit on the y axis denotes current measured in nA, indicating a diminutive current that is very low.

The final ZRA test was to determine the thermodynamic corrosion behaviour and directional current flow of the novel coating system containing 20 wt% Zn and 80 wt% Bi-Sn. This was achieved by pairing the coating galvanically with the steel substrate. This would allow for analysis of the current flow of the system and confirm or negate previously postulated theories.

For this test, IFS was chosen to be the counter/reference electrode and 20Z was chosen as the working electrode.

A positive current of 46.99 $\mu$ A was observed from the outset at hour 1. This does decrease somewhat to 23.7 $\mu$ A by hour 3. Another rise and then slight decrease took place from hour 4 to hour 6, where the measured current was 25.88 $\mu$ A. From that point, the current increased with each consecutive hour until a current of 54.47 $\mu$ A

was recorded at hour 23. This leads to a miniscule drop at hour 24 with a current of  $53.97\mu\text{A}$ .

The current measurements here were all positive. This indicates that the working electrode had become the anode, and the counter/reference electrode was acting as the cathode. 20Z acting anodically confirms its galvanic protection of IFS through the entire test.

The findings detailed above are crucial in proving the standard to which 20Z has been able to achieve the goals set out in chapter 1 for the development of a new coating as investigated by the current body of work. *Figure 4.9* suggests that the Zn in 20Z is galvanically protecting the steel.

#### **4.3.6 Potentiodynamic Sweeps**

The very low current flow (nA) between IFS and Bi-Sn in *figure 4.9* indicates very little self-corrosion of the Bi-Sn. Despite there being a thermodynamic driving force for the steel to sacrificially protect the Bi-Sn, shown in the OCP data by steel being less noble than Bi-Sn, the kinetics in the ZRA do not support this. To investigate the reasons behind this behaviour, potentiodynamic sweeps of the cathodic branch of the corrosion reaction were carried out for both steel and Bi-Sn.

The result for steel is shown below in *figure 4.10*.

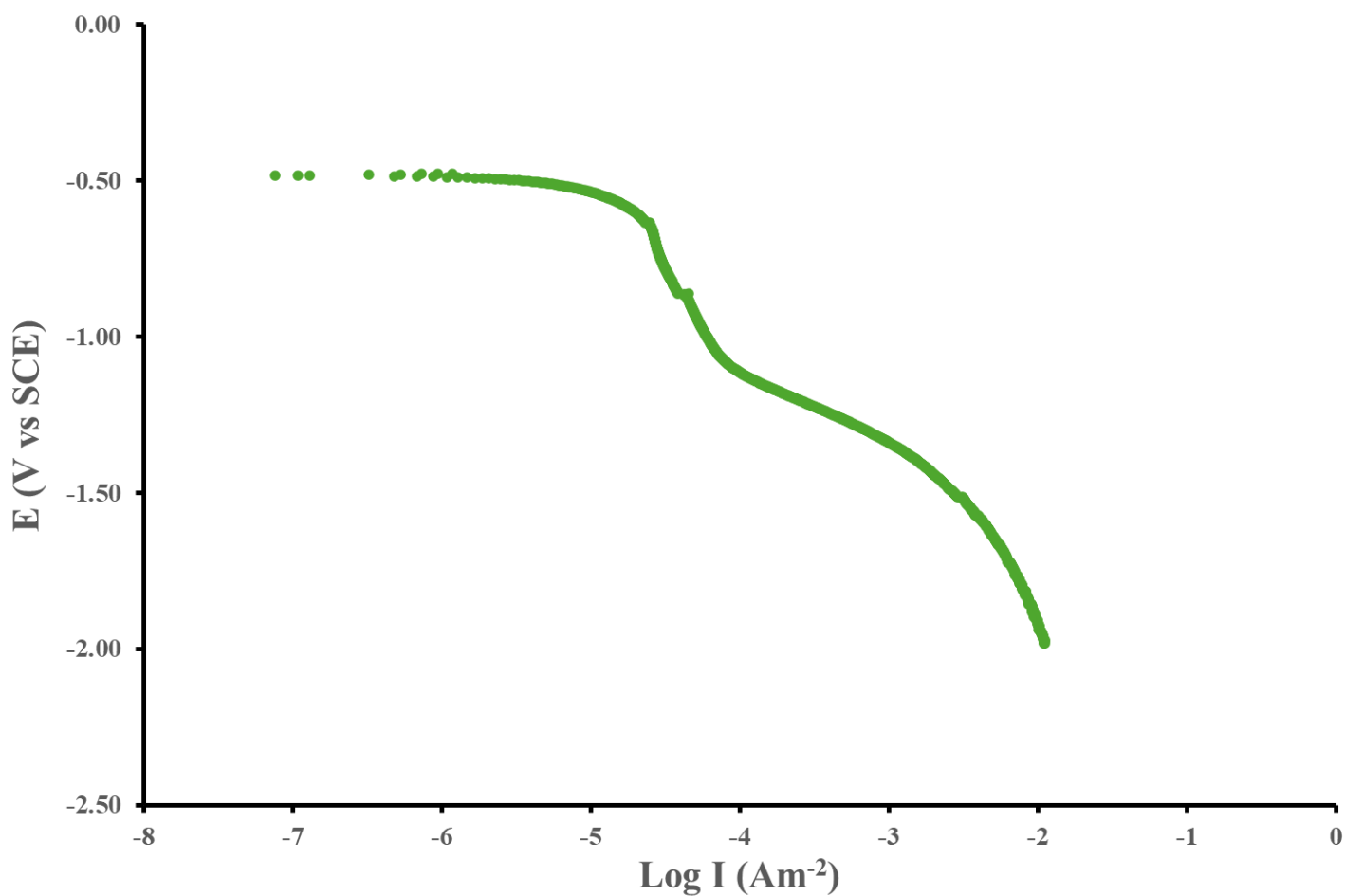


Figure 4. 10 - Cathodic Potentiodynamic Sweep for IFS in 1% NaCl at  $1 \text{ mVs}^{-1}$  with an external potential of  $\pm 1.5 \text{ V}$

The plot in *figure 4.10* shows a small vertical region from around -0.67 V to -1.06 V.

This means that the current is not changing while the voltage does, across a voltage range of  $\sim 0.39 \text{ V}$ .

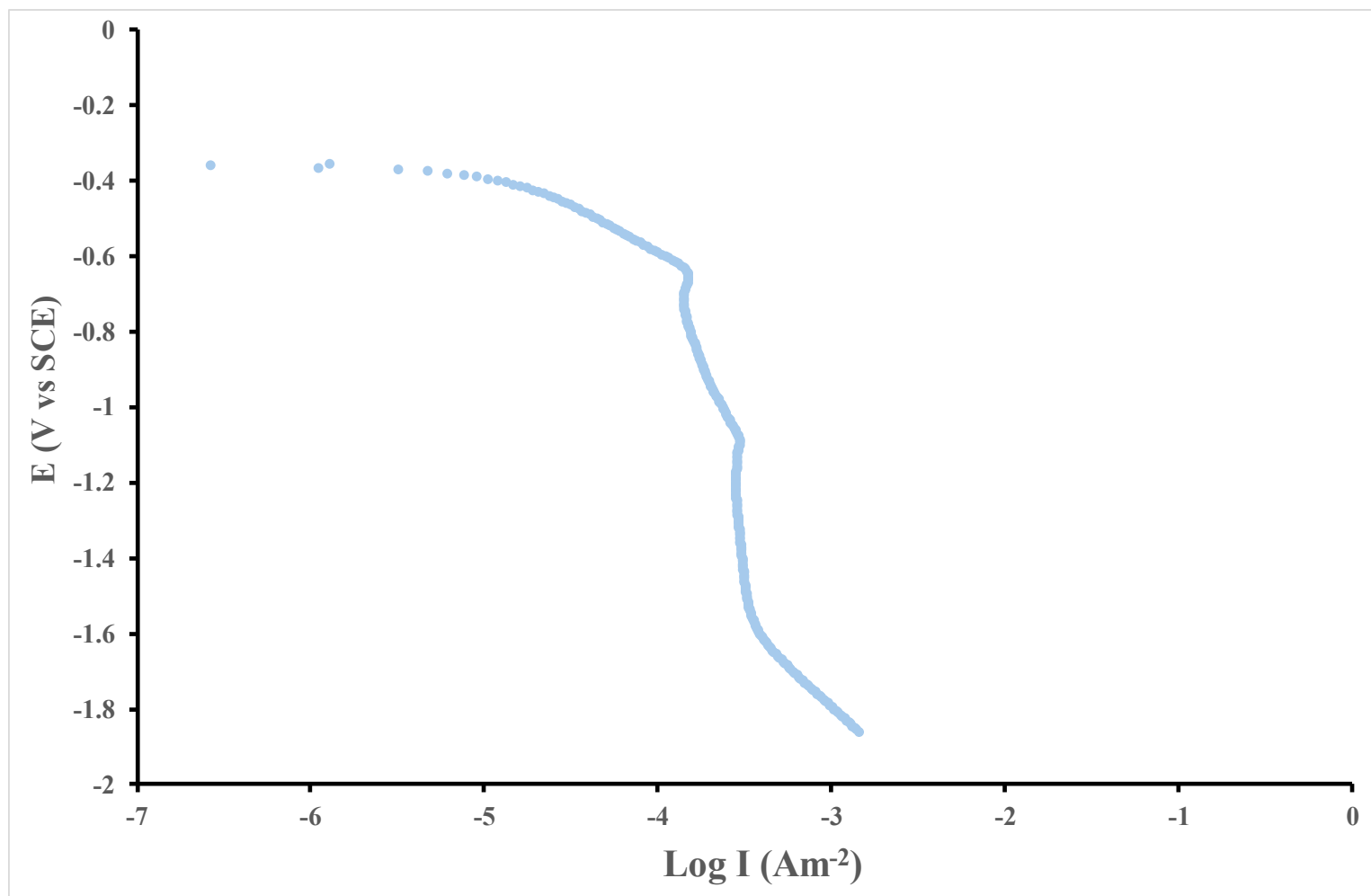


Figure 4. 11 - Cathodic Potentiodynamic Sweep for 100BiSn in 1% NaCl with an external potential of  $\pm 1.5\text{V}$  at a rate of  $1\text{ mVs}^{-1}$

Figure 4.11 shows the cathodic sweep for 100BiSn, which comprised of 100 wt% Bi-Sn. Here, there is also a vertical region from -0.68 V to -1.61 V. The passivation region spans approximately 0.93 V, a much larger voltage span than that of steel in the previous plot.

#### 4.3.7 Long-Term Exposure Testing

It was deemed necessary to gain a qualitative understanding of the coating's performance in a real-life scenario, representing the exposure experienced by many



GSE products, as well as other large steel structures. In order to replicate this, it was decided to perform long-term environmental exposure testing.

To allow for comparison of the new coating to industrial standard coatings, 20Z HDG and ZRP were all exposed. Sample preparation, parameters and location details are outlined in sections 2.9 and 4.2.6. *Figure 4.12* shows the samples immediately after being placed in the testing position.

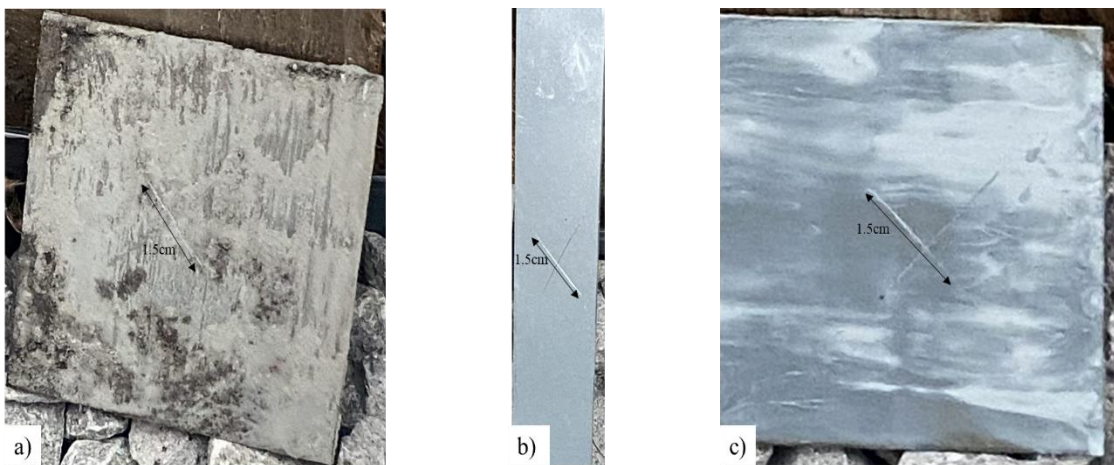


*Figure 4. 12 - Digital Camera images of samples laid out for long-term exposure testing. Each one is comprised of interstitial-free steel, coated in a) 20Z, b) HDG and c) ZRP.*

At the beginning of testing, all coatings are completely intact. *Figure 4.12 a* does show some dirt on the surface of 20Z. This was residue from the furnace and was washed off immediately before the test began. 20Z shows to be intact and cohesive on the steel surface, bar the X scribe. *Figures 4.12 b and c* show HDG and ZRP respectively, both clean and without any defects apart from the corrosion initiator “X” scribe.

The first images taken during the test were after 6 months had passed. These are presented in *figure 4.14*.

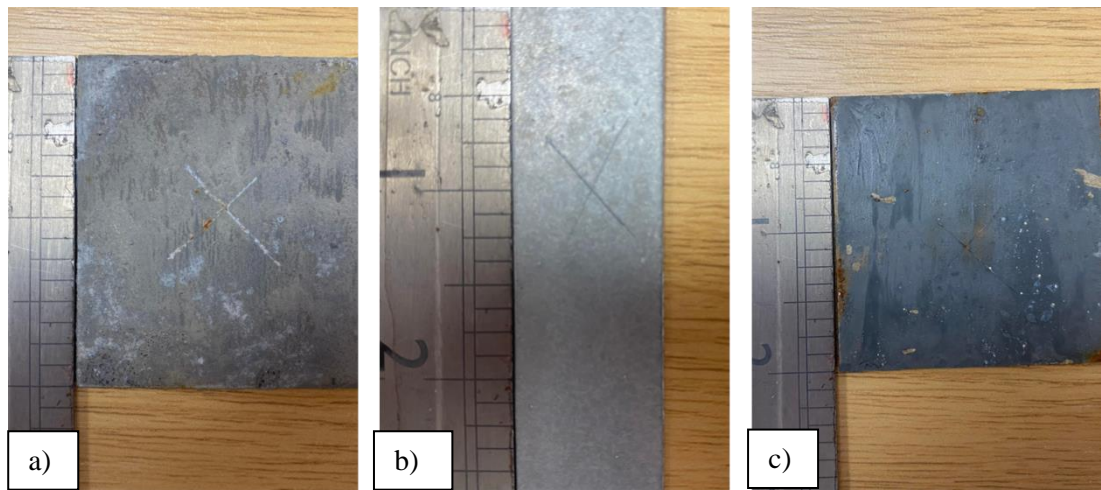


Figure 4. 13 - Digital Camera images of after 6 months of long-term exposure testing. Each one is comprised of interstitial-free steel, coated in a) 20Z, b) HDG and c) ZRP.

The updates from the images taken after 6 months in *figure 4.13* show some expected results. The HDG in *figure 4.13 b* shows exactly why hot-dip galvanising is the industry standard for corrosion protection. There appears to be no corrosion on the sample with the Zn layer maintaining full protection of the steel substrate beneath. This solidifies HDG as the premier method of galvanic protection, where possible. As discussed, HDG processes can be impractical when considering large items. Current alternatives centre around cold galvanising techniques such as ZRP.

ZRP is represented in *figure 4.13 c*. It is evident from analysing this image that there is a large amount of corrosion product present, as well as some delamination.

20Z is presented in *figure 4.13 a*. The novel Bi-Sn + Zn coating shows no sign of delamination at all. There is a small amount of corrosion product built up on the corrosion initiating defect, with a small area near the edge of the sample also showing signs of rust. No other testing was carried out to do samples being destroyed during testing.

#### **4.3.8 Lifetime Estimation Calculations**

Using the image of a 20 wt% Zn/ 80 wt%Bi-Sn in Figure 3.12 and the mass loss information in chapter 4, it is possible to gain an estimation of the galvanic lifetime of Zn in the coating.

Making the assumption that all Zn regions are spherical,, the volume of a Zn sphere can be calculated using their diameter which was measured using the GIMP image manipulation software.

The scale bar was measured to find out the length in pixels of 1 $\mu$ m.

10 $\mu$ m scale bar was equal to 252 px (pixels)

Therefore, 1 $\mu$ m is equal to 25.2 px.

This is shown in Figure 4.14.

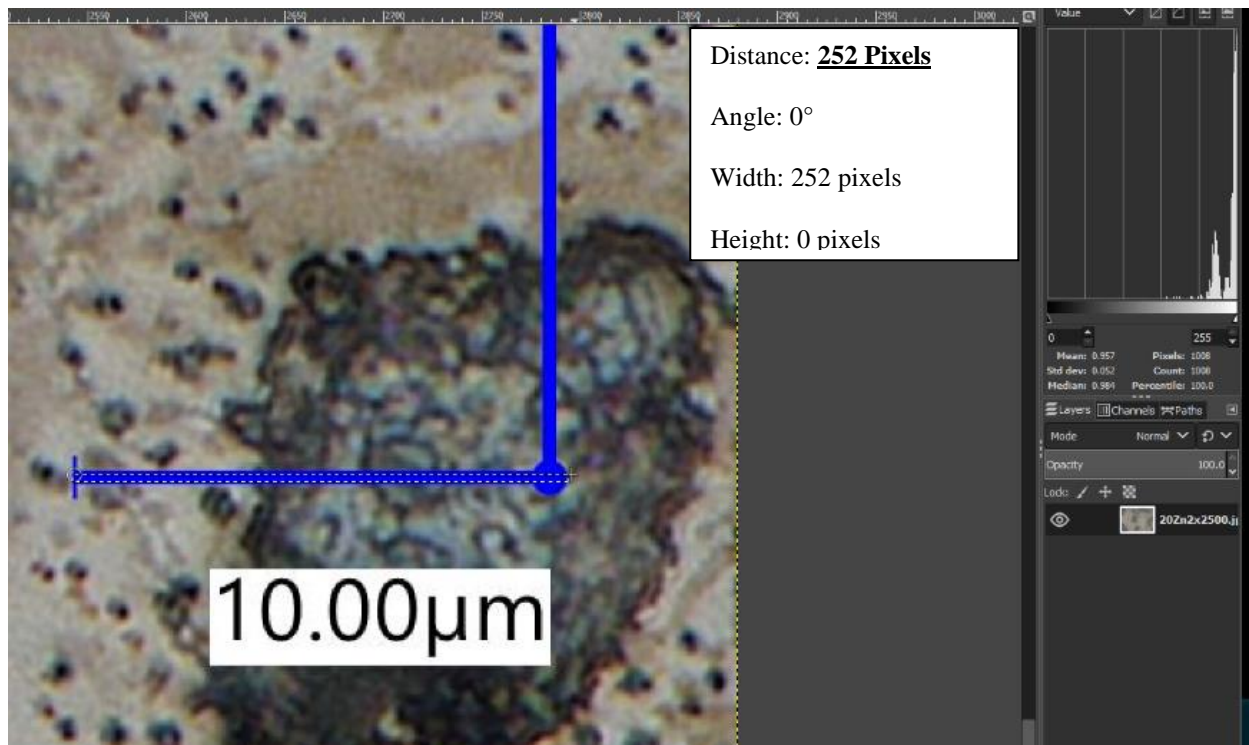


Figure 4. 14 - Representative of use of GIMP software, showing distance of 10m in pixels.

Once the radii were measured, Equation 4.1 was used to estimate the spherical volume of each region.

$$Volume = \frac{4}{3}\pi r^3 \quad \text{Equation 4.1}$$

Where;

r is the radius of the sphere

$\pi$  is pi, a mathematical constant that is the ratio of a circle's circumference to its diameter, approximately equal to 3.14159.



Once the volume was known, it was possible to find out the mass of the Zn region, using the density of Zn which is  $7.14 \text{ g cm}^{-3}$ . This was done using Equation 4.2.

$$M = D \times V \quad \text{Equation 4.2}$$

Where;

M is mass in grams,

D is density in  $\text{g cm}^{-3}$ ,

V is volume in  $\text{cm}^3$ .

The corresponding diameter, radii, for each region is given in Table 4.4

The reason for also giving radius in cm is so that the mass value comes out in g.

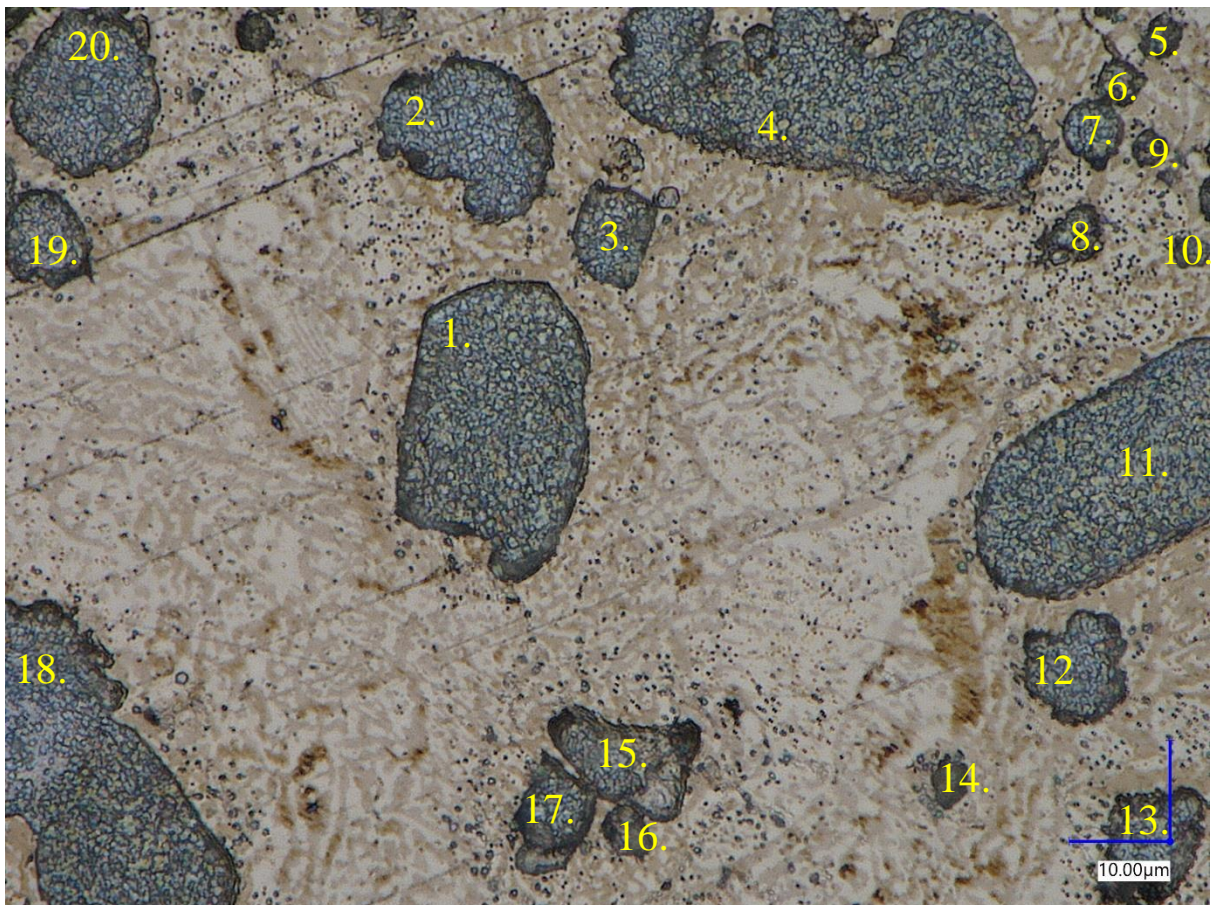


Figure 4. 95 – Digital Microscope image showing numbered Zn regions on a 20wt% Zn/80wt%Bi-Sn sample. Numbers were assigned to perform volume measurements.

Table 4. 3 - Measurements and calculations for Zn regions shown in Figure 4.15

Region Number	Diameter (pixels)	Diameter (μm) (3 d.p.)	Radius (μm) (3 d.p.)	Radius (cm)	Volume (cm <sup>3</sup> )	Mass (g)
1	426	16.905	8.452	0.00085	0.0000000025	0.000000018
2	405	16.071	8.036	0.00080	0.0000000022	0.000000018
3	183.3	7.269	3.635	0.00036	0.0000000020	0.000000016
4	1026.2	40.714	20.357	0.0020	0.000000035	0.000000014
5	93	3.690	1.845	0.00018	0.000000000026	0.000000025
6	97.7	3.877	1.938	0.00019	0.000000000030	0.00000000019
7	142.5	5.655	2.827	0.00028	0.000000000095	0.00000000022
8	143	5.675	2.837	0.00028	0.000000000096	0.00000000068
9	84	3.333	1.667	0.00017	0.000000000019	0.00000000068
10	87.5	3.472	1.736	0.00017	0.000000000022	0.00000000014
11	751.1	29.806	14.903	0.0015	0.000000014	0.00000000016
12	238.5	9.464	4.732	0.00047	0.00000000044	0.000000099
13	235.5	9.345	4.673	0.00047	0.00000000043	0.000000032
14	82	3.254	1.627	0.00016	0.000000000018	0.000000031
15	312.4	12.393	6.196	0.00062	0.00000000010	0.00000000013
16	131.2	5.206	2.603	0.00026	0.000000000074	0.0000000071
17	176.4	7	3.5	0.00035	0.00000000018	0.00000000053
18	916.3	36.361	18.181	0.0018	0.000000025	0.000000013
19	232.6	9.230	4.615	0.00046	0.00000000041	0.000000018
20	395.7	15.702	7.851	0.00079	0.0000000020	0.000000029

Once the individual masses of each Zn region were known, it was possible to estimate the total mass of Zn in the Figure 3.12 image area.

The image measured:

Width: 2883 px, so in μm:  $2883/25.2 = 114 \mu\text{m}$

Height: 2160 px, so in μm,  $2160/25/2 = 86 \mu\text{m}$

The area of the Figure 3.12 image is  $114 \times 86 = 9084 \mu\text{m}^2$  or  $0.9084 \text{ cm}^2$  or  $0.009084 \text{ m}^2$ .

The total mass of Zn in this area was calculated using Excel and scaled up for unit areas given in table below. To do this, all unit areas were converted to  $\mu\text{m}^2$ , divided by 9084 to find the multiplying factor for each unit, and this was then multiplied by the mass of Zn in the image.

It was assumed that Zn is evenly distributed in the coating such as in the image in Figure 3.12

*Table 4. 4 - Zn mass in grams for different unit areas of Bi-Sn + Zn coating.*

	Per Image area	Per $\text{cm}^2$	Per $\text{m}^2$
Total Zn Mass (g)	0.00000060	0.0066	66.15

The figures in Table 4.5 above have only taken into account the visible Zn in the image and scaled that up on a 2-dimensional basis. In reality, the coating is 800  $\mu\text{m}$  thick.

To get the mass through the coating thickness, it is necessary to assume that the image is representative of the top layer of the coating.

It could be assumed that this represents the top 2  $\mu\text{m}$  of the coating, as some of the diameters of the Zn areas are very small and it's a possibility that more Zn areas are immediately below them. And so, to get an estimate of Zn mass in 800  $\mu\text{m}$  of coating thickness, the mass value is multiplied by 400.

Through coating mass of Zn in  $1\text{m}^2$  of area =  $66.15 \times 400 = 26461.48 \text{ g}$

To find out the lifetime of 1m<sup>2</sup> of coating, the mass of Zn in grams was divided by the 24-hour mass loss (in g), and the number of days until total Zn dissolution is given. Shown below

$$\frac{26461.48}{2.48} = 10669.95 \text{ days} = 29.2 \text{ years}$$

To get a possible range for lifetime, a different assumption could be made for the coating thickness represented in the image. Again, considering some of the larger diameters, it could be assumed that the coating represents 5µm of coating thickness. So, to calculate the equivalent mass, the figure in table is multiplied by 160.

Through coating mass of Zn in 1m<sup>2</sup> of area = 66.1537054656313 x 160 = 10584.59g

$$\frac{10584.59}{2.48} = 4267.98 \text{ days} = 11.7 \text{ years}$$

Meaning a possible estimated lifetime range of 11.7 – 29.2 years. This represents a large range of lifetime possibilities, and it should be noted that these are estimations with several assumed factors. A figure somewhere between these two lifetime suggestions would be more realistic.

#### **4.4 Discussion**

SVET analysis showed that a novel coating containing 20 wt% Zn / 80 wt% Bi-Sn showed significantly better galvanic protection than 100 % Bi-Sn. As is evident from *figure 4.4*, the Bi-Sn offers no galvanic protection to steel. This is a result of steel corroding more readily than Bi-Sn, due to its lower OCP value as recorded in



literature [172,173] and in agreement with *figure 4.8*. The mechanism of corrosion for Bi-Sn is selective attack on the Sn-rich continuous phase, which is less noble than the lamella Bi phase [103]. Steel is however even less noble than Sn and thus, readily corrodes when in electrical contact [103,173]. The coating with 10% Zn addition shows an improvement in performance, as evidenced by *figure 4.3*. The superior protection here is down to the galvanic properties of Zn when coupled with steel [15,41,147]. With 20 wt% Zn addition, there is an even further improvement in galvanic protection, shown in *figure 4.6* as the SVET map shows a more prominent anode on the coating throughout. The aforementioned galvanic properties of Zn with steel are yet again responsible for this result, again reinforced by *figure 4.7*. The OCP of IFS is around -700mV and that of Zn is approximately -1V, meaning that Zn would protect steel under the given conditions of a 1% NaCl electrolyte, as was expected [106,173]. Additionally, the 20 wt% Zn sample showed a much more negative OCP than steel in *figure 4.7*, in agreement with the SVET result in *figure 4.5*. The OCP of the 20 wt% is approximately -950 mV, 250 mV lower than that of steel. A mixed potential of the Bi-Sn and Zn has resulted in a less noble potential than that of steel. It is postulated that this is due to the galvanic properties of Zn along with the metallic Bi-Sn matrix, allowing for constant contact between the substrate and the galvanic element (Zn) and also between Zn particles. This allows for superior electron transfer from Zn anodes to the steel cathodes due to better percolation pathways as well as the widely known electrical conductivity exhibited by metallic materials [19,25,31,41,42,174–177]. The reason for 20Z showing a more positive OCP than Zn is thought to be due to the Bi-Sn in the coating pulling the potential upwards, away from that of Zn [172]. The combined effect of these actions is deemed responsible for the protection the novel coating offers.

It should be noted from *figure 4.7* that ZRP and HDG/Zn have an almost identical OCP value. This is expected, due to the chemical makeup of ZRP being minimum 92 % Zn dust [178]. This means that it will exhibit similar electrochemical properties to Zn [19,129,179] but as previously mentioned there are issues surrounding its longevity [27,77,78].

The ZRA results shown in *figures 4.9* agree with the SVET and OCP results. *Figure 4.9* shows a negative current flow between 100BiSn and IFS, meaning that the steel is galvanically protecting the 100BiSn, although the current here is in nA so this shows little evidence of actual Bi-Sn self-corrosion. This effect was expected to be more exaggerated due to the OCP results in *figure 4.7*. The OCP of IFS is around -700 mV while that of Bi-Sn is around -425 mV, approximately 275 mV higher, indicating that the steel is more likely to corrode when paired galvanically with the 100Bi-Sn, as shown in literature [172,173]. This is also evident in *figure 4.2* showing the SVET map for the same couple. An interesting feature in *figure 4.9* is that there seems to be negligible current flow at all until hour 9 and a very small current afterwards, it is thought that this could be due to oxide formation on either the steel or the 100BiSn. It is known that Bi-Sn undergoes selective attack of the Sn phase in an electrolytic atmosphere, to which there could have been unwanted exposure, meaning SnO would be present on the surface of the Bi-Sn. The repeats showed this same behaviour [103]. The same could be true of the steel, which is susceptible to oxidation in the presence of moisture [180–183]. The low current flow level seen here is confirmed by the cathodic sweep results in *figures 4.10 and 4.11*. The sweeps were carried out to assess Bi-Sn's role as a cathode compared to steel's role as the same, within the overall novel coating system. The vertical region of the steel plot is much smaller than that in the Bi-Sn sweep. This is evidence that Bi-Sn is a poor

cathode compared to steel, which explains the low current levels in *figure 4.9*, as passivation is known to promote corrosion resistance [184].

The ZRA/ Galvanic Corrosion plot in *figure 4.9* also confirms the protection of Zn on Steel, the current flow is positive from the Zn WE to the Steel CE/RE due to its lower nobility and open circuit potential value, as shown in *figure 4.8*, it will more readily corrode when in electrical contact with the IFS and therefore offer galvanic protection. This phenomenon is utilised in HDG, ZRPs and other forms of galvanising and has been extensively reported in literature [15,18,19,39,129,131–133,179,185,186]. *Figure 4.9* also shows the ZRA plot for 100BiSn against Zn, representing the coating itself. There is an overall positive current flow from the Zn to the 100BiSn, meaning the Zn is acting sacrificially in this galvanic couple. This is in agreement with the OCP values in *figure 4.7* where 100BiSn has a value of around -400mV and the OCP of Zn was around -1V, so this behaviour is as predicted and shown by reported OCP values in wider research [103,179,187]. It is also known that in Bi-Sn-Zn alloys, the mechanism of corrosion is the oxidation of a Zn-rich phase, confirming that it is the Zn which acts galvanically when coupled with Bi and Sn [188] While the current flow is positive, it is also very small, rising a total of around 3nA, this is an indication that very little mass will be lost and that the coating should have a good lifetime. For steel, a corrosion current of 1 mA/m<sup>2</sup> corresponds to an approximate weight loss of 10 g/m<sup>2</sup> per year, which equates to a section loss of about 1 mm per year over 1 m. In laboratory settings, corrosion currents are often expressed in  $\mu\text{A}/\text{cm}^2$ , with 1  $\mu\text{A}/\text{cm}^2$  being equivalent to 10 mA/m<sup>2</sup>. Corrosion rates of reinforcing steel at 1 mA/m<sup>2</sup> or lower are considered negligible and are unlikely to cause significant damage [189]. Being as the currents here are in nA which is  $\times 10^3$  smaller than  $\mu\text{A}$  and our area was only 0.78cm<sup>2</sup>, this current can be

considered negligible.

Metal loss values show a better performance than HDG and ZMA alloys under similar conditions [53,56]. This would indicate that the rate of corrosion and depletion of anodic protection would be slower, due mostly to the zinc content and its galvanic protection of steel. However, LPR values in Figure 4.9 would tend to disagree as these appear to be similar to values presented in literature for other metals of around  $7 \text{ gm}^{-2}$  [53], possibly due to the dispersion and concentration areas of Zn in the coating, and a possible insufficient amount of Zn [21,179].

*Figure 4.9* confirms the findings of the SVET and OCP results with a positive current flowing from the 20 wt% Zn coating to the steel substrate. As explained earlier, this is a result of the galvanic protection of the Zn, bolstered by the metallic conductivity and percolation of Bi-Sn [42,131,175,176]. Another interesting point is that the current level shown at the maximum for 20Z vs steel in figure 4.9 is similar to that in for Zn vs IFS. The maximum shown for the 20 wt% Zn vs Steel coating is around  $55 \mu\text{A}$  while that for Zn vs Steel is approximately  $62 \mu\text{A}$ . This is due to Zn being the galvanic element in both and the driving force of the current flow [25,41,134].

In the case of the long exposure tests, the HDG shows far superior performance to both ZRP and 20Z. The HDG sample remains corrosion-free and the coating is intact and shows no signs of failure, as expected from the industrial standard [39,132,133]. ZRP in *figure 4.13 c)* shows areas of red rust near the edges and propagating from the scribe area, indicating corrosion of steel, confirming that the ZRP is not protecting the coating[185]. There are also areas where the coating is no longer intact, in agreement with literature surrounding the mechanical issues of ZRPs including evidence of peeling, flaking and UV degradation being detrimental to

performance [27,77,185,190]. These issues mostly affect the adhesion of ZRPs and as such, leave the substrate exposed, as is the case in *figure 4.13 c)* [22,28,79,129]. 20Z is shown in *figure 4.13 a)*. There are some signs of corrosion onset from the scribe. However, there appears to be far less corrosion present than on the ZRP and absolutely no signs of coating failure as the surface coating remains intact. This will be due to the metallic nature of the matrix, offering better long-term adhesion than a ZRP, [94,95,191]. The low melting point of the Bi-Sn matrix has allowed for good adhesion to the steel and remains mechanically sound [36,93]. This result shows the real-world capability of the novel Bi-Sn + Zn coating, although not superior to HDG, it has performed much better than a ZRP, as shown in *figure 4.13*.

Lifetime calculations for the novel Bi-Sn + Zn coating in section 4.3.8 show estimates for a good coating lifetime of around 12-30 years. While this is a big span of time, the calculations used took several assumptions and should be taken as an estimation only. These figures are, however, in line with lifetime calculations for some better-performing ZRPs [17]. This shows that the coating can possibly last as long, if not longer than some ZRPs.

## **4.5 Conclusions**

This chapter has presented an electrochemical investigation into the corrosion mechanisms of a novel Bi-Sn + Zn coating. The goal was to assess the corrosion protection of the coating and gain an understanding of the thermodynamic properties of its corrosion protection to a steel substrate. The ability of the coating to provide excellent galvanic protection to steel is critical.

To achieve the results presented here, the coating was subjected to a number of electrochemical and real-world tests including SVET, OCP and ZRA testing, as laid out in section 4.2.

Key findings from the present chapter are as follows:

- SVET scans showed that 20Z offered sustained protection to a steel substrate in an electrolyte.
- Also shown by SVET scans was that 5Z offered great protection to a steel substrate, a pathway to determining a minimum viable amount of zinc for galvanic protection.
- OCP testing showed that the addition of 20 wt% Zn to Bi-Sn lowered the corrosion potential to a value very similar to that of HDG and ZRP.
- ZRA showed that electron flow between 20Z and the steel substrate was similar to that between Zn and the steel substrate, confirming the galvanic action of Zn to be the protection mechanism of the coating.
- Long-term exposure testing proves that 20Z performs better than ZRP when exposed a coastal, marine, industrial environment. However, HDG performed better than both.

Considering the context of these findings, 20Z has proved to provide galvanic protection to steel. These findings show that its superior corrosion performance is due to the Zn addition and its constant electrical contact with the substrate due to the metallic matrix, made up of Bi-Sn. The galvanic action of the Zn to the steel provides this protection. The key findings show all coatings containing Zn and Bi-Sn to offer sufficient protection to steel, 20Z as our main candidate has proved to be an

exceptional candidate for use in corrosion protection applications throughout industry.

# **Chapter 5: Physical Properties of a Novel Bi-Sn + Zn Coating**



## 5.1 Introduction

A key criterion for any new coating is good adhesion to the substrate and to remain mechanically intact and stable. The mechanical failure of coatings overtime is a widespread issue, due to the development of detrimental effects such as fatigue, alongside external and environmental factors [192–194]. These failures can usually lead to a substandard coating performance as the substrate will be exposed or attacked [195–197]. This is especially true in coatings designed to prevent corrosion of metal substrates, any defect in the coating could expose the metal beneath to corrosive attack [198].

This chapter will address the mechanical suitability of several coating compositions for use on steel structures of GSE. Adhesion of a coating to its substrate is of utmost importance when considering a candidate, poor adhesion can lead to separation of coating and substrate [199,200]. To promote adhesion, several steps can be taken to prepare the surface of the substrate, in this case steel. The processes of surface treatment for HDG are widely known and explained elsewhere, including pickling and fluxing to remove oxides and scale [15,120,200–202]. Similar pre-treatments are essential to all types of coating and metal finishing procedures, ranging from cleaning methods to surface deformation [203–207].

ZRPs are known to have lower adhesion to steel substrates than HDG. A primary reason is the high Zn content of such coatings, allowing for extremely minimal inclusion of a binder to adhere to the substrate [77], as a result the coating can flake and physically fail [187,208,209]. This also affects its impact resistance, rendering it unsuitable for many applications [77]. Another issue is the compromise and degradation of ZRPs by ingress of water or corrosive electrolyte into the coating

itself, again detrimentally affecting the adhesion of the coating and establish corrosive attack [77].

This chapter will analyse the mechanical properties and strength of the coatings presented in chapters 3 and 4. A comprehensive testing regime will seek to quantify the behaviour of this coating when subject to tests of several facets of its mechanical characteristics in order to deem the coating suitable for the applications intended.

## **5.2 Experimental Details and Methods**

The experimental methods for testing carried out in this chapter are described in detail in sections 2.5 and 2.6.

### **5.2.1 Sample Preparation**

Hardness testing was undertaken as described in Section 2.5. This section tested eight samples, split into two groups of four samples based on heat treatment time.

One set of four samples were heated for 20 minutes and another set of four samples were heated for 40 minutes – all at 245 °C. The oven was heated to 245 °C and the samples were then inserted. Each set contained four samples of differing Zn content.

These are outlined below in *Table 5.1*.

Table 5. 1 - Table of samples used in Vickers Hardness testing.

Sample Code	Zn Content (wt%)	Bi-Sn Content (wt%)	Heat Treatment Time (mins)
S6	0	100	20
S7	20	80	20
S8	50	50	20
S9	90	10	20
S16	0	100	40
S17	20	80	40
S18	50	50	40
S19	90	90	40

### 5.2.2 Vickers Hardness Testing

Each sample was tested five times, ensuring that each chosen indent site was at least 5 mm away from previously tested areas. This was done to avoid the effects of work-hardening. The average Hv (arbitrary unit for Vickers Hardness) was taken from the set of four results and presented as a representative value in *section 5.3.1*.

### 5.2.3 Adhesion Testing

Adhesion testing was carried out, firstly using a tensile tester to bend samples, prepared as described in *section 2.6*. The test carried out was a 0t test as shown in figure 5.1.

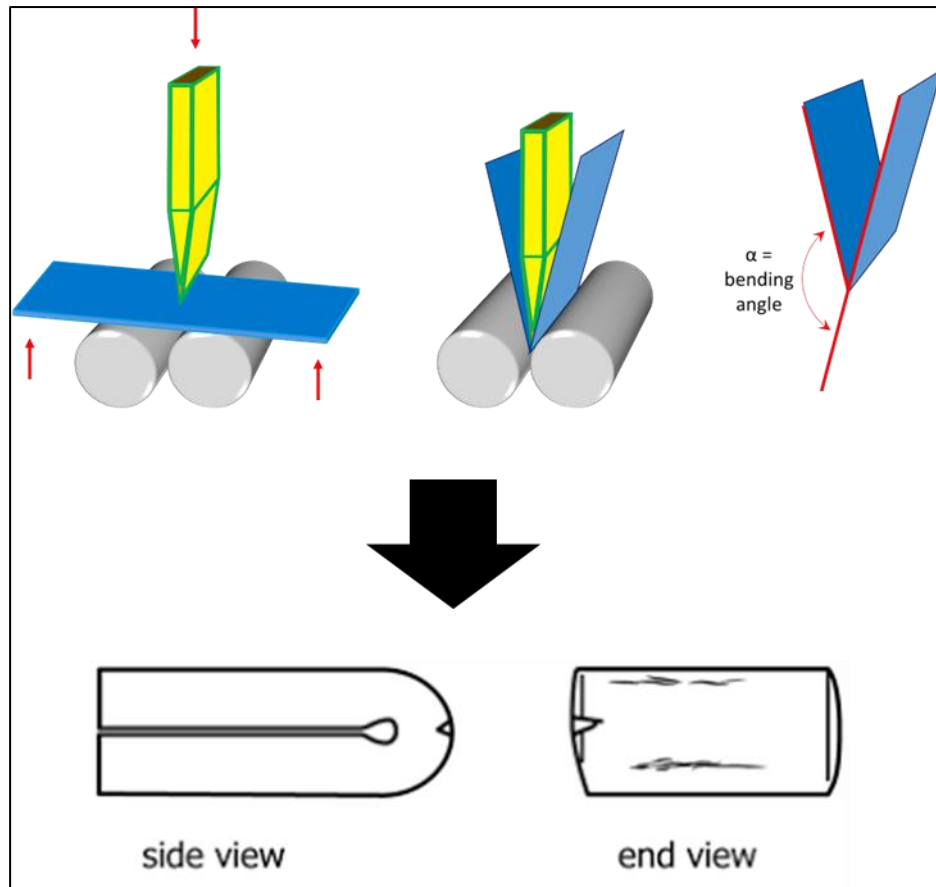


Figure 5. 1 - Schematics for Ot bend test showing a sample bent in a tensile/compression tester then fully bent using a vice until the "legs" are parallel.

The method provides a qualitative measure of adhesion by visually examining the ability of a coating to stay intact and adhered on the substrate surface under extremely harsh bend testing.

Samples tested were 0% Zn, 20% Zn and 50% Zn as they represent no zinc, a middle/medium amount of zinc and a fairly high percentage of Zn. Three repeats of each sample were taken; the results included are representative of all repeats.

#### 5.2.4 Wetting

Testing was carried out to analyse the wetting and wettability of certain coating components to each other. This was done by melting one constituent and creating a drop on the solid surface of another constituent. The main objective in undertaking

these experiments was to assess the interaction between Zn and Bi-Sn.

Bi-Sn paste was melted and dropped onto the surface of a Zn sample, pre-heated at 200 °C for 60 minutes to help facilitate any possible diffusion or adhesion at a higher temperature. A picture was then taken and analysed using image manipulation software (GIMP). The software was used to quantify the wetting angle between the Zn and the Bi-Sn, to determine the quality of wetting between the constituents. Three repeat experiments were undertaken, the results included here are representative of all repeats.

## 5.3 Results

### 5.3.1 Vickers Hardness Testing as a Function of Zn Content

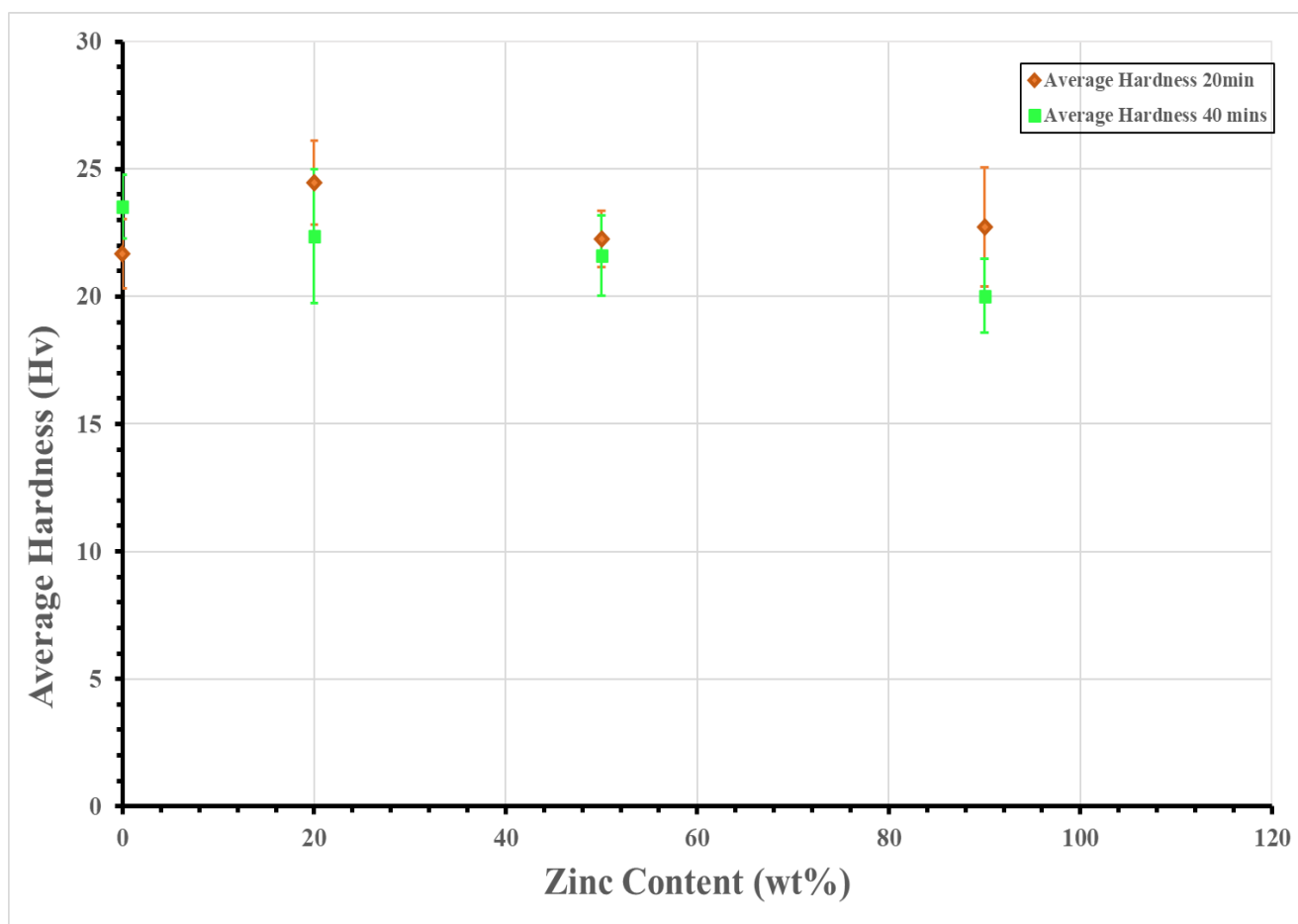


Figure 5. 2 - Plot showing average Vickers hardness (Hv) of coating samples heat treated at 245 °C for 20 mins and 40 mins as a function of Zn content. Error bars show standard deviation.

Vickers hardness values for samples heat treated for 20 minutes are presented in *Figure 5.2*. There is very little change with Zn addition. The highest value is 20 wt% Zn addition at 24.456Hv and the lowest value 21.662Hv is that of 100% Bi-Sn.

The plot in *figure 5.2* also shows the hardness of samples with varying zinc content, that were heat treated for 40 mins. The highest average value shown is 23.526Hv for 100BiSn and the lowest is 20.03HV. These values are also very soft when compared

to other metals, owing to the fusible nature of Bi-Sn and the powder/dust from of the Zn, expanded upon in *section 5.4*.

### 5.3.2 Adhesion Testing

0t bend testing was conducted as described in *sections 2.6 and 5.2.2* respectively.

#### 5.3.2.1 0% Zn (100% Bi-Sn)



*Figure 5. 3 - Image of a 100% Bi-Sn coating on a 50 x 50 mm coupon of IF Steel, during a 0t bend test.*

The sample pictured in *figure 5.3* is an interstitial-free steel sample coated with 100% Bi-Sn paste, heat treated at 245 °C for 40mins and cooled, then subjected to a 0t bend test, used as an experimental control.

#### 5.3.2.2 20 wt% Zn / 80wt% Bi-Sn



*Figure 5. 4 - Image of a 20wt% Zn / 80wt% Bi-Sn coating on IF Steel, during a 0t bend test.*

The sample in *figure 5.4* is a 20 wt% Zn coating on an IF steel substrate during a 0t bend test. There is no evidence of flaking or peeling and no cracking of the coating has occurred.

### 5.3.2.3 50 wt% Zn / 50 wt% Bi-Sn



Figure 5. 5 - Image of a 50wt% Zn / 50wt% Bi-Sn coating on IF Steel, during a 0t bend test.

The sample in *figure 5.5* is coated with a 50 wt% Zn and 50 wt% Bi-Sn composition. There are several cracks visible at the bend and it is evident the coating has peeled in places.

### 5.3.3 Wettability of Coating Constituents.

Wettability was tested as described in *section 5.2.3*. The specimens tested were molten Bi-Sn and Zn sheet, to test the wettability of the Bi-Sn to the Zn due to their role as key coating components. A molten droplet of 20g Bi-Sn heated to 150 for 30 mins, to ensure complete melting, was poured onto a pre-heated section of Zn sheet while being video-recorded. The results in this section are stills from the resulting video. The wetting angle was then measured using an image manipulation software. The image in *figure 5.6* shows the droplet of Bi-Sn on the Zn sheet, as captured.





*Figure 5. 6 - As-taken image of a molten Bi-Sn droplet on a 50mm x 30 mm Zn sheet section.*

While there is a discreet and obvious angle between the droplet and the Zn sheet, it is difficult to determine from *figure 5.6* if this is a good or bad wetting angle. In order to do so, an angle measure tool was used on the image, shown in *figure 5.7*.

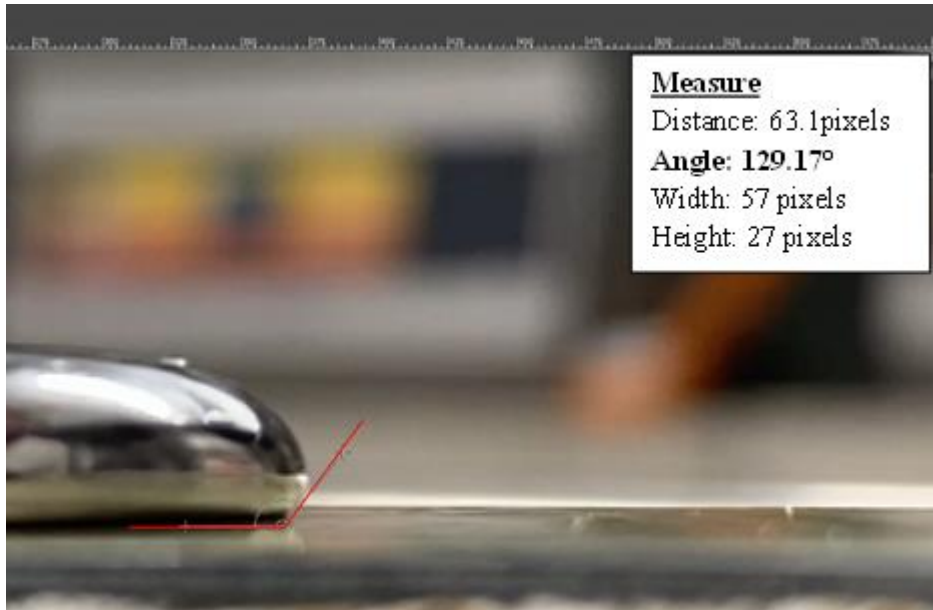


Figure 5. 7 - Close up image of the wetting angle between the Bi-Sn droplet and the Zn Sheet, displaying the angle measure tool in the red box.

The measurement of the wetting angle between Bi-Sn and Zn is shown in *figure 5.7* as  $129.17^\circ$ . This is classified as a poor contact angle and constitutes low wetting [130,142].

#### 5.4 Discussion

From the Vickers hardness data in *figures 5.2*, it is evident that Zn content has no effect on hardness values for the coating. It has been shown previously that alloying Zn improves the hardness of alloys, the results in Figure 5.2 indicates that no alloying has taken place, this is positive as alloying was not the intention [210].

There is also little to discern the 20-minute-heat-treated samples from the 40-minute-heat-treated samples. This shows that heat treatment time has no bearing on the hardness results presented in *figures 5.2*. This is attributable to the fusible nature of Bi-Sn and its constituents [102,211–213], as well as the powder form of Zn present [214].

*Figure 5.2* shows that testing of S6 gave an average value 21.662Hv which, in comparison to other materials, does seem soft [215–218], however Bi-Sn is known to be a durable and widely used material for several applications as outlined in chapter 1 [93–95,219]. The reason for such a low value is Bi-Sn's inherent softness as a fusible alloy and the individual softness of both Sn and Bi [102,211–213].

*Figure 5.2* shows very little overall change in Hv as Zn content is increased. The highest value of 24.456Hv is found in S7 which contains 20 wt% Zn. A marginal increase over the 100% Bi-Sn sample is observed but when the wider scope of comparative Hv values of metals is considered, the increase is practically negligible. The same principle is true for the other two samples in this experiment, S8 and S9. These samples had average Vickers Hardness' of 22.258Hv and 22.718Hv, showing an inconsequential change in hardness value over S6. For these samples, it is evident that increasing Zn content has no discernible effect on hardness as it is not alloying, as outlined above.

Referring to *table 5.1* we see that S16 is 100% Bi-Sn and registers a similar value to S6 with an average hardness of 23.526Hv, shown in *figure 5.2*. The other 40-minute-heated samples all exhibited very slightly lower hardness values: 22.378Hv, 21.59Hv and 20.03Hv respectively for S17, S18 and S19. These values, just like those in *figure 5.2*, show a negligible decrease in hardness from the 100% Bi-Sn sample. Therefore, it is evident that Zn content has no effect on hardness values for these samples. These values are also similar to the HV value of Zn itself, of around 32Hv – which explains why the addition of Zn had very little effect on the HV value of Bi-Sn which was as reported by other research [146,220].

As expected, the adhesion of 100BiSn was good, shown in *figure 5.4*, one of the properties owing to the widespread use of Bi-Sn [93–95,103,219]. This was as

expected, there are no signs of peeling, flaking, or coating cracking and the coating has endured the 0t test. The reasons for this are the low melting point and fusibility of Bi-Sn alloy, meaning that the Bi-Sn readily adheres the steel owing to its low melting temperature and although it is known to make intermetallic compounds when used on copper, there has been no evidence of that with steel [221]. As a result, we see a cohesive and intact coating post-bend test. The coating shows excellent performance, as was expected from its properties and wide range of industrial applications, as mentioned in [32,38,93–95,142,219,222]. There is no sign of flaking or cracking within the coating and the coating remains in a cohesive layer after testing. This is because of the properties mentioned previously, particularly the low melting temperature of the alloy [36], as well the surface preparation mentioned in *section 2.2.1*.

The same properties of Bi-Sn are deemed to result in the bend test outcome for a 20 wt% Zn coating shown in *figure 5.5*. The properties of the Bi-Sn matrix [32,36,38,142,222] have allowed the coating to fuse to the substrate strongly, meaning the coating has remained intact during the harsh 0t test. The coating has remained cohesive without any defects or flaws present. This is due in part to surface preparation and the factors mentioned above. 20 wt% powdered Zn does not appear to have compromised the bonding between substrate and coating. This coating showed excellent adhesion to the substrate.

There are very obvious cracks spanning the entire width of the 50 wt% Zn coating at the bend apex in *figure 5.6*. Cracking of the coating has been prolific, with numerous instances, sometimes diverging into each other as crack paths cross. This has caused several areas of coating to flake or peel away, with the steel substrate visible where this has occurred. The reason for this happening is thought to be due to the high

powder content of the coating, which is known to highly compromise adhesion properties of many powder or pigment-containing coatings [209,214]. Due to reasons listed above, the adhesion of this coating composition is deemed to be poor.

The wetting of coating constituents is analysed in *figure 5.8*. A wetting angle of  $129.17^\circ$  is shown between the Bi-Sn droplet and the Zn sheet. This means that the two constituents do not have a good wetting relationship, an angle of above  $90^\circ$  is considered a bad wetting angle and below  $90^\circ$  is considered good [130,142]. This result could be used to explain some of the results seen in *section 3.4.1*. The lack of mixing between the constituents could be a result of their lack of mutual wetting. The poor contact angle exhibited in *figure 5.7* is a strong indicator of the reason why more Zn results in poorer dispersion, the low wetting of the two elements has hampered the flow of the Bi-Sn solder around the Zn, leading to the poor melting/flow of many of the samples shown in *Chapter 3*. Reasons for bad wetting have been also postulated in detail in *section 3.7*. Please refer to figures 3.21 and 3.22 and the discussion around them.

## 5.5 Conclusions

This chapter has analysed some of the mechanical properties of the proposed novel Bi-Sn + Zn coatings. Through the results found from the experiments described above, it is possible to reach the following conclusions.

- The addition of Zn powder does not affect the Vickers Hardness of Bi-Sn and as such, does not have an adverse effect on the hardness of the coating.

- Increasing Zn powder content results in worse results during 0t bend adhesion testing, with the highest Zn content (50 wt%) showing severe cracking and flaking in the coating.
- 20 wt% Zn is the best addition seen here for adhesion to remain good. The coating remained intact and adhered to the surface fully.
- Poor wetting between the Bi-Sn and Zn within the coating is a probable reason for previous microscopic results showing an inadequate microstructure with the addition of Zn above ~20 wt%. The low wetting angle seen here explains results in *section 3*.

With these findings taken into account, it is evident that the 20 wt% Zn coating offers the best candidate here. Exhibiting the best result for adhesion testing and a similar score to all other samples for hardness, it is an excellent choice. The wetting section has found an explanation for earlier results and also why 20 wt% Zn may be the best composition, a lack of wetting between Zn and Bi-Sn is apparent and it is probable that this would be exacerbated with a higher amount of Zn powder.

# **Chapter 6: Alternative Production Methods for a Novel Galvanic Coating**

## 6.1 Introduction

In order to fully meet the demands of the industry, it is necessary to develop a way to heat treat the coating after application to large-scale components and structures. In a bid to facilitate a scale-up of this work from lab-based to actual industry-sized structures, the feasibility of an alternative heating was analysed. For the repair application, the alternative heating method must be somewhat “portable” and usable on large structures, as opposed to the relatively small furnaces used in the previous chapters.

Near-infrared (NIR) heating is known as an extremely power-dense heating method, capable of reaching high temperatures extremely quickly, up to almost 800°C in 10 seconds [223,224]. It is also worth noting that NIR equipment is relatively cheap when compared to other common and frequently used industrial and lab-based furnaces [224]. On the electromagnetic spectrum, the NIR region lies between visible light and infrared (IR) waves with wavelengths of 780-2500nm [223,225].

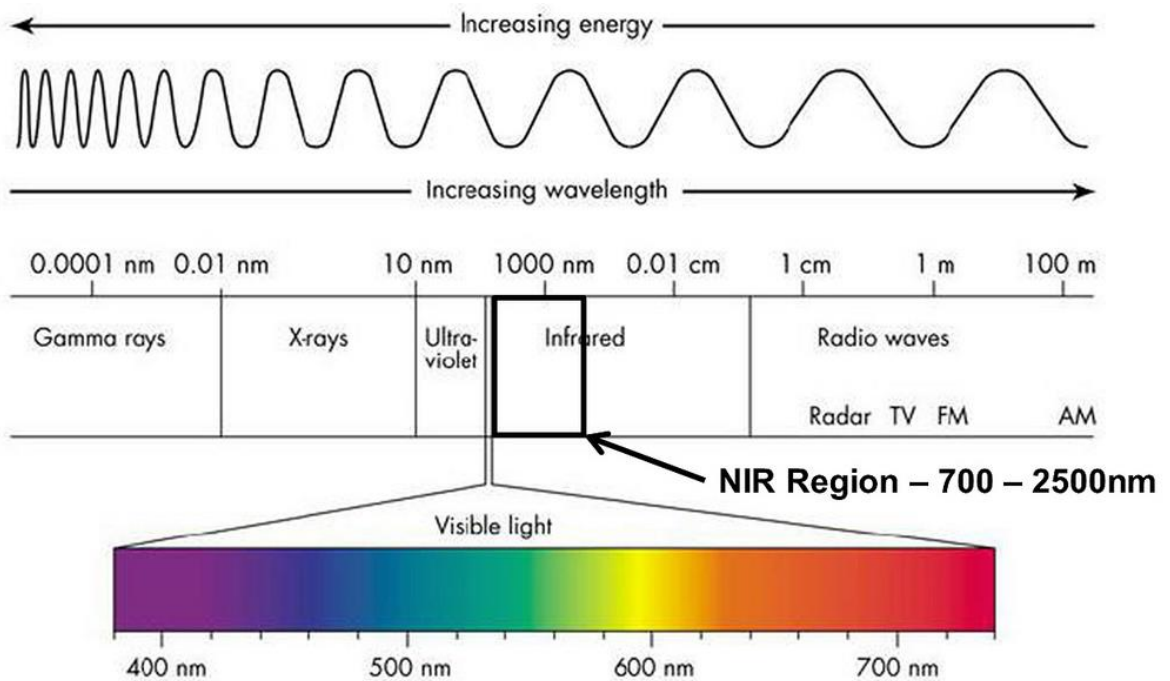


Figure 6. 1 - Diagram of electromagnetic spectrum with the NIR region pointed out. [225]



Commercial-grade NIR ovens peak at around 1000nm[223] and the radiation in this region is capable of exciting combinations and overtones of molecular vibrations [226]. Furthermore, molar absorptivity is small in this region and NIR can selectively heat a material with strong absorptivity within said region and can do so at high speeds due to its inherent energy density [223]. This energy density means NIR has been used extensively across industry and science to advance several fields including aviation, life science, nanoscience, materials science, robotics and medicine [227–232].

This chapter will assess the feasibility of NIR to cure the coating rapidly. Heat treatments will be analysed in terms of temperature and microstructure. It is known from previous chapters, the benchmarks which must be hit in order to achieve a successful coating.

NIR presents a potential to upscale and industrialise the coating, and this chapter will address the viability of using an NIR source to cure the coating on a steel substrate.

## **6.2 Experimental Details and Methods**

Experimental details for this chapter are given in *section 2.2*.

### **6.2.1 NIR Curing**

The Adphos CoilLab furnace was used to conduct the NIR experiments. This furnace does not have a temperature setting, but a power percentage setting alongside a belt speed setting. Samples are placed on a stage at one end of a belt, when experiments are started the belt begins to move and travels through the furnace and out the other side. This setup is shown in *figure 6.1*.

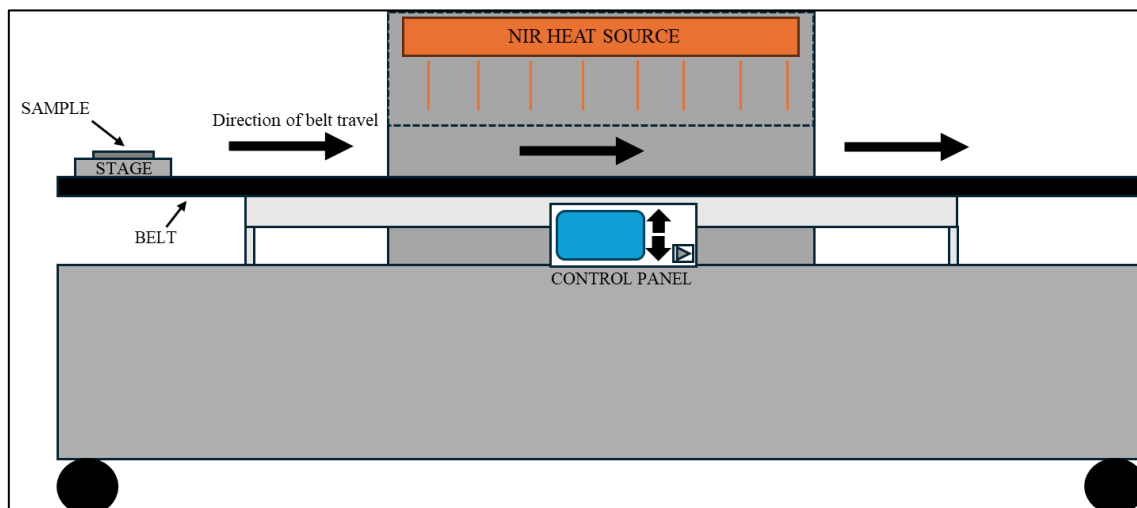


Figure 6. 2 - Schematic of NIR AdPhos NIR Furnace.

There were two controllable variables within the NIR experiments:

- Percentage power of the NIR heat source – controls the intensity of the NIR emitted upon the sample as it travels through the furnace.
- Belt Speed – controls the speed at which the stage, and sample, travel through the furnace, thus allowing control over the time period of sample exposure to the NIR.

To find the optimal heat treatment, a variety of combinations of speed and percentage power were trialled. These are detailed in *table 6.1*. The NIR variable is percentage of total power, as outlined in section 2.2.2.

Samples were produced as detailed in *section 2.2* before being cured using the NIR furnace instead of the conventional (Nabertherm) furnace.

Table 6. 1 - Parameters used to heat treat samples of 20wt% Zn / 80wt% Bi-Sn coated steel in this chapter.

Power (% of total NIR power)	Belt Speed (m/min)
20	1
20	0.5
30	1
30	0.5
40	1
40	0.5
50	1
50	0.5

### 6.2.1.1 Temperature Logging

To record the temperature of the sample during NIR cure, K-type thermocouple was utilised, having been shielded with ceramic sheath with only the tips of the sensors exposed. This thermocouple was spot-welded to the underside of the sample, in order to avoid disrupting any facets of coating performance. This was then fed through a hole in the stage, allowing the sample to lay flat. The thermocouple was then connected to a PicoLog data logger via ceramic-sheathed thermocouple wire to avoid false data pick up at any point. The data logger was in turn connected to a laptop with the relevant software installed and set up. This recorded the temperature at each second and presented the data at the conclusion of the run.

### 6.2.2 Alternative Fluxing

The process for utilising alternative fluxes was the exact same as the process outlined in *sections 2.1.2, 2.2 and 2.2.1*, except that instead of using diluted Zinc Ammonium Chloride, two different fluxes were applied in a fume hood by dipping the substrate into 50ml of the flux. The fluxes explored are detailed in *table 6.2*. Each experiment was repeated three times with the results shown in this chapter being representative of all repeats.

*Table 6. 2 - Table showing details of fluxes investigated in this chapter.*

Flux Name	Composition
Zinc Chloride Flux	Zinc Chloride ( $\text{ZnCl}_2$ ) (30-40%), DI Water (Balance)
Phosphoric Acid Flux	Phosphoric Acid ( $\text{H}_3\text{PO}_4$ ) (~75%), DI Water (Balance)

It should be noted that the fluxes were provided by the supplier in a premixed, already dilute state.

### 6.2.3 Microscopy

Microstructural images were captured using a Keyence VHX Digital Microscope, as described in *section 2.4*.

## 6.3 Results

### 6.3.1 NIR Heat Treatment

#### 6.3.1.1 20% NIR Power

The first parameters analysed were 20% power at 1m/min. The temperature profile is shown in *figure 6.3*.

The max temperature recorded during this run is 147.64 °C, at a time of 28 seconds from the ambient temperature of 24 °C upon initial temperature rise at the 16 second mark. This shows an ability to heat the sample at a rapid rate, 5.53 °C s<sup>-1</sup>. While this rate is high when compared to a conventional furnace.

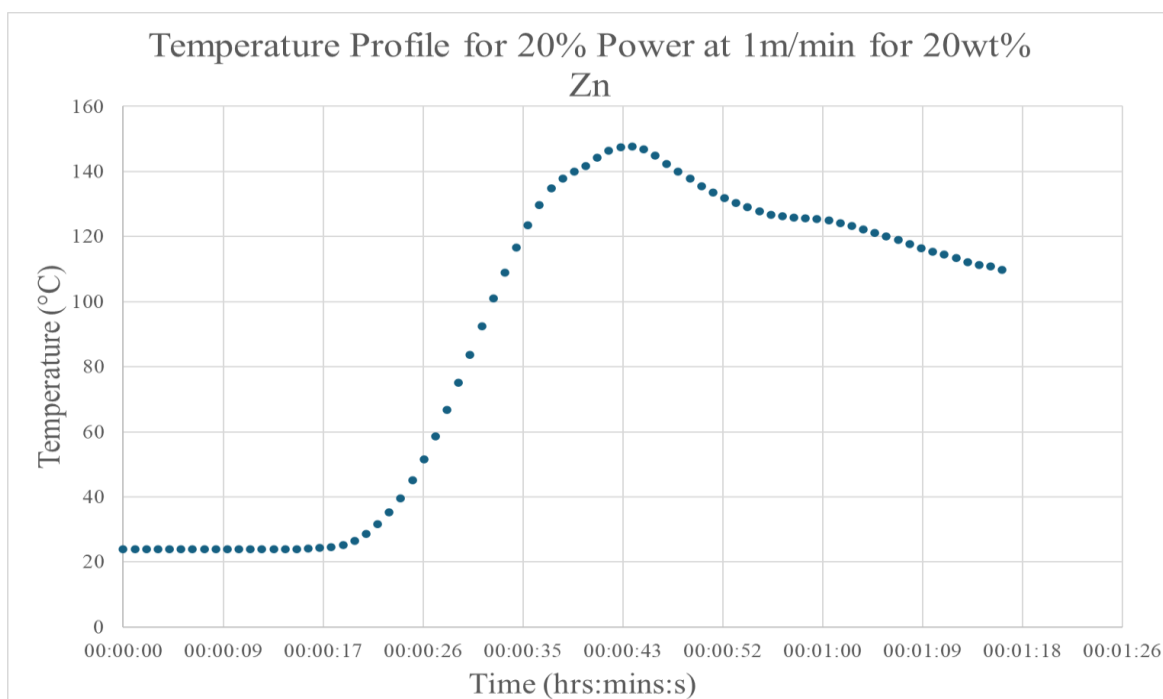


Figure 6. 3 - Time vs Temperature graph for 20% Power NIR at 1m/min

It is evident from *figure 6.3* that 20% of the NIR's power capacity is not providing enough heat for the sample to reach the desired temperature at the 1m/min belt speed. The peak temperature here is only around 9 °C higher than the melting temperature of the Bi-Sn eutectic alloy [93]. It should also be noted that this is below the reflow temperature of 180 -220°C for Bi-Sn. This is the temperature needed to reach in order to achieve a fully molten, liquid state and is higher than melting point, the temperature at which a solid begins to melt [115].

Figure 6.4 shows an optical micrograph of the sample producing during the cure profiled in figure 6.3. It is evident that the Bi-Sn has not completely melted during the trial as it appears in circular and spherical form, with areas of only up to 50 µm observed, as opposed to one coalesced matrix as desired.

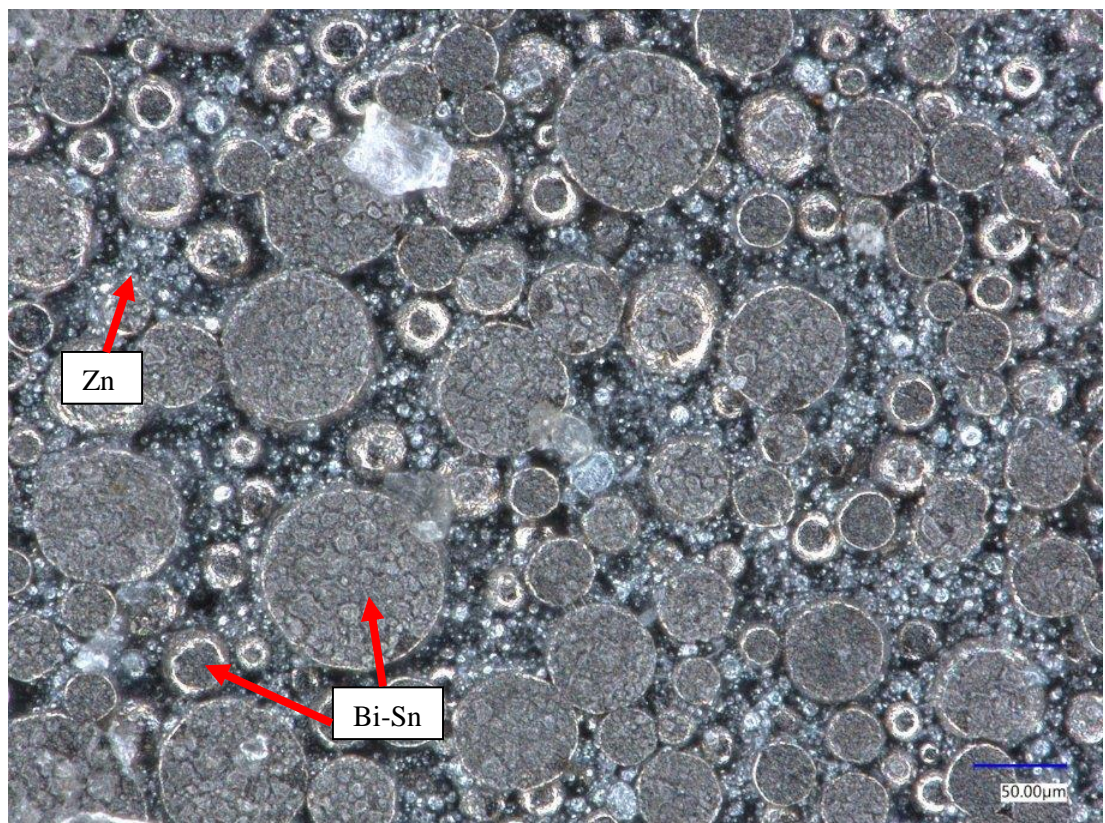
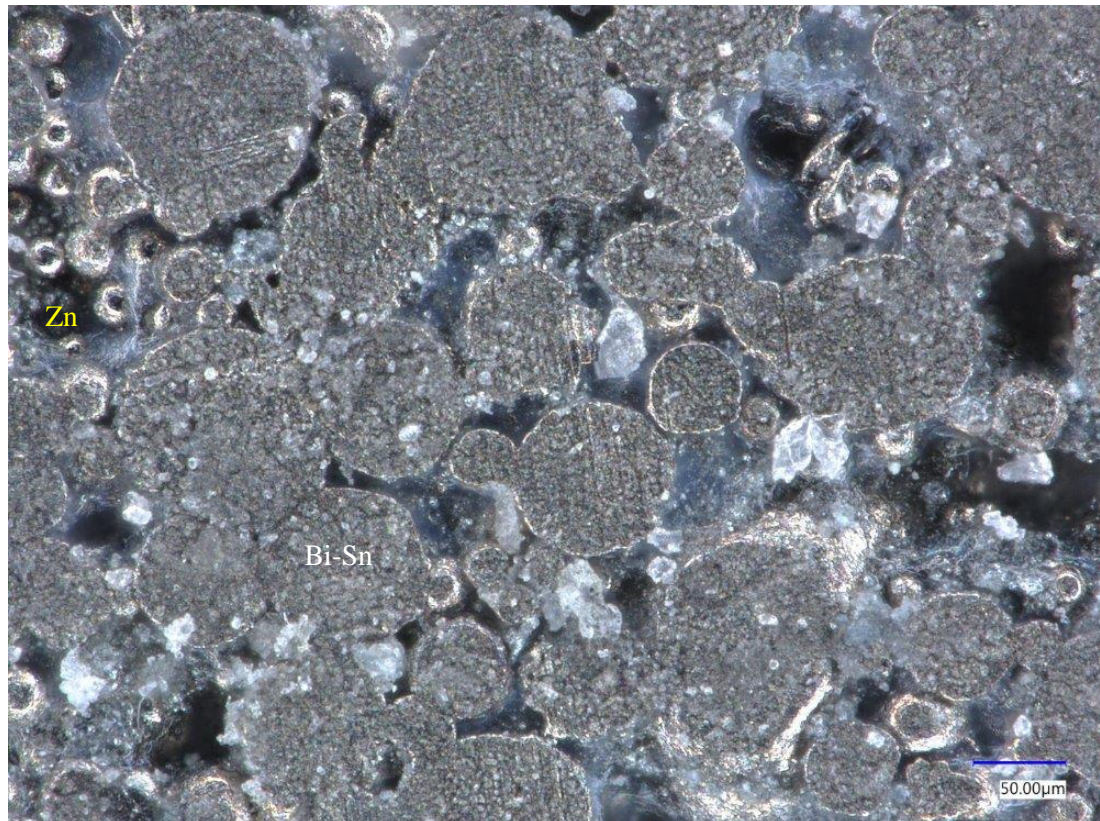


Figure 6. 4 - Keyence Optical Image of 20wt% Zn / 80wt% Bi-Sn cured at 1m/min with 20% NIR Power.



However, *figure 6.5* shows an image of 20 wt% Zn coating, cured at 20% power at a belt speed of 0.5m/min. There appears to be much more flow and melting of Bi-Sn with more coalesced areas surrounding the Zn regions. These areas of Bi-Sn are much larger than in *figure 6.4* (up to 50  $\mu\text{m}$ ), measuring up to 200  $\mu\text{m}$  in width.



*Figure 6. 5 - a digital microscope image of a 20wt% Zn / 80wt% Bi-Sn sample heated at 20% NIR power at a belt speed of 0.5m/min.*

#### **6.3.1.2 30% NIR Power**

The temperature profile for 30% NIR power is shown in *figure 6.6*.

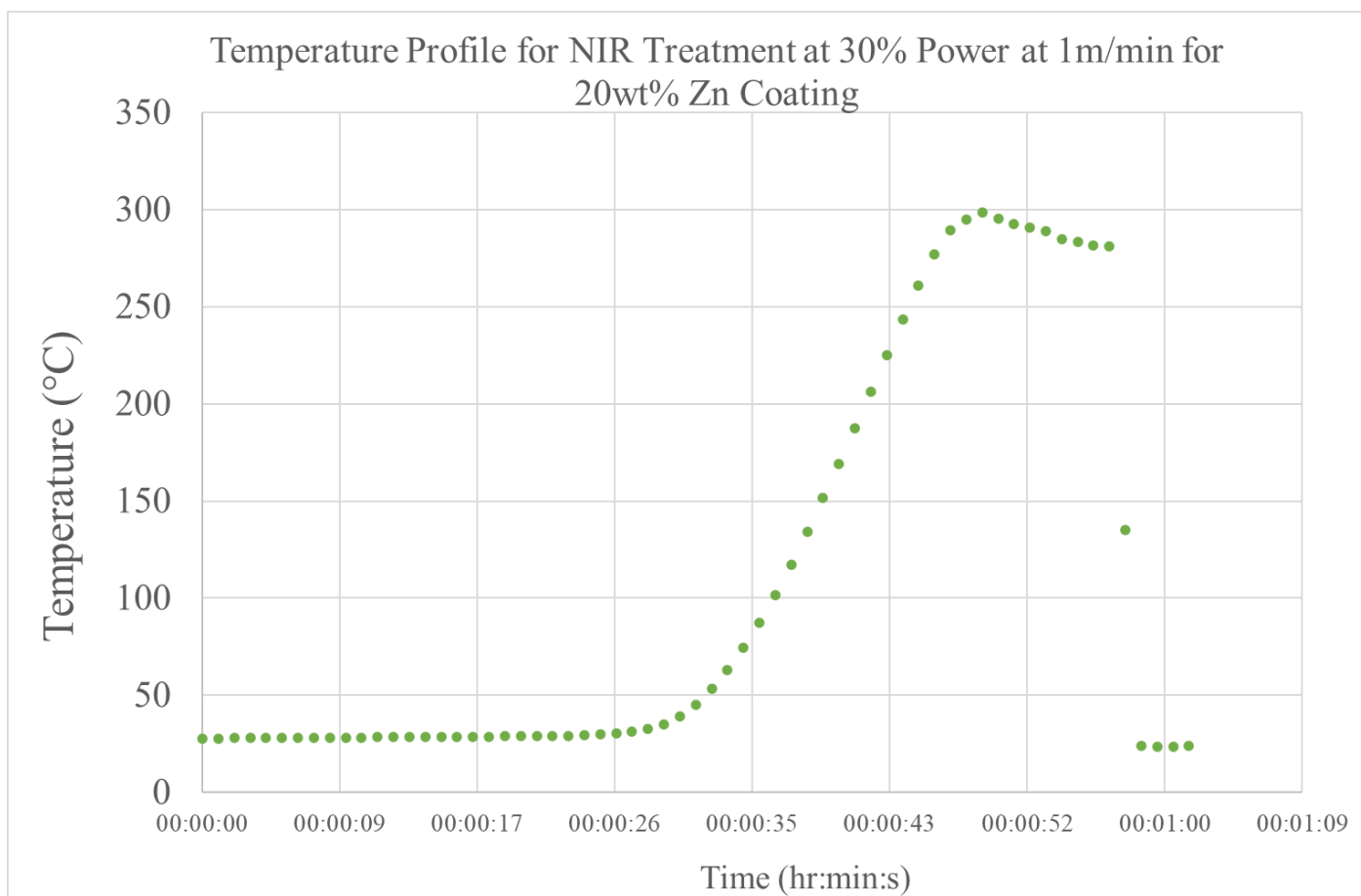


Figure 6. 6 - Temperature profile for 20wt% Zn / 80wt% Bi-Sn at 30% NIR Power and 1m/min belt speed.

Figure 6.6 shows a rapid heating of the sample from a starting temperature of 27.7°C to a peak temperature of 298.6 °C at 49s. This is an average rate of  $\frac{298.6-27.7}{49} = \frac{270.9}{49}$  to give 5.53 °C s<sup>-1</sup>. This is comparable to the heating rate of 20% NIR power, the difference being that this sample's heating time was slightly longer. The maximum heat reached is also much higher than that of *figure 6.2*, by a margin of 150.96 °C. This is also higher than the 220 °C reflow temperature of Bi-Sn.



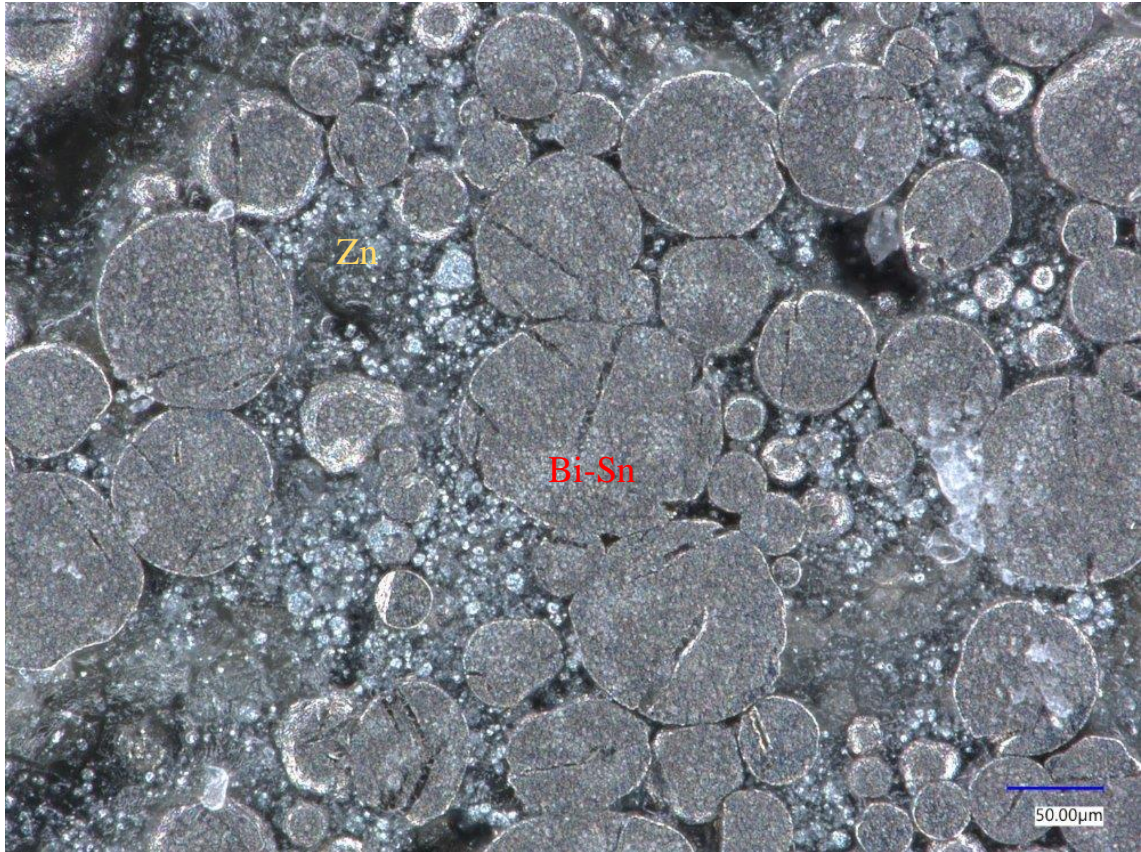


Figure 6. 7 - Digital Microscope Image of 20wt% Zn / 80wt% Bi-Sn coating, heated at 30% NIR power at a belt speed of 1 m/min.

The image in *figure 6.7* shows the microstructure of the sample after heating. There are many large regions of Bi-Sn, measuring over 100 x 100 µm. Despite this, most of the Bi-Sn visible is in discrete circular regions and not melted together, although many of these appear to be touching and so would provide electron pathways. Some areas of Bi-Sn regions in contact with one another measure approximately 300 µm in length and up to ~400 µm in some areas.

The same composition was heated at 0.5 m/min and the resulting microstructure is shown in *figure 6.8*. This heat treatment yielded much better melting of the Bi-Sn, with much larger coalesced areas present. These areas measure up to approximately 400 µm x 200 µm. There are also many more of these regions, and less discrete Bi-Sn regions. However, the Bi-Sn has not fully melted but does all appear to be in contact with other Bi-Sn regions, indicating a move toward coalescence.



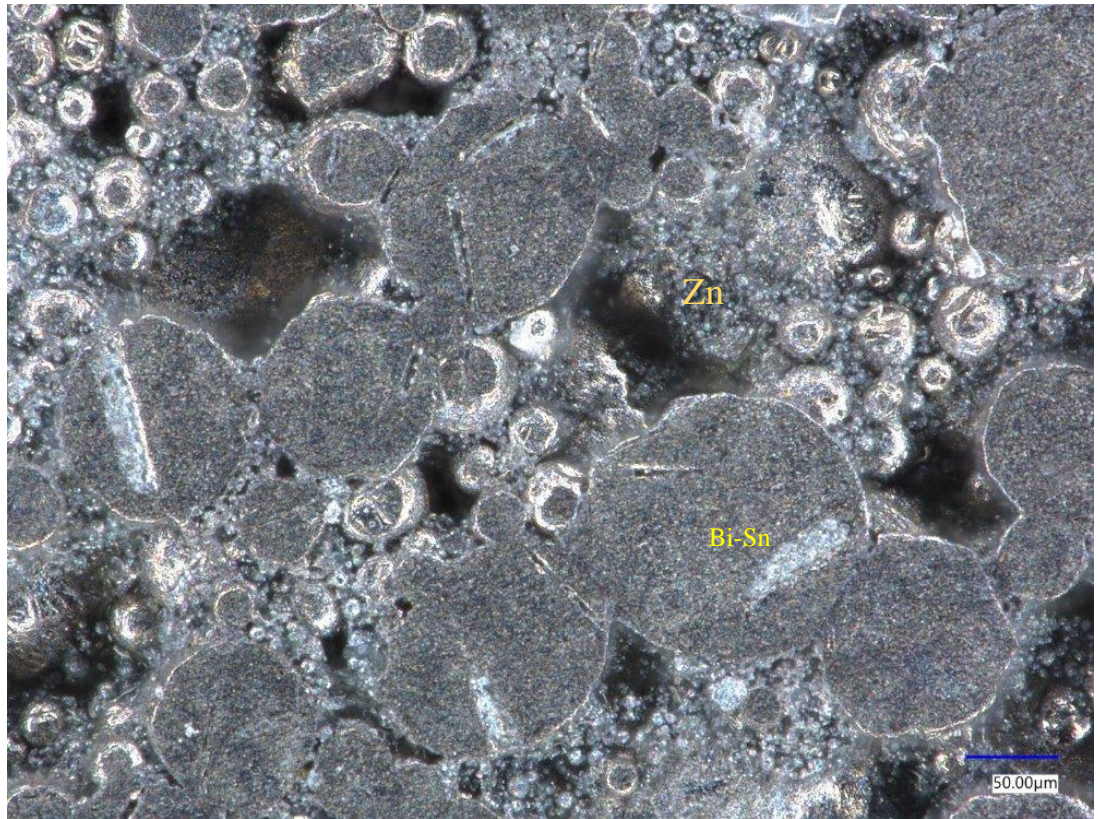


Figure 6. 8 - Digital microscope image of 20wt% Zn / 80wt% Bi-Sn sample heated at 30% NIR power at belt speed of 0.5m/min.

### 6.3.1.3 40% NIR Power

Another 20 wt% Zn / 80 wt% Bi-Sn sample was heat treated at 40% NIR. The temperature profile for a sample heated at 1m/min is shown in *figure 6.9*.

The temperature reached here is far greater than the previous two logged temperatures in *figures 6.3 and 6.6*, reaching 493.94°C at 36s from a starting temperature of 23.9 °C at 9s.

The average rate of heating can be found by  $\frac{493.94-23.9}{36-9} = \frac{470.04}{27}$ . This equals a rate of 17.41°C s<sup>-1</sup>, a much faster heating rate than the previous Nir power percentages trialled. The sheer energy density of NIR is on display here as the sample is heated up to almost 500 °C in less than half a minute.



Figure 6. 9 - Temperature profile for 20wt% Zn / 80wt% Bi-Sn heated at 40% NIR power and belt speed of 1m/min.

The microstructure for this sample is shown in figure 6.10.

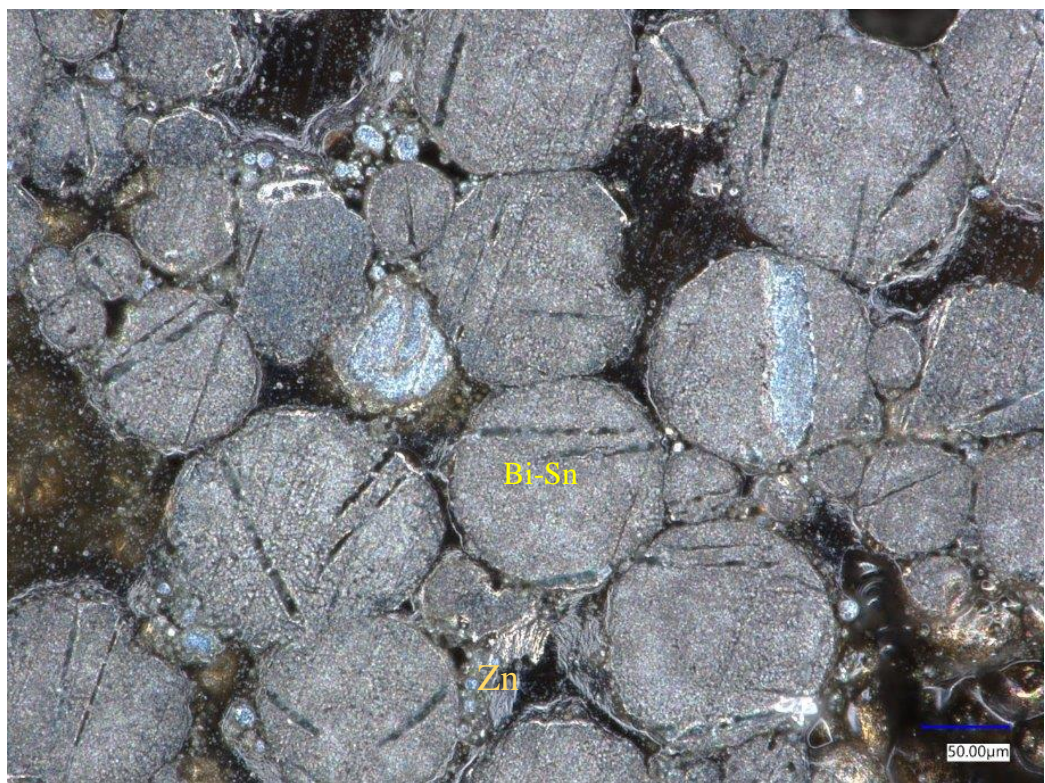


Figure 6. 10 - Digital microscope image of 20wt% Zn / 80wt% Bi-Sn heated at 40% NIR power with belt speed of 1m/min.



There are many large regions of Bi-Sn present, all interconnected or touching but with some areas remaining discrete. The area of melted and/or touching Bi-Sn regions spans the whole micrograph, around  $350\text{-}400\text{ }\mu\text{m}^2$ . An interesting feature here are many black regions which appear to be mounting resin or voids. It should be noted that the max temperature reached here is  $\sim 500\text{ }^{\circ}\text{C}$ , which is higher than the melting temperature of Zn.

The same composition was heated at 40% Power with a slower belt speed of  $0.5\text{m/min}$ , the obtained microstructure is presented in *figure 6.11*.

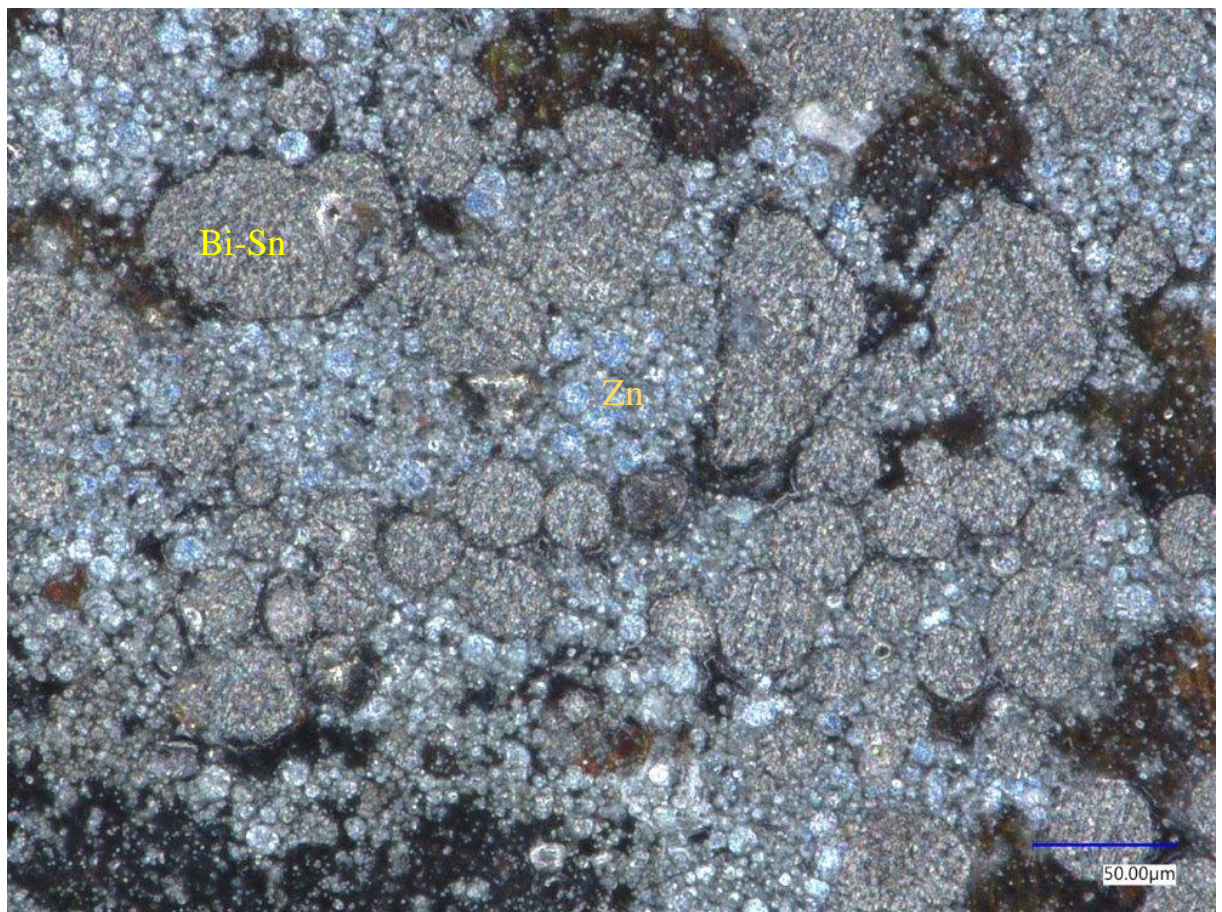


Figure 6. 11 - Digital microscope image of 20wt% Zn / 80wt% Bi-Sn coating heat treated at 40% NIR power at  $1\text{m/min}$ .

The micrograph in *figure 6.11* shows much fewer melted and fused regions of Bi-Sn with many discrete circular regions, measuring up to approximately only  $60\text{ }\mu\text{m}$  across but as small as around  $10\text{ }\mu\text{m}$ . This is a worse performance than on *figure 6.10* and to consolidate that fact, the black regions of resin are also present in this

sample.

#### 6.3.1.4 50% NIR Power

Figure 6.12 shows the temperature profile for 50% NIR Power at 1m/min.

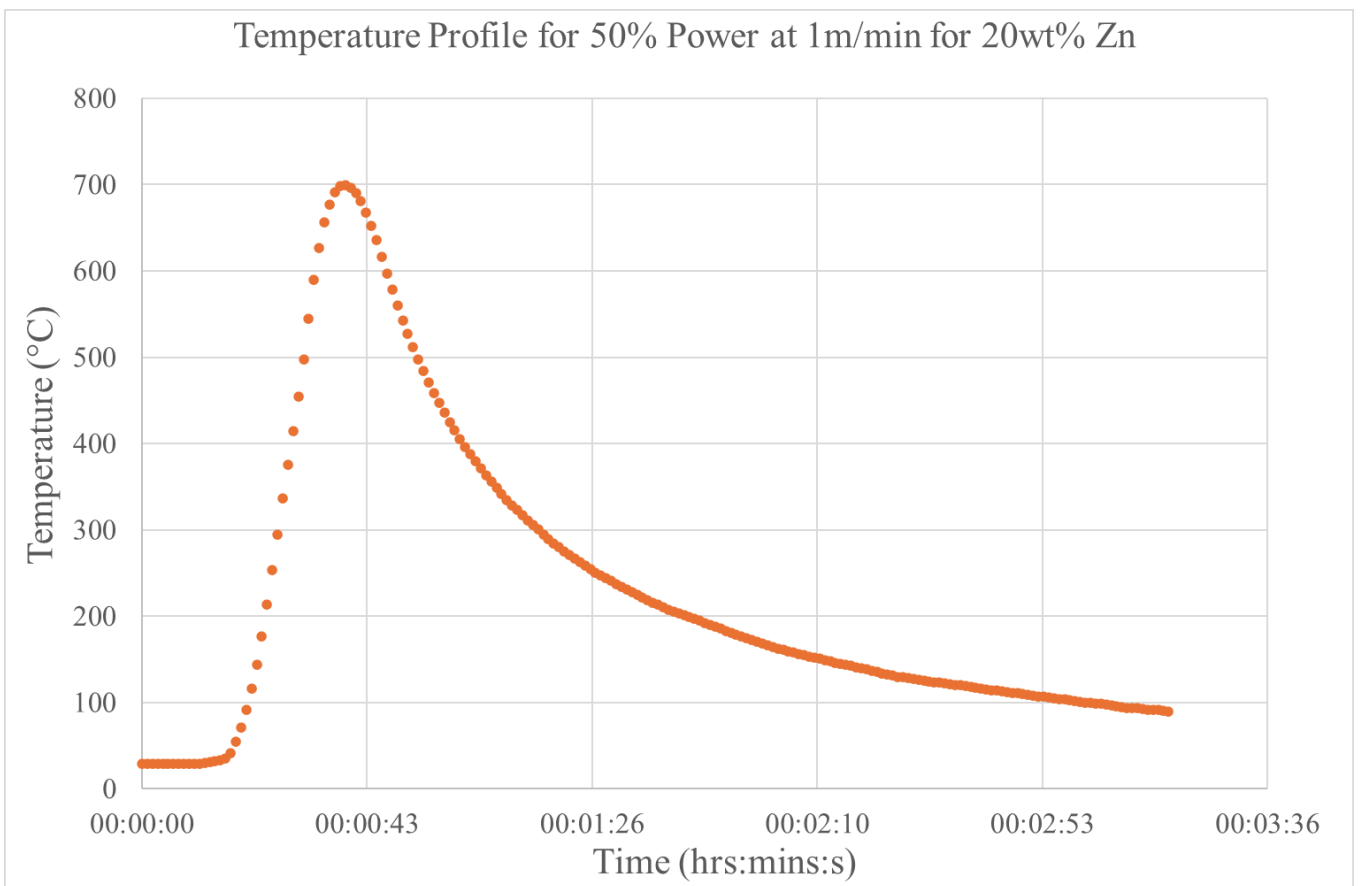


Figure 6. 12 - Temperature profile for 20wt% Zn / 80wt% Bi-Sn at 50% NIR Power at 1m/min

The maximum temperature reached at 50% power is 699.9 °C at 39s after a starting temperature of 28.69 °C, which begins to climb at 9s,

To get an average heating rate, the equation  $\frac{699.902-28.69}{39-9} = \frac{671.212}{30}$  is used. This



gives an average heating rate of  $22.38\text{ }^{\circ}\text{C s}^{-1}$ . This is, again much faster than the previous heating trials, as is expected due to the immense power of NIR heating. The maximum temperature is again much higher than the previous experiment of 40% by  $205.96\text{ }^{\circ}\text{C}$  and also much higher than the  $T_m$  of Zn which is  $419\text{ }^{\circ}\text{C}$ .

In the resulting microstructure, shown in *figure 6.13*, shows a further deterioration in performance from the previous run of 40% with even smaller Bi-Sn particles, showing much less melting and flow. The impedance of which is evident as many of the Bi-Sn regions measure only  $5\text{ }\mu\text{m}$  but up to around  $75\text{ }\mu\text{m}$  in diameter, all of which appear to be discrete. There are also holes or depressions present in the microstructure. Zn also has concentrated in one area but does not appear to have burnt this time.

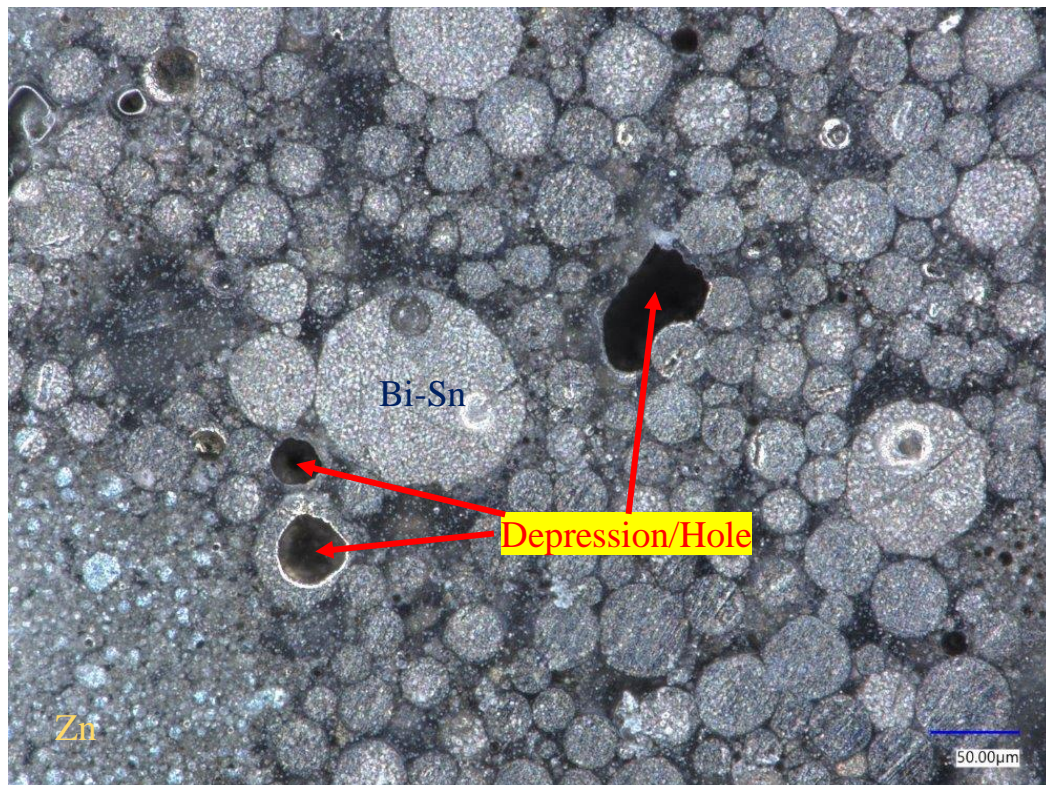


Figure 6. 13 - Digital microscope image of 20wt% Zn / 80wt% Bi-Sn heat treated at 50% NIR power and belt speed of 1m/min



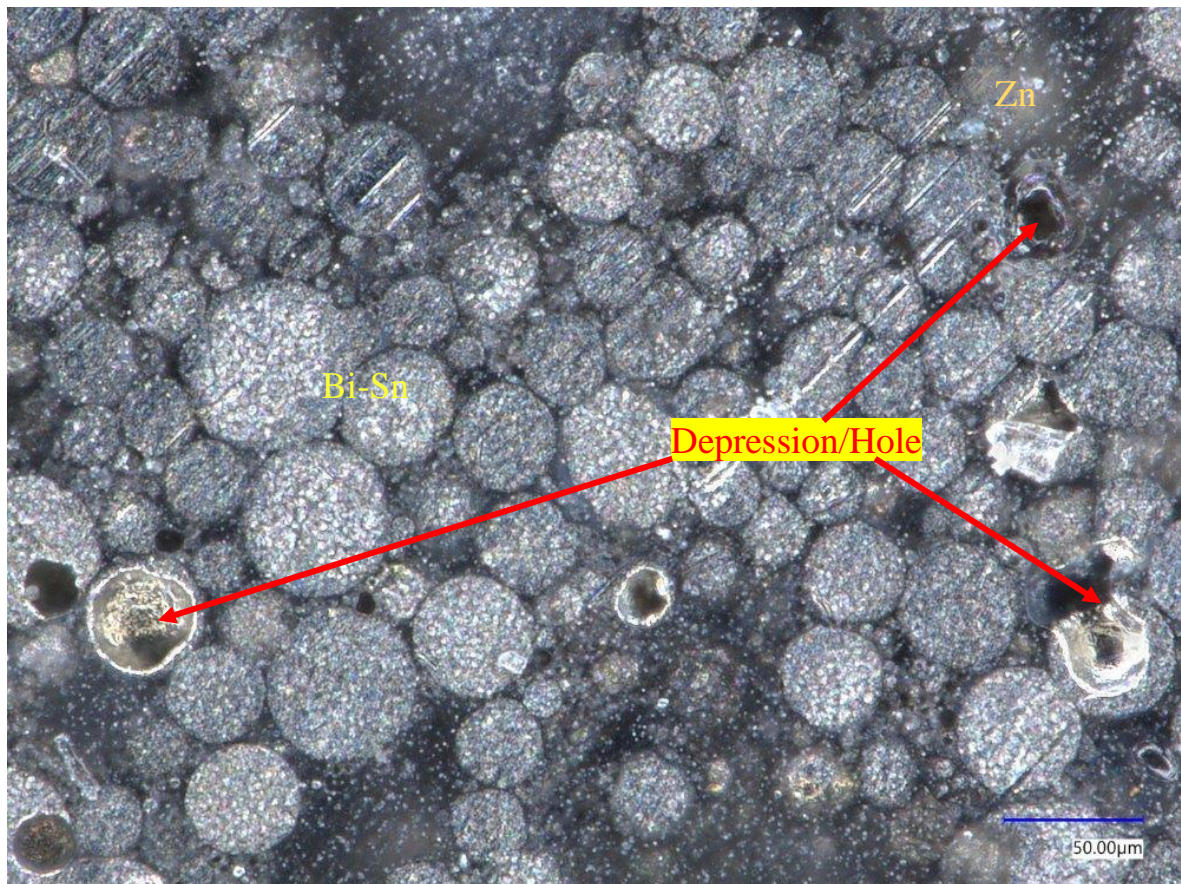


Figure 6. 14 - Digital microscope image of 20wt% Zn / 80wt% Bi-Sn heated at 50% power at belt speed of 0.5m/min.

Figure 6.14 presents the same composition heated at the same NIR power but at a belt speed of 0.5m/min instead of 1m/min. The discrete regions of Bi-Sn are even smaller than in figure 6.12, with a maximum diameter of around 50  $\mu\text{m}$  and as small as 2-3  $\mu\text{m}$ . Black areas of Zn are again evident as are the depressions/holes, visible in the previous image. It should be noted that the temperature reached by the 50% NIR power was far above that of the melting point of Zn.

### 6.3.2 Alternative Fluxes

The performances of the two alternative fluxes were assessed by qualitative means using digital microscopy. Fluxes are used in the cleaning of substrates in many metal-coating processes, namely HDG. The primary use for fluxes is to rid the substrate of oxides or other contaminations and prevent the growth of new oxides

[121,202]. Flux helps to promote adhesion of a coating and wetting of the coating to the substrate. Alternative fluxes are explored here to improve the flow and wetting of Bi-Sn to the steel substrate.

### 6.3.2.1 Zinc Chloride Flux

In *figure 6.145* a cross section of Bi-Sn coated onto IFS using the Zinc Chloride flux is presented.

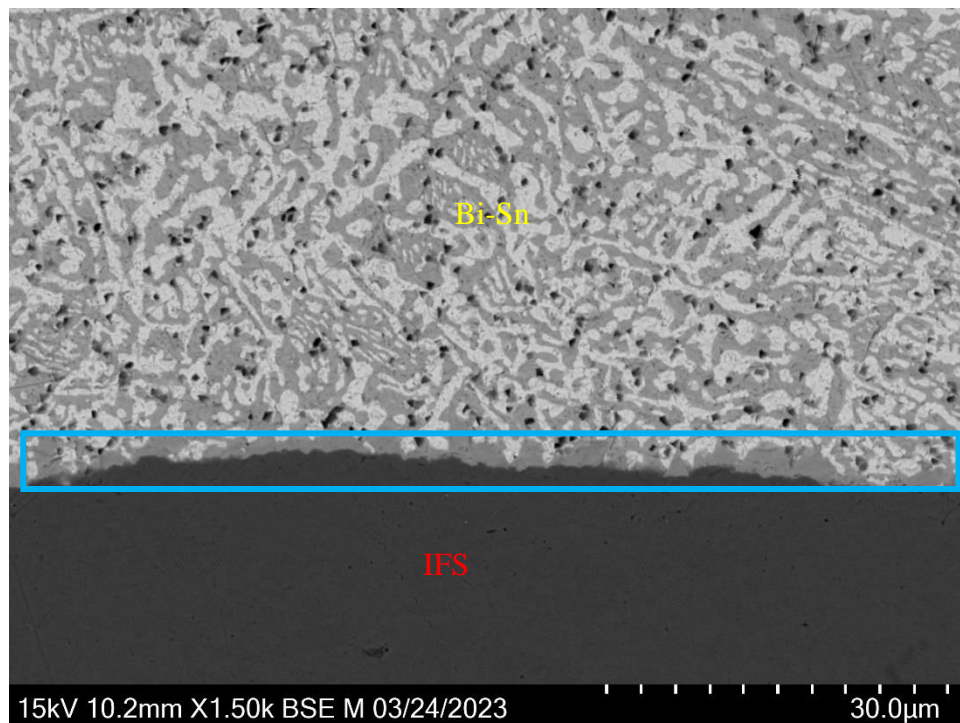


*Figure 6. 15 - Digital microscope image at 1500x magnification. of a cross-section of Bi-Sn coated onto IFS with a production process using Zinc Chloride flux. The area highlighted by the blue box is a layer of Sn at the substrate surface.*

The image in *figure 6.15* shows good wetting between the steel and Bi-Sn, as the coating is fully spread along the surface of the substrate. There is a distinct layer of Sn along the substrate/coating interface, highlighted by a blue box. This layer of Sn has formed and fused to the steel surface, this is a widely known phenomena, as seen in the tinning industry where Sn on steel substrates was melted and formed an

alloy layer with the steel substrate to achieve a brighter tinplate finish [233]. This allows for a better adhesion to the substrate as they are physically fused together [233]. From this image, the Zinc Chloride flux shows potential to improve adhesion of the novel coating.

### 6.3.2.2 Phosphoric Acid Flux

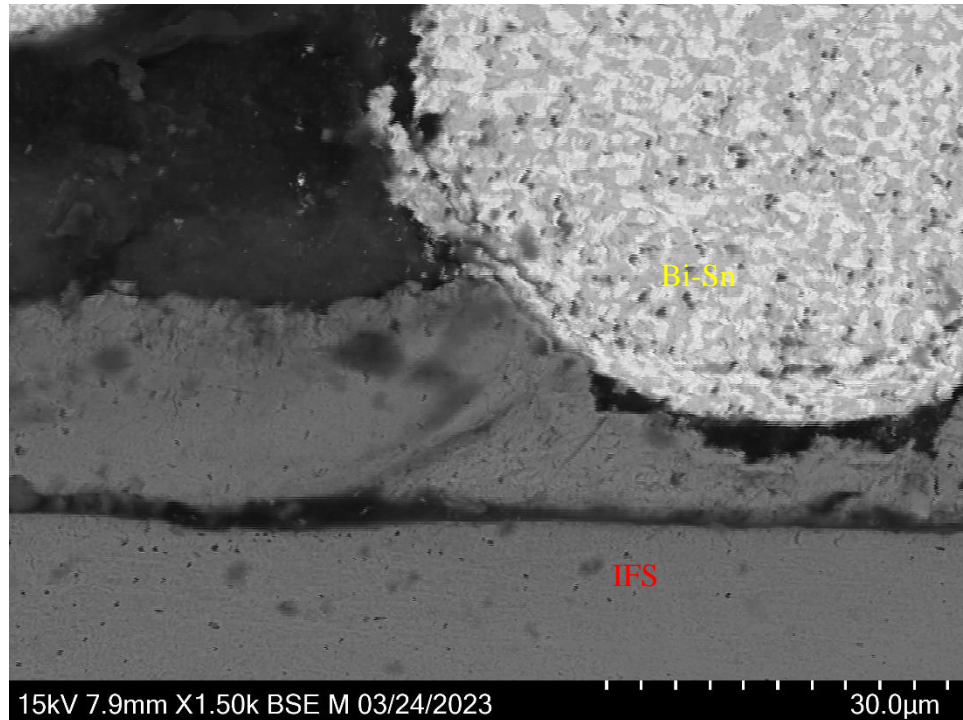


Figure 6. 16 - Digital microscope image at 1500x magnification. of a cross-section of Bi-Sn coated onto IFS with a production process using Phosphoric Acid flux.

The microstructure in *figure 6.16* shows Bi-Sn applied to steel, with Zinc Chloride flux used instead of Zinc Ammonium Chloride, as outlined in *section 2.2.1*. A round area of Bi-Sn is visible and is discrete. It does not appear that the wetting between the Bi-Sn and the steel is good as the Bi-Sn has retained a spherical shape and there is no visible spread across the substrate. To confirm this, another image, taken at 500x magnification, is presented in *figure 6.17*.

There are several more instances of discrete and un-fused Bi-Sn regions in *figure 6.17*. This confirms that the Bi-Sn has not flowed effectively and has not been able



to coalesce under the conditions of this experiment. It is possible that this is due to the Phosphoric Acid flux not performing as well as the Zinc Chloride flux, showing no signs of Sn fusion with the substrate. The area circled does show some signs of good wetting, where the substrate appears to have been abraded.

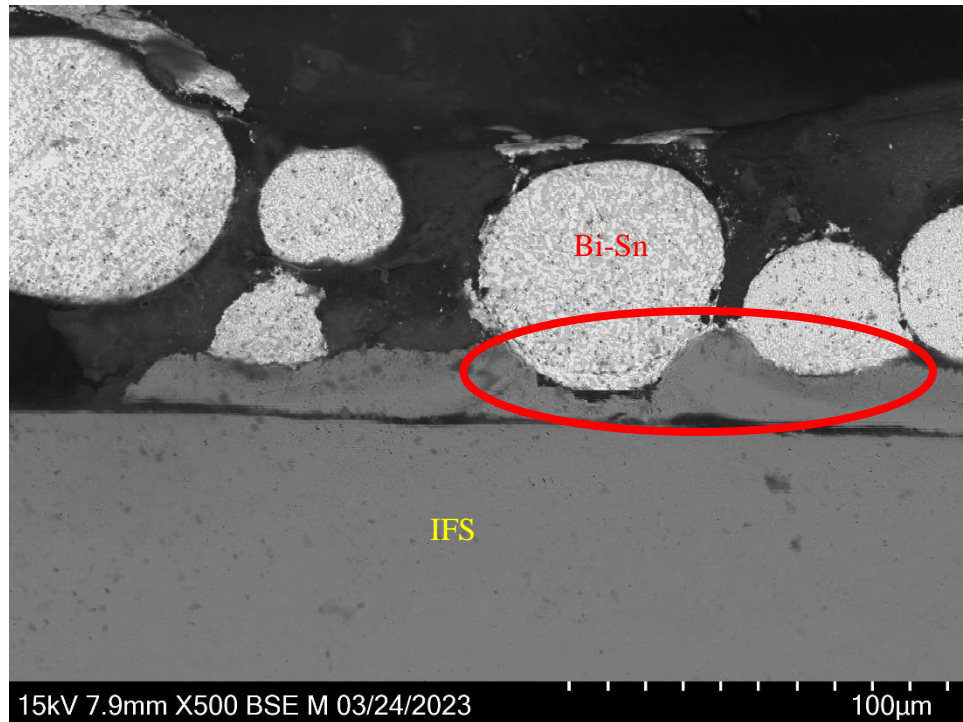


Figure 6. 17 - Digital microscope image at 500x magnification. of a cross-section of Bi-Sn coated onto IFS with a production process using Phosphoric Acid flux. The area circled in red shows signs of good adhesion.

## 6.4 Discussion

NIR heating of the 20 wt% Zn / 80 wt% Bi-Sn coating at 20% NIR power did not render a cohesive matrix, as shown in *figure 6.4*. This agrees with *figure 6.3* which shows that the sample did not reach a temperature much higher than the  $T_M$  of Bi-Sn. Discrete areas of round Bi-Sn are evident, measuring up to only 50  $\mu\text{m}$ , with no encompassing of Zn apparent from *figure 6.4*. The peak temperature reached here is below the benchmark of 180 °C – 220 °C for reflow [164,165]. This is possibly due to the comparatively weak power output not being enough to excite the plasmons on

the surface of the material in order to heat them up to the required temperature [234]. Plasmons are free (conduction band) electrons that occur at the frequency of an incident light (in this case, NIR light). The incident light excites “resonant coherent oscillations” of the plasmons. Plasmonic excitation occurs due to the absorption of the light and leads to a series of “temperature-related phenomena”, resulting in the heating up of the material [234]. Plasmons can lose their energy by emitting a photon or by generating a “hot” electron-hole pair, known as Landau damping [234,235]. This process causes interband and intraband electron transitions in the metal due to the electric field caused by the surface plasmon resonance [236]. These hot electrons have been raised above the Fermi level by absorption of the energy of incident light, described by a model known as the two temperature model (TTM), as described elsewhere [234]. The TTM also describes the heating of the lattice by the hot electrons. The lattice then transfers energy in the form of heat to the environment, leading to a rise in temperature [237]. Goldenberg and Tranter developed a model to describe temperature  $T(\mathbf{r}, t)$  at position  $\mathbf{r}$  outside the heated surface:

$$\rho(\mathbf{r}) c(\mathbf{r}) \frac{\partial T(\mathbf{r}, t)}{\partial t} = K \Delta T(\mathbf{r}, t) + S(\mathbf{r}, t) \quad \text{Equation 6.1}$$

Where  $\rho(\mathbf{r})$  is the mass density,  $c(\mathbf{r})$  is the specific heat,  $K$  is the thermal conductivity (assumed constant for simplicity) and  $S(\mathbf{r}, t)$  is a source term. The source term is a result of the heat generation inside the metal, due to incident light [237]. This can be written as  $S = \sigma_{\text{abs}} I$ , where;  $\sigma_{\text{abs}}$  is the absorption cross section of the particle and  $I$  is the intensity of light [238]. Surface plasmon resonance has been shown to bring about a peak in  $\sigma_{\text{abs}}$  that translates into a peak in temperature increase [239]. Proving that plasmonic theory and plasmonic oscillation are directly linked to

the rise in temperature and that more incident light theoretically means more surface plasmon resonance and thus a larger rise in temperature.

This could be due to colour – NIR works best on darker colour samples, as darker colours absorb more wavelengths of light, with black objects absorbing all wavelengths [240].

An alternative reason could be the crystal structure of any of the components not being optimal for NIR absorption, certain oxides are known to have high absorption rates and are manipulated for this reason, Bi-Sn and Zn are not among these and this could explain the low temperature here [241,242]. However, a slower belt speed showed a better flow and coalescence performance, seen in *figure 6.5*. Regions of Bi-Sn measuring up to approximately 200-250  $\mu\text{m}$  are present, with most regions of Bi-Sn in contact with one and other and appearing to have flowed around Zn regions. A reason for this could be the slower belt speed meaning that the sample spent longer under the NIR heat source, allowing more time for the melting and flowing of Bi-Sn. Although the temperature wasn't measured in this case, it is known that temperature of a metal will rise with more time exposed to a heat source, due to conduction of heat [243,244]. This means that in theory more of the Bi-Sn is able to melt as the temperature rises with time. It has also been noted that Bi exhibits behaviour that show it melting over a temperature range rather than at a defined sharp temperature and, it's possible that with more time under the NIR source that the alloy has been able to melt more fully [245].

The same theory applies to the images shown in *figures 6.7 and 6.8*, showing the microstructures of 20 wt% Zn / 80 wt% Bi-Sn after heat treatment at 30% NIR power at belt speed of 1m/min and 0.5m/min respectively. A higher power has led to a higher temperature, shown in *figure 6.6* to be 298.6 °C - a comparable temperature

to that used across the previous chapters of this work of 245 °C. This was due to a higher density of incident light on the sample leading to more plasmon oscillation, resulting in a higher temperature being reached by the sample [223,234,246]. The microstructure shown in *figure 6.7* shows many melted regions of Bi-Sn measuring up to approximately 250  $\mu\text{m}$  x 100  $\mu\text{m}$ , confirming that a higher temperature has led to a hotter sample and more melting [245]. More time under the heat source, shown in *figure 6.8*, allows yet again for fuller melting and flowing of the Bi-Sn matrix with regions of the melted matrix measuring up to approximately 400-425  $\mu\text{m}$  in diameter, a larger size than previously seen.

When the NIR power is raised above 30%, there is an immediate decline in coalescence, evidenced in *figures 6.10, 6.11, 6.13 and 6.14*. 40% NIR Power at 1m/min leads to a maximum temperature of 493.94 °C, shown in the graph of *figure 6.9*. The corresponding microstructure in *figure 6.10* shows large Bi-Sn regions, as expected from the prevailing trend from 20 and 30% power. These areas are made of several round regions which have fused together to what could be argued is a cohesive matrix, owing to the reasons outlined above around plasmonic oscillation and heat conduction and melting [234,243–245]. However, large black areas are present within the matrix as well as very small Zn powder regions, captured in the Bi-Sn and around it in areas. It should be noted that the temperature reached by the sample is above the melting point of Zn, so there is a possibility that Zn has melted, or entered solid solution or alloyed with the Bi-Sn [109]. The black regions appear to be the mounting resin, as previously stated. The Bi-Sn regions in *figure 6.11* are more discrete while there is much more Zn visibly present. It is a possibility that the Bi-Sn experienced a limiting factor to its thermal performance after a certain temperature due to broadening of possible intermetallic compounds (IMC) while

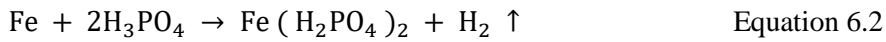
alloying with Zn, as this temperature is above the  $T_M$  of Zn, such a phenomenon has been recorded in other fusible alloys at alloying interfaces with other elements [33].

Microstructures obtained from those samples heated at 50% could be explained the same way, as they reached even higher temperatures; almost 700°C, shown in *figure 6.12*. The regions of Bi-Sn in *figures 6.13* and *6.14* are all discrete and very small, as well as totally separate from any Zn areas. Showing that the temperatures reached at 40% and 50% NIR power are too high for both the adequate heat treatment of the coating and the practicality of industry.

The performance analysis of alternative fluxes showed that Zinc Chloride Flux-treated steel showed good wetting and adhesion of applied Bi-Sn paste, heat treated for 40 mins at 245 °C. This is shown in *figure 6.15* and highlighted by the blue box, which shows that a layer of Sn or possible iron-tin intermetallics, such as  $FeSn_2$ , which is known to form during reflow of tinned steel [233,247,248], has formed at the substrate/coating interface. This is known to happen at temperatures both above and below the melting point of Sn, 232 °C, and up to 496 °C [249]. The formation of  $FeSn_2$  is a diffusion reaction of Sn into Fe or steel which obeys the parabolic rate law [249].  $FeSn_2$  is known to aid corrosion resistance and IMCs in general are known to promote adhesion [51,233,247–249]. Zinc Chloride flux is thought to have promoted this occurrence with surface cleaning and oxidation-resistance properties, and was historically used in tinplate manufacture for these reasons [250]. This gives rise to the cross-section shown in *figure 6.14*, showing good wetting and adhesion.

The same cannot be said for the performance of phosphoric acid flux, shown in *figure 6.16*. The Bi-Sn has not spread across the steel surface and has retained its spherical shape. This is indicative of bad wetting and is a precursor to insufficient

adhesion performance. Orthophosphoric acid has shown to remove oxides on steel surfaces by the equation:



Whereby the acid first reacts with any oxide films formed and then the substrate itself, removing the oxide film causing a shift in a solid/liquid interface from flux/oxide interface with low binding energy to flux/steel interface with high binding energy [121]. This means that the interfacial reaction between the acid and the substrate should promote wetting [121]. However, this isn't the case seen in *figures 6.16 and 6.17*. This could be due to an unsuccessful removal of oxides and therefore a resulting low binding energy [121]. However there does appear to be good wetting and adhesion in the circled red in *figure 6.17* where it appears that circular regions of Bi-Sn have adhered well to abraded areas of the substrate. Hitchcock et al, found that abrasion and roughening of a substrate causes a decrease in wettability unless the substrate is extremely rough [251]. The contact angle was found to increase linearly with the substrate surface texture parameter:

$$R_a / \lambda_a \quad \text{Equation 6.3}$$

Where  $R_a$  is the average amplitude and  $\lambda_a$  is the average wavelength of the surface abrasion texture features [251]. This could be one explanation for the results in *figures 6.16 and 6.17*. This was also proved to be true of Bi-Sn on copper substrates at temperatures above melting point of Bi-Sn, that the wetting angle increases with surface roughness [252]. Contact angles in both the A and B direction,  $\theta_A$  and  $\theta_B$  respectively, shown below in figure 6.18 from [252] both increased with surface roughness.

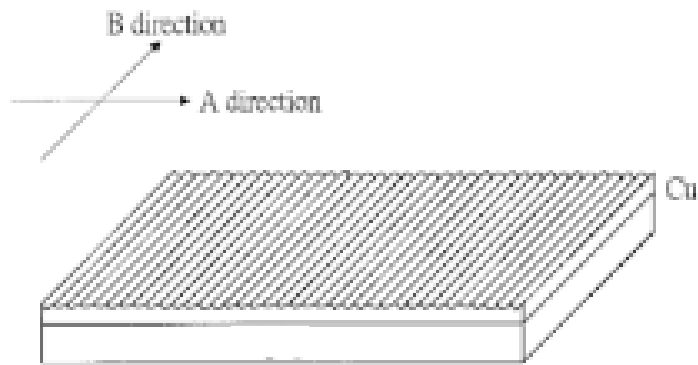


Figure 6. 18 - Schematic diagram of the polished Cu substrate from [161].

It was shown that the effect of the substrate surface geometry is dominant as Bi-Sn wets the abraded substrate, the contact angle hysteresis is enhanced when a surface is rough and the contact angle does not reduce unless the energy of IMC formation between the substrate and the Bi-Sn can overcome the barriers of the hysteresis [252]. Therefore, the geometry of the rough surface and the contact angle hysteresis cause the wetting to increase with the surface roughness and this could be an explanation of the microstructure in *figure 6.17* [252].

## 6.5 Conclusions

In this chapter, alternatives were considered for two facets of the novel Bi-Sn + Zn coating production process.

Firstly, Near-Infrared (NIR) heating was used to determine the potential of rapid heat treatment of the coating, as opposed to the furnace heat treatment optimised in *section 3.4.2*. Changeable variables were NIR power percentage and belt speed; several different parameter combinations were tested, and the resultant

microstructures analysed.

Secondly, two alternative fluxes were used in the production process in place of the Zinc Ammonium Chloride introduced in *sections 2.2.1 and 3.1*. The fluxes investigated were Zinc Chloride Flux and Phosphoric Acid Flux and were used to coat 100Bi-Sn on to a steel substrate. This section employed the standard heat treatment using a furnace at 245 °C, as in *section 3.4.2*. The cross-sectional microstructure of the coated steel was then analysed for wetting and interfacial adhesion.

Conclusions reached from this chapter are as follows:

- NIR heat treatment at 30% NIR Power with belt speed of 0.5m/min showed the best heat treatment of the tested parameters. Several large areas of flowed and coalesced Bi-Sn surrounding Zn regions were visible.
- The method of NIR heating is thought to be via plasmonic oscillation due to incident NIR waves. This is thought to be resulting in the heating of the lattice of the metal and a rise in temperature correlating from a rise in intensity in light incident on the surface.
- NIR powers of 40% and 50% rendered unsatisfactory results, with less coalescence of Bi-Sn and much less Zn visible, possibly owing to heating above the  $T_M$  of Zn. A reason postulated for this is a limiting factor in the thermal performance of Bi-Sn at a certain temperature owing to broadening of potential IMCs.
- Zinc Chloride Flux facilitated good wetting of the Bi-Sn to the steel substrate, owing to the possible development of an  $FeSn_2$  inter-metallic layer at the coating substrate interface due to diffusion of Sn into Fe. This has been historically noted in the reflow process of tinplate.



- Phosphoric Acid Flux does not show good wetting of the Bi-Sn to the steel and no facilitation of an inter-metallic layer. This is possibly due to the roughness of the samples used in all 3 repeats per test, as it has been shown that increase in roughness causes an increase in contact angle. However, it is also possible that the flux has not fully removed oxides from the surface leading to low binding energy between the coating and substrate and promoting bad wetting and adhesion.

# Chapter 7 : Conclusions and Further Work

## 7.1 Conclusions

Several conclusions have been made from the work put forward in this thesis. These conclusions are outlined in this chapter, along with suggestions for further work.

The development process for the production of a Bi-Sn + Zn low-temperature corrosion resistant coating for use on steel substrates was analysed and optimised. It was found that varying Zn loading led to an obvious variation in microstructure, with 20 wt% Zn and 80 wt% Bi-Sn showing the best flowing and coalescence of the Bi-Sn regions into a matrix. Zn additions below this amount were shown to offer an undesired microstructure, with Bi-Sn and Zn totally segregated. The addition of Zn above 20 wt% produced a granular and powdery microstructure, unsuitable for the application.

Time and temperature variation led to promising results; samples heated to 245 °C offered good microstructural results. Time increase brought about more favourable results, with images showing the growth of the Bi-Sn matrix as time increased, with a coarsening of Bi-Sn regions apparent. This showed that time of heat treatment was of importance. Ultimately the 20 wt% Zn / 80 wt% Bi-Sn sample heated at 245 °C for 45 minutes showed a microstructure of Zn islands in a Bi-Sn matrix, akin to a ZRP with Bi-Sn replacing the binder. 245 °C is a lower temperature than that used in traditional HDG and will allow for more flexibility in application – whether on site at a production facility or in-situ in industry.

Further tests were conducted for academic purposes in Chapter 3. Heating the coating for 24 hours showed coalescence of the Bi-Sn phase to surround Zn regions. The Bi-Sn regions were slightly larger than those in the 45 minute sample mentioned above. Heating the constituents to 480 °C to allow for melting of Zn and the creation of a Bi-Sn-Zn alloy showed a microstructure of a Bi-Sn matrix interspersed with

large Zn flakes. Further work to test this alloy in terms of corrosion and mechanical performance would determine the trade-off between logistical viability and performance.

Corrosion tests were carried out on several Bi-Sn + Zn coatings. All Zn containing coatings of 20 wt% Zn and above showed good galvanic protection of steel under SVET testing over 24 hours in 1%NaCl electrolyte. 10 wt% Zn coating and 100 wt% Bi-Sn coating did not offer a good corrosion performance with coupling on the coating and on the steel substrate visible. Mass loss for the 20 wt% Zn/ 80 wt% Bi-Sn coating was calculated and showed better performance than other coatings used in industry. LPR values dispute this however, with lower values than those found in literature gleaned in all repeats.

ZRA tests confirmed that 20 wt% Zn coating offered galvanic protection to a steel substrate over 24 hours. A galvanic couple of steel and 100 wt% Bi-Sn showed an interesting relationship, with very little current flow at all. The reason for this was investigated by conducting cathodic sweeps of the two materials. The results showed that the Bi-Sn remained passive over a larger range of potentials than steel, meaning it is a poor cathode and thus steel dominates the cathodic reaction within the Bi-Sn + Zn coating system.

Testing of mechanical properties was carried out in Chapter 5. An increase in Zn content showed no effect on Vickers hardness values for samples heat treated for 20 and 40 minutes respectively. This is proof that the coating created was not an alloy, as alloying with Zn is known to increase hardness. Vickers hardness values were low in general, thought to be due to the soft nature of Bi-Sn and the powder state of the Zn added, offering no extra resistance to deformation.

Adhesion testing was carried out via OT method. It was found that 20 wt% Zn showed good adhesion with no cracks or flaking, and no signs of delamination or damage. 30 wt% exhibited poor adhesion performance, with cracks across the width of the coating, with many intersecting and joining. There was also evidence of delamination at the bend site.

The wetting of Bi-Sn and Zn was investigated. This was undertaken to explain the lack of Bi-Sn flow around Zn islands seen in some samples in Chapter 3. A poor wetting angle of 129.17 ° was shown between a droplet of Bi-Sn and a pre-heated

sheet section of Zn. Poor wetting of coating constituents is postulated as one reason for poor flow of Bi-Sn to envelope Zn regions.

NIR heating of 20 wt% Zn / 80 wt% Bi-Sn was explored as an alternative heat treatment method. Various power and belt speeds were tested to find the optimal performance and temperatures were logged using a thermocouple. 30% NIR power with a belt speed of 0.5 m/min showed the best heat treatment of the sample, many large regions of flowed and coalesced Bi-Sn were apparent, surround Zn islands. It was postulated that plasmonic oscillation due to incident NIR waves is the method of NIR heating. Samples heated at NIR powers of 40% and 50% showed little coalescence and were deemed unsatisfactory, possibly due to temperatures above those of Zn's melting point.

Zinc Chloride flux offered good wetting of Bi-Sn to steel, with the suspected development of an  $\text{FeSn}_2$  intermetallic layer promoting adhesion. Phosphoric acid flux did not offer good wetting performance, possibly due to the roughness of the substrate increasing wetting angle or poor fluxing and incomplete removal of oxides.

Overall, a coating of 20 wt%Zn / 80 wt% Bi-Sn was developed that exhibited good performance across all aspects of investigation: corrosion, adhesion, hardness and microstructure at low temperature, with a microstructural development process detailed. This coating shows potential for use as a flexible low-temperature application coating for the protection of steel substrates and potentially the repair of failed HDG components.

## **7.2 Future Work**

Future work in this field of study could take on many aspects of research. The following are suggestions on possible routes forward.

- Investigation of the effect of longer heat treatments on corrosion and mechanical properties to understand what the optimal heat treatment time is.
- Investigation of the corrosion performance of a Bi-Sn-20Zn alloy to assess if alloying could produce a new powder coating if this was ground up and made into a slurry..
- Performance of 20 wt%Zn / 80 wt% Bi-Sn in different environmental atmospheres around the world. This would show the effect of changes in

environment on the coating, allowing for broader applications as a result.

- Characterisation of Bi-Sn + Zn corrosion products using SEM, XRD etc. to fully understand the chemistry of the coating.
- Further investigation into the issue of Bi-Sn flow in a novel Bi-Sn + Zn coating to facilitate a consistent microstructure
- Investigation of lower Zn levels in a Bi-Sn + Zn coating, discover lower limit of Zn for performance.
- Perform experiments on industrial benchmarks to understand where the novel coating sits in terms of overall performance.
- Wetting investigation of Bi-Sn + Zn coating to steel substrate to give a comprehensive analysis of adhesion performance and likelihood of wear for use with GSE.

# Chapter 8

## References

1. Allied Market Research. Ground Support Equipment Market by Type (Powered GSE and Non-powered GSE), Application (Aircraft Handling, Passenger Handling, and Cargo Handling), and Power Source (Electric, Non-Electric, and Hybrid): Global Opportunity Analysis and Industry Forecast, 2 [Internet]. New Castle, DE; 2020. Available from: <https://marketpublishers.com/r/GF288839789EN.html>
2. Alruwaili M, Cipcigan L. Airport electrified ground support equipment for providing ancillary services to the grid. *Electr Power Syst Res* [Internet]. Elsevier B.V.; 2022;211:108242. Available from: <https://doi.org/10.1016/j.epsr.2022.108242>
3. Tabuchi H. Many Major Airports Are Near Sea Level. A Disaster in Japan Shows What Can Go Wrong. [Internet]. New York Times. 2018. p. 1. Available from: <https://www.nytimes.com/2018/09/07/climate/airport-global-warming-kansai.html>
4. White WJ. Corrosion Control For Aircraft - US Department of Transportation Advisory Circular [Internet]. Washington, D.C.; 1991. Available from: [https://www.faa.gov/documentlibrary/media/advisory\\_circular/ac\\_43-4a\\_.pdf](https://www.faa.gov/documentlibrary/media/advisory_circular/ac_43-4a_.pdf)
5. Diler AA, Gürgen S, Sert A. Failure analysis of an axle shaft in an airport ground support vehicle. *Proc Inst Mech Eng Part L J Mater Des Appl* [Internet]. 2023;237:925–40. Available from: <https://journals.sagepub.com/doi/10.1177/14644207221130316>
6. Thaxton EA. NASA Technical Report: Facility Systems, Ground Support Systems, and Ground Support Equipment General Design Requirements [Internet]. 2014. Available from: <https://ntrs.nasa.gov/api/citations/20150001362/downloads/20150001362.pdf>
7. Tang Z. A review of corrosion inhibitors for rust preventative fluids. *Curr Opin Solid State Mater Sci* [Internet]. Elsevier; 2019;23:100759. Available from: <https://doi.org/10.1016/j.cossms.2019.06.003>
8. Chatterjee UK, Bose SK, Roy SK. Environmental Degradation of Metals [Internet]. CRC Press; 2001. Available from: <https://www.taylorfrancis.com/books/9781482292244>
9. Trabanelli G, Carassiti V. Mechanism and Phenomenology of Organic Inhibitors. *Adv Corros Sci Technol* [Internet]. Boston, MA: Springer US; 1970. p. 147–228. Available from: [http://link.springer.com/10.1007/978-1-4615-8252-6\\_3](http://link.springer.com/10.1007/978-1-4615-8252-6_3)
10. François R, Khan I, Dang VH. Impact of corrosion on mechanical properties of steel embedded in 27-year-old corroded reinforced concrete beams. *Mater Struct* [Internet]. 2013;46:899–910. Available from: <https://doi.org/10.1617/s11527-012-9941-z>
11. Li L, Mahmoodian DM, Li CQ. Maintenance, Safety, Risk, Management and

Life-Cycle Performance of Bridges [Internet]. Powers N, Frangopol DM, Al-Mahaidi R, Caprani C, editors. CRC Press; 2018. Available from: <https://doi.org/10.1201/9781315189390>

12. Zhu W. Effect of corrosion on the mechanical properties of the corroded reinforcement and the residual structural performance of the corroded beams [Internet]. National Institute of Applied Sciences of Toulouse; 2015. Available from: <https://theses.hal.science/tel-01222175v1>

13. Wu H, Lei H, Chen YF, Qiao J. Comparison on corrosion behaviour and mechanical properties of structural steel exposed between urban industrial atmosphere and laboratory simulated environment. *Constr Build Mater* [Internet]. Elsevier Ltd; 2019;211:228–43. Available from: <https://doi.org/10.1016/j.conbuildmat.2019.03.207>

14. Koch G, Varney J, Thompson N, Moghissi O, Gould M, Payer J. NACE IMPACT: International Measures of Prevention, Application, and Economics of Corrosion Technologies Study [Internet]. Houston, TX; 2016. Available from: <http://impact.nace.org/documents/Nace-International-Report.pdf>

15. Marder AR. The metallurgy of zinc-coated steel. *Prog Mater Sci* [Internet]. 2000;45:191–271. Available from: [https://doi.org/10.1016/S0079-6425\(98\)00006-1](https://doi.org/10.1016/S0079-6425(98)00006-1)

16. Fratesi R, Ruffini N, Malavolta M, Bellezze T. Contemporary use of Ni and Bi in hot-dip galvanizing. *Surf Coatings Technol* [Internet]. 2002;157:34–9. Available from: [https://doi.org/10.1016/S0257-8972\(02\)00137-8](https://doi.org/10.1016/S0257-8972(02)00137-8)

17. Abdou MI, Fadl AM. Assessment of nano-FeTiO<sub>3</sub> / non crystalline silica cold galvanizing composite coating as a duplex corrosion guard system for steel electricity transmission towers in severe aggressive media. *Constr Build Mater* [Internet]. Elsevier Ltd; 2019;223:705–23. Available from: <https://doi.org/10.1016/j.conbuildmat.2019.07.017>

18. Al-sabagh AM, Abdou MI, Migahed MA, Fadl AM, El-shahat MF. Influence of surface modified nanoilmeneite / amorphous silica composite particles on the thermal stability of cold galvanizing coating. *Egypt J Pet* [Internet]. Egyptian Petroleum Research Institute; 2018;27:137–44. Available from: <https://doi.org/10.1016/j.ejpe.2017.02.002>

19. Meroufel A, Touzain S. EIS characterisation of new zinc-rich powder coatings. *Prog Org Coatings* [Internet]. 2007;59:197–205. Available from: <https://doi.org/10.1016/j.porgcoat.2006.09.005>

20. Wint N, Wijesinghe SL, Yan W, Ong WK, Wu LY, Williams G, et al. The Sacrificial Protection of Steel by Zinc-Containing Sol-Gel Coatings. *J Electrochem Soc* [Internet]. 2019;166:C434–44. Available from: <https://iopscience.iop.org/article/10.1149/2.1071913jes>

21. Chavan NM, Kiran B, Jyothirmayi A, Phani PS, Sundararajan G. The Corrosion Behavior of Cold Sprayed Zinc Coatings on Mild Steel Substrate. *J Therm Spray Technol* [Internet]. 2013;22:463–70. Available from: <https://doi.org/10.1007/s11666-013-9893-z>

22. Fedrizzi L, Rodriguez FJ, Rossi S, Deflorian F, Maggio R Di, Metalurgica DI, et al. The use of electrochemical techniques to study the corrosion behaviour of organic

- coatings on steel pretreated with sol – gel zirconia films. 2001;46:3715–24. Available from: [https://doi.org/10.1016/S0013-4686\(01\)00653-3](https://doi.org/10.1016/S0013-4686(01)00653-3)
23. Livelli G, Langill T. Guidelines for welding Galvanized Steel. PCI J [Internet]. 1998;43:40–8. Available from: <https://doi.org/10.15554/pcij.05011998.40.48>
  24. Nakamura S, Suzumura K. Experimental Study on Repair Methods of Corroded Bridge Cables. J Bridg Eng [Internet]. 2012;17:720–7. Available from: [https://doi.org/10.1061/\(asce\)be.1943-5592.0000299](https://doi.org/10.1061/(asce)be.1943-5592.0000299)
  25. Bierwagen G, Allahar K, Hinderliter B, Jung H. Zn-rich Coatings Revisited. Tri-Service Corros Conf [Internet]. 2007; Available from: [https://www.researchgate.net/publication/242550538\\_Zn-rich\\_Coatings\\_Revisited](https://www.researchgate.net/publication/242550538_Zn-rich_Coatings_Revisited)
  26. Twite RL, Bierwagen GP. Review of alternatives to chromate for corrosion protection of aluminum aerospace alloys. Prog [Internet]. 1998;33:91–100. Available from: [https://doi.org/10.1016/S0300-9440\(98\)00015-0](https://doi.org/10.1016/S0300-9440(98)00015-0)
  27. Marson F. Zinc Dust Pigmented Paints. In: Francis RA, editor. Inorg ZINC COATINGS Hist Chem Prop Appl Altern [Internet]. 1st ed. Preston, Australia: Australian Corrosion Association; 1997. p. 105–10. Available from: <https://shorturl.at/kViJf>
  28. Khanna AS. Key issues in applying organic paint coatings [Internet]. High-Performance Org. Coatings. Woodhead Publishing Limited; 2008. Available from: <https://dx.doi.org/10.1533/9781845694739.1.3>
  29. Cao X, Huang F, Huang C, Liu J, Cheng YF. Preparation of graphene nanoplate added zinc-rich epoxy coatings for enhanced sacrificial anode-based corrosion protection. Corros Sci [Internet]. Elsevier; 2019;159:108120. Available from: <https://doi.org/10.1016/j.corsci.2019.108120>
  30. Francis RA, Szokolik A. A Comparison of the Corrosion Behaviour of Inorganic Zinc and Conventionally-Coated Bridges. Corros Prev [Internet]. 2000;172–80. Available from: [https://www.academia.edu/16979240/A\\_Comparison\\_Of\\_The\\_Corrosion\\_Behaviour\\_Of\\_Inorganic\\_Zinc\\_And\\_Conventionally\\_Coated\\_Bridges](https://www.academia.edu/16979240/A_Comparison_Of_The_Corrosion_Behaviour_Of_Inorganic_Zinc_And_Conventionally_Coated_Bridges)
  31. Balberg I. Percolation Theory and Its Application in Electrically Conducting Materials. Semicond Polym Compos Princ Morphol Prop Appl [Internet]. 2013;145–69. Available from: <https://doi.org/10.1002/9783527648689.ch5>
  32. Kotadia HR, Howes PD, Mannan SH. A review: On the development of low melting temperature Pb-free solders. Microelectron Reliab [Internet]. Elsevier Ltd; 2014;54:1253–73. Available from: <http://dx.doi.org/10.1016/j.microrel.2014.02.025>
  33. Chen CH, Yang CL, Chuang TH. Intermetallic growth and thermal impedance at the In<sub>32.5</sub>Bi<sub>16.5</sub>Sn/Cu interface. J Alloys Compd [Internet]. Elsevier; 2023;936:168309. Available from: <https://doi.org/10.1016/j.jallcom.2022.168309>
  34. Liu Y, Tu KN. Low melting point solders based on Sn , Bi , and In elements. Mater Today Adv [Internet]. 2020; Available from: <https://doi.org/10.1016/j.mtadv.2020.100115>
  35. Sakuyama S, Akamatsu T, Uenishi K, Sato T. Effects of a Third Element on Microstructure and Mechanical Properties of Eutectic Sn-Bi Solder. Trans Japan Inst



- Electron Packag [Internet]. 2009;2:98–103. Available from: [http://www.jstage.jst.go.jp/article/jiepeng/2/1/2\\_1\\_98/\\_article](http://www.jstage.jst.go.jp/article/jiepeng/2/1/2_1_98/_article)
36. Okamoto H. Bi-Sn (bismuth-tin). J Phase Equilibria Diffus [Internet]. 2010;31:205. Available from: <https://doi.org/10.1007/s11669-010-9659-y>
  37. Kang SK, Buchwalter S, Tsang C. Characterization of electroplated bismuth-tin alloys for electrically conducting materials. J Electron Mater [Internet]. 2000;29:1278–83. Available from: <https://doi.org/10.1007/s11664-000-0025-4>
  38. Li JF, Mannan SH, Clode MP, Whalley DC, Hutt DA. Interfacial reactions between molten Sn–Bi–X solders and Cu substrates for liquid solder interconnects. Acta Mater [Internet]. 2006;54:2907–22. Available from: <https://doi.org/10.1016/j.actamat.2006.02.030>
  39. Yeomans SR. Galvanized Reinforcement: Recent Developments and New Opportunities. 5th Int fib Congr [Internet]. 2018; Available from: <https://www.researchgate.net/publication/328303325>
  40. Hosking NC, Ström MA, Shipway PH, Rudd CD. Corrosion resistance of zinc-magnesium coated steel. Corros Sci [Internet]. 2007;49:3669–95. Available from: <https://doi.org/10.1016/j.corsci.2007.03.032>
  41. Gergely A, Pászti Z, Mihály J, Drotár E, Török T. Galvanic function of zinc-rich coatings facilitated by percolating structure of the carbon nanotubes . Part II : Protection properties and mechanism of the hybrid coatings. Prog Org Coatings [Internet]. Elsevier B.V.; 2014;77:412–24. Available from: <http://dx.doi.org/10.1016/j.porgcoat.2013.11.004>
  42. Kirkpatrick S. Percolation and Conduction. Rev Mod Phys [Internet]. 1973;45:574–88. Available from: <https://doi.org/10.1103/RevModPhys.45.574>  
url:<http://dx.doi.org>
  43. Pourbaix M. Thermodynamics and corrosion. Corros Sci [Internet]. 1990;30. Available from: [https://doi.org/10.1016/0010-938X\(90\)90205-J](https://doi.org/10.1016/0010-938X(90)90205-J)
  44. Rivetti M, Neto J, de Amarim Junior N, Ribeiro DV. Corrosion inhibitors for reinforced concrete. Corros Inhib Princ Recent Appl [Internet]. 2018. p. 35–58. Available from: <https://doi.org/10.5772/intechopen.72772>
  45. McCafferty E. Thermodynamics of Corrosion: Pourbaix Diagrams. Introd to Corros Sci [Internet]. 2009. p. 95–117. Available from: [https://doi.org/10.1007/978-1-4419-0455-3\\_6](https://doi.org/10.1007/978-1-4419-0455-3_6)
  46. Wagner C, Traud W. On the Interpretation of Corrosion Processes Through the Superposition of Electrochemical Partial Processes and on the Potential of Mixed Electrodes. Corros Sci [Internet]. 2006;62:843–55. Available from: <https://doi.org/10.5006/1.3279894>
  47. Tafel J. Über die Polarisation bei kathodischer Wasserstoffentwicklung. Zeitschrift für Phys Chemie [Internet]. 1905;50U:641–712. Available from: <https://doi.org/10.1515/zpch-1905-5043>
  48. Burstein GT. A hundred years of Tafel's Equation: 1905-2005. Corros Sci [Internet]. 2005;47:2858–70. Available from: <https://doi.org/10.1016/j.corsci.2005.07.00>

49. PlamSens. Tafel Plot and Evans Eiaogram [Internet]. 2020. Available from: <https://www.palmsenscorrosion.com/knowledgebase/tafel-plot-and-evans-diagram/>
50. Chakraborty A, Govardhana P, Mondal A, Laha T, Dutta M, Singh SB. Microstructural development of prior nickel coated hot dipped galvanised coatings. *J Alloys Compd* [Internet]. Elsevier B.V; 2017;699:648–56. Available from: <http://dx.doi.org/10.1016/j.jallcom.2016.12.354>
51. Sarkar K, Mondal A, Chakraborty A, Sanbui M, Rani N, Dutta M. Investigation of microstructure and corrosion behaviour of prior nickel deposited galvanised steels. *Surf Coat Technol* [Internet]. Elsevier; 2018;348:64–72. Available from: <https://doi.org/10.1016/j.surfcoat.2018.05.036>
52. Mondal A, Halder AK, Dutta M. Effect of Al on phase evolution in Prior-Ni coated galvanized steel : Thermodynamic and kinetic assessment. *J Alloys Compd* [Internet]. Elsevier B.V; 2020;830:154351. Available from: <https://doi.org/10.1016/j.jallcom.2020.154351>
53. Malla AD, Sullivan J, Goldsworthy M, Britton D, Mills C, Challinor C. The effect of coating thickness on the surface corrosion of zinc-aluminium-magnesium coatings on steel. *GALVATECH 2023* [Internet]. 2023. p. 175–84. Available from: [https://www.researchgate.net/publication/374921237\\_THE\\_EFFECT\\_OF\\_COATING\\_THICKNESS\\_ON\\_THE\\_SURFACE\\_CORROSION\\_OF\\_ZINC-\\_ALUMINIUM-MAGNESIUM\\_COATINGS\\_ON\\_STEEL](https://www.researchgate.net/publication/374921237_THE_EFFECT_OF_COATING_THICKNESS_ON_THE_SURFACE_CORROSION_OF_ZINC-_ALUMINIUM-MAGNESIUM_COATINGS_ON_STEEL)
54. Sullivan J, Mehraban S, Elvins J. In situ monitoring of the microstructural corrosion mechanisms of zinc-magnesium-aluminium alloys using time lapse microscopy. *Corros Sci* [Internet]. Elsevier Ltd; 2011;53:2208–15. Available from: <http://dx.doi.org/10.1016/j.corsci.2011.02.043>
55. Sullivan J, Cooze N, Gallagher C, Lewis T, Prosek T, Thierry D. In situ monitoring of corrosion mechanisms and phosphate inhibitor surface deposition during corrosion of zinc-magnesium-aluminium (ZMA) alloys using novel time-lapse microscopy. *Faraday Discuss* [Internet]. Royal Society of Chemistry; 2015;180:361–79. Available from: <http://dx.doi.org/10.1039/C4FD00251B>
56. Prosek T, Persson D, Stoulil J, Thierry D. Composition of corrosion products formed on Zn-Mg, Zn-Al and Zn-Al-Mg coatings in model atmospheric conditions. *Corros Sci* [Internet]. Elsevier Ltd; 2014;86:231–8. Available from: <http://dx.doi.org/10.1016/j.corsci.2014.05.016>
57. Salgueiro Azevedo M, Allély C, Ogle K, Volovitch P. Corrosion mechanisms of Zn(Mg,Al) coated steel: 2. The effect of Mg and Al alloying on the formation and properties of corrosion products in different electrolytes. *Corros Sci* [Internet]. Elsevier Ltd; 2015;90:482–90. Available from: <http://dx.doi.org/10.1016/j.corsci.2014.07.042>
58. Schuerz S, Fleischanderl M, Luckeneder GH, Preis K, Haunschmied T, Mori G, et al. Corrosion behaviour of Zn-Al-Mg coated steel sheet in sodium chloride-containing environment. *Corros Sci* [Internet]. Elsevier Ltd; 2009;51:2355–63. Available from: <http://dx.doi.org/10.1016/j.corsci.2009.06.019>
59. Thierry D, Persson D, Luckeneder G, Stellnberger KH. Atmospheric corrosion of ZnAlMg coated steel during long term atmospheric weathering at different

- worldwide exposure sites. *Corros Sci* [Internet]. Elsevier; 2019;148:338–54. Available from: <https://doi.org/10.1016/j.corsci.2018.12.033>
60. Volovitch P, Vu TN, Allély C, Abdel Aal A, Ogle K. Understanding corrosion via corrosion product characterization: II. Role of alloying elements in improving the corrosion resistance of Zn-Al-Mg coatings on steel. *Corros Sci* [Internet]. 2011;53:2437–45. Available from: <https://doi.org/10.1016/j.corsci.2011.03.016>
61. Duchoslav J, Arndt M, Keppert T, Luckeneder G, Stifter D. XPS investigation on the surface chemistry of corrosion products on ZnMgAl-coated steel. *Anal Bioanal Chem* [Internet]. 2013;405:7133–44. Available from: <https://doi.org/10.1007/s00216-013-7099-3>
62. Wint N, Malla AD, Cooze N, Savill T, Mehraban S, Dunlop T, et al. The ability of Mg<sub>2</sub>Ge crystals to behave as ‘smart release’ inhibitors of the aqueous corrosion of Zn-Al-Mg alloys. *Corros Sci* [Internet]. 2021;179. Available from: <https://doi.org/10.1016/j.corsci.2020.109091>
63. Salgueiro Azevedo M, Allély C, Ogle K, Volovitch P. Corrosion mechanisms of Zn(Mg, Al) coated steel in accelerated tests and natural exposure: 1. The role of electrolyte composition in the nature of corrosion products and relative corrosion rate. *Corros Sci* [Internet]. Elsevier Ltd; 2015;90:472–81. Available from: <http://dx.doi.org/10.1016/j.corsci.2014.05.014>
64. Qiao D, Wang S, Ning P, Liu Q, Chen N, Wang J, et al. Corrosion resistance of zinc-magnesium-aluminium alloy coated steel in marine atmospheric environments. *Int J Electrochem Sci* [Internet]. Elsevier B.V.; 2024;19:100705. Available from: <https://doi.org/10.1016/j.ijoes.2024.100705>
65. Powell SM, McMurray HN, Worsley DA. Use of the scanning reference electrode technique for the evaluation of environmentally friendly, nonchromate corrosion inhibitors. *Corrosion* [Internet]. 1999;55:1040–51. Available from: <https://doi.org/10.5006/1.3283941>
66. Aramaki K. Inhibition effects of chromate-free, anion inhibitors on corrosion of zinc in aerated 0.5 M NaCl. *Corros Sci* [Internet]. 2001;43:591–604. Available from: [https://doi.org/10.1016/S0010-938X\(00\)00085-8](https://doi.org/10.1016/S0010-938X(00)00085-8)
67. Simões AM, Torres J, Picciochi R, Fernandes JCS. Corrosion inhibition at galvanized steel cut edges by phosphate pigments. *Electrochim Acta* [Internet]. 2009;54:3857–65. Available from: <https://doi.org/10.1016/j.electacta.2009.01.065>
68. Zin IM, Lyon SB, Pokhmurskii VI. Corrosion control of galvanized steel using a phosphate/calcium ion inhibitor mixture. *Corros Sci* [Internet]. 2003;45:777–88. Available from: [https://doi.org/10.1016/S0010-938X\(02\)00130-0](https://doi.org/10.1016/S0010-938X(02)00130-0)
69. Wint N, Eaves D, Williams G, McMurray HN. The use of anion exchange pigments to inhibit the filiform corrosion of zinc-aluminium-magnesium coated steel. *Corros Sci* [Internet]. Elsevier Ltd; 2021;193:109886. Available from: <https://doi.org/10.1016/j.corsci.2021.109886>
70. McMurray HN, Williams G. 2. 14 Under Film / Coating Corrosion. Shrier’s *Corros* [Internet]. 2010;2:988–1004. Available from: <https://doi.org/10.1016/B978-044452787-5.00040-8>

71. Bautista A. Filiform corrosion in polymer-coated metals. *Prog Org Coatings* [Internet]. 1996;28:49–58. Available from: [https://doi.org/10.1016/0300-9440\(95\)00555-2](https://doi.org/10.1016/0300-9440(95)00555-2)
72. Hussain AK, Seetharamaiah N, Pichumani M, Chakra CS. Research progress in organic zinc rich primer coatings for cathodic protection of metals – A comprehensive review. *Prog Org Coatings* [Internet]. Elsevier B.V.; 2021;153:106040. Available from: <https://doi.org/10.1016/j.porgcoat.2020.106040>
73. Cheng L, Luo Y, Ma S, Guo W, Wang X. Corrosion resistance of inorganic zinc-rich coating reinforced by Ni-coated coal fly ash. *J Alloys Compd* [Internet]. Elsevier B.V.; 2019;786:791–7. Available from: <https://doi.org/10.1016/j.jallcom.2019.01.368>
74. Liu D, Li QF, Li CH, Xue LL. Improvement of MIC Behavior of Low Alloy Steel with Zn-Rich Epoxy Coating. *Key Eng Mater* [Internet]. 2007;348–349:509–12. Available from: <https://doi.org/10.4028/www.scientific.net/kem.348-349.509>
75. Helsel J, Lanterman R, Wissmar K. EXPECTED SERVICE LIFE AND COST CONSIDERATIONS FOR MAINTENANCE AND NEW CONSTRUCTION PROTECTIVE COATING WORK. *Corrosion* [Internet]. Houston, TX: NACE International; 2008. Available from: <https://onepetro.org/NACECORR/proceedings-abstract/CORR08/All-CORR08/NACE-08279/118853>
76. Cubides Y, Su SS, Castaneda H. Influence of zinc content and chloride concentration on the corrosion protection performance of zinc-rich epoxy coatings containing carbon nanotubes on carbon steel in simulated concrete pore environments. *Corrosion* [Internet]. 2016;72:1397–423. Available from: <https://doi.org/10.5006/2104>
77. Park SM, Shon MY. Effects of multi-walled carbon nano tubes on corrosion protection of zinc rich epoxy resin coating. *J Ind Eng Chem* [Internet]. The Korean Society of Industrial and Engineering Chemistry; 2015;21:1258–64. Available from: <http://dx.doi.org/10.1016/j.jiec.2014.05.042>
78. Feliu S. J, Morcillo M, Feliu S. Deterioration of cathodic protection action of zinc-rich paint coatings in atmospheric exposure. *Corrosion* [Internet]. 2001;57:591–7. Available from: <https://doi.org/10.5006/1.3290386>
79. Sun W, Xing C, Tang X, Zuo Y, Tang Y, Zhao X. Comparative study on the degradation of a zinc-rich epoxy primer/acrylic polyurethane coating in different simulated atmospheric solutions. *J Coatings Technol Res* [Internet]. Springer US; 2021;18:397–413. Available from: <https://doi.org/10.1007/s11998-020-00410-8>
80. Izquierdo M, Nóvoa XR, Pena G, Espada L. The Mechanism of Protection of Zinc-Rich Inorganic Coatings. A Study Based on Electrochemical Impedance Spectroscopy (EIS). *Mater Sci Forum* [Internet]. 1992;111–112:257–68. Available from: <https://doi.org/10.4028/www.scientific.net/msf.111-112.257>
81. Weinell CE, Rasmussen SN. Advancement in Zinc Rich Epoxy Primers for Corrosion Protection. *Corros 2007* [Internet]. Nashville, TN.; 2007. p. 1–13. Available from: <https://doi.org/10.5006/C2007-07007>
82. Feliu S, Barajas R, Bastidas JM, Morcillo M. Mechanism of cathodic protection of zinc-rich paints by electrochemical impedance spectroscopy. I. Galvanic stage. *J*

Coatings Technol. 1989;61:63–9.

83. Ding R, Zheng Y, Yu H, Li W, Wang X, Gui T. Study of water permeation dynamics and anti-corrosion mechanism of graphene/zinc coatings. *J Alloys Compd* [Internet]. Elsevier B.V; 2018;748:481–95. Available from: <https://doi.org/10.1016/j.jallcom.2018.03.160>

84. Bastos AC, Zheludkevich ML, Ferreira MGS. A SVET investigation on the modification of zinc dust reactivity. *Prog Org Coatings* [Internet]. 2008;63:282–90. Available from: <https://doi.org/10.1016/j.porgcoat.2008.01.013>

85. Xu L, Liu F, Wang Z, Ke W, Han EH, Jie G, et al. The effect of surface modification of zinc particles with phosphoric acid on the corrosion resistance of cold galvanizing coatings. *Prog Org Coatings* [Internet]. Elsevier; 2018;114:90–101. Available from: <https://doi.org/10.1016/j.porgcoat.2017.10.011>

86. Bastos AC, Zheludkevich ML, Klüppel I, Grundmeier G, Ferreira MGS. Modification of zinc powder to improve the corrosion resistance of weldable primers. *Prog Org Coatings* [Internet]. Elsevier B.V.; 2010;69:184–92. Available from: <http://dx.doi.org/10.1016/j.porgcoat.2010.04.021>

87. Yun TH, Park JH, Kim JS, Park JM. Effect of the surface modification of zinc powders with organosilanes on the corrosion resistance of a zinc pigmented organic coating. *Prog Org Coatings* [Internet]. Elsevier B.V.; 2014;77:1780–8. Available from: <http://dx.doi.org/10.1016/j.porgcoat.2014.06.008>

88. Plueddemann EP. 5. Nature of Adhesion Through Silane Coupling Agents. *Silane Coupling Agents* [Internet]. 1st ed. New York, NY.: Springer; 1991. p. 115–51. Available from: [https://doi.org/10.1007/978-1-4899-2070-6\\_5](https://doi.org/10.1007/978-1-4899-2070-6_5)

89. Kalendová A, Veselý D, Kohl M, Stejskal J. Anticorrosion efficiency of zinc-filled epoxy coatings containing conducting polymers and pigments. *Prog Org Coatings* [Internet]. 2015;78:1–20. Available from: <https://doi.org/10.1016/j.porgcoat.2014.10.009>

90. Jagtap RN, Patil PP, Hassan SZ. Effect of zinc oxide in combating corrosion in zinc-rich primer. *Prog Org Coatings* [Internet]. 2008;63:389–94. Available from: <https://doi.org/10.1016/j.porgcoat.2008.06.012>

91. Drozd SA, Hawkins T, Clark L, Surratt M, Kingsley J, Palutke K, et al. Demonstration of a Nanomaterial-Modified Primer for Use in Corrosion-Inhibiting Coating Systems Construction Engineering [Internet]. DoD Corros. Prev. Control Progr. Washington, D.C.; 2011. Available from: <https://apps.dtic.mil/sti/citations/ADA558997>

92. Cho S, Chiu TM, Castaneda H. Electrical and electrochemical behavior of a zinc-rich epoxy coating system with carbon nanotubes as a diode-like material. *Electrochim Acta* [Internet]. Elsevier Ltd; 2019;316:189–201. Available from: <https://doi.org/10.1016/j.electacta.2019.05.116>

93. Felton LE, Raeder CH, Knorr DB. The Properties of Tin-Bismuth Alloy Solders. *J Miner Met Mater Soc* [Internet]. 1993;45:28–32. Available from: <https://doi.org/10.1007/BF03222377>

94. Wee A, Schneider R, Aquilino S. Use of low fusing alloy in dentistry. *J Prosthet*

Dent [Internet]. 1998;80:540–5. Available from: [https://doi.org/10.1016/S0022-3913\(98\)70029-0](https://doi.org/10.1016/S0022-3913(98)70029-0)

95. Ajiboye TO, Oyewo OA, Onwudiwe DC. The performance of bismuth-based compounds in photocatalytic applications. *Surfaces and Interfaces* [Internet]. Elsevier B.V.; 2021;23:100927. Available from: <https://doi.org/10.1016/j.surfin.2021.100927>

96. Arı M, Aksöz S, Ata Esener P, Öztürk E. Thermal, electrical, and mechanical properties of Sn-Ag-Zn solder alloys for BGA packaging. *Phys B Condens Matter* [Internet]. 2025;699. Available from: <https://doi.org/10.1016/j.physb.2024.416868>

97. Chaudhari R, Pardeshi O, Chandak D, Barawkar T, Dhanpalwar G. To study the effect of Ni particles on microstructures and mechanical properties of Indium-Bismuth solder alloy. *Mater Today Proc* [Internet]. Elsevier Ltd; 2023;113:101–5. Available from: <https://doi.org/10.1016/j.matpr.2023.08.043>

98. Handschuh-Wang S, Gan T, Rauf M, Yang W, Stadler FJ, Zhou X. The subtle difference between Galinstan (R) and eutectic GaInSn. *Materialia* [Internet]. Elsevier B.V.; 2022;26:101642. Available from: <https://doi.org/10.1016/j.mtla.2022.101642>

99. Lipchitz A, Harvel G, Sunagawa T. Experimental investigation of the thermal conductivity and viscosity of liquid In-Bi-Sn eutectic alloy (Field's metal) for use in a natural circulation experiential loop. *Int Conf Nucl Eng Proceedings, ICONE* [Internet]. 2015;2015-Janua. Available from: [https://doi.org/10.1299/jsmeicone.2015.23.\\_icone23-1\\_440](https://doi.org/10.1299/jsmeicone.2015.23._icone23-1_440)

100. Belmont Metals Inc. Low-Melting (Fusible) Alloys [Internet]. 2019. p. 3. Available from: [https://www.belmontmetals.com/wp-content/uploads/2017/09/LM5.pdf?srltid=AfmBOoov9ildg6tb8E0d7BFGcU1fuMu4YVT0J1dqWimo3u35Bxwk6f\\_2](https://www.belmontmetals.com/wp-content/uploads/2017/09/LM5.pdf?srltid=AfmBOoov9ildg6tb8E0d7BFGcU1fuMu4YVT0J1dqWimo3u35Bxwk6f_2)

101. Vianco PT, Rejent JA. Properties of ternary Sn-Ag-Bi solder alloys: Part I - thermal properties and microstructural analysis. *J Electron Mater* [Internet]. 1999;28:1127–37. Available from: <https://doi.org/10.1007/s11664-999-0250-4>

102. Fazal MA, Liyana NK, Rubaiee S, Anas A. A critical review on performance , microstructure and corrosion resistance of Pb-free solders. *Measurement* [Internet]. Elsevier Ltd; 2019;134:897–907. Available from: <https://doi.org/10.1016/j.measurement.2018.12.051>

103. Farina S, Morando C. Comparative corrosion behaviour of different Sn-based solder alloys. *J Mater Sci Mater Electron* [Internet]. 2015;26:464–71. Available from: <https://doi.org/10.1007/s10854-014-2422-0>

104. Ahmido A, Sabbar A, Zouihri H, Dakhsi K, Guedira F, Serghini-idrissi M, et al. Effect of bismuth and silver on the corrosion behavior of Sn – 9Zn alloy in NaCl 3 wt .% solution. *Mater Sci Eng B* [Internet]. Elsevier B.V.; 2011;176:1032–6. Available from: <http://dx.doi.org/10.1016/j.mseb.2011.05.034>

105. Liu G, Khorsand S, Ji S. Electrochemical corrosion behaviour of Sn-Zn- x Bi alloys used for miniature detonating cords. *J Mater Sci Technol* [Internet]. The editorial office of Journal of Materials Science & Technology; 2019;35:1618–28. Available from: <https://doi.org/10.1016/j.jmst.2019.03.026>

106. Thomas Goh FW, Liu Z, Hor TSA, Zhang J, Ge X, Zong Y, et al. A Near-Neutral Chloride Electrolyte for Electrically Rechargeable Zinc-Air Batteries. *J Electrochem Soc* [Internet]. 2014;161:A2080–6. Available from: <https://doi.org/10.1149/2.0311414jes>
107. Mori M, Miura K, Sasaki T, Ohtsuka T. Corrosion of tin alloys in sulfuric and nitric acids. *Corros Sci* [Internet]. 2002;44:887–98. Available from: [https://doi.org/10.1016/S0010-938X\(01\)00094-4](https://doi.org/10.1016/S0010-938X(01)00094-4)
108. Sun M, Yang X, Du C, Liu Z, Li Y, Wu Y. Distinct beneficial effect of Sn on the corrosion resistance of Cr – Mo low alloy steel. *J Mater Sci & Technol* [Internet]. Elsevier Ltd; 2021;81:175–89. Available from: <https://doi.org/10.1016/j.jmst.2020.12.014>
109. Yang C, Chen F, Gierlotka W, Chen S, Hsieh K, Huang L. Thermodynamic properties and phase equilibria of Sn – Bi – Zn ternary alloys. 2008;112:94–103. Available from: <https://doi.org/10.1016/j.matchemphys.2008.05.034>
110. Zhou S, Yang C han, Shen YA, Lin S kang, Nishikawa H. The newly developed Sn–Bi–Zn alloy with a low melting point, improved ductility, and high ultimate tensile strength. *Materialia* [Internet]. Elsevier Ltd; 2019;6:100300. Available from: <https://doi.org/10.1016/j.mtla.2019.100300>
111. Dezellus O, Eustathopoulos N. Fundamental issues of reactive wetting by liquid metals. *J Mater Sci* [Internet]. 2010;45:4256–64. Available from: <https://doi.org/10.1007/s10853-009-4128-x>
112. Carroll GT, Turro NJ, Mammana A, Koberstein JT. Photochemical Immobilization of Polymers on a Surface: Controlling Film Thickness and Wettability. *Photochem Photobiol* [Internet]. 2017;93:1165–9. Available from: <https://doi.org/10.1111/php.12751>
113. Pochly F, Fialova S, Kozubkova M, Zavadil L. Study of the Adhesive Coefficient Effect on the Hydraulic Losses and Cavitation. *Int J Fluid Mach Syst* [Internet]. 2010;3:386–95. Available from: <https://doi.org/10.5293/ijfms.2010.3.4.386>
114. Liu PL, Shang JK. Interfacial embrittlement by bismuth segregation in copper/tin–bismuth Pb-free solder interconnect. *J Mater Res* [Internet]. 2001;16:1651–9. Available from: <https://doi.org/10.1557/JMR.2001.0229>
115. Shafiq I, Chan YC, Xu S, Li QQ. Electro-migration study of nano Al doped lead-free Sn-58Bi on Cu and Au/Ni/Cu ball grid array (BGA) packages. *EMPC-2011 - 18th Eur Microelectron Packag Conf Proc* [Internet]. 2011;1–7. Available from: <https://ieeexplore.ieee.org/document/6142385>
116. Zhang L, Sun L, Guo Y huan. Microstructures and properties of Sn58Bi, Sn35Bi0.3Ag, Sn35Bi1.0Ag solder and solder joints. *J Mater Sci Mater Electron* [Internet]. Springer US; 2015;26:7629–34. Available from: <https://doi.org/10.1007/s10854-015-3400-x>
117. Zhang C, Liu SD, Qian GT, Zhou J, Xue F. Effect of Sb content on properties of Sn - Bi solders. *Trans Nonferrous Met Soc China (English Ed)* [Internet]. 2014;24:184–91. Available from: [https://doi.org/10.1016/S1003-6326\(14\)63046-6](https://doi.org/10.1016/S1003-6326(14)63046-6)

118. Dong W, Shi Y, Xia Z, Lei Y, Guo F. Effects of trace amounts of rare earth additions on microstructure and properties of Sn-Bi-based solder alloy. *J Electron Mater* [Internet]. 2008;37:982–91. Available from: <https://doi.org/10.1007/s11664-008-0458-8>
119. El-Bediwi AB, El-Bahay MM. Influence of silver on structural, electrical, mechanical and soldering properties of tin-indium based alloys. *Radiat Eff Defects Solids* [Internet]. 2004;159:133–40. Available from: <https://doi.org/10.1080/10420150410001670288>
120. Sjoukes F. Chemical reactions in fluxes for hot dip galvanizing. *Anti-Corrosion Methods Mater* [Internet]. 1990;37:12–4. Available from: <https://doi.org/10.1108/eb007267>
121. Sui R, Chang J, Cao R, Lin Q. Study of Flux/E-GaIn Interfacial Tension and Wetting Behavior of Fluxes. *J Electron Mater* [Internet]. Springer US; 2023;52:293–303. Available from: <https://doi.org/10.1007/s11664-022-09989-7>
122. Bastos AC, Quevedo MC, Karavai O V., Ferreira MGS. Review—On the Application of the Scanning Vibrating Electrode Technique (SVET) to Corrosion Research. *J Electrochem Soc* [Internet]. 2017;164:C973–90. Available from: <https://doi.org/10.1149/2.0431714jes>
123. Gnedenkov AS, Sinebryukhov SL, Mashtalyar D V., Gnedenkov S V. Localized corrosion of the Mg alloys with inhibitor-containing coatings: SVET and SIET studies. *Corros Sci* [Internet]. Elsevier Ltd; 2016;102:269–78. Available from: <http://dx.doi.org/10.1016/j.corsci.2015.10.015>
124. Gnedenkov AS, Mei D, Lamaka S V., Sinebryukhov SL, Mashtalyar D V., Vyaliy IE, et al. Localized currents and pH distribution studied during corrosion of MA8 Mg alloy in the cell culture medium. *Corros Sci* [Internet]. Elsevier; 2020;170:108689. Available from: <https://doi.org/10.1016/j.corsci.2020.108689>
125. Wint N, Barrett ZS, Williams G, McMurray HN. The Study of AA2024 De-Alloying Using Luminol Electrogenenerated Chemiluminescence Imaging. *J Electrochem Soc* [Internet]. 2019;166:C3417–30. Available from: <https://doi.org/10.1149/2.0481911jes>
126. Williams G, McMurray HN, Grace R. Inhibition of magnesium localised corrosion in chloride containing electrolyte. *Electrochim Acta* [Internet]. 2010;55:7824–33. Available from: <https://doi.org/10.1016/j.electacta.2010.03.023>
127. Williams G, Neil McMurray H. Localized Corrosion of Magnesium in Chloride-Containing Electrolyte Studied by a Scanning Vibrating Electrode Technique. *J Electrochem Soc* [Internet]. 2008;155:C340. Available from: <https://doi.org/10.1149/1.2918900>
128. Calado LM, Taryba MG, Morozov Y, Carmezim MJ, Montemor MF. Novel smart and self-healing cerium phosphate-based corrosion inhibitor for AZ31 magnesium alloy. *Corros Sci* [Internet]. Elsevier; 2020;170:108648. Available from: <https://doi.org/10.1016/j.corsci.2020.108648>
129. Sofian A, Noda K. Corrosion analysis of zinc rich epoxy coatings on steel in NaCl solution. 8th Pacific Rim Int Congr Adv Mater Process 2013, PRICM 8 [Internet]. 2013;3:2171–6. Available from: <https://doi.org/10.1007/978-3-319->



130. Adnan R, Chan YC, Jillek W, Islam S. Comparative study of wetting behavior and mechanical properties ( microhardness ) of Sn – Zn and Sn – Pb solders. *Microelectronics J* [Internet]. 2006;37:705–13. Available from: <https://doi.org/10.1016/j.mejo.2005.12.010>
131. Sorel M. Specification of a patent for a process for protecting articles made of Iron or Steel from Oxidation. *J Franklin Inst* [Internet]. 1895;22:54–6. Available from: <https://patents.google.com/patent/US1072091A/en>
132. Soufeiani L, Foliente G, Nguyen KTQ, San Nicolas R. Corrosion protection of steel elements in façade systems – A review. *J Build Eng* [Internet]. Elsevier Ltd; 2020;32:101759. Available from: <https://doi.org/10.1016/j.jobbe.2020.101759>
133. O'Reilly M, Farshadfar O, Darwin D, Browning J, Locke CE. Corrosion-induced concrete cracking for uncoated and galvanized reinforcing bars. *ACI Mater J* [Internet]. 2018;115:825–32. Available from: <https://doi.org/10.14359/5170683>
134. Pistofidis N, Vourlias G, Konidaris S, Pavlidou E, Stergiou A, Stergioudis G. The effect of bismuth on the structure of zinc hot-dip galvanized coatings. *Mater Lett* [Internet]. 2007;61:994–7. Available from: <https://doi.org/10.1016/j.matlet.2006.06.029>
135. Ikeda Y, Yuan R, Chakraborty A, Ghassemi-Armaki H, Zuo JM, Maaß R. Early stages of liquid-metal embrittlement in an advanced high-strength steel. *Mater Today Adv* [Internet]. Elsevier Ltd; 2022;13:100196. Available from: <https://doi.org/10.1016/j.mtadv.2021.100196>
136. Ikeda Y, Ni HC, Chakraborty A, Ghassemi-Armaki H, Zuo JM, Kamachali RD, et al. Segregation-induced grain-boundary precipitation during early stages of liquid-metal embrittlement of an advanced high-strength steel. *Acta Mater* [Internet]. 2023;259:37–40. Available from: <https://doi.org/10.1016/j.actamat.2023.119243>
137. Hong SH, Kang JH, Kim D, Kim SJ. Si effect on Zn-assisted liquid metal embrittlement in Zn-coated TWIP steels: Importance of Fe-Zn alloying reaction. *Surf Coatings Technol* [Internet]. Elsevier; 2020;393:125809. Available from: <https://doi.org/10.1016/j.surfcoat.2020.125809>
138. Murugan SP, Jeon JB, Ji C, Park Y Do. Liquid zinc penetration induced intergranular brittle cracking in resistance spot welding of galvanized advanced high strength steel. *Weld World* [Internet]. Welding in the World; 2020;64:1957–69. Available from: <https://doi.org/10.1007/s40194-020-00975-3>
139. Matsunaga H. X-Ray Structural Study of the Successive Phase Transitions in Ammonium Tetrachlorozincate, (NH<sub>4</sub>)<sub>2</sub>ZnCl<sub>4</sub>. I. Crystal Structure Determination. *J Phys Soc Japan* [Internet]. 1982;51:864–72. Available from: <https://doi.org/10.1143/JPSJ.51.864>
140. Gusakova O, Shepelevich V, Scherbachenko L. Effect of melt cooling rate on microstructure of Sn - Bi and Sn - Pb eutectic alloys. *Adv Mater Res* [Internet]. 2014;856:236–40. Available from: <https://doi.org/10.4028/www.scientific.net/AMR.856.236>
141. Kang H, Rajendran SH, Jung JP. Low Melting Temperature Sn-Bi Solder:

Effect of Alloying and Nanoparticle Addition on the Microstructural, Thermal, Interfacial Bonding, and Mechanical Characteristics. *Metals* (Basel) [Internet]. 2021;11:364. Available from: <https://doi.org/10.3390/met11020364>

142. Wu CML, Yu DQ, Law CMT, Wang L. Properties of lead-free solder alloys with rare earth element additions. *Mater Sci Eng R Reports* [Internet]. 2004;44:1–44. Available from: <https://doi.org/10.1016/j.mser.2004.01.001>

143. Luiz B, Reinhart G, Nguyen-thi H, Mangelinck-noël N, Garcia A, Eduardo J. Microstructural development and mechanical properties of a near-eutectic directionally solidified Sn – Bi solder alloy. *Mater Charact* [Internet]. Elsevier Inc.; 2015;107:43–53. Available from: <http://dx.doi.org/10.1016/j.matchar.2015.06.026>

144. Tan XF, Hao Q, Zhou J, Gu Q, McDonald SD, Sweatman K, et al. In-situ investigation of the time-temperature dependent lattice and microstructure of Sn-Bi alloys. *Materialia* [Internet]. Elsevier B.V.; 2024;33:101974. Available from: <https://doi.org/10.1016/j.mtla.2023.101974>

145. Gusakova O V., Galenko PK, Shepelevich VG, Alexandrov D V., Rettenmayr M. Diffusionless (chemically partitionless) crystallization and subsequent decomposition of supersaturated solid solutions in Sn-Bi eutectic alloy. *Philos Trans R Soc A Math Phys Eng Sci* [Internet]. 2019;377. Available from: <https://doi.org/10.1098/rsta.2018.0204>

146. Galib RH, Sharif A. Development of Zn-Mg Alloys as a Degradable Biomaterial. *Columbia Int Publ Adv Alloy Compd* [Internet]. 2016;1:1–7. Available from: <https://doi.org/10.7726/aac.2016.1001>

147. Huot JY. Chemistry, Electrochemistry, and Electrochemical Applications | Zinc. *Encycl Electrochem Power Sources* [Internet]. 2009;883–92. Available from: <https://doi.org/10.1016/B978-044452745-5.00061-7>

148. Lead-Free BGA Solder Joint Assembly Evaluation [Internet]. Free. *Semicond. Eng. Bull.* 2005. Available from: <https://www.nxp.com/docs/en/engineering-bulletin/EB635.pdf>

149. Yang Y, Wei Y, Wei T, Yan D, Zhang J, Wang L. Influence of composite powders' microstructure on the microstructure and properties of Al<sub>2</sub>O<sub>3</sub>–TiO<sub>2</sub> coatings fabricated by plasma spraying. *Mater Des* [Internet]. 2015;65:814–22. Available from: <https://doi.org/10.1016/j.matdes.2014.09.078>

150. Hartley PA, Parfitt GD, Pollack LB. The role of the van der Waals force in the agglomeration of powders containing submicron particles. *Powder Technol* [Internet]. 1985;42:35–46. Available from: [https://doi.org/10.1016/0032-5910\(85\)80036-X](https://doi.org/10.1016/0032-5910(85)80036-X)

151. Arai T. The thermo-reactive deposition and diffusion process for coating steels to improve wear resistance [Internet]. *Thermochem. Surf. Eng. Steels*. Woodhead Publishing Limited; 2015. Available from: <http://dx.doi.org/10.1533/9780857096524.5.703>

152. Blumenau M, Norden M, Friedel F, Peters K. Wetting force and contact angle measurements to evaluate the influence of zinc bath metallurgy on the galvanizability of high-manganese-alloyed steel. *Surf Coatings Technol* [Internet]. Elsevier B.V.; 2010;205:828–34. Available from:

<http://dx.doi.org/10.1016/j.surfcoat.2010.07.123>

153. Meng Y, Liu L, Zhang D, Dong C, Yan Y, Volinsky AA, et al. Initial formation of corrosion products on pure zinc in saline solution. *Bioact Mater* [Internet]. Elsevier; 2019;4:87–96. Available from: <https://doi.org/10.1016/j.bioactmat.2018.08.003>

154. Pourzolfaghar H, Hosseini S, Zuki FM, Alinejad M, Li YY. Recent advancements to mitigate zinc oxide formation in zinc-air batteries: A technical review. *Mater Today Commun* [Internet]. Elsevier Ltd; 2021;29:102954. Available from: <https://doi.org/10.1016/j.mtcomm.2021.102954>

155. Shith JA, Groover PE, Lennox Jr. TJ, Peterson MH. Naval Research laboratory Memorandum 2187: Marine Corrosion Studies. The Electrochemical Potential of High Purity Metals in Seawater [Internet]. Washington, D.C.; 1970. Available from: <https://apps.dtic.mil/sti/tr/pdf/AD0717340.pdf>

156. Berman A, Epstein M. Kinetic model for carboreduction of zinc oxide. *J Phys IV JP* [Internet]. 1999;9:3–8. Available from: <https://doi.org/10.1051/jp4:1999349>

157. Mitchell AR, Parker RH. The reduction of SnO<sub>2</sub> and Fe<sub>2</sub>O<sub>3</sub> by solid carbon. *Miner Eng* [Internet]. 1988;1:53–66. Available from: [https://doi.org/10.1016/0892-6875\(88\)90066-0](https://doi.org/10.1016/0892-6875(88)90066-0)

158. Karakaya N, Zhang M, Zhang J, Zuniga J. Chemical and Electrochemical Reduction of Solid Oxide Fuel. *J Nucl Mater* [Internet]. Elsevier B.V.; 2024;596:155089. Available from: <https://doi.org/10.1016/j.jnucmat.2024.155089>

159. Bychkov A V., Ishunin VS, Kormilitsyn M V. Reduction of uranium oxides with lithium in a lithium chloride melt. *Radiochemistry* [Internet]. 2009;51:464–8. Available from: <https://doi.org/10.1134/S1066362209050051>

160. Arenas MF, Acoff VL. Contact angle measurements of Sn-Ag and Sn-Cu lead-free solders on copper substrates. *J Electron Mater* [Internet]. 2004;33:1452–8. Available from: <https://doi.org/10.1007/s11664-004-0086-x>

161. Zhang XR, Yuan ZF, Zhao HX, Zang LK, Li JQ. Wetting behavior and interfacial characteristic of Sn-Ag-Cu solder alloy on Cu substrate. *Chinese Sci Bull* [Internet]. 2010;55:797–801. Available from: <https://doi.org/10.1007/s11434-010-0056-z>

162. Silva BL, Gouveia GL, Cheung N, Garcia A, Spinelli JE. Analysis of extensive wetting angle vs. cooling rate data in Bi-, Zn- and Sn-based solder alloys. *Microelectron Reliab* [Internet]. 2022;135. Available from: <https://doi.org/10.1016/j.microrel.2022.114593>

163. Eustathopoulos N. Wetting by liquid metals—application in materials processing: The contribution of the grenoble group. *Metals (Basel)* [Internet]. 2015;5:350–70. Available from: <https://doi.org/10.3390/met5010350>

164. Ribas M, Kumar A, Kosuri D, Rangaraju RR, Choudhury P, Telu S, et al. Low Temperature Soldering Using Sn-Bi Alloys. *Proc SMTA Int* [Internet]. 2017;1:201–6. Available from: <https://smtnet.com/library/files/upload/Sn-Bi-alloys-soldering.pdf>

165. Chen OH, Gao J, Pan TCC, Kwan Tang K, Aspandiar R, Byrd K, et al. Solder Joint Reliability on Mixed Sac-Bisn Ball Grid Array Solder Joints Formed With

- Resin Reinforced Bi-Sn Metallurgy Solder Pastes. Proc SMTA Int [Internet]. 2016;216–28. Available from: [http://www.circuitinsight.com/pdf/Solder\\_Joint\\_Reliability\\_Mixed\\_SAC-BISN\\_Ball\\_Grid\\_Array\\_Solder\\_Joints\\_Formed\\_With\\_Resin\\_Reinforced\\_BI-SN\\_Metallurgy\\_Solder\\_Pastes\\_smta.pdf](http://www.circuitinsight.com/pdf/Solder_Joint_Reliability_Mixed_SAC-BISN_Ball_Grid_Array_Solder_Joints_Formed_With_Resin_Reinforced_BI-SN_Metallurgy_Solder_Pastes_smta.pdf)
166. Alvarez V, Beaulieu P, Lee K-W, Nah J-W, Turlapati L. No clean flux composition and methods for use thereof [Internet]. 2019. Available from: <https://patents.justia.com/patent/10350713>
167. Khan NZ, Islam SSU, Khan MM, Siddiquee AN. Steel heat treatment: Equipment and process design [Internet]. 2nd ed. Ref. Modul. Mater. Sci. Mater. Eng. Elsevier Ltd.; 2024. Available from: <http://dx.doi.org/10.1016/B978-0-323-96020-5.00249-1>
168. Kumar V, Kumar MR, Behera CK. Analysis Of Corrosion Behavior And Its Characterization Of In-Sn- Bi Alloy. Mater Today Proc [Internet]. Elsevier Ltd.; 2019;18:2322–8. Available from: <https://doi.org/10.1016/j.matpr.2019.07.015>
169. Tunthawiroon P, Kanlayasiri K. Effects of Ag contents in Sn – x Ag lead-free solders on microstructure , corrosion behavior and interfacial reaction with Cu substrate. Trans Nonferrous Met Soc China [Internet]. The Nonferrous Metals Society of China; 2019;29:1696–704. Available from: [http://dx.doi.org/10.1016/S1003-6326\(19\)65076-4](http://dx.doi.org/10.1016/S1003-6326(19)65076-4)
170. Delong H, Defu L, Li H, Lianqin J. Effect of lanthanum addition on microstructure and corrosion behavior of Al-Sn-Bi anodes. J Rare Earths [Internet]. The Chinese Society of Rare Earths; 2011;29:129–32. Available from: [http://dx.doi.org/10.1016/S1002-0721\(10\)60417-6](http://dx.doi.org/10.1016/S1002-0721(10)60417-6)
171. Kikuchi T, Hara Y, Sakairi M, Yonezawa T, Yamauchi A. Corrosion of Al–Sn–Bi alloys in alcohol at high temperatures. Part I : Effects of the metallurgical structure of the alloys and the metal salt additions to alcohol. Corros Sci [Internet]. Elsevier Ltd; 2010;52:1482–91. Available from: <http://dx.doi.org/10.1016/j.corsci.2009.12.007>
172. Tsai Y-D, Yu C-Y, Hu C-C, Duh J-G. Pulse Electroplating of Sn-Bi Alloys on Micropatterned Electrodes for Lead-Free Solder Bumping. J Electrochem Soc [Internet]. 2011;159:D108–13. Available from: <https://doi.org/10.1149/2.083202jes>
173. Choudhary S, Garg A, Mondal K. Relation Between Open Circuit Potential and Polarization Resistance with Rust and Corrosion Monitoring of Mild Steel. J Mater Eng Perform [Internet]. Springer US; 2016;25:2969–76. Available from: <https://doi.org/10.1007/s11665-016-2112-6>
174. Nanna ME, Bierwagen GP. Mg-rich coatings: A new paradigm for Cr-free corrosion protection of Al aerospace alloys. J Coatings Technol Res [Internet]. 2004;1:69–80. Available from: <https://doi.org/10.1007/s11998-004-0001-7>
175. Forero-Sandoval IY, Franco-Bacca AP, Cervantes-Álvarez F, Gómez-Heredia CL, Ramírez-Rincón JA, Ordonez-Miranda J, et al. Electrical and thermal percolation in two-phase materials: A perspective. J Appl Phys [Internet]. 2022;131. Available from: <https://doi.org/10.1063/5.0091291>
176. Bardeen J. Electrical conductivity of metals. J Appl Phys [Internet].

- 1940;11:88–111. Available from: <https://doi.org/10.1063/1.1712751>
177. Chester GV, Thellung A. On the electrical conductivity of metals. *Proc Phys Soc [Internet]*. 1959;73:745. Available from: <https://doi.org/10.1088/0370-1328/73/5/308>
178. Zingametall. Zinga Safety Data Sheet [Internet]. 2015. Available from: <https://www.zingausa.com/wp-content/uploads/2014/02/ZINGA-MSDS.pdf>
179. Shreepathi S, Bajaj P, Malik BP. Electrochemical impedance spectroscopy investigations of epoxy zinc rich coatings: Role of Zn content on corrosion protection mechanism. *Electrochim Acta*. 2010;55:5129–5134.
180. Vernon WHJ. First (experimental) report to the atmospheric corrosion research committee (of the British Non-Ferrous Metals Research Association). *Trans Faraday Soc [Internet]*. 1923;19:839–45. Available from: <https://doi.org/10.1038/115417a0>
181. Vernon WHJ. Second (experimental) report to the atmospheric corrosion research committee (of the British Non-Ferrous Research Association). *Trans Faraday Soc [Internet]*. 1927;23:113–83. Available from: <https://doi.org/10.1039/TF9272300113>
182. Hudson JC. Third (experimental) report to the atmospheric corrosion research committee (of the British Non-Ferrous Metals Research Association). *Trans Faraday Soc [Internet]*. 1929;25:178–252. Available from: <https://doi.org/10.1039/TF9292500177>
183. Yamashita M, Konishi H, Kozakura T, Mizuki J, Uchida H. In situ observation of initial rust formation process on carbon steel under Na<sub>2</sub>SO<sub>4</sub> and NaCl solution films with wet/dry cycles using synchrotron radiation X-rays. *Corros Sci [Internet]*. 2005;47:2492–8. Available from: <https://doi.org/10.1016/j.corsci.2004.10.021>
184. Tuthill AH, Avery RE. Specifying Stainless Steel Surface Treatments [Internet]. *NiDI Tech. Ser.* 1992. Available from: <https://doi.org/10.1108/eb030017>
185. Abreu CM, Izquierdo M, Merino P, Nóvoa XR, Pérez C. A new approach to the determination of the cathodic protection period in zinc-rich paints. *Corrosion [Internet]*. 1999;55:1173–81. Available from: <https://doi.org/10.5006/1.3283955>
186. Association EGG. The Coating [Internet]. European General Galvanizers Association; 2010. Available from: <https://www.galvanizingeurope.org/galvanizing/the-coating/>
187. Mahdavian Ahadi M, Mohammadzadeh Attar M. OCP measurement: A method to determine CPVC. *Sci Iran [Internet]*. 2007;14:369–72. Available from: [https://scientiairanica.sharif.edu/article\\_2861\\_e5039ced241d2d9dee91188bd6f265da.pdf](https://scientiairanica.sharif.edu/article_2861_e5039ced241d2d9dee91188bd6f265da.pdf)
188. Zhang X, Li C, Gao Z, Liu Y, Ma Z, Yu L, et al. Correlation between Zn-Rich Phase and corrosion/oxidation behavior of Sn–8Zn–3Bi alloy. *Metals (Basel) [Internet]*. 2016;6. Available from: <https://doi.org/10.3390/met6080175>
189. Glass GK. Deterioration of Steel Reinforced Concrete. *Compr Struct Integr [Internet]*. 2003;6:321–250. Available from: <https://doi.org/10.1016/B0-08-043749-4/06140-1>

190. Francis RA. Sixty Years of Inorganic Zinc Coatings: History, Chemistry, Properties, Applications and Alternatives [Internet]. 1st ed. Francis RA, editor. Preston, Australia: Australian Corrosion Association; 1997. Available from: <https://shorturl.at/kViJf>
191. Pan D, Zhang L, Zhuang J, Lu W, Zhu R, Qin W. New application of tin – bismuth alloy for electrochemical determination of cadmium. *Mater Lett* [Internet]. Elsevier B.V.; 2012;68:472–4. Available from: <http://dx.doi.org/10.1016/j.matlet.2011.11.038>
192. Slot HM, Gelinck ERM, Rentrop C, Van der Heide E. Leading edge erosion of coated wind turbine blades: Review of coating life models. *Renew Energy* [Internet]. Elsevier Ltd; 2015;80:837–48. Available from: <http://dx.doi.org/10.1016/j.renene.2015.02.036>
193. Li HJ, Feng T, Fu QG, Wu H, Shen XT. Oxidation and erosion resistance of MoSi<sub>2</sub>-CrSi<sub>2</sub>-Si/SiC coated C/C composites in static and aerodynamic oxidation environment. *Carbon N Y* [Internet]. Elsevier Ltd; 2010;48:1636–42. Available from: <http://dx.doi.org/10.1016/j.carbon.2010.01.005>
194. Peng S, Wang T, Huang G, Tang Z, Shao Z, Feng Z, et al. Unraveling the complex infiltration and repairing behaviors in defect coatings. *J Mater Sci Technol* [Internet]. Elsevier Ltd; 2024;187:258–69. Available from: <https://doi.org/10.1016/j.jmst.2023.11.037>
195. Hu M, Tang Y, Han X, Guo C, Lu X, Pan M. Failure behavior of Cr coating on PCrNi<sub>3</sub>MoVA steel under thermal-mechanical factors. *Mater Chem Phys* [Internet]. Elsevier B.V.; 2024;312:128691. Available from: <https://doi.org/10.1016/j.matchemphys.2023.128691>
196. Voorwald HJC, Padilha R, Costa MYP, Pigatin WL, Cioffi MOH. Effect of electroless nickel interlayer on the fatigue strength of chromium electroplated AISI 4340 steel. *Int J Fatigue* [Internet]. 2007;29:695–704. Available from: <https://doi.org/10.1016/j.ijfatigue.2006.07.004>
197. de Godoi RP, Camilo Magalhães DC, Avalos M, Bolmaro RE, Sordi VL, Kliauga AM. Microstructure, texture and interface integrity in sheets processed by Asymmetric Accumulative Roll-Bonding. *Mater Sci Eng A* [Internet]. 2020;771. Available from: <https://doi.org/10.1016/j.msea.2019.138634>
198. Daniel EF, Wang C, Li C, Dong J, Udoh II, Zhang D, et al. Evolution of corrosion degradation in galvanised steel bolts exposed to a tropical marine environment. *J Mater Res Technol* [Internet]. 2023;27:5177–90. Available from: <https://doi.org/10.1016/j.jmrt.2023.10.295>
199. Gonczy ST, Randall N. An ASTM standard for quantitative scratch adhesion testing of thin, hard ceramic coatings. *Int J Appl Ceram Technol* [Internet]. 2005;2:422–8. Available from: <https://doi.org/10.1111/j.1744-7402.2005.02043.x>
200. Li LF, Caenen P, Daerden M, Vaes D, Meers G, Dhondt C, et al. Mechanism of single and multiple step pickling of 304 stainless steel in acid electrolytes. *Corros Sci* [Internet]. 2005;47:1307–24. Available from: <https://doi.org/10.1016/j.corsci.2004.06.025>
201. Homjabok W, Permpoon S, Lothongkum G. Pickling Behavior of AISI 304

- Stainless Steel in Sulfuric and Hydrochloric Acid Solutions. *J Met Mater Miner* [Internet]. 2010;20:1–6. Available from: <https://jmmm.material.chula.ac.th/index.php/jmmm/article/view/202/229>
202. Cook TH. Composition, testing, and control of hot dip galvanizing flux. *Met Finish* [Internet]. 2003;101:22–35. Available from: [https://doi.org/10.1016/S0026-0576\(03\)90187-5](https://doi.org/10.1016/S0026-0576(03)90187-5)
203. Joseph R. Wash Primer Improves Paint Adhesion on Aluminum Extrusions. *Met Finish* [Internet]. 2005;103:50–1. Available from: <https://www.paintcenter.org/rj/jan05h.php>
204. Brunet M, Cochard A, Deshayes C, Brouca-Cabarrecq C, Robbiola L, Olivier JM, et al. Study of Post-World War II French Aeronautical Aluminium Alloy and Coatings: Historical and Materials Science Approach. *Stud Conserv* [Internet]. Taylor & Francis; 2020;65:103–17. Available from: <https://doi.org/10.1080/00393630.2019.1610846>
205. Hosoda AY., Takatsuki TS, Suzuki N, Ikeda S. Anticorrosive primer composition: U.S. Patent 5,468,461. Nov. 21, 1995. *Met Finish* [Internet]. 1996;94:93. Available from: [https://doi.org/10.1016/S0026-0576\(96\)97968-4](https://doi.org/10.1016/S0026-0576(96)97968-4)
206. Meijun L, Xu L, Zhu C, Li Z, Wei S. Research progress of high entropy alloy: Surface treatment improves friction and wear properties. *J Mater Res Technol* [Internet]. Elsevier B.V.; 2024;28:752–73. Available from: <https://doi.org/10.1016/j.jmrt.2023.12.011>
207. Hatano A, Namiki K. Application of hard shot peening to automotive transmission gears. *SAE Tech Pap 920760* [Internet]. 1992; Available from: <https://doi.org/10.4271/920760>
208. Shen L, Zhao W, Wang K, Xu J. GO-Ti<sub>3</sub>C<sub>2</sub> two-dimensional heterojunction nanomaterial for anticorrosion enhancement of epoxy zinc-rich coatings. *J Hazard Mater* [Internet]. Elsevier B.V.; 2021;417:126048. Available from: <https://doi.org/10.1016/j.jhazmat.2021.126048>
209. Kalendova A. Effects of particle sizes and shapes of zinc metal on the properties of anticorrosive coatings. *Prog Org Coatings* [Internet]. 2003;46:324–32. Available from: [https://doi.org/10.1016/S0300-9440\(03\)00022-5](https://doi.org/10.1016/S0300-9440(03)00022-5)
210. Alemdag Y, Beder M. Effects of zinc content on strength and wear performance of Al–12Si–3Cu based alloy. *Trans Nonferrous Met Soc China (English Ed)* [Internet]. The Nonferrous Metals Society of China; 2019;29:2463–71. Available from: [http://dx.doi.org/10.1016/S1003-6326\(19\)65154-X](http://dx.doi.org/10.1016/S1003-6326(19)65154-X)
211. Seemuth PD, Zimmer H. Germanium, Tin and Lead. *Annu Reports Inorg Gen Synth* [Internet]. 1977;49–63. Available from: <https://doi.org/10.1016/b978-0-12-040705-7.50008-4>
212. Wardell JL. Arsenic, Antimony and Bismuth. *Compr Organomet Chem* [Internet]. 1982;2:681–707. Available from: <https://doi.org/10.1016/B978-008046518-0.00021-0>
213. Hampshire WB. Tin Alloys: Alloying, Properties, and Applications. *Encycl Mater Sci Technol (Second Ed)* [Internet]. 2001;9351–4. Available from:

<https://doi.org/10.1016/B0-08-043152-6/01686-7>

214. Pepin X, Simons SJR, Blanchon S, Rossetti D, Couarraze G. Hardness of moist agglomerates in relation to interparticle friction, granule liquid content and nature. *Powder Technol* [Internet]. 2001;117:123–38. Available from: [https://doi.org/10.1016/S0032-5910\(01\)00324-2](https://doi.org/10.1016/S0032-5910(01)00324-2)

215. Nayebi A, El Abdi R, Bartier O, Mauvoisin G. Hardness profile analysis of elasto-plastic heat-treated steels with a gradient in yield strength. *Mater Sci Eng A* [Internet]. 2002;333:160–9. Available from: [https://doi.org/10.1016/S0921-5093\(01\)01830-5](https://doi.org/10.1016/S0921-5093(01)01830-5)

216. Caprili S, Mattei F, Mazzatura I, Ferrari F, Gammino M, Mariscotti M, et al. Evaluation of mechanical characteristics of steel bars by nondestructive Vickers micro-hardness tests. *Procedia Struct Integr* [Internet]. Elsevier B.V.; 2022;44:886–93. Available from: <https://doi.org/10.1016/j.prostr.2023.01.115>

217. Cestari A, de Araújo M, de Oliveira DC. Corrosion behavior of metallic surfaces in biodiesel evaluated by Atomic Force Microscopy, Vickers Micro Hardness, and Copper Strip Test. *Eng Fail Anal* [Internet]. Elsevier Ltd; 2021;124:105329. Available from: <https://doi.org/10.1016/j.engfailanal.2021.105329>

218. Callister WD, Rethwisch DG. *Materials Science And Engineering An Introduction*. 8th ed. Hoboken, New Jersey: John Wiley & Sons, Inc.; 2009.

219. Sinha VR, Trehan A. Biodegradable microspheres for protein delivery. *J Control Release* [Internet]. 2003;90:261–80. Available from: [https://doi.org/10.1016/s0168-3659\(03\)00194-9](https://doi.org/10.1016/s0168-3659(03)00194-9)

220. Kamal M, Mazen S, El-Bediwi AB, Kashita E. Microstructure, electrical, mechanical and thermal properties of melt-spun bismuth-tin eutectic alloy. *Radiat Eff Defects Solids* [Internet]. 2006;161:143–8. Available from: <https://doi.org/10.1080/10420150500493709>

221. Kaya M. Current WEEE recycling solutions [Internet]. *Waste Electr. Electron. Equip. Recycl. Aqueous Recover. Methods*. Elsevier Ltd; 2018. Available from: <http://dx.doi.org/10.1016/B978-0-08-102057-9.00003-2>

222. Takaku Y, Liu XJ, Ohnuma I, Kainuma R, Ishida K. Interfacial reaction and morphology between molten Sn base solders and Cu substrate. *Mater Trans* [Internet]. 2004;45:646–51. Available from: <https://doi.org/10.2320/matertrans.45.646>

223. Bryant D, Mabbett I, Greenwood P, Watson T, Wijdekop M, Worsley D. Ultrafast near-infrared curing of PEDOT:PSS. *Org Electron physics, Mater Appl* [Internet]. Elsevier B.V.; 2014;15:1126–30. Available from: <http://dx.doi.org/10.1016/j.orgel.2014.03.001>

224. Lee EH, Hwang JS, Lee CW, Yang DY, Yang WH. A local heating method by near-infrared rays for forming of non-quenchable advanced high-strength steels. *J Mater Process Technol* [Internet]. Elsevier B.V.; 2014;214:784–93. Available from: <http://dx.doi.org/10.1016/j.jmatprotec.2013.11.023>

225. Pike C. Near Infrared Measurements - How Do They Work? [Internet]. *KPM Anal.* [cited 2024 Jun 1]. Available from: <https://www.kpmanalytics.com/blog/near->



infrared-measurements-how-do-they-work

226. Banwell CN. Raman Spectroscopy. Fundam Mol Spectrosc [Internet]. 3rd ed. London; 1983. p. 124–54. Available from: <http://www.rnlkwc.ac.in/pdf/study-material/chemistry/Spectroscopy.pdf>
227. Wang L, Li Q. Photochromism into nanosystems: Towards lighting up the future nanoworld. Chem Soc Rev [Internet]. Royal Society of Chemistry; 2018;47:1044–97. Available from: <http://dx.doi.org/10.1039/c7cs00630f>
228. Xue P, Bisoyi HK, Chen Y, Zeng H, Yang J, Yang X, et al. Near-Infrared Light-Driven Shape-Morphing of Programmable Anisotropic Hydrogels Enabled by MXene Nanosheets. Angew Chemie - Int Ed [Internet]. 2021;60:3390–6. Available from: <https://doi.org/10.1002/anie.202014533>
229. Chen Y, Valenzuela C, Zhang X, Yang X, Wang L, Feng W. Light-driven dandelion-inspired microfliers. Nat Commun [Internet]. 2023;14:1–10. Available from: <https://doi.org/10.1038/s41467-023-38792-z>
230. Ma S, Xue P, Valenzuela C, Zhang X, Chen Y, Liu Y, et al. Highly Stretchable and Conductive MXene-Encapsulated Liquid Metal Hydrogels for Bioinspired Self-Sensing Soft Actuators. Adv Funct Mater [Internet]. 2024;34:1–12. Available from: <https://doi.org/10.1002/adfm.202309899>
231. Xue P, Valenzuela C, Ma S, Zhang X, Ma J, Chen Y, et al. Highly Conductive MXene/PEDOT:PSS-Integrated Poly(N-Isopropylacrylamide) Hydrogels for Bioinspired Somatosensory Soft Actuators. Adv Funct Mater [Internet]. 2023;33:1–11. Available from: <https://doi.org/10.1002/adfm.202214867>
232. Schmitz C, Oprych D, Kutahya C, Strehmel B. NIR light for initiation of Photopolymerization. In: Lalevée J, Fouassier J-P, editors. Photopolymerisation Initiat Syst [Internet]. The Royal Society of Chemistry; 2018. p. 431–78. Available from: <https://doi.org/10.1039/9781788013307-00431>
233. Gabe DR, Clarke M. 4 . 07 Plated Coatings. Shreir’s Corros [Internet]. 2010;4:2577–609. Available from: <https://doi.org/10.1016/B978-044452787-5.00138-4>
234. Kuppe C, Rusimova KR, Ohnoute L, Slavov D, Valev VK. “Hot” in Plasmonics: Temperature-Related Concepts and Applications of Metal Nanostructures. Adv Opt Mater [Internet]. 2020;8. Available from: <https://doi.org/10.1002/adom.201901166>
235. Watanabe K. Photochemistry on nanoparticles [Internet]. Encycl. Interfacial Chem. Surf. Sci. Electrochem. Elsevier; 2018. Available from: <http://dx.doi.org/10.1016/B978-0-12-409547-2.13211-1>
236. Jang YH, Jang YJ, Kim S, Quan LN, Chung K, Kim DH. Plasmonic Solar Cells: From Rational Design to Mechanism Overview. Chem Rev [Internet]. 2016;116:14982–5034. Available from: <https://doi.org/10.1021/acs.chemrev.6b00302>
237. Goldenberg H, Tranter CJ. Heat flow in an infinite medium heated by a sphere. Br J Appl Phys [Internet]. 1952;3:296–8. Available from: <https://doi.org/10.1088/0508-3443/3/9/307>

238. Baffou G, Quidant R, Girard C. Heat generation in plasmonic nanostructures: Influence of morphology. *Appl Phys Lett* [Internet]. 2009;94:1–4. Available from: <https://doi.org/10.1063/1.3116645>
239. Govorov AO, Richardson HH. Generating heat with metal nanoparticles. *Nano Today* [Internet]. 2007;2:30–8. Available from: [https://doi.org/10.1016/S1748-0132\(07\)70017-8](https://doi.org/10.1016/S1748-0132(07)70017-8)
240. Nassau K. The causes of color. *Sci Am* [Internet]. 1980;243:124–54. Available from: <https://doi.org/10.1038/scientificamerican1080-124>
241. Qi F, Yang Z, Zhang J, Wang Y, Qiu Q, Li H. Interfacial Reaction-Induced Defect Engineering: Enhanced Visible and Near-Infrared Absorption of Wide Band Gap Metal Oxides with Abundant Oxygen Vacancies. *ACS Appl Mater Interfaces* [Internet]. 2020;12:55417–25. Available from: <https://doi.org/10.1021/acsami.0c16543>
242. Embden J Van, Latham K, Tachibana Y. Near-Infrared Absorbing Cu<sub>12</sub>Sb<sub>4</sub>S<sub>13</sub> and Cu<sub>3</sub>SbS<sub>4</sub> Nanocrystals: Synthesis, Characterization, and Photoelectrochemistry. *J Am Chem Soc* [Internet]. 2013;135:11562. Available from: <https://doi.org/10.1021/ja402702x>
243. Van Dusen MS. Note on the theory of heat conduction. *Bur Stand J Res* [Internet]. 1930;4:753–6. Available from: [https://nvlpubs.nist.gov/nistpubs/jres/4/jresv4n6p753\\_A2b.pdf](https://nvlpubs.nist.gov/nistpubs/jres/4/jresv4n6p753_A2b.pdf)
244. Storm ML. Heat conduction in simple metals. *J Appl Phys* [Internet]. 1951;22:940–51. Available from: <https://doi.org/10.1063/1.1700076>
245. Webster WL. Phenomena Occurring in the Melting of Metals. *Proc R Soc London Ser A, Contain Pap a Math Phys Character* [Internet]. 1933;140:653–60. Available from: <https://doi.org/10.1098/rspa.1933.0094>
246. Hooper K, Carnie M, Charbonneau C, Watson T. Near Infrared Radiation as a Rapid Heating Technique for TiO<sub>2</sub> Films on Glass Mounted Dye-Sensitized Solar Cells. *Int J Photoenergy* [Internet]. 2014;2014:1–8. Available from: <https://doi.org/10.1155/2014/953623>
247. Mabbett I, Geary S, Warren DJ, Sullivan JH, Penney D, Watson TM, et al. Near Infrared Heat Treatment to Flow Melt Tinplate. *ECS Trans* [Internet]. 2013;50:155–64. Available from: <https://doi.org/10.1149/05037.0155ecst>
248. Gines MJL, Benítez GJ, Egli W, Zubimendi JL, Pérez T. Formation of an Fe-Sn Intermetallic Layer during the Reflow Process after Tin Plating. *Plat Surf Finish* [Internet]. 2003;90:44–9. Available from: <https://sterc.org/pdf/psf2003/100344.pdf>
249. Frankenthal RP, Loginow AW. Kinetics of the Formation of the Iron - Tin Alloy Kinetics of the Formation of the Iron-Tin Alloy FeSn<sub>2</sub>. *J Electrochem Soc* [Internet]. 1960;107:920–3. Available from: <https://doi.org/10.1149/1.2427542>
250. Jones JC. A study of the zinc chloride flux used in the manufacture of tinplates. *Trans Faraday Soc* [Internet]. 1930;26:249–54. Available from: <https://doi.org/10.1039/TF9302600249>
251. Hitchcock SJ, Carroll NT, Nicholas MG. Some effects of substrate roughness on wettability. *J Mater Sci* [Internet]. 1981;16:714–32. Available from:

<https://doi.org/10.1007/bf00552210>

252. Chen YY, Duh JG, Chiou BS. Effect of substrate surface roughness on the wettability of Sn-Bi solders. *J Mater Sci Mater Electron* [Internet]. 2000;11:279–83. Available from: <https://doi.org/10.1023/A:1008917530144>